DEVELOPMENT OF AN INSULATING CROSS-ARM FOR OVERHEAD LINES

A thesis submitted to The University of Manchester for the degree of

Doctor of Philosophy

in the Faculty of Engineering and Physical Sciences

2014

CHRISTOS ZACHARIADES

SCHOOL OF ELECTRICAL AND ELECTRONIC ENGINEERING

TABLE OF CONTENTS

Word count: 51910

LIST OF FIGURES

LIST OF TABLES

LIST OF ABREVIATIONS

ABS : Acrylonitrile Butadiene Styrene

AC : Alternating Current

ATH : Alumina Trihydrate

BEM : Boundary Element Method

CAD : Computer Aided Design

CI : Confidence Interval

CIV : Corona Inception Voltage

DAQ : Data Acquisition

DC : Direct Current

DIAS : Digital Impulse Analysing System

EMF : Electromagnetic Field

EPDM : Ethylene Propylene Diene Monomer

EPRI : Electric Power Research Institute

FEA : Finite Element Analysis

FEM : Finite Element Method

FRP : Fibre Reinforced Polymer

FTP : File Transfer Protocol

HTM : Hydrophobicity Transfer Material

HV : High Voltage

IBVP : Interior Boundary Value Problem

ICA : Insulating Cross-arm

IEEE : Institute of Electrical and Electronics Engineers

LMW : Low Molecular Weight

LV : Low Voltage

NCI : Non-Ceramic Insulator

OHL : Overhead Line

PDE : Partial Differential Equation

PWD : Present Weather Detector

SE : Standard Error

SiR : Silicone Rubber

SMD : Sauter Mean Diameter

SML : Specified Mechanical Load

ABSTRACT

A novel insulating cross-arm (ICA) was developed for new and existing overhead transmission lines of up to 400 kV. The cross-arm consists of four insulating members, end fittings, field grading devices and a nose connection for the attachment of the conductor. The two main structural elements of the assembly have a unique non-cylindrical geometry which gives them improved mechanical characteristics compared to conventional overhead line insulators.

The profile for the compression insulator was designed. After examining six profile variations, it was determined that the lateral orientation which would give the best performance would be with the flat face of the core facing upwards and tilted by 6^{o}. Using the results obtained from performing flashover tests on a conventional 145 kV insulator, the elevation angle for the compression insulator was set to 6^{o}. The dimensions of the compression insulator were calculated based on the assumption that the ICA would be used to uprate an OHL with L3 towers from 275 kV to 400 kV. The optimal insulator profile was determined to be an alternating profile with three different shed sizes, an arcing distance of 3083 mm and a creepage distance of 12470 mm.

Electric field grading devices for the ICA were designed. For the LV end, a grading device resembling a ring which follows the general shape of the cross-section of the insulator was designed. For the HV end, an iterative process yielded two designs. First, the 'butterfly' grading device was a unibody piece of cast aluminium for all four ICA members. FEA simulations and tests in the laboratory showed that it could effectively control the electric field at voltages of up to 132 kV. The design was patented and the device was used on six cross-arms installed on a live line in Scotland in August 2013. Second, the 'M-W' grading device, was a solution made out of four components for managing the field at voltages of up to 400 kV. The device was designed to be easy to install and service, easy and cheap to manufacture and to have minimal visual impact.

The compression insulator and the cross-arm assembly were subjected to a multitude of tests adapted from international standards and the Technical Specifications of National Grid. The performed tests aimed to test the electrical characteristics of the cross-arm and the quality of the materials and manufacturing process of the compression insulator. All of the tests were completed successfully except from the corona extinction test for which the appropriate equipment was not available at the time.

Two trials were commissioned to examine how the cross-arm performs in a service-like environment. The snow and ice accretion patterns recorded at the mechanical trial site were used for optimising the profile of the compression insulator. The results after a year of continuous monitoring of leakage current and weather conditions at the live trial site showed that there were humidity and visibility thresholds, above 93% for the former and below 400 m for the latter, which increased the average leakage current by 15% on the tension insulators and by 20% on the compression insulators. It was found that when the longitudinal axis of the cross-arm was perpendicular to the weather the leakage current was higher because more of its surface was exposed. The performance of the novel compression insulators was found to be as good as that of the industry standard tension insulators, reaffirming the potency of the design. Finally, on-site observations showed that the 'butterfly' grading device could not effectively manage the electric field on the cross-arm at 400 kV, confirming the results of the FEA simulations and testing.

DECLARATION

No portion of the work referred to in the thesis has been submitted in support of an application for another degree or qualification of this or any other university or other institute of learning.

COPYRIGHT STATEMENT

i. The author of this thesis (including any appendices and/or schedules to this thesis) owns certain copyright or related rights in it (the "Copyright") and s/he has given The University of Manchester certain rights to use such Copyright, including for administrative purposes.

ii. Copies of this thesis, either in full or in extracts and whether in hard or electronic copy, may be made only in accordance with the Copyright, Designs and Patents Act 1988 (as amended) and regulations issued under it or, where appropriate, in accordance with licensing agreements which the University has from time to time. This page must form part of any such copies made.

iii. The ownership of certain Copyright, patents, designs, trademarks and other intellectual property (the "Intellectual Property") and any reproductions of copyright works in the thesis, for example graphs and tables ("Reproductions"), which may be described in this thesis, may not be owned by the author and may be owned by third parties. Such Intellectual Property and Reproductions cannot and must not be made available for use without the prior written permission of the owner(s) of the relevant Intellectual Property and/or Reproductions.

iv. Further information on the conditions under which disclosure, publication and commercialisation of this thesis, the Copyright and any Intellectual Property and/or Reproductions described in it may take place is available in the University IP Policy (see http://documents.manchester.ac.uk/DocuInfo.aspx?DocID=487), in any relevant Thesis restriction declarations deposited in the University Library, The University Library's regulations (see http://www.manchester.ac.uk/library/aboutus/regulations) and in The University's policy on Presentation of Theses.

PREFACE

This PhD thesis contains the results of research undertaken at the National Grid Power Systems Research Centre of the University of Manchester. The research was funded by National Grid while the trial installations were supported by Scottish and Southern Energy Power Distribution (SSEPD).

Bringing the research described herein to a conclusion would not have been possible without the contribution of the Arago Technology team which consisted from the following exceptionally talented individuals: Simon Rowland, Ian Cotton, Frank Allison, David Chambers, Peter Green, Vidyadhar Peesapati, Peter Rhodes, Chithambaram Anand Veerappan, Xiaolang Hu and Tingyan Guo.

The designs of the end-fitting for the compression insulator and the nose cone for the insulating cross-arm were led by David Chambers. Chithambaram Anand Veerappan, Xiaolang Hu and Tingyan Guo were involved with the programming of the data acquisition modules used for the trial installations. The 'Butterfly' grading device was conceptualised during a brainstorming session among David Chambers, Vidyadhar Peesapati, Peter Rhodes and the author. The testing regime for the insulating cross-arm was drafted by Simon Rowland and the author. The protection system for the live trial was designed by Ian Cotton who also contributed in the design of the monitoring system.

The author's original contribution includes the design of the angle test experiment and the design of the compression insulator profile in *Chapter 2,* prior to the adjustments made for manufacturing purposes. All the grading devices shown in *Chapter 3*, except from the 'Butterfly' device which was designed with input from the team, have been exclusively designed by the author. The spray system for performing the wet high voltage tests on the cross-arm assembly shown in *Chapter 4* and the entire analysis of the results from the live trial in *Chapter 5* are also the author's original work.

Portions of Chapter 5 have been published [Zachariades, C. Cotton, I. Rowland, S.M. Peesapati, V. Green, P.R. Chambers, D. Queen, M., "A Coastal Trial Facility for High Voltage Composite Cross-arms," IEEE International Symposium on Electrical Insulation (ISEI), San Juan, Puerto Rico, 2012], [Zachariades, C. Rowland, S. M. Cotton, I. Green, P. R. Veerappan, C. A. Chambers, D., "A Trial Installation of High Voltage Composite Cross-Arms," XVII International Symposium on High Voltage Engineering (ISH), Hannover, Germany, 2011].

1. INTRODUCTION

1.1 Impact of overhead lines

The demand for electrical power driven by technological growth and the subsequent improvement in living standards is constantly growing. At the same time distributed generation and renewable resources are changing the power flows across the transmission network. In the UK the 2020 target set by the Department of Energy and Climate Change (DECC) is for the percentage of electricity generated from renewable resources and nuclear power to reach 40 % [1]. To satisfy the increased demand for electricity and connect the new methods of generation, the transmission network will have to expand by mainly building additional overhead lines when the upgrade of existing infrastructure is not possible.

However, the erection and operation of overhead lines is faced with increased public scrutiny due to their environmental, social and economic impact. The size and scale of overhead lines can dramatically change the surrounding landscape. Of particular concern has been the routeing of overhead lines through or near areas of outstanding natural beauty, sites of nature conservation and archaeological sites [2]. Another potential threat to the local environment has been the increasing bird mortality rates caused by collision with manmade structures such as overhead lines [3].

In addition to the visual impact, residents living in close proximity to overhead lines can be affected by noise pollution from crackling and humming noises caused mainly by corona discharges on overhead line conductors, especially during humid and rainy days. Corona has also been found to interfere with television and radio reception [4]. More importantly, there have been concerns regarding potential health issues, such as childhood cancer [5], caused by the exposure to the electromagnetic field (EMF) emitted by overhead lines . Although most of the studies conducted have failed to provide conclusive evidence that show a link between overhead lines and risks to health, the fear of exposure to EMF persists [6].

Furthermore, the visual presence and physical proximity to overhead lines have also been shown to negatively affect household property values because of the perceived environmental and social impacts [7, 8]. Hence, it is not uncommon for residents and

local land owners to have developed strong, negative attitudes towards the construction of new overhead lines.

Because of the opposition of the public due to the aforementioned environmental, social and economic impact to the local communities, significant problems and delays can arise in obtaining planning permission for new overhead lines. As a result, the power industry has been seeking solutions to improve the power transfer capabilities of existing infrastructure.

1.2 Methods for upgrading overhead lines

Several methods are available for uprating overhead lines. Conductor re-tensioning or the re-purposing of suspension towers as tension towers is used to allow for additional conductor sag resulting from the increased thermal rating of an uprated line. However, the additional current and consequent higher temperatures can produce high temperature creep and annealing which alter the physical properties of the conductor resulting in plastic deformation and increased risk of fracture [9].

The replacement of existing conductors with novel conductors or conductors with bigger cross-sectional area can reduce the electrical resistance hence increasing the power transfer capability of the line. Still, the increased cost, increased weight and complex installation techniques which often include tower reinforcements make the decision for adoption of this solution all but straightforward [10].

Incremental voltage uprating of existing lines is another option for increasing system transmission capabilities since by increasing the line voltage the current value can be reduced for the same power rating. Yet, the difficulties and costs associated with its implementation often outweigh the benefits. Substation equipment needs to be able to operate at this higher voltage while the electrical isolation on the towers has to be increased which requires modifications and reinforcements of the towers and replacement of the insulators. Furthermore, in order to comply with radio interference and corona requirements the conductor would have to be replaced [11].

One of the most attractive propositions for increasing the power transfer capabilities of overhead lines is the replacement of the steel lattice tower cross-arms with ones made out of insulating materials. The insulating cross-arm concept is not new. Designs

featuring two or four insulator cross-arms were conceived from the 1960s. Most of them however relied on the ceramic insulators that were available at the time which made the cross-arms too heavy for practical applications [12]. In recent years, advances in composite technology, reduction in manufacturing costs and the challenges faced by the energy sector have resulted in insulating cross-arms emerging as a financially viable alternative for compact overhead lines or for upgrading the existing ones. The products currently available have mostly been used on monopole structures rather than on traditional lattice towers and in the industry are more commonly known as braced insulators, braced posts or horizontal-V insulators.

Contrary to other competing solutions, the deployment of insulating cross-arms requires minimal modifications to the existing towers while eliminating the need for a separate insulator string. In addition to the increased power rating, other benefits of the technology include a narrower right-of-way requirement, the reduction of electromagnetic radiation at ground level and reduction of the visual impact of lines due to the compaction of tower dimensions [13].

1.3 The insulating cross-arm

Working towards the commercialisation of the insulating cross-arm technology, the University of Manchester in cooperation with Arago Technology and EPL Composite Solutions have developed an innovative solution designed for new and existing overhead lines of up to 400 kV.

The cross-arm consists of four insulating members, end fittings, electric field grading devices and a nose connection for the attachment of the conductor (Figure 1.1). The horizontal members, which are the main structural elements of the cross-arm, are designed to be under compression when installed, unlike other OHL insulators. The unique, non-cylindrical shape of their core enables them to exhibit improved resistance to bending and buckling while being lighter and cheaper than cylindrically-shaped alternatives of comparable cross-sectional area.

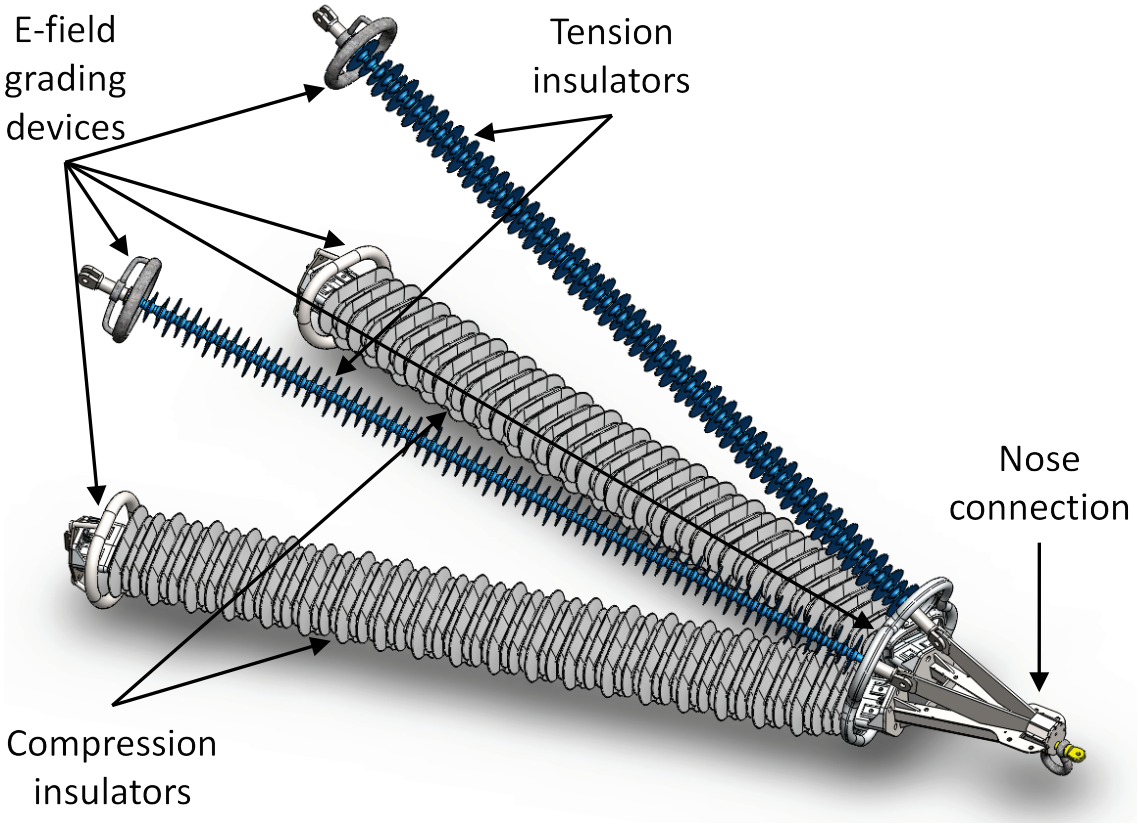

Figure 1.1 - The insulating cross-arm

The major advantage of the Arago cross-arm is that it can be used to directly replace the steel cross-arm on existing lattice towers. Since the cross-arm itself is insulating, the need for an additional insulator disappears and with it the insulator swing. This allows for increased clearance between the conductor and the body of the tower. Also, the conductor can be raised higher providing additional clearance from the ground (Figure 1.2).

Given the increased phase-to-earth clearances, an existing tower can be upgraded to a higher voltage. Additionally the increased clearance from ground could potentially be used to increase the current carrying capacity of the conductors by allowing for increased conductor sag. An example of a tower retrofitted with insulating cross-arms is shown in Figure 1.3 (a) where a 275 kV tower can be converted to a 400 kV tower while maintaining the same footprint. Theoretical calculations have shown that by replacing the steel cross-arms with insulating cross-arms and maintaining the same voltage and the same conductor, the power transfer capability of the line can be increased by 20% to 30%. If the cross-arm replacement is combined with the replacement of the existing conductor by a novel conductor and the simultaneous voltage uprate from 275 kV to 400 kV, the improvement can reach 150% [13].

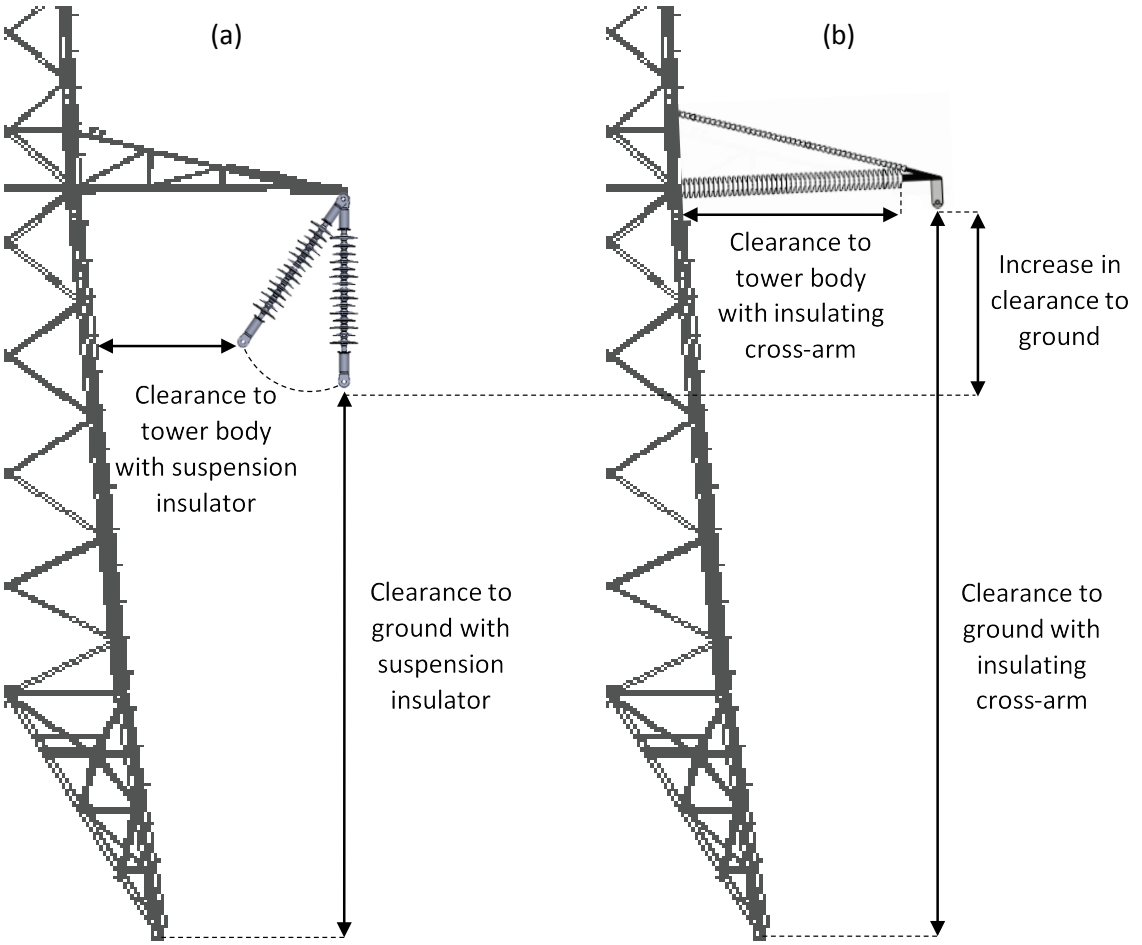

Figure 1.2 - Comparison of phase-to-tower body and phase-to-ground clearances between a tower employing suspension insulators (a) and insulating cross-arms (b)

The use of the Arago cross-arm is not limited to retrofit installations. It can also be used for new build tower designs. Comparing a standard 400 kV tower with a new tower employing insulating cross-arms, the latter can be up to 11.2 m or 26% shorter and up to 1.7 m or 13% narrower while still conforming to the statutory clearances (Figure 1.3 (b)). In addition to the reduced visual impact, the new tower offers other benefits as well. The reduced height translates to reduced bending moment acting at the base of the tower. As a result, the amount of steel required for the tower can be reduced, the foundations can be made cheaper and construction times can become shorter. Additionally, the overall compaction of tower dimensions, which will reduce the phase-to-phase spacing, can result in lower EMF emitting from the overhead line.

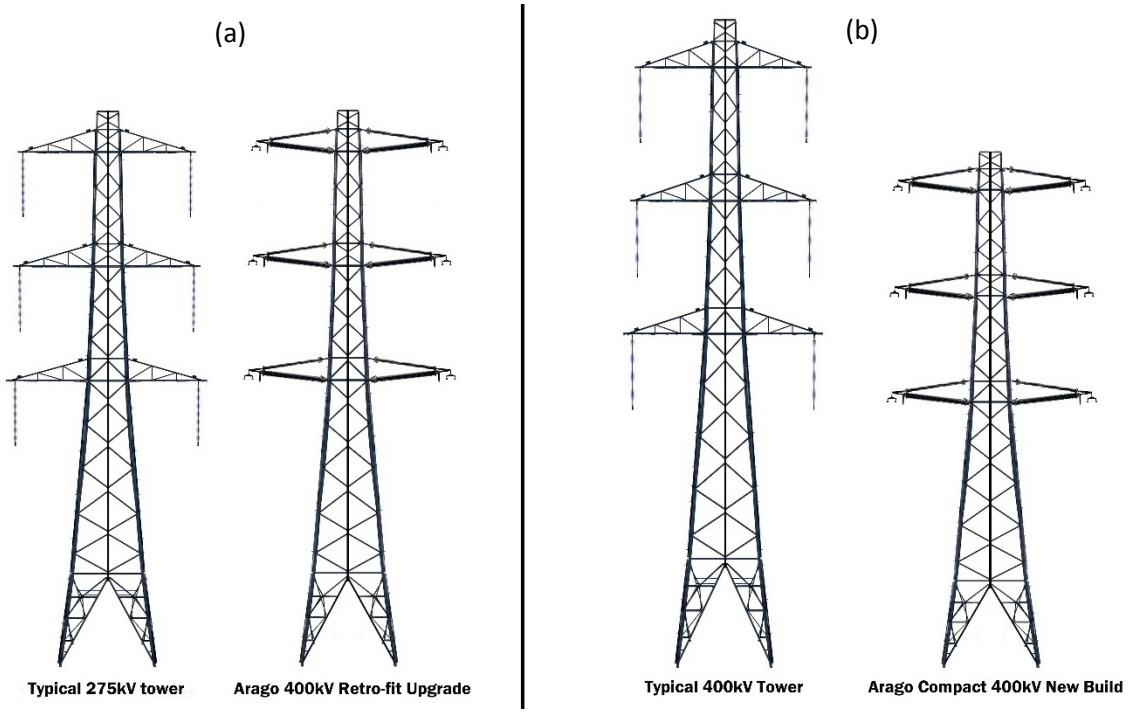

Figure 1.3 – 400 kV Arago insulating cross-arm used for retrofit installation (a) or new build (b)

1.4 Objectives

The aim of the research described in this thesis was to progress the insulating cross-arm from the proof-of-principle prototype stage to the functional prototype stage; in other words to develop a cross-arm model as close as possible to the finished product in terms of design, materials and functionality, certified for operation on the transmission network at 400 kV. To achieve this, four primary objectives were established:

1. Develop a design of a novel composite insulator revolving around a patented, non-cylindrical core which offers improved mechanical characteristics that can serve as the main strength member for the insulating cross-arm using the guidelines presented in the existing international standards for composite insulators. The insulator must enable the cross-arm to be retrofitted on existing lattice towers without infringing the statutory clearances, facilitating the upgrade of overhead lines from 275 kV to 400 kV.
2. Design electric field grading devices for the low-voltage-end and the high-voltage-end of the insulating cross-arm suitable for use at 132 kV and 400 kV levels and ensure they conform to international standards and the Technical Specifications of National Grid by performing electrostatic field simulations using Finite Element Analysis.

3. Test the insulating cross-arm assembly and the compression insulator to verify that both are suitable for operation at 400 kV by adapting, where necessary, the existing testing procedures for composite insulators described in international standards.
4. Examine the electrical performance of the insulating cross-arm prototype and its relation to the weather by analysing the data from a live, instrumented, outdoor trial to identify differences in ageing mechanisms compared to traditional insulators and areas where the design can be improved.

The thesis is organised in such a manner that reflects the distinctiveness of the objectives. Hence, each of the four main chapters tackles one of the objectives starting with its own introduction, to provide a clear narrative, which is followed by a review of the relevant theoretical background, methodology, results and discussion. This particular structure was adopted also because of the amount of work undertaken which would make a single literature review chapter too convoluted.

It is important to note that due to its extent, undertaking the project on which this thesis is based would not have been possible without the contribution of the Arago team and support from industrial partners. Any activities that are not entirely the author's are highlighted in the text.

2. COMPRESSION INSULATOR DESIGN

2.1 Introduction

Like the majority of engineering design problems the design of insulators for overhead lines evolves by combining theory and practice. Theoretical aspects of the problem aim to identify the ideal design while the practical aspects consider more tangible issues such as manufacturing process, cost of manufacturing and materials as well as service experience [14]. Over the past few decades the gradual replacement of porcelain and glass OHL insulators with NCIs has introduced new challenges because of the different materials and processes used in their manufacture.

The first part of this chapter examines the design criteria utilised and the issues that have to be addressed in order to produce a composite insulator which is fit for purpose, starting with the aspects of the design affecting the mechanical and electrical performance of the insulator. A brief look into the materials used for the core and housing follows. Emphasis is given at the recommendations of international standards regarding the parameters governing the design of the insulator profile. Also, a review of the literature associated with snow and ice accretion on composite insulators is presented as well as an overview of the contamination flashover process.

The second part describes the design of a novel composite insulator with improved mechanical characteristics that can serve as the main strength member in insulating cross-arm structures. The work undertaken prior to this study for designing the core and the end-fitting of the insulator is described. The original contribution of this chapter to the research is the design of the profile for the insulator using the recommendations of international standards and existing literature mentioned earlier as well as experimentation in the high voltage laboratory. The design was based on the assumption that the insulator would be part of an insulating cross-arm used for uprating existing overhead lines with L3-type towers from 275 kV to 400 kV.

2.2 Composite insulator structure

A composite insulator consists of a core usually made out of fibre-reinforced polymer (FRP), a sheath and weather sheds made out of EPDM or silicone rubber (SiR), and end-fittings made of forged steel, cast iron or aluminium (Figure 2.1).

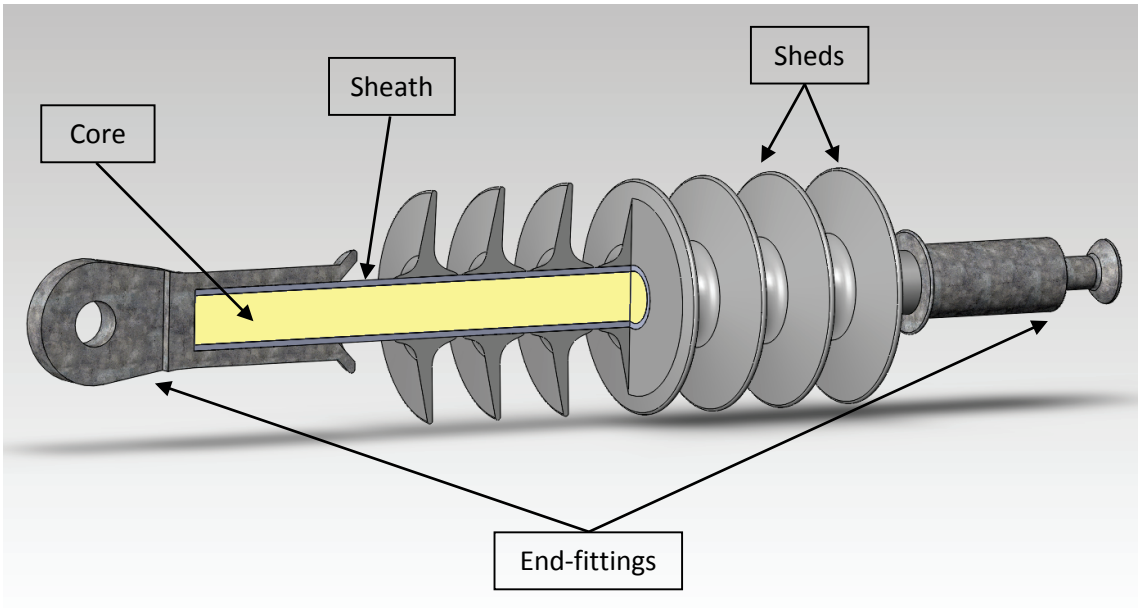

Figure 2.1 - Composite insulator structure

2.3 Design considerations

2.3.1 Mechanical performance

The function of the core of polymeric insulators is twofold: it is the primary load-bearing component and the main insulating part. It is made out of polyester, epoxy or vinylester resin reinforced with E- or E-CR type glass fibres and is formed using a pultrusion process [15].

The majority of composite overhead line insulators are designed to be able to withstand tensile forces while line post and cross-braced insulators are subjected to cantilever or compression forces, or a combination of the two. The maximum occurring mechanical load, also known as specified mechanical load (SML), is calculated for a number of load cases that take into consideration the following parameters:

- conductor weight
- wind load
- ice load

- construction and maintenance loads
- security loads (failure containment, broken wire)

The design load of the insulator for each load case is determined by multiplying the SML by a partial factor which ranges between 1.0 and 2.0 [16]. The National Normative Aspects (NNA) for each country, for example the BS EN 50341-3-9 [17] for the UK, specify methods for calculating the parameters mentioned above and recommend partial factors for specific load cases. Some of them that depend on specific project requirements can be changed accordingly but they cannot infringe the minimum limit set by the NNA.

To assess the long-term mechanical performance and establish the rating of composite insulators, the damage limit concept is used, which was originally introduced by Dumora and Feldmann [18] and later adopted by the IEC 61109 [19]. The damage limit is the critical load limit after which the core starts showing plastic behaviour as the weaker fibres start breaking. Well-designed insulators are able to withstand more than 50% extra of their SML in order to avoid permanent deformation of the core which can ultimately lead to mechanical failure [20].

The mechanical longevity of a composite insulator is dependent on the strength and quality of the core. Exposure of the core to moisture can compromise the mechanical integrity of the insulator by inciting the stress corrosion cracking mechanism that leads to brittle fracture [21]. Acids from the environment or created as a result of partial discharges can chemically attack the fibres. The erosion, when combined with application of mechanical load, leads initially to small, sharp cracks of the individual fibres. These continue to multiply, cracking the core transversely until the remaining fibres are not able to support the load and complete breakage occurs [22]. The vast majority of brittle fractures have been observed near the energised end-fitting of the insulator, often in the region of the highest electric field stress [23]. Due to the complex and unpredictable nature of the brittle fracture mechanism it is recommended to select chemically optimised materials for the core of composite insulators, ensure the adequacy of the seal provided by the end-fittings and manage effectively the electric field in order to avoid the occurrence of this failure in service [24].

2.3.2 Electrical performance

The electrical purpose of an OHL insulator is to isolate the energised conductor from the grounded tower. The dielectric material between the metallic end-fittings is essentially a high resistance path for electric current flow. Like all other components of a power system, the insulator should be designed to operate under high voltage with a high degree of reliability. At the same time, it must be able to withstand stresses other than those arising from the continuous application of service voltage, specifically, overvoltage impulses caused by lightning strikes or switching operations on the line.

For the design of the insulator, the operating voltage is the primary parameter that determines the leakage distance, the shortest distance along the surface of the insulator. The lightning and switching impulse levels are considered when determining the dry arc distance, the shortest distance in air between the high voltage and ground end-fittings. The withstand voltage levels are specified in the NNA for each country. Table 2.1 shows the relationship between operating voltage, impulse levels and minimum clearance distances for UK transmission.

Table 2.1 *- Withstand voltage levels for the UK*

Nominal system voltage (kV)	**132**	**275**	**400**
Lightning impulse level (kV)	550	1050	1425
Switching Impulse Level (kV)	650	850	1050
Phase to earth clearance (m)	1.1	2.1	2.8
Phase to phase clearance (m)	1.4	2.4	3.6

The quality of materials used for the core and housing helps to maintain the electrical integrity of the insulator. In the early days of composite insulators, electrical failures due to tracking along the core were common [15]. The core must have a low void percentage to reduce the probability of electrical discharges that result in degradation and reduce its resistance to puncture. These properties of the core material are validated by the dye penetration and water diffusion tests specified in the BS EN 61109 [19].

Meanwhile, the housing material must exhibit high resistance to tracking and erosion in the presence of arcing activity [20]. To achieve these properties, the basic material of

the housing, SiR (Figure 2.2) or EPDM, is combined with filler materials, the most common of which is Alumina Trihydrate (ATH) [25]. These materials increase the thermal conductivity of the housing, conducting heat generated from discharges away from hot areas of the surface, thus decreasing the rate of erosion [26]. ATH in particular breaks down endothermically to create aluminium oxide (Al_2O_3), which is a thermally stable material with high thermal conductivity, and water. The endothermic reaction also takes heat out of the system.

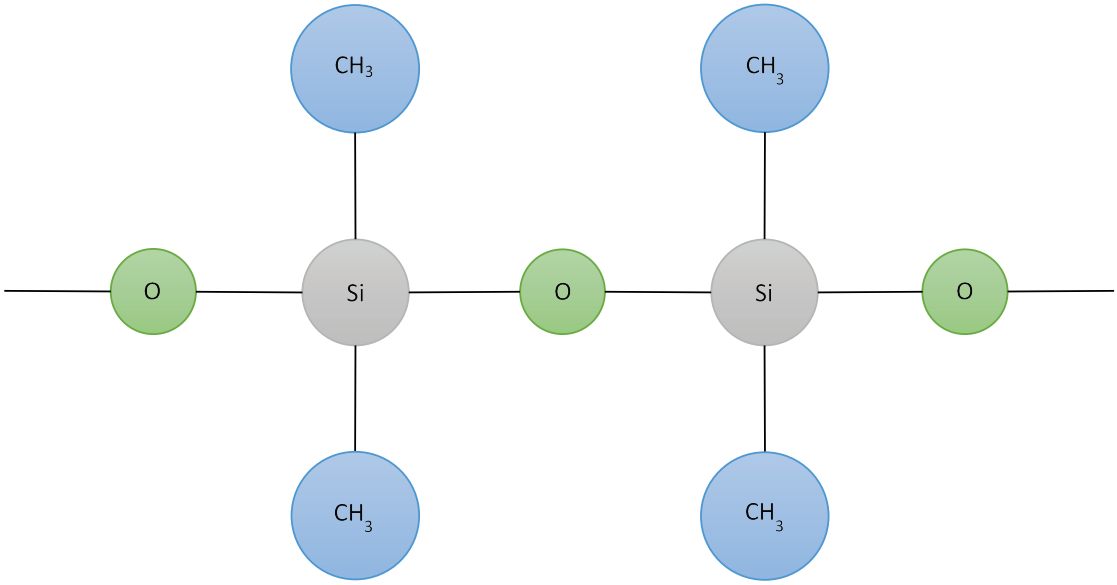

Figure 2.2 - Typical silicone polymer chemical structure

Of equivalent importance to the long-term electrical performance of the insulator is the quality of the interfaces. The problems faced in the first generation designs of composite insulators regarding the bonding of the sheath with the sheds have been resolved by using advanced manufacturing technologies like injection moulding, albeit at the expense of increased tooling cost. Even this technology is not perfect however. The excess material protruding from the mould creates mould lines on the sheds and sheath. The geometry of these mould lines can distort the electrical field distribution which in turn can accelerate the degradation of the material on the mould line [27, 28].

2.3.3 Housing material performance

The base material used for the manufacturing of composite insulators (EPDM, SiR) on its own is not sufficient to ensure the longevity of the unit when it is exposed to an outdoor environment. In service, in addition to the electrical stresses, the insulator will be subjected to solar radiation and exposed to various pollutants and biological growth.

Therefore, in addition to anti-tracking agents (e.g. ATH), several other additives are used such as UV stabilisers, antioxidants and ionic scavengers, which can significantly affect the performance of the housing material [29].

Composite insulators perform better than glass or porcelain in wet and polluted environments primarily because of the hydrophobic nature of their housing material [30]. This is accomplished with the use of hydrophobicity transfer materials (HTM). Such materials allow the migration of low molecular weight (LMW) polymer chains from the bulk of the material to the surface, forming a thin film on top of the contamination, effectively transferring the hydrophobicity to the pollution layer [31].

2.3.4 Profile design

The term 'profile' refers to the dimensions of the insulator and the shape of its housing. The pollution performance benefits of polymeric insulators can only be realised if the profile has been designed appropriately based on the service conditions the insulator will be subjected to and taking into consideration any changes to these conditions that might happen during its service life.

The main types of profiles used for polymeric insulators are the uniform (or non-alternating) and the alternating (Figure 2.3), differentiated by whether the sheds have the same size or not. Alternating profiles offer the advantage of increased creepage per unit length without compromising the insulator's wet performance or self-cleaning properties [29].

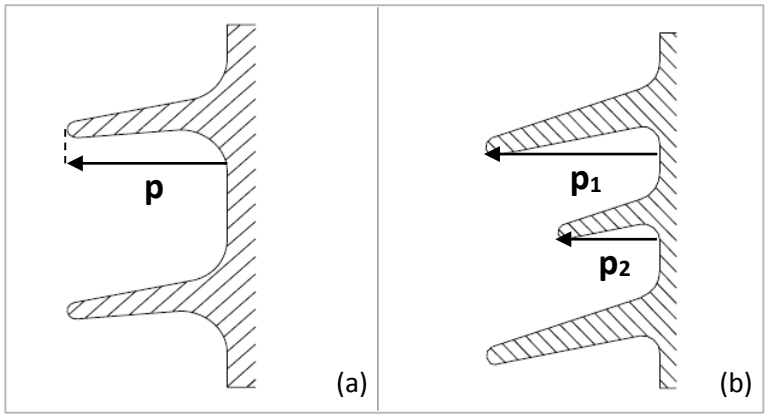

Figure 2.3 - Uniform (a) and alternating (b) profile

To classify a profile as uniform or alternating, the difference in shed overhang (***p***) between the largest and smaller sheds is used. Shed overhang is the distance between

the insulator trunk and the tip of the shed. Table 2.2 shows how this parameter is used to classify insulators of different orientation and overall diameter.

Table 2.2 *- Uniform and alternating profile classification*

		Classification	
Orientation	**Diameter**	**Uniform**	**Alternating**
Vertical	> 200 mm	$p_1 = p_2$ $p_1 - p_2 < 15$ mm	$p_1 - p_2 \geq 15$ mm
Other	≤ 200 mm	$p_1 = p_2$ $p_1 - p_2 < 0.18\ p_1$ mm	$p_1 - p_2 \geq 0.18\ p_1$ mm

Profiles can also be classified as open or steep (Figure 2.4) based on the slope of their sheds. Open profiles have a top slope of 20^o or less and can be used in all environments in both vertical and horizontal orientations. They perform exceptionally well in dry climates and near areas where the wind transfers solid pollution onto the insulators. They can also be cleaned easily during maintenance. Steep profiles are more suited for locations where liquid pollutants, such as salt water or acid rain [32], are more frequently deposited on the insulator surface.

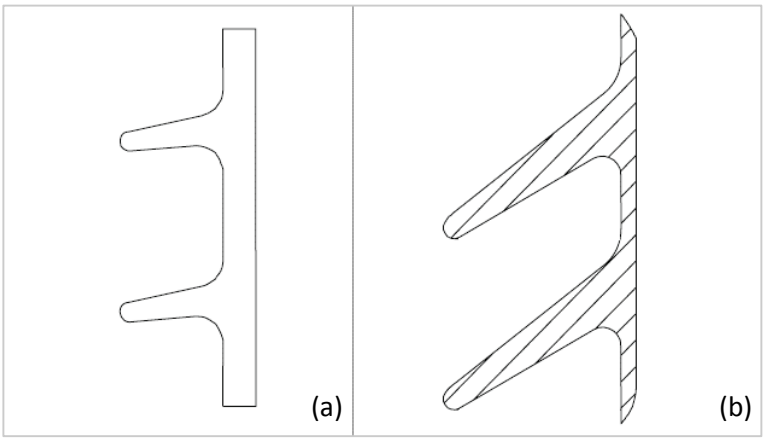

Figure 2.4 - Open (a) and steep (b) profile

Furthermore, there are polymeric profiles with shallow or deep (Figure 2.5) under-ribs. Under-ribs increase the protected creepage distance of the insulator and are known to perform better in environments with heavy salt fog or spray. On the other hand, they are not suitable for areas where solid pollution can be accumulated on the insulator surface since the under-ribs tend to fill up with contaminants and are difficult to clean.

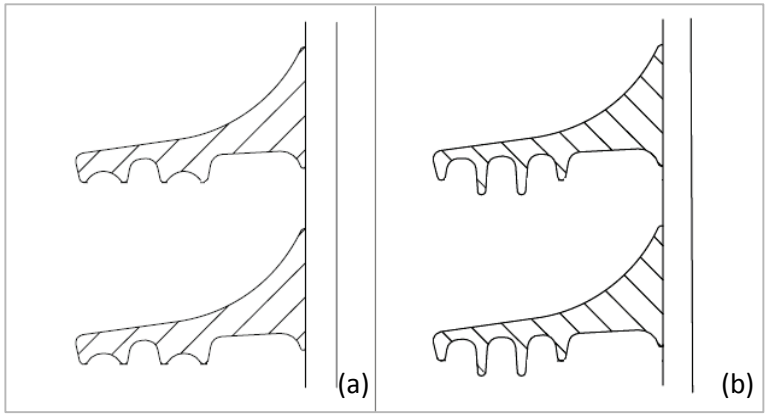

Figure 2.5 - Profile with shallow (a) and deep (b) under-ribs

2.3.5 Profile performance parameters

In addition to the type of the profile, there are several other parameters that need to be considered when designing the insulator housing that can affect the performance of the insulator in various ways. The ratio of the vertical distance between two successive sheds of the same diameter over the vertical distance between the insulator trunk and the tip of the shed (Figure 2.6) is known as spacing (***s***) versus shed overhang (***p***). Small values of this parameter indicate a deep and/or narrow profile with reduced self-cleaning properties, which can experience decreased performance when heavily polluted.

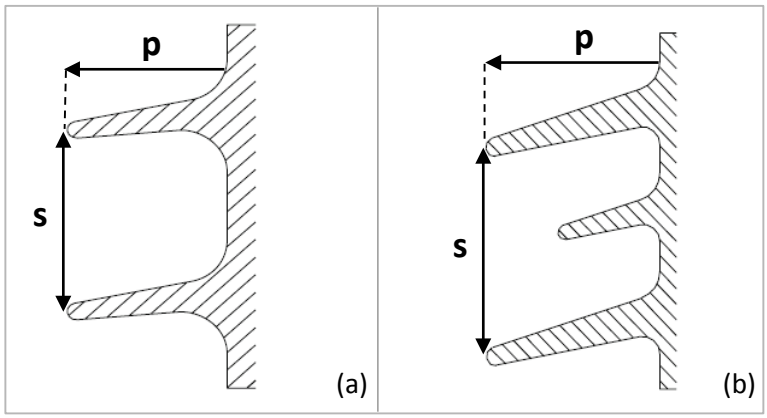

Figure 2.6 - Spacing vs shed overhang

The minimum distance between sheds (***c***) is the shortest distance from the bottom of a shed to the top of the next shed of the same diameter (Figure 2.7). The smaller this parameter is the easiest it is for an arc to develop across sheds, bridging the creepage path. If the shed-to-shed distance is too small, the benefit of adding additional creepage to the profile might be cancelled out.

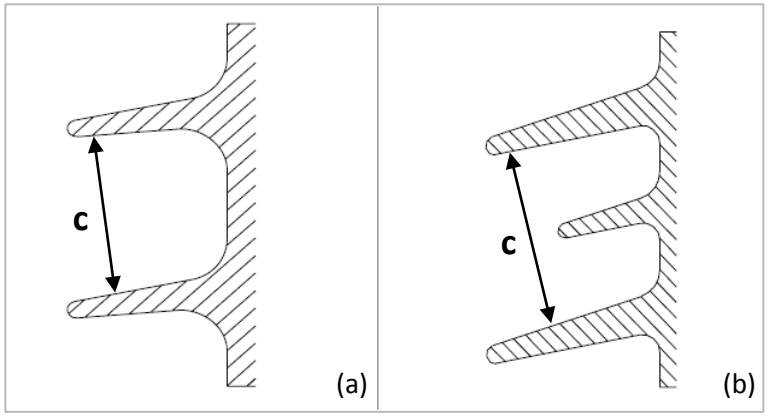

Figure 2.7 - Minimum distance between sheds

The shortest distance in air between the tips of two successive sheds or the tip of a shed and the nearest metallic part is called clearance (***d***) while the path on the insulator surface between these two points is the creepage distance (***l***). The ratio of creepage distance versus clearance (Figure 2.8) is important to control bridging by arcs in the occurrence of dry bands or uneven hydrophobicity.

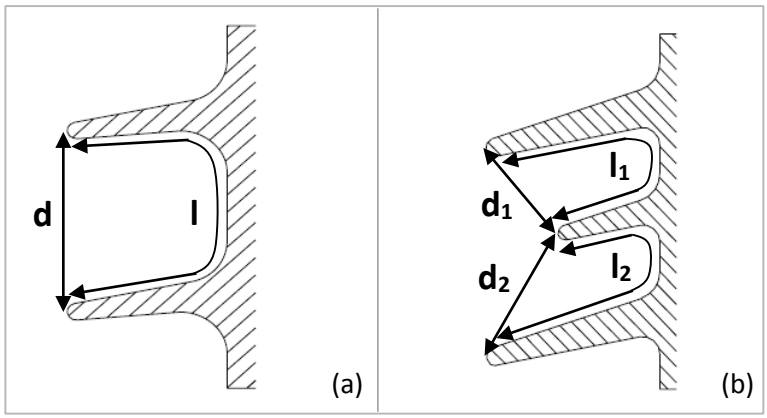

Figure 2.8 - Creepage distance vs clearance

The shed angle (***α***) is a measure of the steepness of the profile. It determines the water run-off behaviour on the surface of the insulator. Provided that this angle is not excessively small, insulators with acute shed angle (open profile) exhibit better self-cleaning properties.

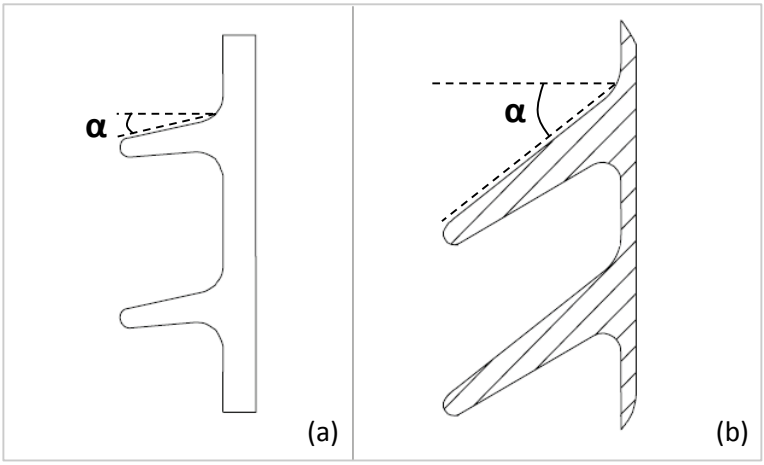

Figure 2.9 - Shed angle

The creepage factor (***CF***), also known as creepage distance density, is specified as the ratio of the total creepage distance (***l***) of the insulator over the arcing distance (***A***). It is a more general parameter that indicates how tightly the sheds are arranged or in other words how dense is the creepage distance per unit length. Due to their improved pollution performance, polymeric insulators tend to be designed with reduced creepage distance compared to their ceramic alternatives. However, it is important to note that heavy pollution can result in temporary loss of hydrophobicity, making the composite insulator behaving more like a glass insulator for short periods of time. This worst case scenario should be considered when deciding the creepage distance. Additionally, it has been shown that as the overall diameter of the insulator increases, the contamination flashover voltage decreases [33]. Therefore, a creepage distance increase is desirable as the diameter of the insulator increases, especially for diameters more than 300 mm.

The IEC/TS 60815-3 [29] categorises the values of the parameters mentioned above in three classes (none, minor, major deviation) based on how much they can reduce the performance of the insulator. It is advised that none of the parameters should lie in the 'major deviation' category and preferably with only one in the 'minor deviation' category. Table 2.3 shows the recommended values of the aforementioned parameters for different insulator positions, dimensions and profile types.

Table 2.3 *- Recommended values of profile parameters according to IEC/TS 60815-3*

			Deviation		
Parameter	**Position / Dimensions**	**Profile**	**None**	**Minor**	**Major**
s/p	Shank diameter ≤ 110 mm	w/ under-ribs	0.85 - 1	0.75 - 0.85	0.4 - 0.75
		w/o under-ribs	0.75 - 1	0.65 - 0.75	0.4 - 0.65
	Shank diameter > 110 mm	w/ under-ribs	0.75 - 1	0.6 - 0.75	0.4 - 0.6
		w/o under-ribs	0.65 - 1	0.5 - 0.65	0.4 - 0.5
c (mm)	All	Uniform	25 - 50	22.5 - 25	20 - 22.5
		Alternating	40 - 50	30 - 40	20 - 30
l/d	All	All	0 - 4.5	4.5 - 5.5	4.5 - 7
α	Vertical	All	5° - 25°	0° - 5° 25° - 35°	35° - 60°
	Horizontal c < 30 mm		0° - 20°	20° - 30°	30° - 60°
CF	All	All	2.5 - 4.25	4.25 - 5	5 - 5.5

2.3.6 Electric field management

Modern composite insulators are designed to distribute the electric field around their fittings more efficiently than their older counterparts. Hence, radio interference issues from insulators tend to be minimal. However, recent studies show that the localised corona discharges near the electrodes can accelerate the degradation of the material and reduce the service life of the insulator. In most cases the area where the highest electric field is observed on an insulator is the triple junction, the point where the housing, the core and the metal work meet [34]. If the insulator is not designed with the protection of this interface in mind it is possible that discharges could start eroding the sealing material that keeps the insulator watertight [35]. For these reasons appropriately designed grading rings are recommended especially for higher voltages. This aspect of the design is examined in more detail in *Chapter 3*.

2.3.7 Snow and ice accretion

Despite the fact that snow and ice accretion is not a problem for many power systems, it can have devastating consequences if not taken into account. A prime example is the icing events that took place in Canada during January 1998. They resulted in destruction of power system infrastructure with an estimated cost of one billion Canadian dollars and left more than four million customers without electricity for periods between three and thirty days [36].

For insulators, ice accretion represents another form of pollution. It tends to be non-uniform, leaving sections along the length of the insulator with no ice coverage. These sections are known as air gaps and are formed either during the icing event or afterwards as a result of melting or ice shedding [37]. Processes including wet ice accretion, condensation, partial discharges, temperature rise or solar irradiance can initiate the formation of a water film on the surface of the insulator which, in most cases, is conductive due to the presence of other contaminants [38]. As a result, the electrical stress across air gaps increases to the point where they are bridged by low energy arcs. If the process continues, arcs will also propagate along the ice surface, forming higher energy arcs. A flashover occurs when the arc exceeds a certain length [39].

To mitigate the effects of ice and snow accretion, insulators should be designed appropriately based on the effects this phenomenon can have on their performance. To a certain extent, snow and ice accretion can alter the shape and surface properties of the insulator often reducing the leakage distance down to the arcing distance. In the most severe cases the new leakage path along the ice surface can approximately become one third of the insulator's leakage distance. Therefore, one of the most important design parameters for insulators in such environments is the arcing distance since the flashover level increases almost linearly with the increase of the arcing distance [40]. Studies show that the power frequency flashover strength of insulators can be reduced by more than 40% [37]. Moreover, while the lightning impulse withstand has been found to remain unaffected, the switching impulse withstand can be lower by as much as 50% compared to clean conditions [41, 42].

Other profile parameters are also of great importance. Insulators with small shed spacing, more common to polymeric insulators, and shallow shed depth are easier to fill

with ice or snow. Alternating profiles and profiles with bigger spacing of larger sheds for insulators of comparable leakage distance have been found to perform better under moderate and heavy icing because they provide increased shed-to-shed separation which delays ice bridging. Furthermore profiles with three or four different shed diameters exhibit better performance than profiles with two different shed diameters because the bigger sheds provide protection to the smaller sheds from ice bridging [43]. The overall insulator diameter is also a factor that affects performance. Insulators with bigger diameters tend to accumulate more ice due to the increased surface area for the same period of ice accretion which not only increases their weight but also reduces their critical flashover voltage [44].

The orientation of the insulator is also a performance affecting factor. Accumulation of snow and ice is more apparent on the windward side of the insulator, usually extending across the entire insulator shed diameter. Vertically installed insulators seem to perform worse under ice and snow conditions. On the contrary, horizontal insulators and insulators installed at an angle, such as V-strings, require longer icicles in order for the sheds to be bridged so they tend to perform better [45, 46]. Frequently, snow is also trapped in the spaces between insulator bundles, which could create issues for configurations such as insulating cross-arms [40].

2.3.8 Contamination flashover

The procedure that potentially can lead to flashover in polymeric insulators made of EPDM or SiR starts with the deposition of contaminants on their surface. If the insulator is located near the sea, the contaminant is usually in the form of salt dissolved in water droplets. In areas further inland the contaminants mainly consist of dust and other airborne particles which after they are deposited on the insulator's surface they can absorb moisture from fog or dew [47]. Initially the hydrophobic properties of the insulating material force the pollution to form individual droplets on the insulator surface (Figure 2.10 (a)).

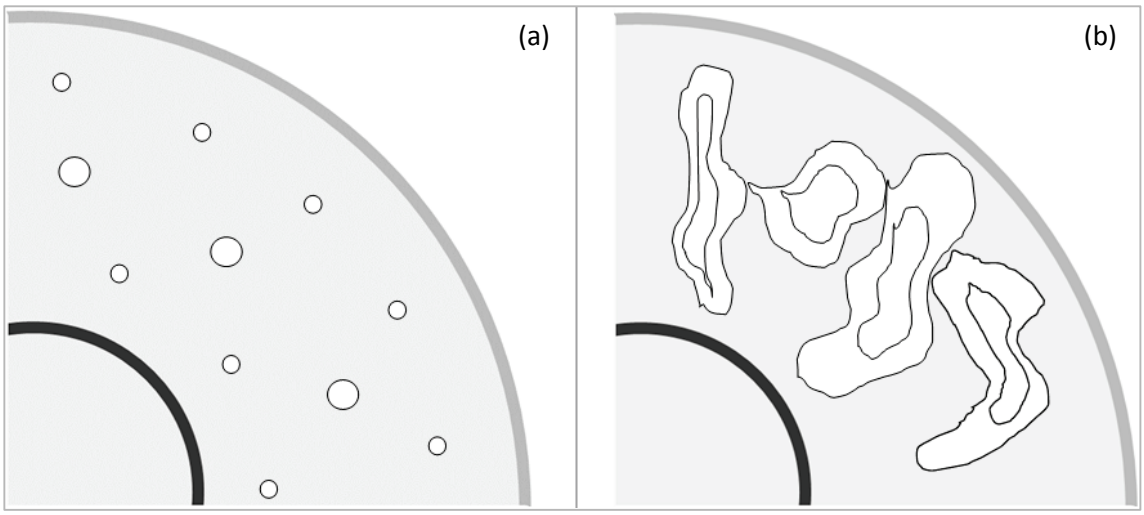

Figure 2.10 - Hydrophobic (a) and hydrophilic (b) insulator surface

However, environmental conditions, such us UV radiation, coupled with surface arcing destroy hydrophobicity and lead eventually to the formation of a uniform pollution layer and a continuous water film on the surface (Figure 2.10 (b)). The loss of hydrophobicity is often determined by contact angle measurements (Figure 2.11).

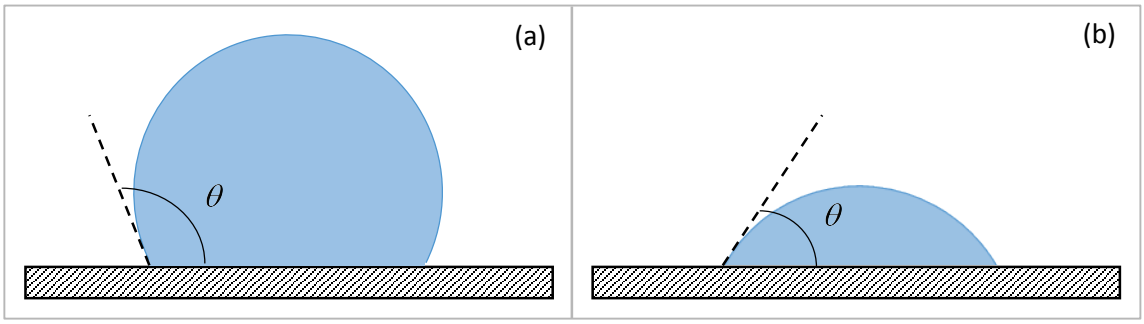

Figure 2.11 - Contact angle measurement – (a) hydrophobic, (b) hydrophilic

Despite the presence of pollution, EPDM and SiR insulators can recover their hydrophobic properties after a short arc-free period (10 – 12 hours), something that differentiates them from older glass and porcelain insulators. This happens due to the diffusion of low molecular weight (LMW) polymer chains from the bulk of the material to the surface, forming a thin layer on top of the contamination [31]. Figure 2.12 (a) shows a tension insulator that has been in service for thirteen years while Figure 2.12 (b) shows an insulator that has been subjected to flashover testing using steam fog after being artificially contaminated. The latter has been left to dry for approximately 24 hours and then sprayed with demineralised water. Although both are obviously polluted (brown/white residue on the surface), it is easy to distinguish the individual water droplets forming on the most part of their surface, evidence of the aforementioned process of LMW fluid diffusion.

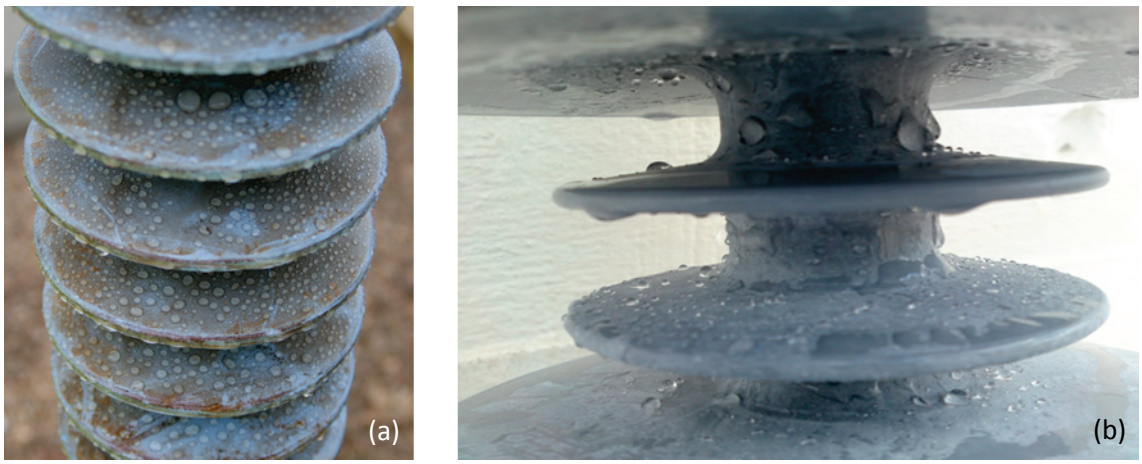

Figure 2.12 - Service-aged (a) and artificially polluted (b) insulators

High humidity, rain or fog wet the surface of the insulator dissolving the salt contained in the pollution layer. The solution rises above the thin layer of LMW polymer chains due to diffusion, creating individual, conductive droplets. The layer around each droplet becomes highly resistive which, if wetting is continued, further increases in resistivity with the joining of the adjacent wet regions.

Leakage current flowing through the resistive layer because of the applied voltage slowly heats the layer. Its resistance decreases while at the same time the surface dries up which has the opposite effect, i.e. increasing the resistance, until equilibrium is reached. The composite insulator at this point is covered with conducting droplets on top of a resistive layer [48].

Droplet density is increased with continuous wetting and the distances between droplets decrease. The droplets elongate as a result of the oscillating force produced from the interaction of the AC field with them. Adjacent droplets can then come together to form random conductive regions surrounded by high resistance areas on the surface of the insulator. These areas effectively reduce the electrical distance between the electrodes which intensifies the electric field between them, eventually causing discharges [49].

The polymer surface is charred by the discharge activity, consequently resulting in reduction of hydrophobicity. Adjacent conductive regions can now come even closer together forming a continuous conductive path on the surface of the insulator for an electric arc to be initiated according to Hampton's criterion. Hampton devised an experiment where a discharge was initiated by an electrode very close to a constantly running saline solution column supplied through an earthed nozzle (Figure 2.13). He

showed that a flashover can be initiated only if the mean voltage stress in the water jet was greater than the mean voltage in the discharge [50]. In practical applications this means that an arc will only extend over the adjacent moisture if the field on the insulator surface exceeds that in the arc. The availability of high currents determines whether the arc can extend to the point it causes a flashover or it remains localised [51]. Hence, if Hampton's criterion is met, the arc can then propagate along the surface of the insulator, bridging the distance between the HV and LV end-fittings and causing flashover [52].

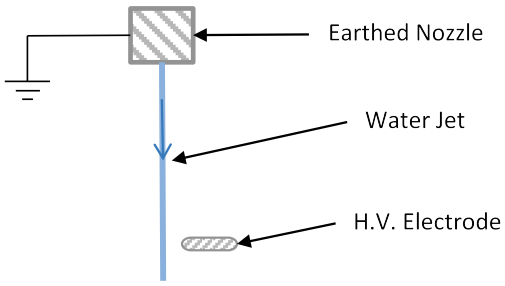

Figure 2.13 - Hampton's experiment

The entire contamination flashover process for composite insulators can be described in ten steps which are summarised in Figure 2.14.

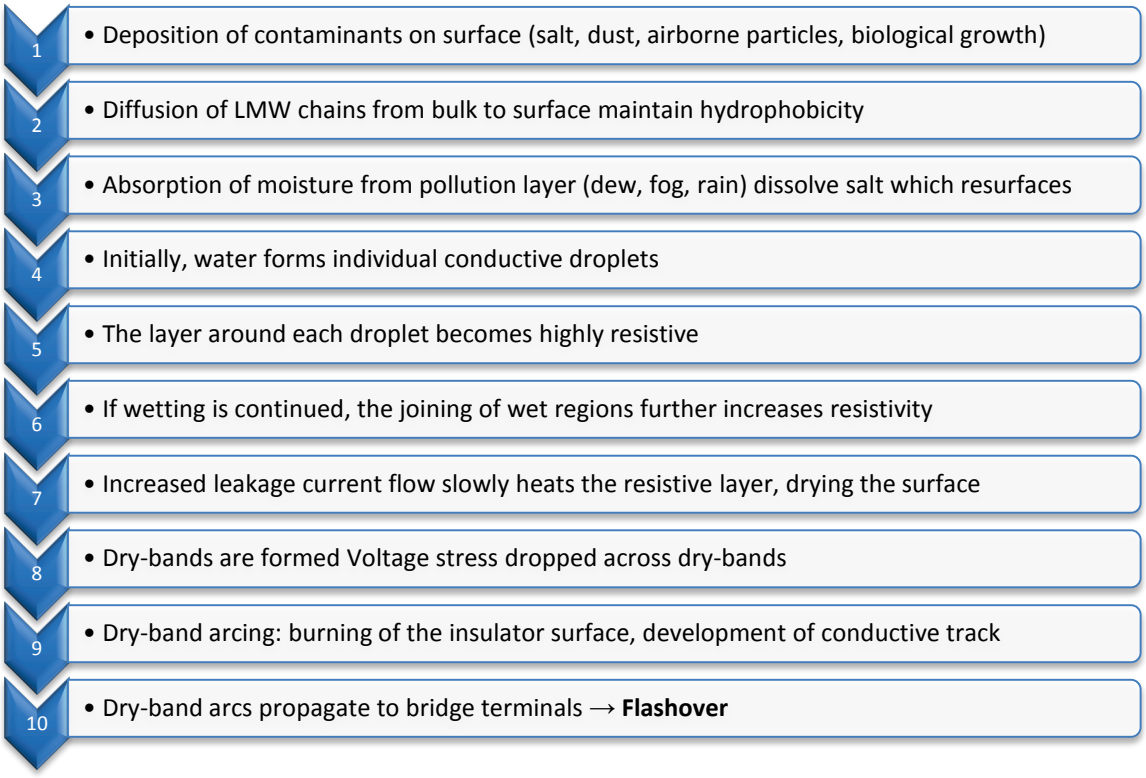

Figure 2.14 - Contamination flashover process

2.4 Compression insulator core

Unlike most other OHL insulators, the two horizontal members of the insulating cross-arm assembly are subjected to compression and cantilever loads. In order to cope with such loads, a core with a unique cross-sectional shape was conceived and patented [53] prior to the start of this project. This core provides the compression insulator with the same second moment of area of a cylindrical core with twice the cross-sectional area. As a result, the core of the compression insulator can be made lighter and manufactured cheaper than a core with a circular cross-section while maintaining the required mechanical strength.

The second moment of area, often mistakenly called 'moment of inertia' for an area [54], is a property of a cross-section that can be used to predict the resistance of beams to bending and deflection since deflection does not only depend on the applied load but on the geometry of the cross-section as well. It is defined as:

$$I_O = \int_A r^2 dA \tag{2.1}$$

where:

I_O : the second moment of area about the pole O

dA : the elemental area of a cross-section

r : the perpendicular distance from pole O to element dA

From the definition we can deduce the second moment of area for regular shapes (Figure 2.15).

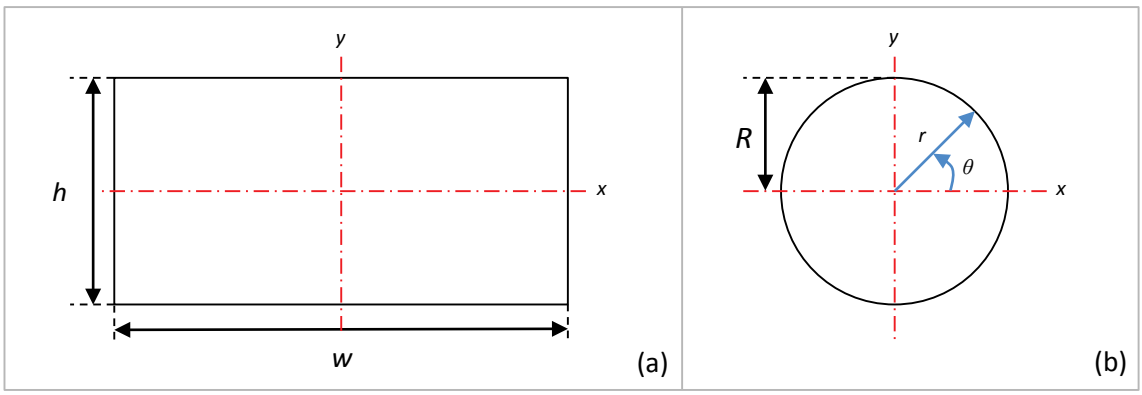

Figure 2.15 - Rectangle (a) and circle (b) dimensions for moment of area calculation

For a rectangle of height ***h***, width ***w*** and centroid located at the origin, the second moment of area with respect to the x axis can be calculated as:

$$\begin{aligned} I_x &= \int_A y^2 dA \\ &= \int_{-w/2}^{w/2}\int_{-h/2}^{h/2} y^2 dy dx = \int_{-w/2}^{w/2}\left[\frac{y^3}{3}\right]_{-h/2}^{h/2} dx = \int_{-w/2}^{w/2}\left[\frac{1}{3}\cdot\left(\frac{h^3}{8}+\frac{h^3}{8}\right)\right]dx \\ &= \int_{-w/2}^{w/2}\frac{h^3}{12}dx = \frac{h^3}{12}\cdot[x]_{-w/2}^{w/2} = \frac{h^3}{12}\cdot\left(\frac{w}{2}+\frac{w}{2}\right) \\ &= \frac{h^3\cdot w}{12} \end{aligned} \tag{2.2}$$

Similarly with respect to the y axis:

$$I_y = \frac{w^3\cdot h}{12} \tag{2.3}$$

For a circle with radius ***r*** and centroid located at the origin, it is easier to calculate the polar second moment of area:

$$\begin{aligned} I_{P_C} &= \int_A r^2 dA \\ &= \int_0^{2\pi}\int_0^R r^2\cdot r dr d\theta = \int_0^{2\pi}\left[\frac{r^4}{4}\right]_0^R d\theta = \int_{-w/2}^{w/2}\left[\frac{1}{4}\cdot\left(R^4-0\right)\right]d\theta \\ &= \int_0^{2\pi}\frac{R^4}{4}d\theta = \frac{R^4}{4}\cdot[\theta]_0^{2\pi} = \frac{R^4}{4}\cdot(2\pi-0) \\ &= \frac{R^4\cdot\pi}{2} \end{aligned} \tag{2.4}$$

In cartesian coordinates, the second moment of area for the circle can be written as:

$$I_{P_C} = I_{x_C} + I_{y_C} \tag{2.5}$$

Since the circle is symmetric, the second moment of area with respect to the x or y axis can be expressed as:

$$I_{x_C} = I_{y_C} = \frac{I_{P_C}}{2} = \frac{R^4\cdot\pi}{4} \tag{2.6}$$

In order to calculate the second moment of area for the core of the compression insulator, the cross-section is simplified and divided into three sections (A, B, C) of regular shape (Figure 2.16).

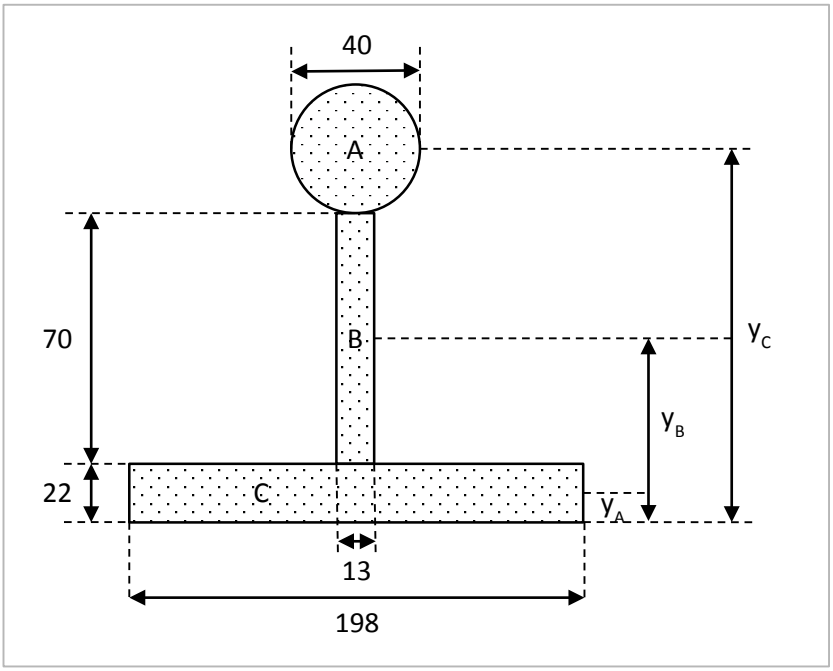

Figure 2.16 - Simplified compression insulator core cross-section

From Figure 2.16 the area and the position of the centroid with respect to the base of the cross-section for each section can be calculated (Table 2.4).

***Table 2.4** - Calculation of the area and position of the centroid*

Section	A (mm^2)	y (mm)	$A \cdot y$
A	1257	112	140784
B	910	57	51870
C	4356	11	47916
Total	6523		240570

From Table 2.4 the position of the centroid of the entire cross-section can be deduced:

$$y_T = \frac{(A \cdot y)_T}{A_T} = \frac{240570}{6523} = 36.88 \text{ mm} \tag{2.7}$$

Since the three sections have a regular shape, the second moment of area for each one with respect to its centroid can be calculated using equations (2.3) and (2.6). The second moment of area with respect to the base, $I_{x'}$, can be found using the parallel axis theorem (Table 2.5).

Table 2.5 *- Calculation of the second moment of area about the x axis*

Section	$I_{S_{x'}}$	$A \cdot y^2$	$I_{x'} = I_{S_{x'}} + A \cdot y^2$
A	125664	15767808	15893472
B	371583	2956590	3328173
C	175692	527076	702768
Total			19924413

Again, using the parallel axis theorem, the second moment of area about the x axis of the whole cross-section with respect to its centroid is calculated:

$$\begin{aligned} I_x &= I_{x'} - A_T \cdot y_T^2 \\ &= 19924413 - 6523 \cdot 36.88^2 \\ &\approx 1.1 \cdot 10^7 \ \text{mm}^4 \end{aligned} \tag{2.8}$$

Similarly, the second moment of area about the y axis is found to be:

$$\begin{aligned} I_y &= I_{y'} - A_T \cdot x_T^2 \\ &\approx 1.4 \cdot 10^7 \ \text{mm}^4 \end{aligned} \tag{2.9}$$

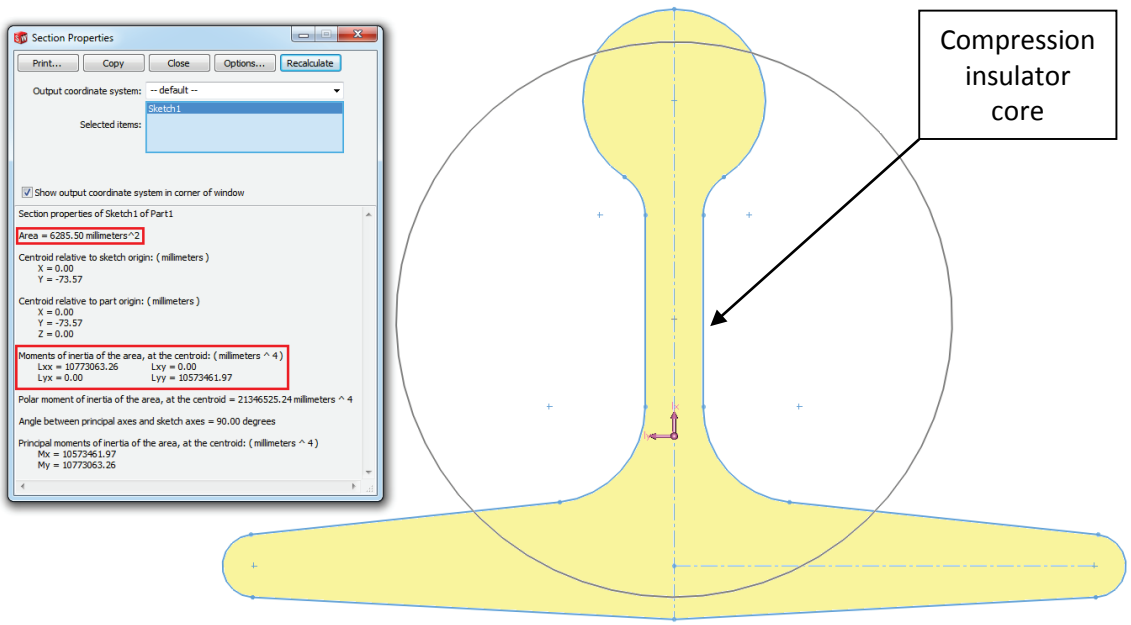

Figure 2.17 - Compression insulator core second moment of area calculation with SolidWorks

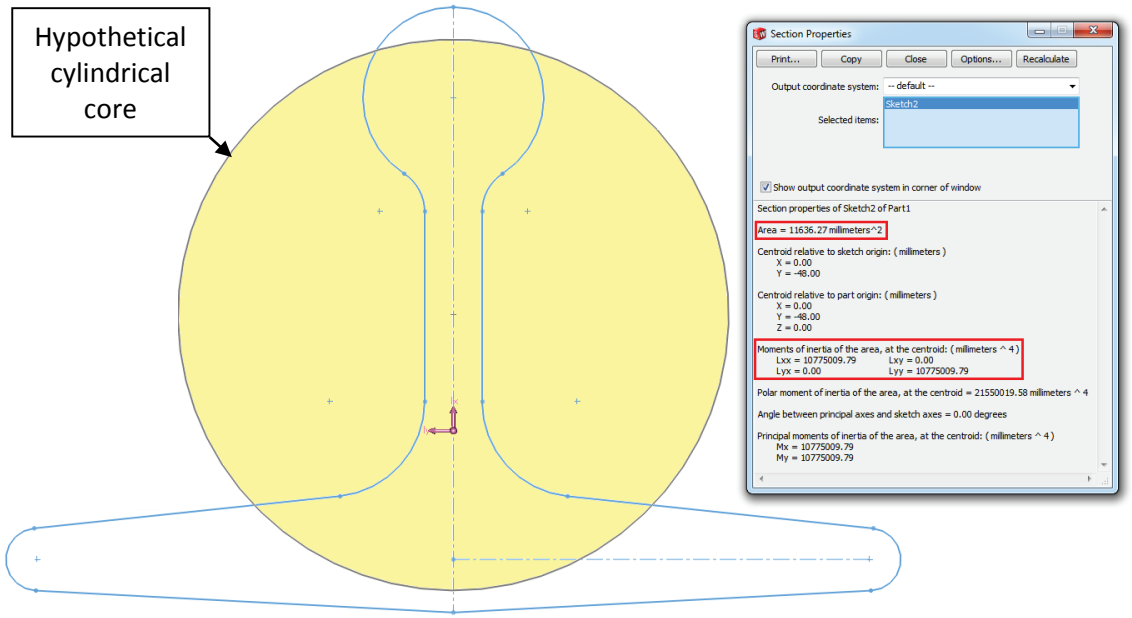

Figure 2.18 - Cylindrical core second moment of area calculation with SolidWorks

The calculation can be verified using SolidWorks, a CAD software package. Figure 2.17 shows the actual cross-section of the compression insulator core and the moment of inertia values as reported by SolidWorks which are:

$$I_x = L_{xx} = 10773063 \text{ mm}^4 \tag{2.10}$$

$$I_y = L_{yy} = 10573462 \text{ mm}^4 \tag{2.11}$$

The actual cross-section is optimised to have similar moment of inertia for both axis. Due to the simplified cross-section used for the hand calculation the results are not identical with a difference of approximately 2.6% for I_x and 35.8% for I_y.

Figure 2.18 shows a cylindrical core with equivalent second moment of area as the compression insulator core. Comparing the two, the area of the compression insulator core cross-section is 6285 mm^2 whereas the area of the circular cross-section is 11636 mm^2 or 85% bigger.

2.5 Compression insulator end-fitting

The main purpose of the end-fitting for any insulator is to provide the means of attachment of the insulator to the tower. Additionally the end-fitting ensures that the insulator remains watertight and it also provides limited electric field stress control at the triple junction. Because of the unconventionally-shaped core of the compression

insulator it was not possible to design an end-fitting that could be crimped onto the core like many of the end-fittings used for tension insulators. EPL Composite Solutions, which handled the mechanical design of the end-fitting, after considering several methods of attachment settled on the pinned end-fitting shown in Figure 2.19.

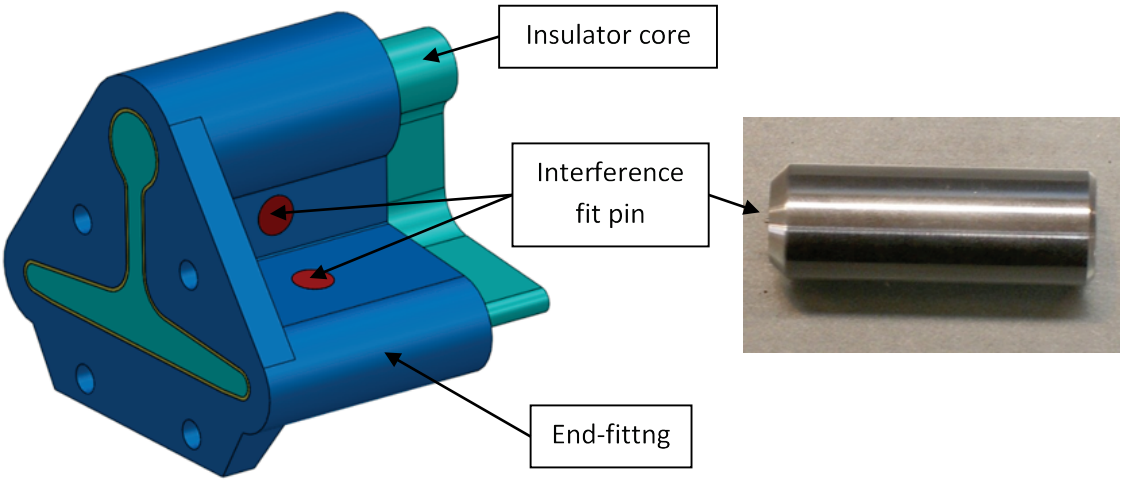

Figure 2.19 - Compression insulator end-fitting fastened to the core with interference fit pins

The end-fitting would be cast from the heat treated LM25-TF aluminium alloy, which is frequently used on transmission infrastructure, to avoid the need for anti-corrosion treatments such as paint or galvanising required for other materials and also keep the mass of the end-fitting as low as possible. To fasten the end-fitting to the core, mechanical fasteners, i.e. pins, were incorporated in the design. The reason for preferring mechanical fasteners to other methods was to avoid the use of adhesive for bonding the core to the end-fitting since controlling the quality of adhesion and ensuring that the adhesive would not break down over time would be difficult. The pins were to be retained using an interference fit where the pins are larger than the holes they are driven into. The pin and casting deform elastically when the pin is inserted and the pressure created at the interface by the deformation is sufficient to retain the pins. The pins were designed to have one of their ends chamfered with a small radius of curvature between the chamfer and the main body of the pin to make it easier for the pin to be guided into the hole.

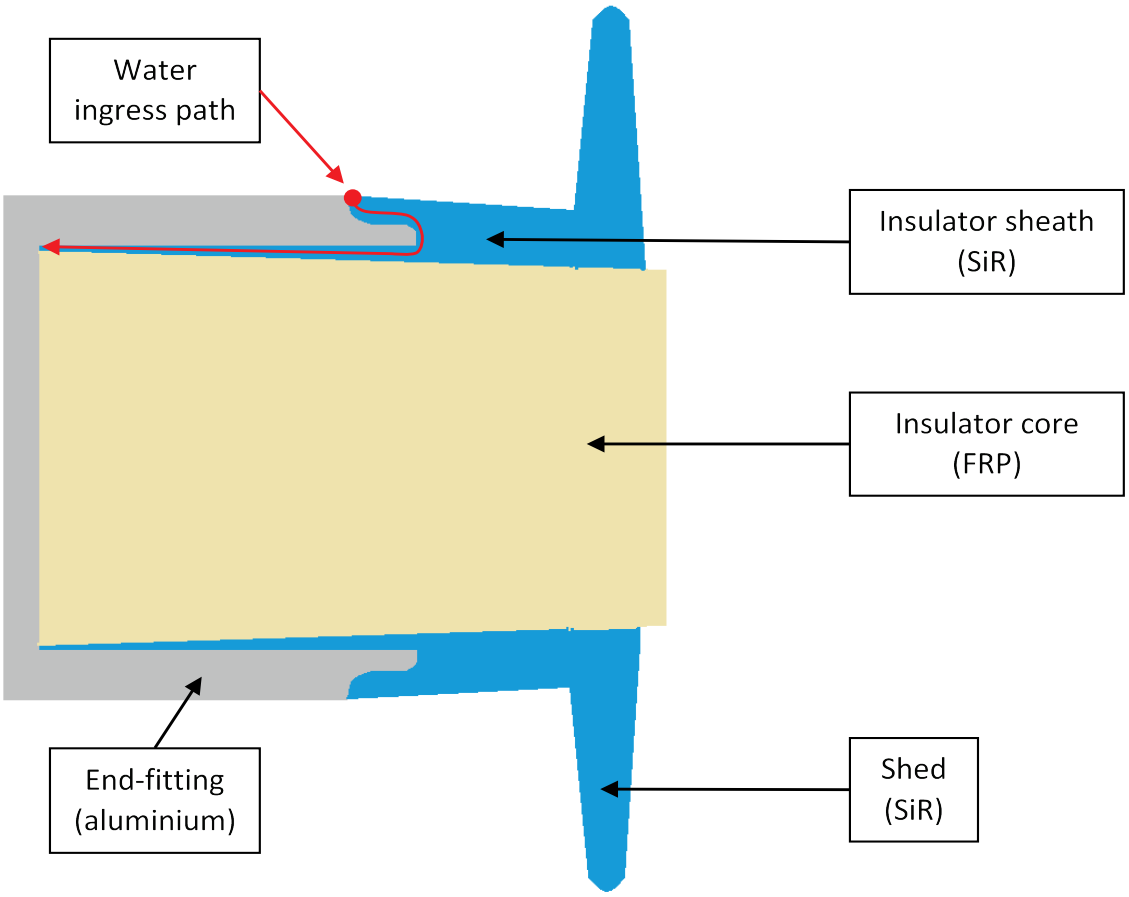

Figure 2.20 - Compression insulator end-fitting cross-cut showing water ingress path

With input from the author the termination of the end-fitting, i.e. the part of the fitting facing the sheds, was designed in such a way as to allow for silicone rubber to be moulded on top of the end-fitting termination. Furthermore it was also decided to fill the area between the core and the end-fitting with silicone rubber since the adhesive was no longer required. These design choices were made to provide a longer water ingress path (Figure 2.20) to prevent moisture from reaching the core in the unlikely scenario that the interface between the end fitting and the housing of the insulator got damaged.

2.6 Compression insulator profile design

2.6.1 Lateral orientation

The unique cross-sectional shape of the core that gives the compression insulator its improved mechanical characteristics also created unique challenges in the design of the profile. In order to keep the cost and weight of the insulator down, the sheath and sheds would have to follow the shape of the core as close as possible. The departure from the conventional cylindrical core design meant that the insulator would not be symmetrical

around its circumference. Additionally, because of the 'T-shaped' core, the profile would have flat sections, unlike traditional insulators. Therefore, its performance could be influenced by its orientation.

2.6.1.1 Profile variations

To explore the different possibilities, six profile variations were examined with different core orientations and sheath shapes. The profiles were classified in terms of wet performance, likelihood of biological growth, ice and snow accretion, weight and cost. Table 2.6 summarises the findings. This was developed in a brainstorming session, led and summarised by the author.

Table 2.6 *- Profile variations*

		Classification: 1 – 5 (Higher is better)					
	Profile	Wet	Bio Growth	Ice Snow	Reduced Weight	Reduced Cost	**Total**
A	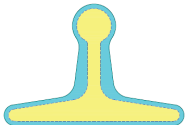	2	3	1	4	4	**14**
B	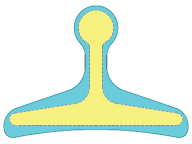	3	3	2	3	3	**14**
C	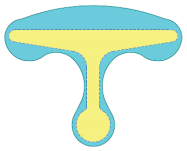	4	2	3	2	2	**13**
D		4	3	4	3	3	**17**
E	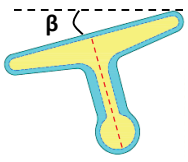	4	3	4	5	5	**21**
F	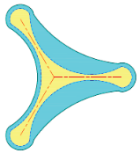	4	4	2	2	1	**13**
	Core (FRP) Sheath (SiR)						

2.6.1.2 Analysis

Profiles A and B have the spine of the core facing upwards which essentially creates two distinct, almost flat areas on the top of the profile. Attempting to increase the water run-off angle, the sheath of Profile B has steeper angles on the top side at the expense of more silicon and hence increased weight and cost. Both these profiles are likely to experience reduced performance in a polluted environment because the vertical spine will hamper their self-cleaning capability depending on the direction of the prevailing weather. Additionally, this orientation could create uneven hydrophobicity and aging because of the different rate that pollutants can accumulate on either side of the spine, which could reduce the lifespan of the insulator. The snow/ice performance capability of the insulator would also be affected since the minimal profile angles on the top could limit ice shedding while the spine could prevent melting on one side of the insulator by shielding in from the sun.

Profiles C, and D have the spine of the core facing downwards making pollution accumulation less of an issue in the areas between the spine and the flat sections of the profile. To facilitate water run-off, the sheath of these Profiles has a curved face on the top. Snow and ice performance would be better compared to Profiles A and B because the areas affected by the spine are facing downwards enabling more effective ice shedding. The sheath of profile C has curved areas on other parts of the profile as well which could further improve water run-off. However, the additional silicon required would not only increase the weight and cost of the insulator but also create areas on the profile shaded from the sun that could accelerate biological growth.

Profile F features a completely different core design with a symmetrical cross-section comprising of three equally spaced spines at 120^{o}. The mechanical properties of this profile are similar to the 'T-shaped' profile with comparable compressive and cantilever load withstand capabilities. The first option of positioning it would be to have one of the spines facing upwards but that would make the configuration almost identical to that of Profile A. The second option is the one shown in Table 2.6 which has one of the spines parallel to the horizontal plane. The more open nature of Profile F would reduce the probability of biological growth and improve the self-cleaning capabilities of the insulator. These benefits, however, are offset by the need for additional silicone which

would be required to fill the concave sections between the spines to avoid pollution and snow trapping, thus increasing the weight and cost of the insulator.

The best orientation was determined to be Profile E. It features the same core as Profiles A to D but it is tilted by an angle ***β*** so that the lateral axis is not perpendicular to the vertical axis of the cross-section. Profile E has all the benefits of Profile D with the addition of one very important property. Water run-off for this design is facilitated by angle ***β*** therefore there in no need to change the shape of the SiR sheath which can follow the shape of the core very closely, saving material. Angle ***β*** can be compared to the shed angle ***α*** for suspension insulators which also affects the water run-off behaviour. As such, the value of angle ***β*** was decided to be **6º** which is within the recommended range of 5º - 25º specified for the shed angle in IEC/TS 60815-3 [29].

2.6.2 Longitudinal orientation

The four members of the insulating cross-arm are arranged in such a way so that it can easily replace an existing lattice cross-arm. However, the ICA assembly is more flexible than the steel cross-arm since it does not have any cross-bracing members complementing the main structural elements to achieve the required mechanical strength. Hence, the compression insulators can be installed in a multitude of positions, varying from the horizontal (Figure 2.21), by adjusting the steel work at the tower end.

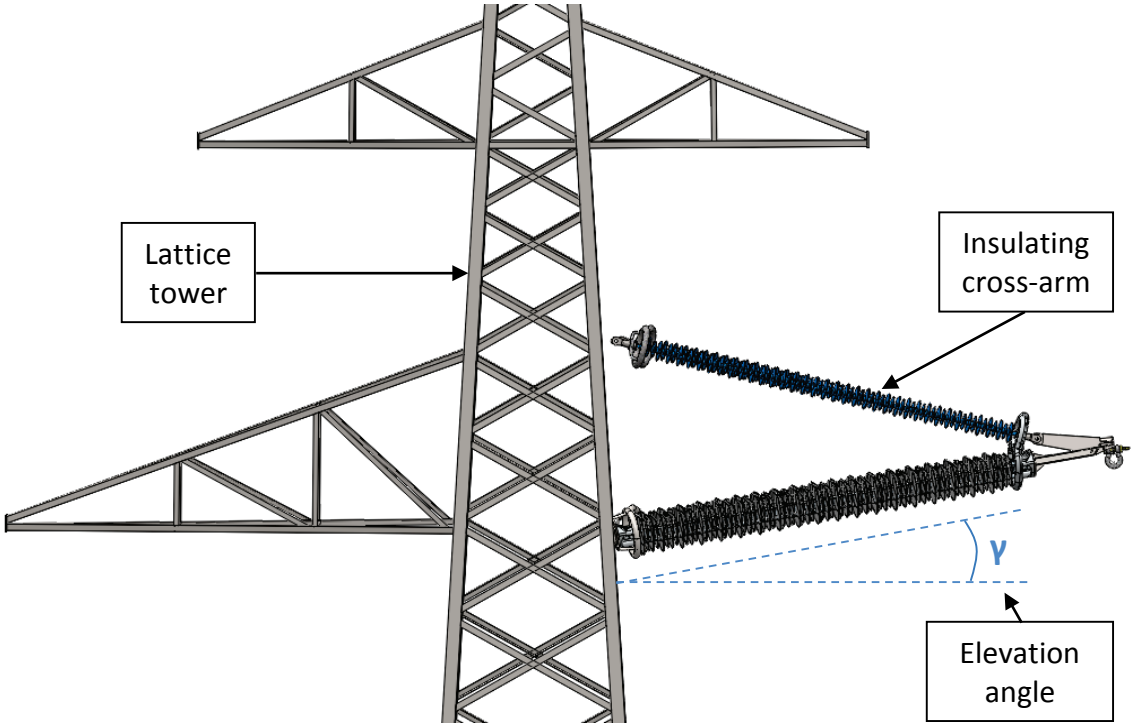

Figure 2.21 - ICA elevation angle

The lateral orientation, determined by the angle between the longitudinal axis of the compression insulator and the horizontal plane parallel to ground, is more important for the compression insulator than for traditional OHL insulators because of the flat sections of the profile. Together with angle $\boldsymbol{\beta}$ defined in the previous section, the elevation angle $\boldsymbol{\gamma}$ determines the water run-off behaviour of the insulator. Review of existing literature did not yield any results that could inform the choice of the appropriate elevation angle for the compression insulator. It was therefore decided to conduct an experiment in the HV laboratory in order to identify the optimal range of elevation angles.

2.6.2.1 Experiment setup

The test object was chosen to be a 145 kV class, SiR insulator. Its specifications are shown in Table 2.7. In addition to the proven design, the specific test object was also chosen because it was readily available in the laboratory. Furthermore, it had been subjected to standard flashover tests in the past and as a result both its dry and wet flashover voltage values were known in advance. Also its small size made it easier to handle than a 400 kV insulator while allowing experimentation at high voltage.

The HV end of the test object, which acted as the pivot point, was fastened to a post insulator of sufficient length to avoid flashover to ground. The LV end of the test object was connected to the crane of the HV laboratory via a bigger insulator which protects the crane from overvoltages. The spray system, which consists of an ABS pipe and four nozzles, was attached onto a nearby lattice structure, over the test object, with the nozzles pointing downwards. The distance between the nozzles and the test object was approximately five meters. The LV end-fitting of the test object was connected to ground while the HV end-fitting was connected to the AC test supply. The test object was not fitted with corona rings or arcing horns. A diagram showing the test setup can be found in Figure 2.22.

Table 2.7 *- Angle test insulator specifications*

Dimensions		**Diagram**
Number of sheds	31	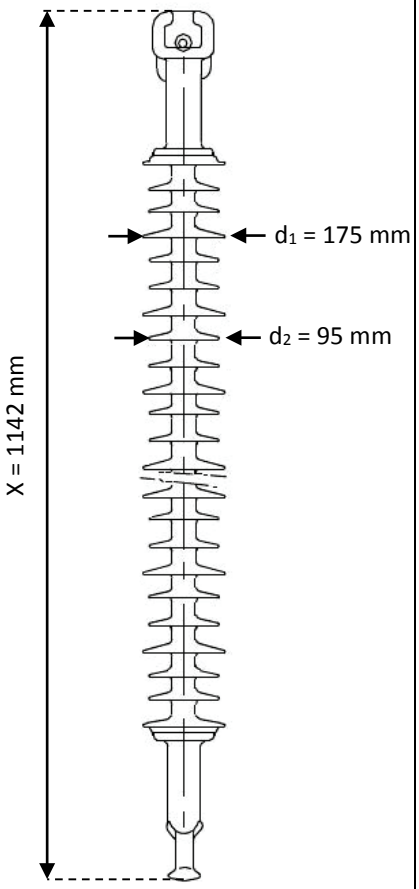
Arcing distance	850 mm	
Leakage distance	3092 mm	
Weight	9.8 kg	
Electrical characteristics		
Power frequency withstand voltage - dry	270 kV	
Power frequency withstand voltage - wet	220 kV	
Lightning impulse withstand voltage	490 kV	
Mechanical characteristics		
Specified mechanical load	210 kN	
Routine test load	105 kN	
Components		
Core	Epoxy & glass fibre, acid resistant	
Sheds	HTV silicone ARMOURSIL	
Fittings	Hot dip galvanized forged steel	

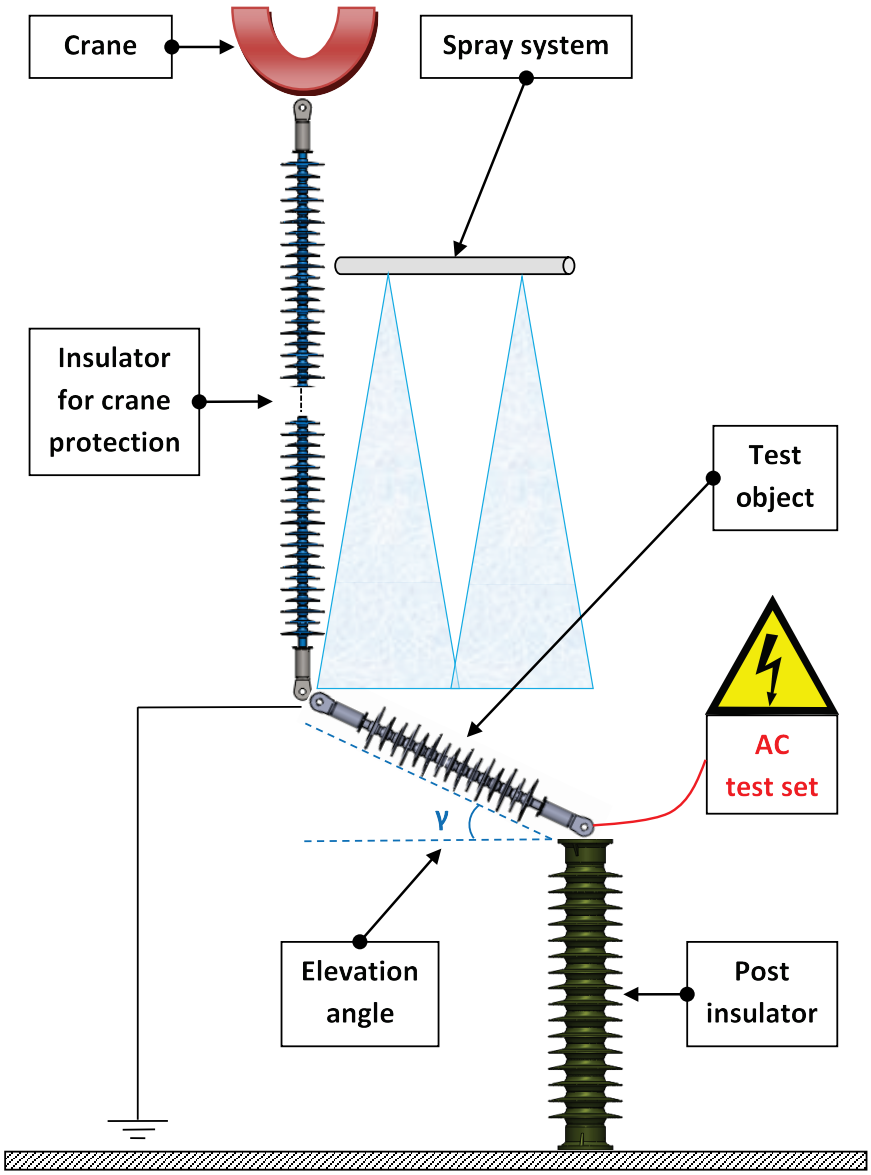

Figure 2.22 - Angle test experiment setup

2.6.2.2 Procedure

Before beginning the experiment, temperature, relative humidity and pressure were recorded. With the spray turned off, the voltage was raised from zero, steadily but rapidly (approximately 4 kV/s), until a flashover occurred. The supply was interrupted automatically and the flashover voltage recorded. The procedure was repeated ten times. The values were corrected to the standard reference atmosphere as described in BS EN 60060-1 [55] before the average dry flashover voltage was calculated. Then, the spray nozzles were aligned to provide uniform wetting and the precipitation rate was measured. Prior to energisation, the spray system was turned on for fifteen minutes to allow for sufficient wetting of the test object. Starting from 0^{o}, the elevation angle $\boldsymbol{\gamma}$ was increased in steps of 10^{o} until 90^{o} by raising the crane. To measure the angle, a digital

level was used with accuracy of ±0.1°. At each step, the flashover procedure described above was repeated ten times and the average flashover voltage for each angle was calculated. Between a flashover and the re-application of voltage to the test object, the surrounding dielectric was allowed to recover for at least one minute.

2.6.2.3 Results

Table 2.8 shows the atmospheric conditions during the experiment and the calculated correction factors. Table 2.9 shows the precipitation rate produced by the spray system measured with the collection vessel specified in BS EN 60060-1 [55]. Table 2.10 shows the dry flashover measurements, the average and the corrected average to standard reference atmospheric conditions. Table 2.11 shows the wet flashover measurements and the average flashover value for each angle.

Table 2.8 *- Atmospheric conditions and correction factors for angle test*

	Standard reference	**Measured**
Pressure (kPa)	101.3	101.93
Temperature (°C)	20	18.0
Relative Humidity (%)	-	42
Absolute Humidity (g/m³)	11	9.73

Correction factor	
k_1	1.0059
k_2	0.9929
K_t	**0.9987**

Table 2.9 *- Spray system precipitation rate*

	Collection area (mm²)	**H2O volume (ml/min)**	**Precipitation rate (mm/min)**
Vertical	25000	30	1.2
Horizontal	25000	2	0.08

Table 2.10 *- Dry flashover measurements*

Flashover Voltage - Dry (kV)										**Average (kV)**	**Corrected (kV)**
339.9	335.9	331.7	334.6	332.8	337.6	331.1	329.9	334.5	336.2	334.5	**334.9**

Table 2.11 *- Wet flashover measurements*

Angle (°)	Flashover Voltage - Wet (kV)										Average (kV)
0	320.4	318.8	320.0	320.4	319.3	314.6	309.9	321.9	319.7	319.1	**318.4**
10	324.2	315.5	319.1	315.5	320.9	320.4	311.4	321.8	311.0	319.7	**318.0**
20	305.8	312.3	309.6	311.7	317.9	302.2	308.5	303.1	314.8	300.9	**308.7**
30	318.8	314.8	318.4	299.7	303.1	312.6	303.1	308.1	301.1	302.2	**308.2**
40	289.9	315.9	316.8	276.4	298.4	301.5	304.0	311.7	302.4	308.1	**302.5**
50	316.4	304.2	310.5	302.0	298.6	308.1	293.0	300.2	297.7	305.6	**303.6**
60	307.8	311.0	301.3	305.1	308.1	288.5	291.9	313.7	288.1	287.2	**300.3**
70	297.5	305.8	310.5	308.7	296.8	302.9	299.1	293.5	296.8	306.0	**301.8**
80	304.0	297.4	299.3	293.5	306.5	301.8	307.6	294.4	302.0	301.5	**300.8**
90	293.0	283.8	282.2	291.7	291.2	276.2	294.6	293.9	291.2	298.6	**289.6**

Finally, Figure 2.23 summarises the results by plotting the wet average flashover values against the angle of elevation. A regression line is plotted in red. The line has the following equation:

$$y = \hat{a} + \hat{b}x \tag{2.12}$$

The coefficients $\hat{a}$, the y intercept, and $\hat{b}$, the slope, can be calculated as:

$$\hat{b} = r_{xy}\frac{s_y}{s_x} \tag{2.13}$$

$$\hat{a} = \overline{y} - \hat{b}\overline{x} \tag{2.14}$$

where $\overline{x}$ and $\overline{y}$ are the sample means, s_x and s_y are the sample standard deviations and r_{xy} is the sample correlation coefficient, calculated according to equation (2.15):

$$r_{xy} = \frac{\overline{xy} - \overline{x}\,\overline{y}}{\sqrt{\left(\overline{x^2} - \overline{x}^2\right)\left(\overline{y^2} - \overline{y}^2\right)}} \tag{2.15}$$

The dashed lines in blue above and below the regression line indicate a 95% confidence interval (CI) calculated as:

$$\left[\bar{x}-\frac{cs}{\sqrt{n}},\bar{x}+\frac{cs}{\sqrt{n}}\right] \tag{2.16}$$

where $\bar{x}$ is the sample mean, s is the sample standard deviation, n is the sample size and c is the percentile of the Student's t-distribution with $n-1$ degrees of freedom.

The error bars show the standard error (SE) calculated according to:

$$SE=\frac{s}{\sqrt{n}} \tag{2.17}$$

where s is the sample standard deviation and n is the sample size.

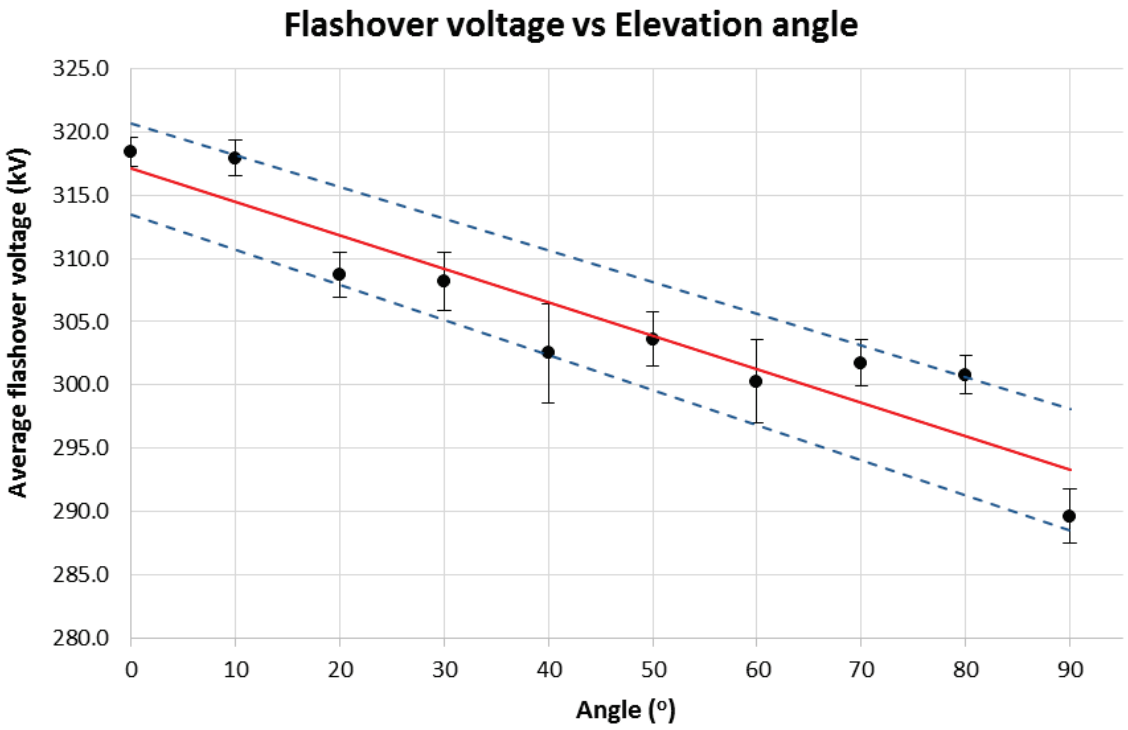

Figure 2.23 - Average flashover voltage vs elevation angle (0° - horizontal, 90° - vertical)

2.6.2.4 Analysis

The regression line of Figure 2.23 has a coefficient of determination $r_{xy}^{\ 2}=0.87$. In other words, 87% of the variation of data can be explained by the fitted line. This indicates a strong (negative in this case) linear relationship between flashover voltage and elevation angle. However, for angles between 20° and 80° the overlapping error bars show that the difference cannot be regarded as statistically significant. The same is true for angles between 0° and 10°. On the other hand, comparing the extreme angles of 0° and 90° there is sufficient evidence to support a significant variation.

The insulator is performing significantly better under wet conditions when installed horizontally or almost horizontally, with an elevation angle between 0° and 10°. The flashover performance drops linearly with the increase in elevation angle, reaching its lowest point at 90°. The results can be partially explained by observing the water runoff behaviour on the surface of the insulator. At the horizontal orientation, the water runs off the insulator from individual drip points formed at the rim of the sheds on the underside of the insulator. Figure 2.24 shows a flashover at 0° elevation angle captured with the night vision camera. The corona activity visible at the HV end of the insulator, starts at approximately 160 kV and continues to intensify until a complete breakdown of the surrounding dielectric occurs, always at the underside of the insulator for the horizontal orientation.

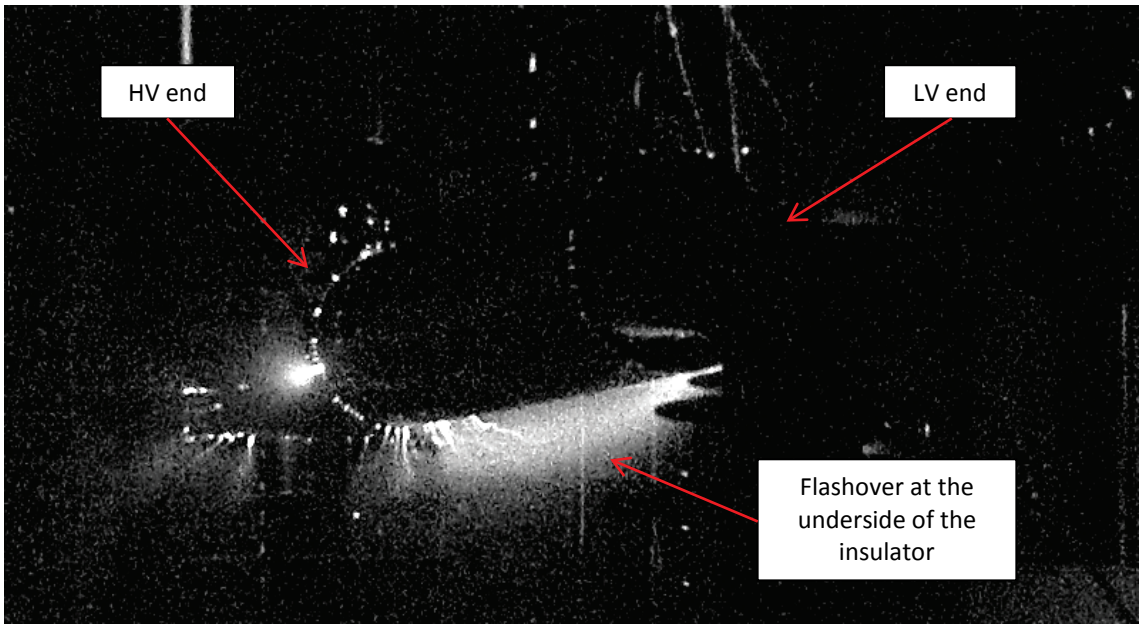

Figure 2.24 - Flashover at 0° elevation angle

When the insulator is placed vertically, under moderate and heavy precipitation the water running off from the sheds forms a continuous water path on one side of the insulator, often bridging many or all of the sheds. The flashover occurs at the side of the insulator where the water path is formed. The flashover voltage for the vertical orientation is lower because most of the creepage distance is bridged by the continuous water path which is not present when the insulator is placed horizontally. It is worth emphasising that the insulator was new and clean. Furthermore the water used for spraying was regular Manchester tap water with a low conductivity of approximately 100 µS/cm. In the presence of pollution it is almost certain that the difference in

flashover performance between horizontal and vertical orientations will increase as the water path will become more conductive.

Based on the findings of the experiment it was decided to set the elevation angle ***γ*** of the compression insulator at 6°. This angle not only ensures the best flashover performance under wet conditions, it also enhances the self-cleaning properties of the insulator by making water run-off easier in a similar manner as the lateral angle ***θ*** discussed before.

2.6.3 Profile design

On a traditional lattice tower, the suspension insulator can swing about its attachment point when subjected to wind. The swing angle ϕ_{ins} is normally used to determine the minimum phase to earth clearance. It can also be used to determine the space envelope of the tower. In the case of the ICA where the swing angle is practically non-existent, the length of the lattice cross-arm and the length allowed for insulator swing can be combined to give the maximum ICA length.

Since a 400 kV ICA is aimed to uprate a 275 kV OHL, a hypothetical 275 kV line employing L3 suspension towers is used to calculate the swing angle. The L3 tower is the smallest tower used in the UK for 275 kV transmission lines with a height of 36.88 m and width of 9.14 m [56]. For the purposes of the calculation it is assumed that the span length is 360 m. A single Araucaria type conductor is used with an overall diameter of 37.26 mm and a weight per unit length of 2.266 kg/m. The insulator is a polymeric suspension unit with an alternating profile and 76 sheds, 3.4 m in length, weighing 25 kg.

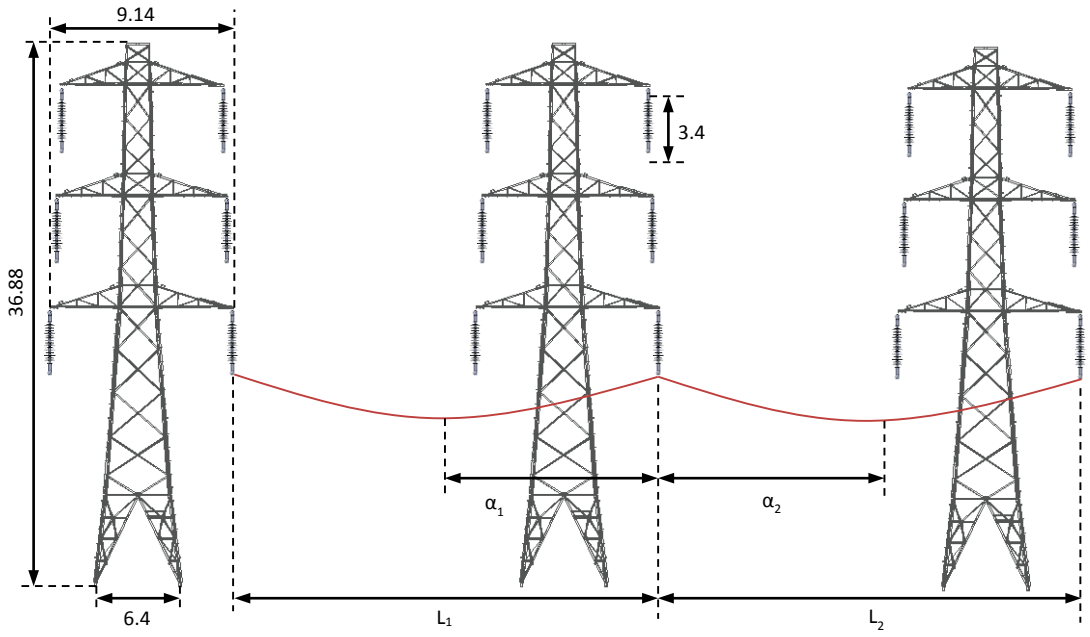

Figure 2.25 - L3 tower and 275 kV OHL dimensions

First, the site reference wind speed V_r is calculated using equation (2.18). The terrain is assumed to be of *Category III* i.e. "Basic open terrain, typical GB farmland, nearly flat or gently undulating countryside, fields with crops, fences or low hedges, or isolated trees", according to BS EN 50341-3-9 [17] and the site located at sea level.

$$\begin{aligned} V_r &= \gamma_v \cdot K_d \cdot K_R \cdot V_B \\ &= 1.2 \cdot 1.0 \cdot 1.0 \cdot 25 \\ &= 30 \ m/s \end{aligned} \tag{2.18}$$

where:

γ_v : the partial safety factor on wind speed

K_d : the wind direction factor

K_R : the terrain roughness factor

V_B : the basic wind speed

Using a height z of 30 m, approximately the height of the second cross-arm on the L3 tower, the mean wind speed V_z can be calculated from equation (2.19).

$$\begin{aligned} V_z &= V_r \cdot \left(\frac{z - h_e}{10} \right)^{\alpha} \\ &= 30 \cdot \left(\frac{30 - 0}{10} \right)^{0.165} \\ &= 35.96 \ {}^{m}\!/\!_{s} \end{aligned} \tag{2.19}$$

where:

a : the power law index of variation of speed with height

h_e : the effective height of surface obstructions

The dynamic pressure q_z at height z is:

$$\begin{aligned} q_z &= \left(\frac{\rho_\alpha}{2} \right) \cdot V_z^2 \\ &= \left(\frac{1.22}{2} \right) \cdot 35.96^2 \\ &= 788.8 \ {}^{kg}\!/\!_{m \cdot s^2} \end{aligned} \tag{2.20}$$

where:

ρ_α : the standard density of air for Great Britain

Now the wind load on the insulator P_{IW} can be calculated using equation (2.21).

$$\begin{aligned} P_{IW} &= q_z \cdot A_I \cdot C_I \cdot \left(1 + G_I\right) \\ &= 788.8 \cdot 0.1833 \cdot 1.2 \cdot \left(1 + 1.3\right) \\ &= 399.06 \text{ N} \end{aligned} \tag{2.21}$$

where:

A_I : the projected area of the insulator in the direction of the wind

C_I : the drag coefficient for the insulator

G_I : the gust factor for the insulator

The swing angle can be found using equation (2.22).

$$\begin{aligned}\phi_{ins} &= \tan^{-1}.\left(\frac{\frac{\rho}{2}\cdot C_C\cdot V_r^2\cdot G_L\cdot D\cdot L+\frac{P_{IW}}{2}}{m_C\cdot g\cdot L\cdot k_s+\frac{m_{ins}\cdot g}{2}}\right)\\ &= \tan^{-1}.\left(\frac{\frac{1.22}{2}\cdot 1.0\cdot 30^2\cdot 0.83\cdot 0.03726\cdot 360+\frac{399.06}{2}}{2.266\cdot 9.81\cdot 360\cdot 1.3+\frac{25\cdot 9.81}{2}}\right)\\ &= \tan^{-1}(0.6)\\ &= 31^o\end{aligned} \qquad (2.22)$$

where:

ρ : air density

C_C : drag coefficient of conductor

V_r : reference wind speed

G_L : span factor

D : conductor diameter

L : wind span

P_{IW} : wind load on insulator

m_C : mass per unit length of conductor

k_s : weight span over wind span ratio

m_{ins} : mass of insulator

Using the swing angle, the horizontal swing distance can be calculated (Figure 2.26). Combining this with the length of the lattice cross-arm, the maximum permissible 400 kV ICA length on an L3 tower that maintains the same space envelop of the tower is found to be approximately 4.76 m.

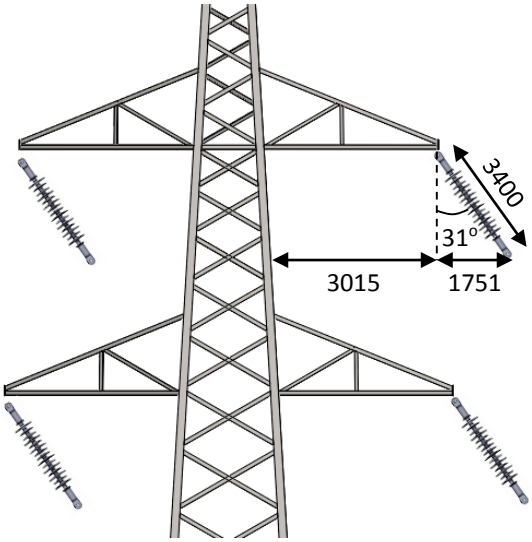

Figure 2.26 - Horizontal swing distance

In addition to the maximum cross-arm length, the other critical dimension affecting the design is the minimum clearance from ground, in this case the distance between the nose cone and the tower. Based on the values of Table 2.1, since the ICA is intended to be used on 400 kV lines this distance is 2.8 m. Additionally, National Grid in TS 3.4.17 [57] specifies the minimum creepage distance and length for insulators to be used on its network. For 400 kV insulators the minimum creepage distance is 12500 mm (approximately 31 mm/kV) and the length for polymeric insulators including fittings is 4100 mm ± 2%. For the ICA the nose cone was considered as part of the fittings. Figure 2.27 shows the above requirements. The nose cone and the end-fittings for the compression insulators were designed by EPL Composite Solutions and their dimensions were mainly determined by the mechanical requirements of the cross-arm.

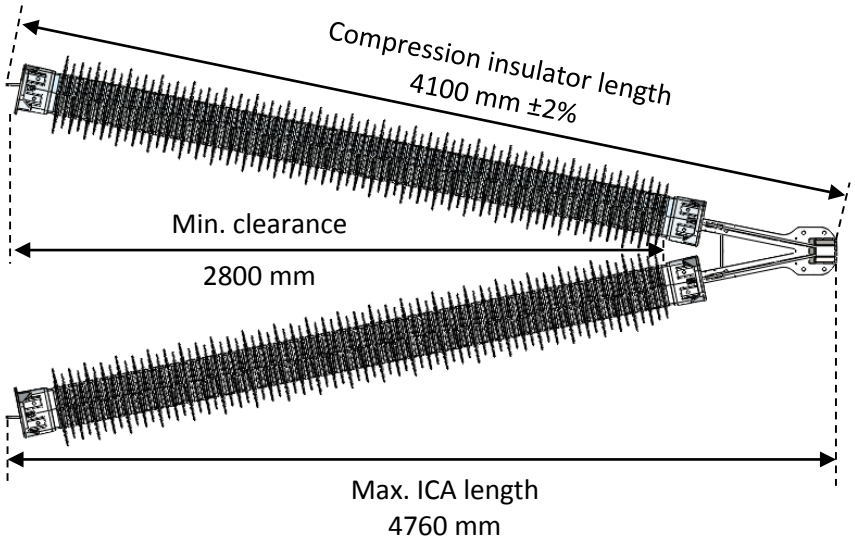

Figure 2.27 - ICA dimension requirements

In order to keep the tower footprint as small as possible it was decided to set the maximum length of the compression insulator together with the nose cone at 4018 mm, the minimum specified by TS 3.4.17 [57]. The nose cone accounted for 672 mm and the end-fittings of the insulator for another 130 mm each. The remaining 3086 mm effectively define the maximum arcing distance of the compression insulator.

2.6.3.1 Profile variations

To identify the optimum profile given the dimensions specified above, three simplistic designs with different shed patterns were considered: ***PR1*** is a uniform profile, ***PR2*** is an alternating profile with two different shed sizes and ***PR3*** is also an alternating profile but with three different shed sizes. The parameters for each profile design were calculated according to IEC/TS 60815-3 [29] and compared to the recommended values of Table 2.3. The target was to have all parameter values lie within the 'None' deviation category.

Table 2.12 *- PR1 parameters*

Drawing (mm)	Parameter	PR1		Deviation
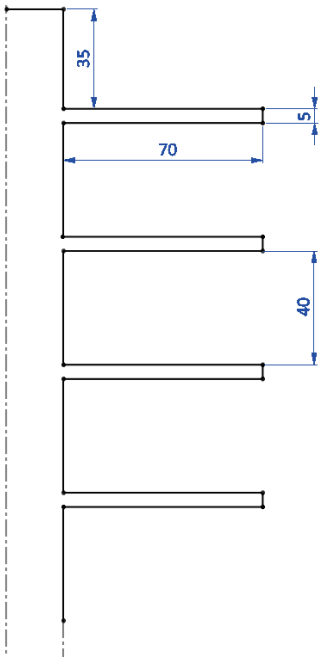	Type/Sheds	Uniform	68	
	Arcing distance	3090 mm		≤ 3086 mm
	Creepage distance	12610 mm		≥ 12500 mm
	Shed overhang	70 mm		
	Difference in shed overhang	$p_1 = p_2$		$p_1 = p_2$
	Spacing vs shed overhang	$\frac{s}{p} = \frac{45}{70} = 0.64$		Minor
	Minimum distance between sheds	$c = 40$		None
	Creepage distance vs clearance	$\frac{l}{d} = \frac{185}{45} = 4.11$		None
	Creepage factor	$\frac{l_T}{A} = \frac{12610}{3090} = 4.08$		None

Table 2.13 *- PR2 parameters*

Drawing (mm)	Parameter	PR2		Deviation
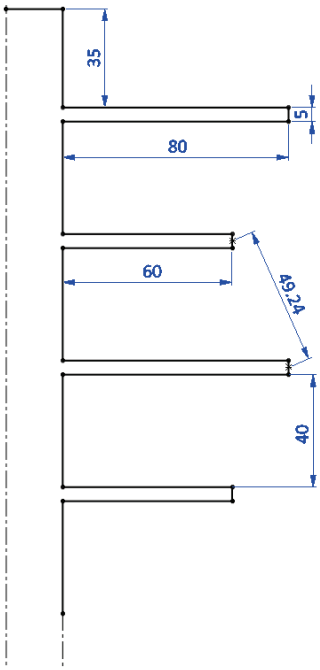	Type/Sheds	Alternating	34 big	
			34 small	
	Arcing distance	3090 mm		≤ 3086 mm
	Creepage distance	12610 mm		≥ 12500 mm
	Shed overhang	Big	80 mm	
		Small	60 mm	
	Difference in shed overhang	$p_1 - p_2 = 20$		$p_1 - p_2 \geq 14.4$
	Spacing vs shed overhang	$\frac{s}{p} = \frac{90}{80} = 1.125$		None
	Minimum distance between sheds	$c = 85$		None
	Creepage distance vs clearance	$\frac{l}{d} = \frac{370}{98.48} = 3.76$		None
	Creepage factor	$\frac{l_T}{A} = \frac{12610}{3090} = 4.08$		None

Table 2.14 *- PR3 parameters*

Drawing (mm)	Parameter	PR3		Deviation
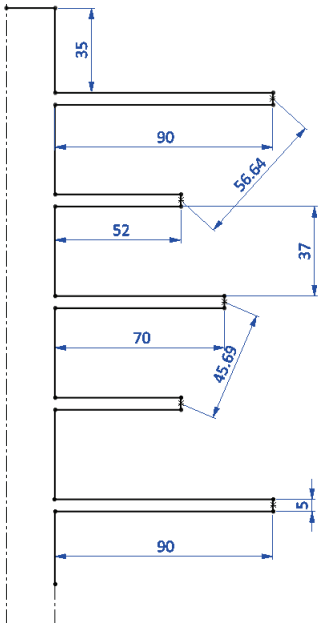	Type/Sheds	Alternating	18 big	
			18 med	
			36 small	
	Arcing distance	3057 mm		≤ 3086 mm
	Creepage distance	12561 mm		≥ 12500 mm
	Shed overhang	Big	90 mm	
		Medium	70 mm	
		Small	52 mm	
	Difference in shed overhang	$p_1 - p_3 = 38$		$p_1 - p_3 \geq 16.2$
	Spacing vs shed overhang	$\frac{s}{p} = \frac{168}{90} = 1.867$		None
	Minimum distance between sheds	$c = 163$		None
	Creepage distance vs clearance	$\frac{l}{d} = \frac{696}{204.66} = 3.40$		None
	Creepage factor	$\frac{l_T}{A} = \frac{12561}{3057} = 4.11$		None

2.6.3.2 Design selection

Table 2.12 shows that the uniform profile design ***PR1*** has a minor deviation in the 'spacing vs shed overhang' parameter. Also the 'creepage distance vs clearance' parameter, although within range, is very close to the acceptable limit. Such a profile would be likely to exhibit reduced performance under heavy pollution or non-uniform hydrophobicity. By adjusting the dimensions of this design multiple times it became obvious that it would be impossible for a uniform profile to satisfy the dimensioning requirements without at least one of the parameters having a minor deviation. For the above reasons, the uniform profile design was rejected.

The two alternating profile designs, ***PR2*** and ***PR3***, both comply with all the requirements and their parameters show no deviation. They also have comparable creepage distance densities due to their similar creepage factors, 4.08 for PR2 and 4.11 for PR3. Profile PR3 however, is superior in almost every aspect with all of its parameter values higher than PR2, indicating that PR3 should have better self-cleaning properties and pollution performance. Additionally, the three-shed pattern, the deeper large sheds and the bigger distance between large sheds should provide better performance under snow and ice conditions as discussed earlier. Consequently, ***PR3*** was chosen as the preferred design for the profile of the compression insulator.

2.6.3.3 Final profile design

To avoid issues with the interfaces between the sheath and the sheds, it was decided to mould the sheath and sheds of the compression insulator together, using an injection moulding process. One of the injection moulding machines is shown in Figure 2.28 (a) while Figure 2.28 (b) shows the aluminium mould.

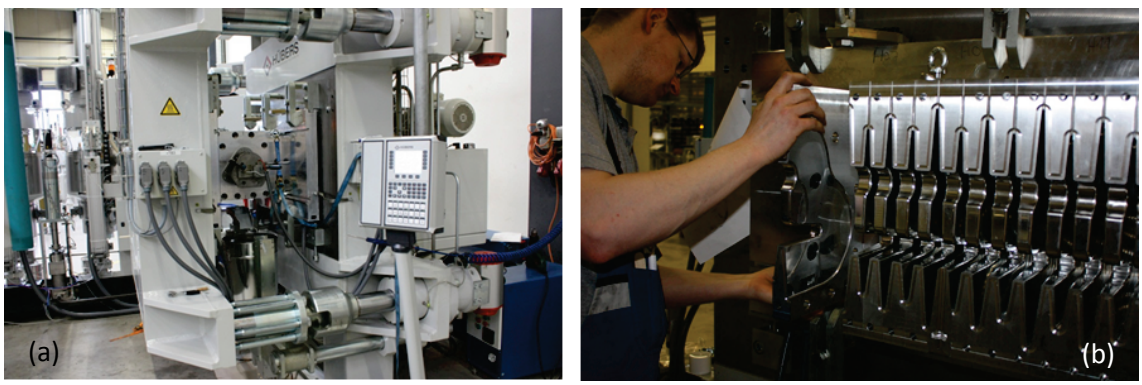

Figure 2.28 - Liquid silicone injection moulding machine (a) and compression insulator mould (b)

In order to give more flexibility to the process that would enable the manufacturing of insulators of different lengths, the mould was divided in a number of segments. The mould segments were designed to overlap and seal onto the silicon moulded using the previous segment (Figure 2.29 (a)). A complete 400 kV compression insulator (Figure 2.29 (b)) required seven mould segments.

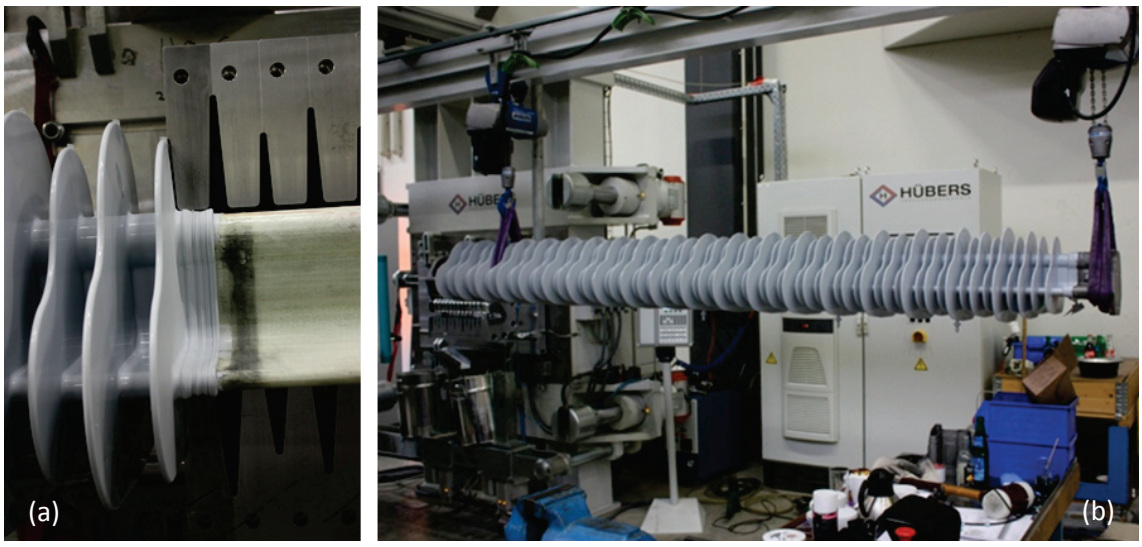

Figure 2.29 - Mould segment sealing against the previously moulded segment (a) and finished compression insulator leaving the manufacturing line

Due to the choice of manufacturing process described above, the basic ***PR3*** design needed to be modified to allow for the more efficient production of the insulator. The sheds were made tapered, starting thicker near the sheath and ending thinner at the tip, with each shed size having a different thickness. This was done to give the sheds better flexibility to avoid damage during transportation and installation and also to facilitate the easier release of the insulator from the mould.

Instead of a 90^{o} angle, the shed-sheath interface and the tip of each shed were rounded with a radius of 2.5 mm to minimise the electric field enhancement from the shed tips that could potentially cause corona discharges. Because of the proximity of the two compression insulators at the nose cone, an additional small shed was introduced at the HV end of the compression insulator to prevent the sheds from clashing when the two compression insulators were installed as parts of the ICA assembly. After these modifications, the dimensions and parameters of the profile were re-evaluated. Figure 2.30 shows the HV-end of the insulator while Table 2.15 shows the final dimensions and parameters. Figure 2.31 shows the final 400 kV ICA dimensions for an L3 OHL tower.

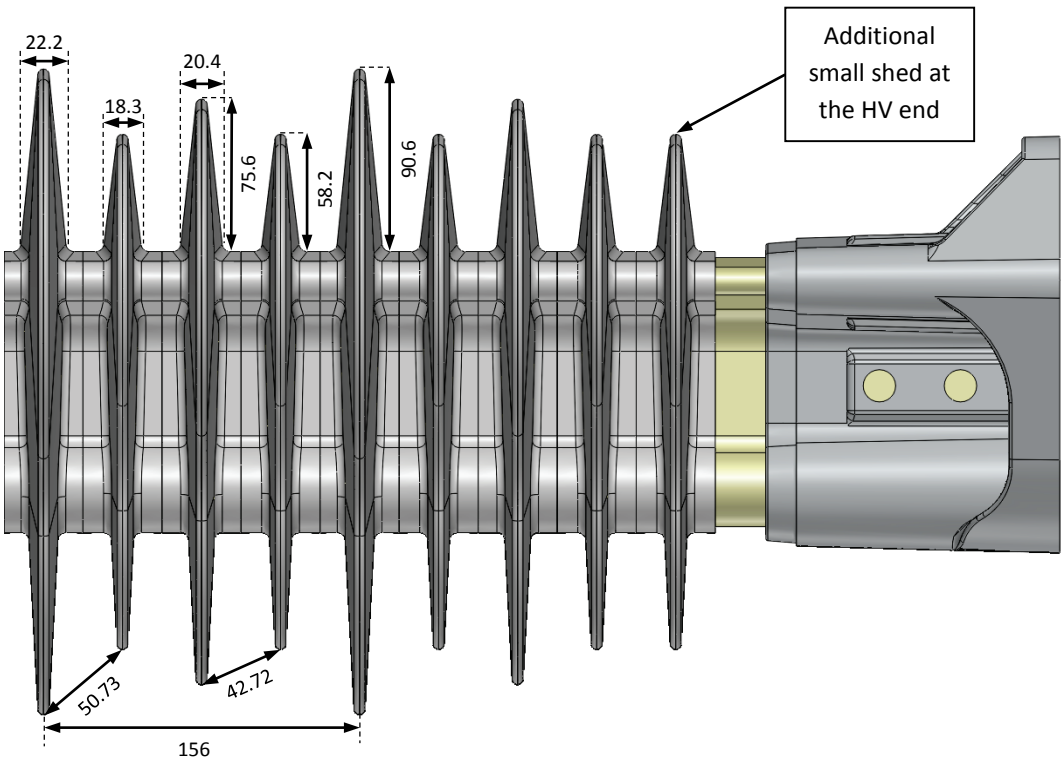

Figure 2.30 - Compression insulator HV-end

Table 2.15 *- Compression insulator profile parameters*

Drawing	Parameter			Deviation
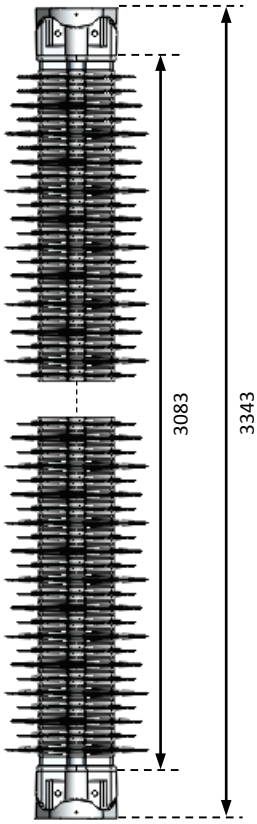	Type/Sheds	Alternating	19 big	
			19 med	
			39 small	
	Arcing distance	3083 mm		≤ 3086 mm
	Creepage distance	12470 mm		≥ 12500 mm
	Shed overhang	Big	90.6 mm	
		Medium	75.6 mm	
		Small	58.2 mm	
	Difference in shed overhang	$p_1 - p_3 = 32.4$		$p_1 - p_3 \geq 16.3$
	Spacing vs shed overhang	$\frac{s}{p} = \frac{156}{90.6} = 1.722$		None
	Minimum distance between sheds	$c = 156$		None
	Creepage distance vs clearance	$\frac{l}{d} = \frac{644.79}{186.90} = 3.45$		None
	Creepage factor	$\frac{l_T}{A} = \frac{12470}{3083} = 4.04$		None

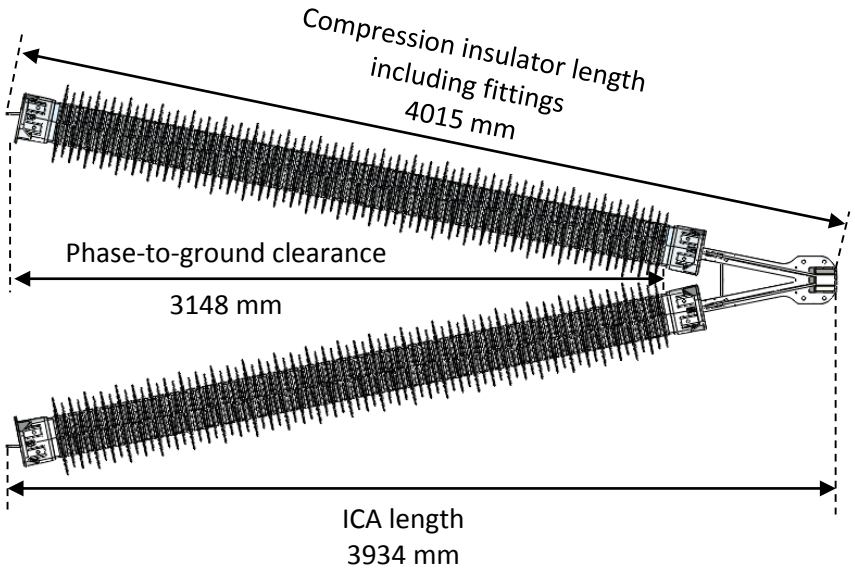

Figure 2.31 - 400 kV ICA dimensions

2.7 Discussion

Polymeric insulators offer many advantages compared to glass or ceramic insulators. They are lighter with higher strength to weight ratio and they perform better electrically under heavy pollution and wetting. On the other hand, composite insulators are more prone to degradation caused by the environment, electric fields and arcing which may affect their lifetime and performance. The choice of materials is crucial for maintaining the mechanical integrity and ensuring the electrical performance consistency of the insulator in the long-term. The material of the core needs to be chemically optimised to withstand acid attacks in case of moisture ingress to avoid brittle fracture and mechanical failure. The rate of pollution accumulation should be considered when selecting the housing material since it varies depending on the material. Together with biological growth, they affect hydrophobicity and hence the performance of the insulator. Additionally, the housing material needs to be resistant to tracking and erosion so it can keep the insulator watertight.

The dimensions and profile design of a composite insulator are also of paramount importance to the performance of the insulator. Concessions are sometimes made by customers because of the improved pollution performance of composite insulators, which means insulators can have less than standard creepage distance. However, this is possible to enhance the discharge activity. If the insulator suffers too much discharge in a short time, it becomes hydrophilic hence eliminating the advantage of improved

pollution performance. Conversely, excessive creepage distance per unit length may result in localised arc activity between sheds due to the decreased shed-to-shed spacing which in turn can increase the risk of degradation. In the majority of cases it is advisable to use the same creepage distance as glass or ceramic insulators to balance the effects of improved pollution performance and increased risk of degradation.

In respect to snow and ice accretion it should be noted that polymeric insulators experience full bridging of sheds sooner than porcelain insulators in some occasions, primarily due to the closer shed-to-shed spacing. Since the break-down voltage in such conditions depends on the length of air gap between the sheds after ice accumulation, bigger shed-to-shed spacing and alternating shed profiles are recommended because they increase the separation between large sheds and consequently the time needed for ice bridging.

The criteria and the issues affecting the design of composite insulators, identified by reviewing the existing literature and international standards, were used to design a composite insulator for use on ICA assemblies. Another factor that greatly influenced the design of this insulator in particular was the unique shape of its core. This shape allows for an 85% smaller cross-sectional area than a cylindrical core while having the same second moment of area. At the same time however, it creates flat and concave sections around the circumference, unlike traditional insulators.

Firstly, the lateral orientation of the insulator was established by examining six different core and sheath combinations. It was determined that the best orientation in terms of water runoff, biological growth, snow and ice accretion, weight and cost was with the flat section of the T-shaped core facing up and tilted by 6^{o} with respect to the lateral axis of the insulator. The effect of the longitudinal orientation on the performance of the insulator was also examined by the means of an experiment designed to evaluate the effect of elevation angle compared to the flashover voltage under wet conditions. The results indicated that the insulator performed better at elevation angles between 0^{o} and 10^{o}. It was therefore decided to set the elevation angle of the insulator when installed as part of the ICA assembly to 6^{o}.

To establish the maximum and minimum dimensions of the compression insulator it was assumed that a 400 kV ICA could be used to uprate a 275 kV OHL with L3 towers. These

dimensions together with the recommendations from international standards provided the basis for designing three candidate profiles. After careful analysis, the profile that was chosen to be the most suitable was an alternating profile with three different shed sizes and a shed pattern that maximized shed-to-shed separation for increased performance.

2.8 Conclusion

The profile of a novel insulator with a non-circular core cross-section and improved mechanical characteristics, capable of serving as the strength member in insulating cross-arm assemblies was designed. The approach followed was the best available under the circumstances, aimed to provide confidence regarding the short-term and long-term performance of the insulator despite the unavailability of similar designs in the market. The design incorporated recommendations from international standards, knowledge from past experience as reported in existing literature and experimental results. The unique appearance of the insulator profile has led to a registered design [58].

3. ELECTRIC FIELD STRESS MANAGEMENT

3.1 Introduction

Managing the electric field distribution around HV composite insulators is critical for maintaining their performance and ensuring their longevity. High electric field magnitudes have been linked with corona discharges, dry-band arcing and discharges internal to the core of insulators. These phenomena can not only compromise the insulator itself but can also create undesirable effects near the overhead line. In the case of the insulating cross-arm, since the number of insulators is quadrupled compared to a standard overhead line, controlling the electric field is even more important. Therefore, to ensure the performance and longevity of an insulator, a well-designed and efficient profile, as described in *Chapter 2*, needs to be complemented by appropriately designed electric field stress control.

This chapter examines the corona discharge phenomenon in detail. Specifically, a review of the relevant literature regarding the various modes that affect corona formation is presented. This is followed by an overview of the effects of corona from AC transmission lines and the effects of high electric fields on composite insulators. Moreover, an introduction to the Finite Element Method (FEM) is presented along with a detailed explanation of the use of Finite Element Analysis (FEA) for the computation of electrostatic fields.

The later part of the chapter, which constitutes its original contribution to the research, is concerned with the design of electric field grading devices for the ICA. For the LV end of the assembly, a non-circular grading ring for the compression insulators has been designed. For the HV end, the iterative design process yielded two novel designs, one suitable for voltages up to 132 kV and the other for voltages up to 400 kV. SolidWorks was used for producing the models of the electric field grading devices while COMSOL Multiphysics was used to perform the electrostatic field calculations on the various sections of the ICA.

3.2 Corona discharge

Corona discharges are low-power, luminous and audible discharges that are observed in non-uniform fields and can be transient or steady state. In high voltage engineering non-uniform fields cannot be avoided so the phenomenon is of particular importance [59]. The name comes from the Greek word '*κορώνα*' which means '*crown*' and it is believed to have been originally used by seafarers to describe the luminous discharges emanating from the masts of their ships during electrical storms [60].

The formation of corona discharges is attributed to an electron avalanche process that ceases before reaching ground. The avalanche is initiated by the presence of an inhomogeneous electric field sufficiently strong to ionize the neutral molecules surrounding the electrode [61]. In air, which is a mixture of mainly nitrogen (79%) and oxygen (20%), the electronegative nature of oxygen molecules significantly affects corona discharge development. The avalanche process can be impeded by the presence of negative ions formed by the ability of oxygen to capture free electrons [62]. The presence of oxygen also enhances the accumulation of ionic space charge at the vicinity of the high voltage electrode which in turn changes the distribution of the local electric field. The different equilibrium states of space charge near the high voltage electrode give rise to several corona discharge modes which are used to categorise corona either as negative or as positive [63].

3.2.1 Negative (cathode) corona

With the high voltage electrode at negative potential, the electron avalanche starts at the cathode, extending towards the anode until it reaches a boundary surface (S_0) where the net ionization coefficient is zero. Two regions of ionic space charge are formed in the gap between electrodes with the higher mobility free electrons at the head and the positive ions at the tail of the avalanche (Figure 3.1). Three distinct corona modes can be observed that influence the development of negative corona that occur at different field intensities [63].

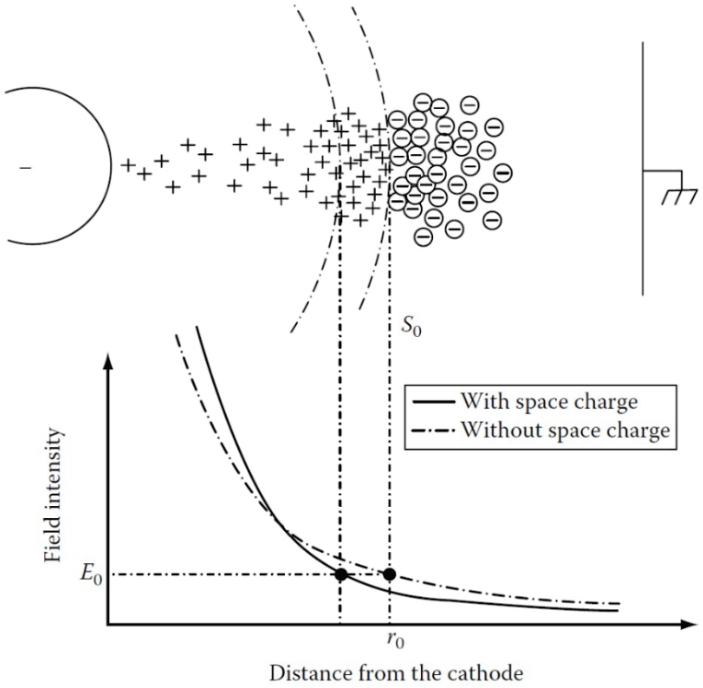

Figure 3.1 - Negative corona

With the voltage just above the corona onset value, the first observable mode is the ***Trichel streamer***. It is caused be a repetitive cycle of initiation, development and suppression of the streamer along a narrow channel from the cathode. The cycle has a very short duration (tens of nanoseconds) with a few milliseconds of dead time before it is repeated. The discharge current resulting from this process appears in the form of short duration, small amplitude pulses called Trichel pulses [64, 65]. The pulsating behaviour of the discharge at this stage is a result of the suppression of the electron avalanche due to a very active recombination process which reduces the field intensity and suppresses the discharge momentarily until a new avalanche is created. The repetition rate depends on the effectiveness of the field to remove the ionic space charge and has a linear relationship with the applied voltage [66].

As the field increases it becomes more efficient in removing the space charge, preventing its accumulation near the cathode and suppressing the ionization activity. Stable emission of electrons from the cathode by ionic bombardment creates a ***negative pulseless glow***, the second negative corona mode [67]. The transition from the Trichel streamer mode to the negative pulseless glow mode is corroborated by the reduction of the repetition rate of the Trichel streamer as the field increases, which indicates the existence of an equilibrium state between the creation and removal of space charge [68].

If the field is increased even further the third negative corona mode can be observed, the ***negative streamer***. A stable streamer channel originating from the cathode is formed that constricts the discharge forcing it further into the gap between electrodes. The discharge current pulsates at low frequency as the streamer channel extends from the cathode into the gap and back. The discharge characteristics are similar to the negative pulseless glow since the electron emission from the cathode is also responsible albeit accompanied by an even more effective space charge removal process, hence the development of the streamer channel [66].

3.2.2 Positive (anode) corona

With the high voltage electrode at positive potential, the electron avalanche develops towards the anode originating from a point on the boundary surface with zero ionization coefficient (S_0). As before, because of the lower mobility of positive ions compared to electrons, the tail of the avalanche consists of positive ion space charge. In this case however, most of the free electrons are neutralised upon reaching the anode due to the higher local field intensity which limits electron attachment. Negative ions tend to appear farther in the gap in the low-field region (Figure 3.2) [67]. For positive corona, four modes with different characteristics can be observed as the field increases, affected by the presence of space charge of both polarities near the anode.

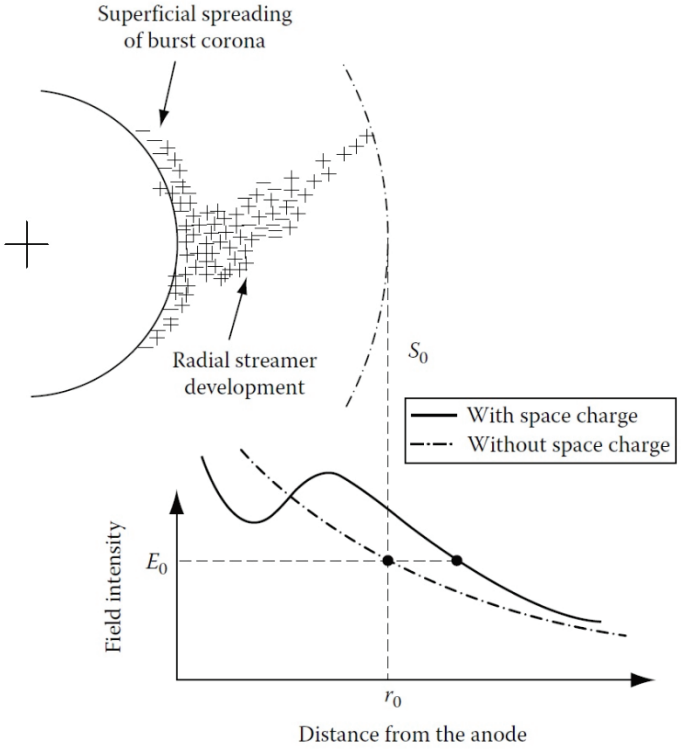

Figure 3.2 - Positive corona

As soon as the voltage exceeds the corona onset value two positive corona modes begin developing in parallel. One of them is ***burst corona***. The highly mobile electrons lose most of their energy before being neutralised at or near the anode as the ionization activity spreads at the surface of the anode. This results in the build-up of a small positive space charge due to the presence of positive ions near the anode which supresses the discharge. The spreading of the ionization over a small area of the anode and its subsequent suppression by the space charge produces a discharge current consisting of small pulses. Burst corona appears as a lucent skin attached to the anode surface [63, 67].

The other positive corona mode that is observed at the same time as burst corona is the ***onset streamer***. A thin streamer channel is formed originating from the anode causing the discharge to extend radially farther into the gap than burst corona. This is the result of the accumulation of positive space charge near the anode which enhances the local field attracting electron avalanches. The creation and subsequent absorption of electron avalanches by the anode supresses the streamer discharge until the field removes the residual space charge enabling the development of a new streamer. Hence the onset streamer appears in the form of short duration, high amplitude, positive current pulses with low repetition rate [60, 63].

By raising the voltage higher, burst corona begins to dominate over the onset streamer, something that gives rise to a new mode, the ***positive glow***. The field is effective enough at removing space charge from the anode but at the same time is not intense enough to enable streamer formation. This results in the creation and removal of positive ions in the gap that gives rise to a primarily direct current with a small pulsating component. The positive glow mode appears as a thin luminous layer very close to the anode [63, 67].

An even further increase of the applied voltage sees the reappearance of streamers which lead to the final mode of positive corona, the ***breakdown streamer***. The nature of the discharge at this stage is similar to the onset streamer but because the field is more effective at removing the space charge near the anode the discharge can extend even further into the gap. The intensity of breakdown streamers increases as the voltage increases until the gap is fully bridged. This does not always cause a breakdown which indicates that the streamer channel is not completely conductive [63].

3.2.3 AC Corona

At the presence of an alternating voltage, the electric field polarity and amplitude changes within a cycle. Depending on the length of the gap between electrodes, more than one corona mode can be observed in one cycle. Trichel streamers, positive onset streamers and burst corona are present just above the corona onset voltage for short gaps as the space charge, positive or negative, created during the corresponding half cycle is neutralised at the end of the half cycle. For longer gaps, Trichel streamers, negative glow, positive glow and positive streamers can be observed because the residual space charge that cannot be absorbed by the electrodes during one half cycle ends up in the high field region during the next half cycle, influencing the development of the discharge [63].

3.3 Peek's law

Peek was one of the first researchers to study the corona phenomenon [69]. Based on empirical observations, Peek's law (3.1) can be used to approximately calculate the corona inception voltage (CIV), the voltage required for the onset of visible corona discharge between two conductors.

$$e_v = m_v \cdot g_v \cdot r \cdot \ln\left(\frac{S}{r}\right) \tag{3.1}$$

Where:

e_v : corona inception voltage

m_v : irregularity factor

g_v : electric field at breakdown

r : radius of the conductor

S : distance between conductors

3.4 Corona from Overhead Lines

On AC overhead lines, a strong electric field exists near the conductor and other line hardware such as insulators. The high voltage gradient, which is the magnitude of the electric field intensity, is responsible for the ionization activity that results in corona

discharges. The energy required to sustain the discharges is mainly converted into heat and in smaller proportions to electromagnetic radiation and acoustic energy. Therefore the main effects of corona from overhead lines, examined in the following sections, are corona losses, radio interference and audible noise. [70, 71]. Corona is also responsible for other less pronounced effects such as generation of ozone and nitrogen oxides, light emission, electrical wind and corona-induced vibrations in the conductor [70].

3.4.1 Corona losses

The loss of power caused by corona can be attributed to the oscillatory movement of the ionic space charge due to the presence of the alternating electric field near the conductors [71]. This movement produces an alternating current component which is mainly in phase with the voltage, drawing energy from the HV power source and resulting in losses. Additionally, corona can increase the capacitance of the conductor configuration, further increasing losses, since a small component of the corona current is in phase with the capacitive current of the line [70]. Corona losses are usually expressed it Watts per kilometre of line. They tend to be negligible in dry conditions but humidity and rainfall aggravate the phenomenon, greatly increasing power loss which can reach several hundreds of kW per kilometre [71].

3.4.2 Radio interference

Streamer discharges can inject current pulses into the OHL conductors. These transient currents and their accompanying electromagnetic field can propagate along the conductors for significant distances until their amplitude attenuates and can cause interference in TV and AM-radio receivers in the vicinity of the line [71, 72]. The interference caused by transmission lines attenuates at relatively short distances away from the line since the frequency spectrum of the pulses can extend up to approximately 100 MHz. For distribution lines however, another kind of discharge is present, gap discharge, caused mostly by loose connections. The spectrum generated by this type of discharge has cut-off frequency close to 1 GHz and is the main source of television reception interference [71, 73].

3.4.3 Audible noise

As explained earlier, negative Trichel streamers and positive onset streamers cause rapid ionization of the molecules surrounding the high voltage conductor and line

hardware. This causes the air in the streamer channel to heat up and the pressure to increase. The local increase in pressure corresponds to the generation of an acoustic wave. The frequency of the acoustic pulse is well within the range of audible frequencies, usually extending above 15 kHz resulting in the characteristic buzzing noise of corona [71]. Another form of audible disturbance caused by overhead lines is an acoustic pure tone called hum with a frequency twice that of the power frequency (100 Hz for a 50 Hz system). The kinetic energy of the oscillating ions is transferred to the air molecules when the two collide resulting in the low-frequency hum [70].

3.5 Electric fields on composite insulators

The electric field distribution on the surface as well as within polymeric insulators influences their short term and long term performance. Because of the size of the insulators the field along them is not uniform with its magnitude being higher near the HV and LV ends. The main factors that affect the electric field distribution are the line voltage, the shape of the insulator, the dielectric properties of the materials, the dimensions and position of grading devices and other line hardware as well as the orientation of the insulator with respect to the conductors [34]. The effects of the field distribution can be divided into four categories detailed below.

3.5.1 Corona on the surface of the polymeric material

High electric fields under wet conditions, exceeding the water drop corona threshold of 4.4 kV/cm, can enhance corona activity on the surface of the insulator and accelerate the aging of the material [74]. Corona has been found to change the chemical properties of the weather shed material by generating hydrophilic hydroxyl groups (-OH) on the surface of corona-aged insulators. Further evidence of degradation is the generation of a silica-like layer resulting from the combination of silicon and oxygen atoms that can be seen as a white trace after the corona activity has ceased [75]. Prolonged exposure to corona can result in the permanent loss of hydrophobicity in addition to the development of cracks to the material which can severely affect the performance of the insulator [76].

3.5.2 Dry-band arcing

Uneven field distribution along the length of the insulator can overstress and ultimately damage parts of the unit. When contaminated and wet the insulator can experience increased leakage current flow on its surface. As a result, preliminary discharges develop surface which usually take place before flashover, a phenomenon known as dry-band arcing. This effect becomes more severe when the weather sheds are closely spaced together which is often the case for composite insulators [20].

3.5.3 Discharges within the core or at the interfaces between materials

Insufficient wetting of the glass fibres during the manufacturing of the core can sometimes lead to the trapping of air bubbles in the core resulting in the formation of elongated cavities. Air-filled cavities can also be created at the interface between the sheath and the core if the bonding of the two is not done properly. Under the influence of high electric field, which is higher near the end-fittings, partial discharges can develop within these cavities. As mentioned earlier, partial discharge in air, or corona, can produce ozone (O_3) and nitrogen oxides (NO_x) which have the ability to oxidise polymer chains, producing a mixture of organic acids. The glass fibres are prone to corrosion by organic acids that when combined with the application of mechanical load, can lead to brittle fracture and mechanical failure of the insulator [77].

3.5.4 Corona from metallic hardware

In the same way that corona appears on OHL conductors, it does on the metallic hardware of insulators (end-fittings, corona rings) since they are also energised at high voltage. Hence, if not controlled properly, corona from insulator hardware can produce radio interference and audible noise [34]. Furthermore, the electric field distribution and magnitude are affected by the position and geometry of the end-fittings and grading rings [78]. Improper dimensions and positioning can result in corona cutting, where corona discharges originating from the metallic parts of the insulator degrade the weather shed material [79]. Except from loss of hydrophobicity, in the more severe cases, this can completely erode the silicone, exposing the core and leaving it vulnerable to acid attacks.

Furthermore, the design of the end fittings of insulators can have a detrimental effect on the electric field distribution near the triple junction, the point where the housing,

the core and the metal work meet. This area is naturally susceptible to electric field enhancement because of the interaction of the different materials that make up the insulator and the surrounding air. If the insulator is not designed with the protection of this interface in mind it is possible that partial arcs could start eroding the sealing material that keeps the insulator watertight [35].

Adding to the above, managing the electric field near and around the composite cross-arm assembly and its four insulating members is crucial for another reason. The compaction of the overhead line dimensions, which is one of the main benefits of the technology, has the effect of reducing phase-to-phase and phase-to-tower spacing when compared to traditional lines for the same voltage. In turn this can increase voltage gradients on conductors and local electric field magnitude which can increase the probability of flashover.

3.5.5 Requirements

The importance of the electric field distribution along a composite insulator has been recognised by the industry. In the UK, National Grid has set specific criteria as part of their technical specifications that an OHL insulator must meet before it can be installed on their network [80]. These criteria coincide with the recommendations of the IEEE taskforce on Electric Fields and Composite Insulators [34] and the EPRI [70] and hence they have been adopted for the ICA:

- Maximum permissible electric field magnitude on the sheath and sheds measured 0.5 mm from the surface: 4.5 kV_{rms}/cm
- Maximum permissible electric field magnitude at the triple junction: 3.5 kV_{rms}/cm
- Maximum permissible electric field magnitude inside the core and weather-shed material: 30 kV_{rms}/cm
- Maximum permissible electric field magnitude on metallic end-fittings and electric field grading devices: 18 kV_{rms}/cm

3.6 Finite Element Method (FEM)

There are several experimental methods available for measuring the electric field including using capacitive electric field probes [81] and electro-optic electric field probes

[82]. However, they are in most cases expensive, time consuming and difficult to implement. Furthermore the introduction of extra hardware near the insulator distorts the electric field and reduces the accuracy of the measurement. Also it is impossible to measure the electric field inside the core or very close to the surface of the insulator [34]. As an alternative to experimental methods, the electric field can be studied using numerical techniques. The most popular are the charge simulation method, the boundary element (BEM) method and the finite element method (FEM). To speed up the study of the electric field distribution and also the development and optimisation of end-fittings and grading devices for the ICA the latter was used.

The FEM is a numerical method for solving mathematical models which are too complex or cannot be solved analytically. It is used to investigate various properties of components or assemblies and predict how they will behave under certain environmental factors. Computer-based simulations that utilise the FEM can be employed to transfer design iterations into the virtual domain, leaving the manufacturing of prototypes for final design verification only [83].

The method works by splitting the model of the object being studied into a sufficiently large number of small elements of simple geometric shape, the finite elements. The shape of the finite elements in most cases is triangular for two dimensions and tetrahedral for three dimensions. The division of the geometry into a mesh of standard shaped elements is advantageous because it enables the representation of complicated functions in a piecewise continuous manner.

The application of the FEM requires the knowledge of the partial differential equations (PDE) that govern the physics of the problem, the boundary conditions at the edges of the regions of interest and the material properties of the object. Because the geometry is divided into simple shapes, the actual PDE is no longer necessary. The PDE can be approximated by a much simpler linear or quadratic function and for each element a Galerkin matrix is assembled. The individual matrices can be added together, creating a single matrix equation for the whole object. In other words, the behaviour of each element can be specified by a set of parameters and simple functions. Since the object is an assembly of individual elements, the summation of their behaviour can be used to determine the behaviour of the entire object [84].

The unknown quantities in the finite element model can be found by minimising the total energy of the system which is described mathematically by an energy functional. The minimum of the energy functional can be obtained by setting the first derivative with respect to the potential to zero. Simply put, the solution must obey the law of conservation of energy which states that the total energy of the system must equal zero. Hence, the finite element energy functional must equal zero.

3.7 Finite element analysis (FEA) of electrostatic fields

In power systems, because of the alternating voltage, the electric field changes with time. However, its frequency is relatively low. As a result, when considering its effects it can be treated as an electrostatic field.

In electrostatics, the electric field is irrotational and arises from a voltage gradient or potential difference, and can therefore be expressed as the gradient of the electric potential φ:

$$\vec{E} = -\nabla\varphi \tag{3.2}$$

Its calculation can be derived from an Interior Boundary Value Problem (IBVP) subject to appropriate boundary conditions by solving Laplace's equation:

$$\nabla^2\varphi = 0 \tag{3.3}$$

On boundaries that are perfect conductors the Dirichlet boundary condition applies:

$$\varphi = V \tag{3.4}$$

where V is a constant.

On all other surfaces the Neumann boundary condition applies:

$$\frac{d\varphi}{dn} = 0 \tag{3.5}$$

where n is the direction normal to the surface.

As mentioned before, the unknowns can be found by minimising the energy functional. The energy functional W takes its minimum value only if the potential φ is a solution to Laplace's equation and satisfies the boundary conditions. This can be expressed as:

$$\frac{\partial W}{\partial \varphi} = 0 \tag{3.6}$$

where W is the energy stored in the electric field within an area *S* and is given by:

$$W = \frac{1}{2}\varepsilon_r \int_S \left|\vec{E}\right|^2 dS = \frac{1}{2}\varepsilon_r \int_S \left|-\nabla\varphi\right|^2 dS \tag{3.7}$$

To demonstrate the FEM, a two-dimensional region AB of arbitrary shape is considered. It consists of two parts, A and B, with areas A_A and A_B respectively. Part A is a conductor with its outer surface at potential $\varphi = V_A$ while Part B is a dielectric with relative permittivity ε_r and its outer surface at potential $\varphi = V_B$. Area AB is divided into triangular elements (Figure 3.3). The aim is to find an approximation for the potential φ_e within an element e and then associate the potential distributions of neighbouring elements to find a continuous potential across the boundaries between elements for the whole region. The potential would be:

$$\varphi = \sum_{e=1}^{K} \varphi_e \tag{3.8}$$

where K is the total number of elements.

The potential distribution within an element can be written as a linear combination of known functions with unknown coefficients. For a triangular element the most common approximation is a first order (linear) polynomial (3.9). Higher order polynomials can be used for improved accuracy but at the expense of computation time and complexity.

$$\varphi_e(x, y) = a + bx + cy \tag{3.9}$$

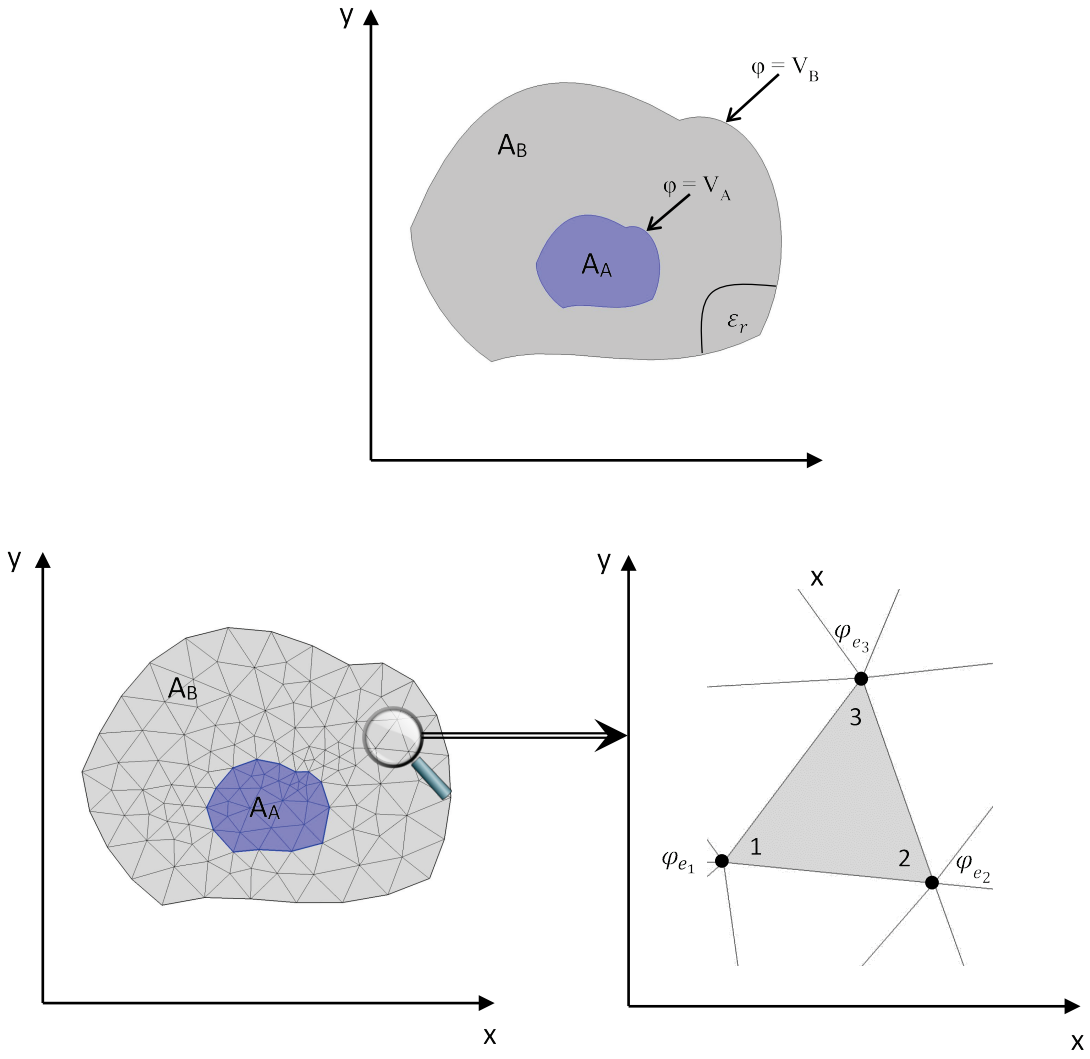

Figure 3.3 - Geometry subdivision into triangular finite elements

The unknown coefficients (a,b,c) can be calculated using the a priori unknown potentials at the nodes of the element:

$$\begin{aligned} \varphi_{e_1} &= a + bx_1 + cy_1 \\ \varphi_{e_2} &= a + bx_2 + cy_2 \\ \varphi_{e_3} &= a + bx_3 + cy_3 \end{aligned} \tag{3.10}$$

The system of linear equations can be solved using Cramer's method:

$$a = \frac{|D_a|}{|D|} \qquad b = \frac{|D_b|}{|D|} \qquad \mathrm{c} = \frac{|D_c|}{|D|} \tag{3.11}$$

where:

$$|D| = \begin{vmatrix} 1 & x_1 & y_1 \\ 1 & x_2 & y_2 \\ 1 & x_3 & y_3 \end{vmatrix} \quad |D_a| = \begin{vmatrix} \varphi_1 & x_1 & y_1 \\ \varphi_2 & x_2 & y_2 \\ \varphi_3 & x_3 & y_3 \end{vmatrix} \quad |D_b| = \begin{vmatrix} 1 & \varphi_1 & y_1 \\ 1 & \varphi_2 & y_2 \\ 1 & \varphi_3 & y_3 \end{vmatrix} \quad |D_c| = \begin{vmatrix} 1 & x_1 & \varphi_1 \\ 1 & x_2 & \varphi_2 \\ 1 & x_3 & \varphi_3 \end{vmatrix} \tag{3.12}$$

Furthermore, the determinant $|D|$ of the coefficient matrix of the system can be expressed in terms of the area of the element A_e as follows:

$$A_e = \frac{1}{2}\begin{vmatrix} 1 & x_1 & y_1 \\ 1 & x_2 & y_2 \\ 1 & x_3 & y_3 \end{vmatrix} \quad \text{and} \quad |D| = \begin{vmatrix} 1 & x_1 & y_1 \\ 1 & x_2 & y_2 \\ 1 & x_3 & y_3 \end{vmatrix} \tag{3.13}$$

$$\Rightarrow |D| = 2A_e \tag{3.14}$$

Hence, the coefficients of (3.11) become:

$$\begin{aligned} a &= \frac{1}{2A_e}\left(a_1\varphi_1 + a_2\varphi_2 + a_3\varphi_3\right) \\ b &= \frac{1}{2A_e}\left(b_1\varphi_1 + b_2\varphi_2 + b_3\varphi_3\right) \\ c &= \frac{1}{2A_e}\left(c_1\varphi_1 + c_2\varphi_2 + c_3\varphi_3\right) \end{aligned} \tag{3.15}$$

where:

$$\begin{aligned} a_1 &= x_2y_3 - x_3y_2 & b_1 &= y_2 - y_3 & c_1 &= x_3 - x_2 \\ a_2 &= x_3y_1 - x_1y_3 & b_2 &= y_3 - y_1 & c_2 &= x_1 - x_3 \\ a_3 &= x_1y_2 - x_2y_1 & b_3 &= y_1 - y_2 & c_3 &= x_2 - x_1 \end{aligned} \tag{3.16}$$

The electric potential for the element can be found by substituting the coefficients into (3.9). In matrix form it becomes:

$$\varphi_e = \frac{1}{2A_e}\cdot\begin{pmatrix} 1 & x & y \end{pmatrix}\cdot\begin{pmatrix} a_1 & a_2 & a_3 \\ b_1 & b_2 & b_3 \\ c_1 & c_2 & c_3 \end{pmatrix}\cdot\begin{pmatrix} \varphi_{e_1} \\ \varphi_{e_1} \\ \varphi_{e_1} \end{pmatrix} \tag{3.17}$$

The equation above can be rewritten as:

$$\varphi_e = \begin{pmatrix} N_1 & N_2 & N_3 \end{pmatrix}\cdot\begin{pmatrix} \varphi_1 \\ \varphi_2 \\ \varphi_3 \end{pmatrix} \tag{3.18}$$

The functions ***N*** are called the '*element shape functions*' and depend only on the shape of the finite element.

For the element e the energy stored in the electric field can be expressed in terms of the partial derivatives of the potential as follows:

$$W_e = \iint_{A_e} \frac{1}{2}\varepsilon_r \left[\left(\frac{\partial \varphi}{\partial x} \right)^2 + \left(\frac{\partial \varphi}{\partial y} \right)^2 \right] dxdy \tag{3.19}$$

Since $\iint dxdy$ gives the area A_e of the element, the energy functional above can be rewritten as:

$$W_e = \frac{1}{2}\varepsilon_r A_e \left[\left(\frac{\partial \varphi}{\partial x} \right)^2 + \left(\frac{\partial \varphi}{\partial y} \right)^2 \right]_e \tag{3.20}$$

The partial derivatives can be found be differentiating (3.9):

$$\frac{\partial \varphi}{\partial x} = b \qquad \frac{\partial \varphi}{\partial y} = c \tag{3.21}$$

For element e the minimising functions can be derived by partially differentiating the energy W_e in terms of the node potentials. With respect to φ_1 this is:

$$\begin{aligned} \frac{\partial W_e}{\partial \varphi_1} &= \frac{1}{2}\varepsilon_r A_e \left(2b\frac{\partial b}{\partial \varphi_1} + 2c\frac{\partial c}{\partial \varphi_1} \right) \\ &= \frac{1}{2}\varepsilon_r \left(bb_1 + cc_1 \right) \\ &= \frac{\varepsilon_r}{4A_e} \left[\left(b_1^2 + c_1^2 \right)\varphi_1 + \left(b_1 b_2 + c_1 c_2 \right)\varphi_2 + \left(b_1 b_3 + c_1 c_3 \right)\varphi_3 \right] \end{aligned} \tag{3.22}$$

The other two can be found in a similar manner. The three equations together can be expressed in matrix form as:

$$\frac{\partial W_e}{\partial \varphi_1} = \frac{\varepsilon_r}{4A_e} \begin{pmatrix} b_1^2 + c_1^2 & b_1 b_2 + c_1 c_2 & b_1 b_3 + c_1 c_3 \\ b_1 b_2 + c_1 c_2 & b_2^2 + c_2^2 & b_2 b_3 + c_2 c_3 \\ b_1 b_3 + c_1 c_3 & b_2 b_3 + c_2 c_3 & b_3^2 + c_3^2 \end{pmatrix} \cdot \begin{pmatrix} \varphi_1 \\ \varphi_2 \\ \varphi_3 \end{pmatrix} \tag{3.23}$$

The above can be written simplified as:

$$\frac{\partial W_e}{\partial \varphi_1} = \begin{pmatrix} c_{11} & c_{12} & c_{13} \\ c_{21} & c_{22} & c_{23} \\ c_{31} & c_{32} & c_{33} \end{pmatrix} \cdot \begin{pmatrix} \varphi_1 \\ \varphi_2 \\ \varphi_3 \end{pmatrix} = \left(c^{[e]}\right) \cdot \left(\varphi^{[e]}\right) \tag{3.24}$$

The element coefficient matrix $c^{[e]}$ is more commonly known as the '*stiffness matrix*' for the element. It takes its name from structural analysis where within a mechanical, elastic system it relates nodal forces to displacements. In this case it expresses the sensitivity of the energy functional to the electric potentials [59].

The element e is surrounded by other elements like in Figure 3.4. The number of the surrounding elements depends on how fine the mesh is at the region but it is usually small. The electric potential at a node inside the mesh depends on the potential of the surrounding nodes.

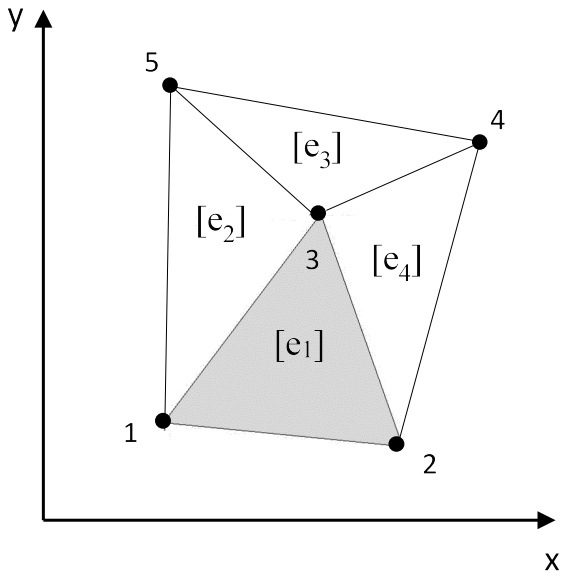

Figure 3.4 - Four connected elements

The unknown potential, φ_3 in Figure 3.4, can be calculated by minimizing the energy functional W of the network of elements. This can be expressed as:

$$\frac{\partial W}{\partial \varphi_3} = 0 \tag{3.25}$$

Using equation (3.25) and the stiffness matrix (which is symmetric) for each element the above becomes:

$$\begin{aligned}\frac{\partial W}{\partial \varphi_3} &= \left(c_{13}{}^{[1]}\varphi_1 + c_{23}{}^{[1]}\varphi_2 + c_{33}{}^{[1]}\varphi_3\right) \\ &+\left(c_{13}{}^{[2]}\varphi_5 + c_{23}{}^{[2]}\varphi_1 + c_{33}{}^{[2]}\varphi_3\right) \\ &+\left(c_{13}{}^{[3]}\varphi_4 + c_{23}{}^{[3]}\varphi_5 + c_{33}{}^{[3]}\varphi_3\right) \\ &+\left(c_{13}{}^{[4]}\varphi_2 + c_{23}{}^{[4]}\varphi_4 + c_{33}{}^{[4]}\varphi_3\right) \\ &= 0\end{aligned} \tag{3.26}$$

By grouping the terms together, equation (3.26) can be written as:

$$C_1\varphi_1 + C_2\varphi_2 + C_3\varphi_3 + C_4\varphi_4 + C_5\varphi_5 = 0 \tag{3.27}$$

where:

$$\begin{aligned}C_1 &= c_{13}{}^{[1]} + c_{23}{}^{[2]} \\ C_2 &= c_{23}{}^{[1]} + c_{13}{}^{[4]} \\ C_3 &= c_{33}{}^{[1]} + c_{33}{}^{[2]} + c_{33}{}^{[3]} + c_{33}{}^{[4]} = \sum_{e=1}^{4}\left(c_{33}\right)^{[e]} \\ C_4 &= c_{13}{}^{[3]} + c_{23}{}^{[4]} \\ C_5 &= c_{13}{}^{[2]} + c_{23}{}^{[3]}\end{aligned} \tag{3.28}$$

It is evident from the above that if the potentials $\varphi_1, \varphi_2, \varphi_4, \varphi_5$ are known, the unknown potential φ_3 can be calculated from equation (3.27). The solution for the entire meshed region can therefore be expressed as an assembly of minimizing equations:

$$\frac{\partial W}{\partial(\varphi)} = (C)(\varphi) = 0 \tag{3.29}$$

3.8 COMSOL Multiphysics

As part of the design and optimisation process for the electric field stress control for the ICA, calculation of the electric field magnitudes was required. To perform the computations, COMSOL Multiphysics was used in this study. COMSOL Multiphysics is an FEA software package for modelling and simulating various physics-based systems such as electrical, mechanical, fluid flow and chemical [85]. It has an easy to use graphical user interface and allows for the coupling of different physics as well as manual input of the PDEs that define the system if this is required. COMSOL is particularly well-suited for the examination of the electric field distribution on the ICA because its CAD import

module enables the easy import and manipulation of the exact CAD models used for the manufacture of the ICA components, thus maintaining the fidelity of their geometry as close as possible to reality. Furthermore, the extensive post processing functionality and LiveLink interface with Microsoft Excel open up many options for presenting the results of the simulations.

3.9 Grading devices for the insulating cross-arm

3.9.1 End-fitting reference model

For traditional insulators it is possible to exploit the rotational symmetry they exhibit along their longitudinal axis and use two dimensional analysis to simplify the electric field calculation [86]. The end-fitting of the compression insulator of the ICA however has to follow closely the shape of the core. The unconventional shape of the fitting results in different radii on its surface which are likely to result in different electric field magnitudes. Because the end-fitting is not symmetric, the FEA in three dimensions was employed to test this assumption.

To demonstrate the variation of the electric field magnitude, a 3D model of the end-fitting was imported from SolidWorks into COMSOL Multiphysics. The model was placed in the centre of two concentric spheres with radii of 1 m and 1.2 m (Figure 3.5). The inner sphere acts as the air surrounding the end-fitting. The outer sphere is an infinite element domain to emulate an infinite open space around the end-fitting which improves the accuracy of the results. The surfaces of the end-fitting were set to 231 kV_{rms} phase-to-ground (equivalent to 400 kV_{rms} phase-to-phase) while the surfaces of the inner sphere were set to 0 V. The results of the computation are presented in Figure 3.6.

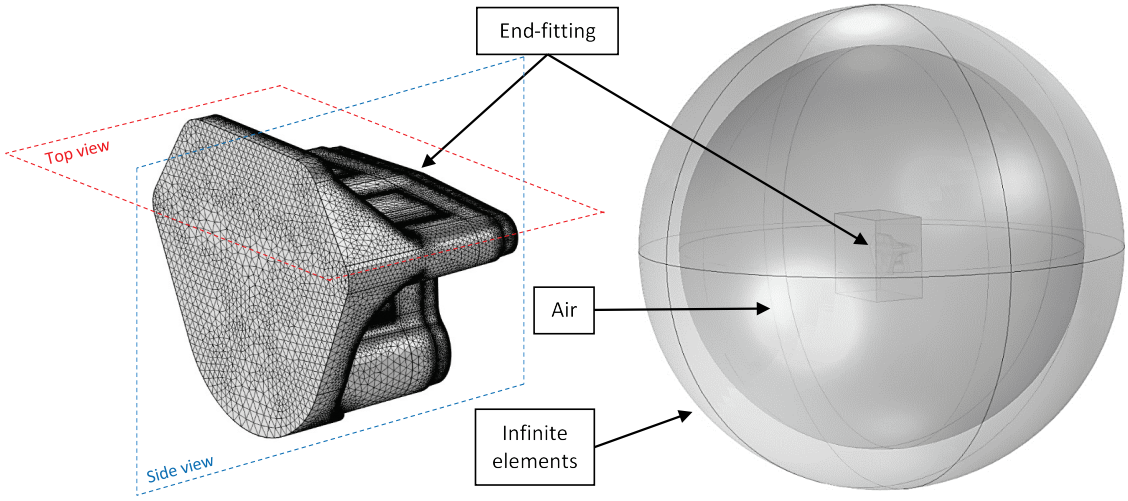

Figure 3.5 - End-fitting meshed model and computational domain

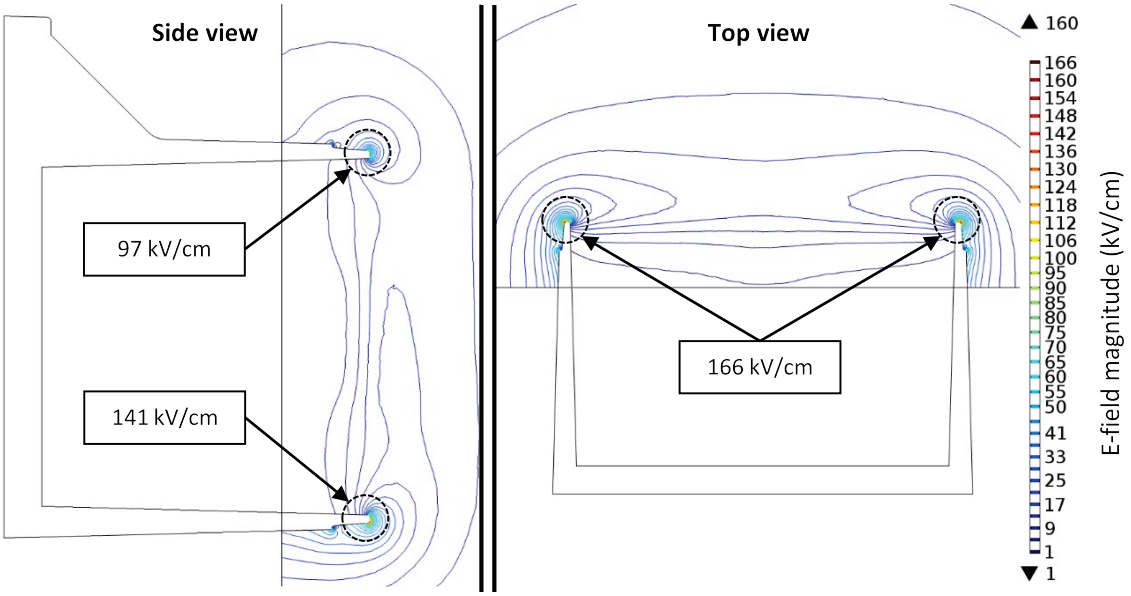

Figure 3.6 - End-fitting reference model electric field contours

Figure 3.6 shows that the highest electric field magnitude is observed on the edge of the end-fitting which would normally be facing the sheds. The results of the computation verify the initial assumption of non-uniform electric field around the end-fitting. The highest magnitude of 166 kV/cm can be found on the sides of the end-fitting while the underside follows with 141 kV/cm and the top side with 97 kV/cm. A limitation of this model is that it does not take into account several parts of the insulator and cross-arm assembly that affect the electric field distribution. The values obtained cannot be considered on their own without additional modelling and further analysis. In essence, this simulation was performed in order to identify the areas of the highest electric field

magnitude on the end-fitting and use the values obtained as a reference for subsequent simulations.

3.9.2 The 'overlap' factor

The fact that the core is not cylindrical limits the options of attaching the end-fitting to the insulator since it cannot be crimped on like in the case of many traditional OHL insulators. As a result, the end-fitting terminates with a rather sharp edge facing the sheds which results is very high electric field as seen in the previous section. This edge is a vital part of the insulator design however since it allows a few millimetres of silicone rubber to be moulded on top of the end-fitting to provide additional protection against water ingress (Figure 3.7).

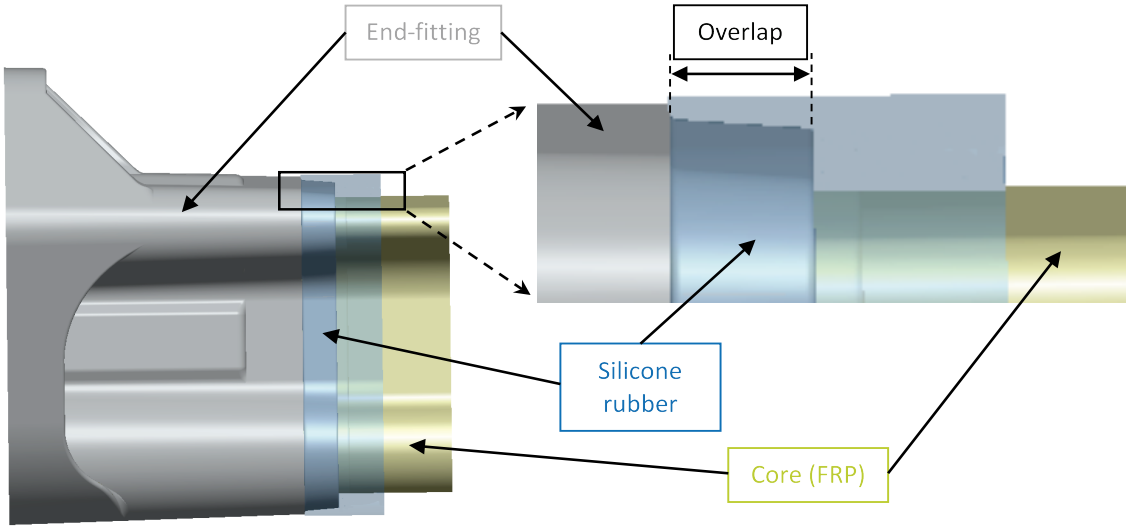

Figure 3.7 - Silicone rubber overlap on compression insulator end-fitting

Since silicone rubber has a different permittivity than air ($\varepsilon_r^{SiR} \approx 3.5$) its presence affects the electric field distribution. Therefore, its inclusion in the FEA model is very important for the accuracy of the results. Despite the author's best efforts and even after seeking assistance from COMSOL's support team it was not possible to successfully import a model of the end-fitting with the overlapping SiR layer. While the initial import of the CAD model into COMSOL was successful, evaluation of the "Finalise" node, the final node in the geometry sequence resulted in errors.

COMSOL provides two geometry finalisation methods: "*Form Union*" and "*Form Assembly*". When the "*Form Union*" method is used, a union is formed from all objects contained or created by the geometry sequence. The *Union* is divided into domains separated by boundaries and by default, continuity is ensured in the physics field across

interior boundaries. When the "*Form Assembly*" method is used, the geometry is treated as a collection of parts. Where a field is continuous, pairs must be used to connect boundaries. An *Assembly* can be useful when the geometry is too complex for forming a *Union*; for example in cases where the model has been imported from CAD [87].

Both methods were tried while attempting to import the end-fitting together with the overlapping SiR layer. When the former was employed, the software was unable to form a *Union* regardless of the tolerance level used. When the latter was employed, the geometry finalisation operation would complete but the resulting geometry could not be meshed.

After examining the errors produced by the software, it was determined that the inability to import the model successfully was most likely due to the very small thickness of the SiR layer at the overlapping region. To test this assumption, the CAD model was modified by changing the thickness of the SiR layer in steps of 0.1 mm. Each of the modified models was imported into COMSOL until a successful import was accomplished.

The first successfully imported model was one with approximately twice the thickness of SiR at the overlapping region. For the electric field calculation, the computation domain and boundary conditions were kept exactly the same as for the reference model of *Section 3.9.1* so that the two simulations could be easily compared. The results are shown in Figure 3.8.

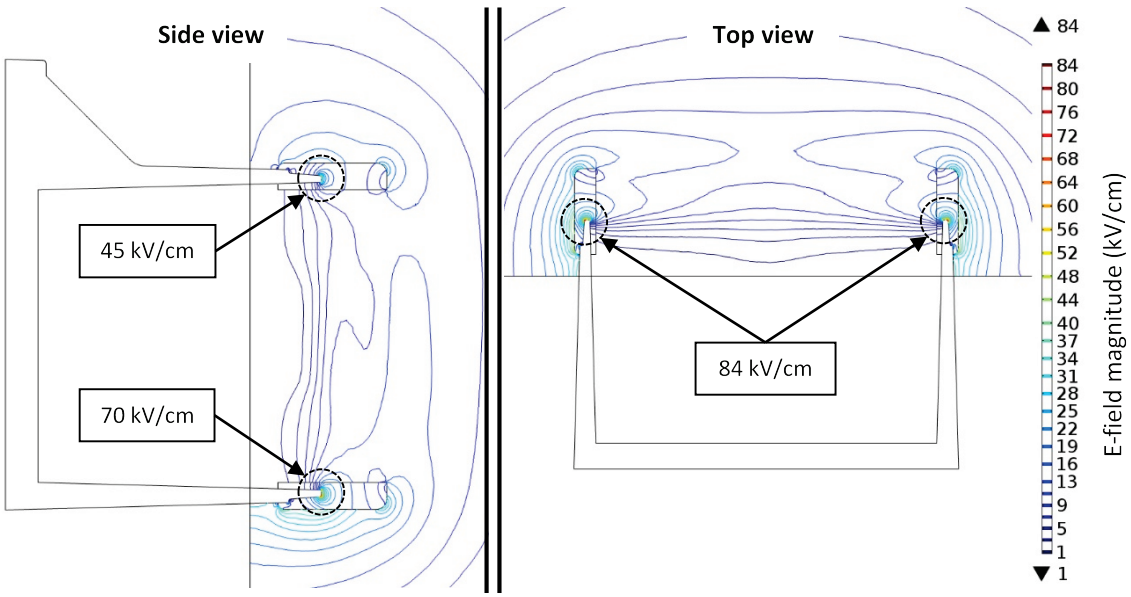

Figure 3.8 - Electric field contours for end-fitting with SiR overlap

Compared to the reference model of *Section 3.9.1,* the maximum electric field magnitude at the triple junction was reduced from 166 kV/cm to 84 kV/cm, a reduction of 49.4%, because of the presence of silicone at the interface. To verify that the thickness of the SiR layer did not affect the electric field calculation, models with even thicker SiR layers, up to a thickness of 5 mm, were imported and simulated. The results showed that increasing the thickness of the SiR layer had an insignificant impact on the electric field magnitude at the triple junction. This can be primarily attributed to the very small radius of the end fitting termination at the triple junction.

In order to account for the missing silicone rubber layer in all subsequent simulations, the concept of using an '***overlap factor***' was conceived, defined to be the reduction in electric field magnitude due to the presence of silicone on top of the end-fitting. This is effectively a method of calibrating results. Because of the importance of the triple junction interface to the reliability of the insulator, in addition to the result of the simulation, it was decided that the '***overlap factor***' should include a safety factor.

Safety factors are widely used in engineering applications when considering overall system performance and the consequences of failure. Equipment, especially when no previous service experience is available, is purposefully manufactured with higher specifications than needed for normal usage to allow for emergency situations, inconsistencies in the quality of fabrication, misuse or degeneration. If a component is slightly overdesigned there will be no harm and the design may even be considered to be of high quality and reliability. Furthermore, in most cases it is cheaper to manufacture a component with higher than needed specifications and provide redundancy than changing its design after it has been commissioned.

For the electric field magnitude at the triple junction a safety factor of 1.6 was deemed appropriate. This safety factor ensures that the electric field at the triple junction will not exceed the recommended value even when power frequency overvoltages occur. This value was agreed by the engineers from University of Manchester, Scottish and Southern Energy and EPL Composite Solutions working on the project. Only power frequency overvoltages were considered since, as detailed in *Section 4.4*, they can reach values of up to 1.6 p.u. and can persist for longer compared to other types of overvoltages.

To summarise, the '***overlap factor***' used in all subsequent simulations incorporates the 50% reduction in electric field magnitude due to the presence of the SiR layer that was not possible to be simulated successfully as well as a safety factor of 1.6 to account for the occurrence of power frequency overvoltages. In essence, the inclusion of the safety factor reduces the effect that the SiR layer is presumed to have on the electric field magnitude from a reduction of 50% to a reduction of 30% which makes achieving the electric field magnitude requirements outlined in *Section 3.5.5* purposely harder. In other words, the electric field magnitude values reported in the following sections after the application of the '***overlap factor***' are 1.6 times higher than what the simulations would produce if the SiR layer was present on top of the end-fitting.

3.9.3 LV-end Grading Device

At the LV-end, the four insulators that comprise the ICA are attached to the tower at different points away from each other. Hence, for designing electric field grading devices for them, they can be considered individually, similarly to traditional OHL insulators. The tension members of the assembly are in fact traditional OHL long-rod insulators and as such they are shipped with their own grading rings. Therefore, the development effort was focused on designing a grading ring for the novel compression member.

3.9.3.1 Reference model

Before designing the grading device, a model representing a short section of the compression insulator was assembled in SolidWorks to help identify the areas with the highest electric field magnitude. The model incorporates all the major components including the end-fitting, the core, the sheath and the eight weather sheds closest to the end-fitting. The length of the model is 600 mm which is approximately one sixth of the complete compression member (Figure 3.9). The CAD model was imported into COMSOL Multiphysics and meshed. The mesh parameters for the model are the following:

- Number of elements: 2 175 163 (tetrahedral)
- Minimum element size: 0.0012 m
- Maximum element size: 0.21 m

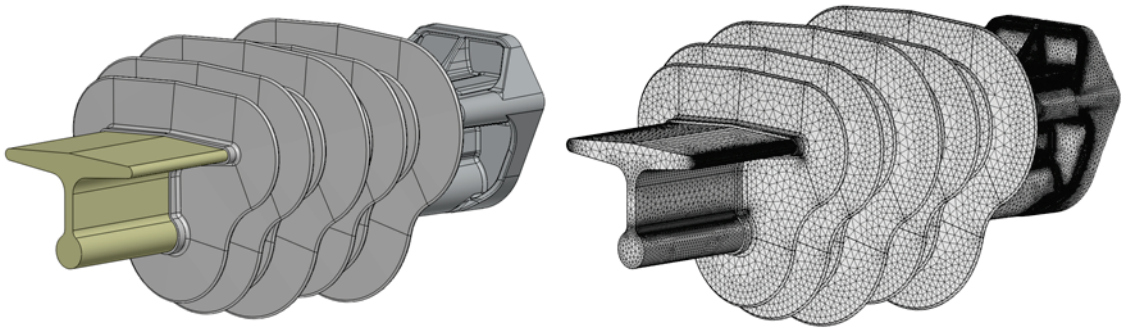

Figure 3.9 - Compression insulator LV-end model

The computational domain for the simulation was set to be a $6\text{m}\times3\text{m}\times3\text{m}$ box containing the model above (Figure 3.10). To further decrease the complexity of the model, the OHL tower was not included. Instead, the rightmost plane of the box played the role of the tower. Also, the nose cone of the ICA was replaced by a conical frustum with roughly the same dimensions and positioned at the appropriate distance from the 'tower' plane. The model of Figure 3.9 was placed within the box near the 'tower' plane and its position adjusted relatively to the conical frustum to simulate the position of the compression insulator in the cross-arm assembly.

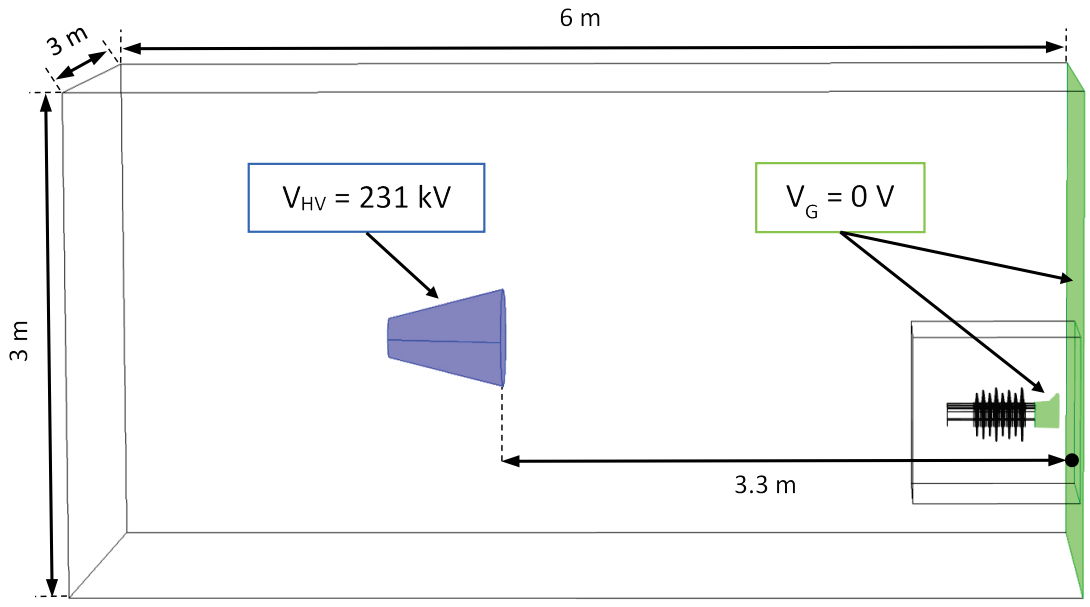

Figure 3.10 - LV-end computational domain

The only material property that is taken into account for the electrostatic field calculation is the permittivity. The materials and corresponding permittivities used for the simulation are summarised in Table 3.1.

Table 3.1 *- Materials and permittivities for electric field computation*

Part	Material	Permittivity (ε_r)
Nose cone	Steel	1.0
Insulator end-fitting	Aluminium	1.0
Core	FRP	5.0
Shed	SiR	3.5
Box	Air	1.0

The boundary conditions used for the computation are the following:

- Nose cone surfaces: $V_{HV} = 231 \text{ kV (phase-to-ground, rms)}$
- Other internal surfaces: continuity
- Tower (rightmost) plane: $V_G = 0 \text{ V}$
- End-fitting surfaces: $V_G = 0 \text{ V}$
- Outer boundaries: zero charge

The simulation showed that the electric field reached its maximum value of approximately 11.5 kV/cm at the triple junction on the underside of the insulator (Figure 3.11). By applying the overlap factor defined earlier this value is reduced to 8.05 kV/cm. Although lower than the corona inception voltage of 22 kV/cm, the magnitude of the field at the triple junction was more than two times higher than the recommended limit of 3.5 kV/cm. This result makes the inclusion of a grading device at the LV-end of the compression insulator mandatory for 400 kV lines.

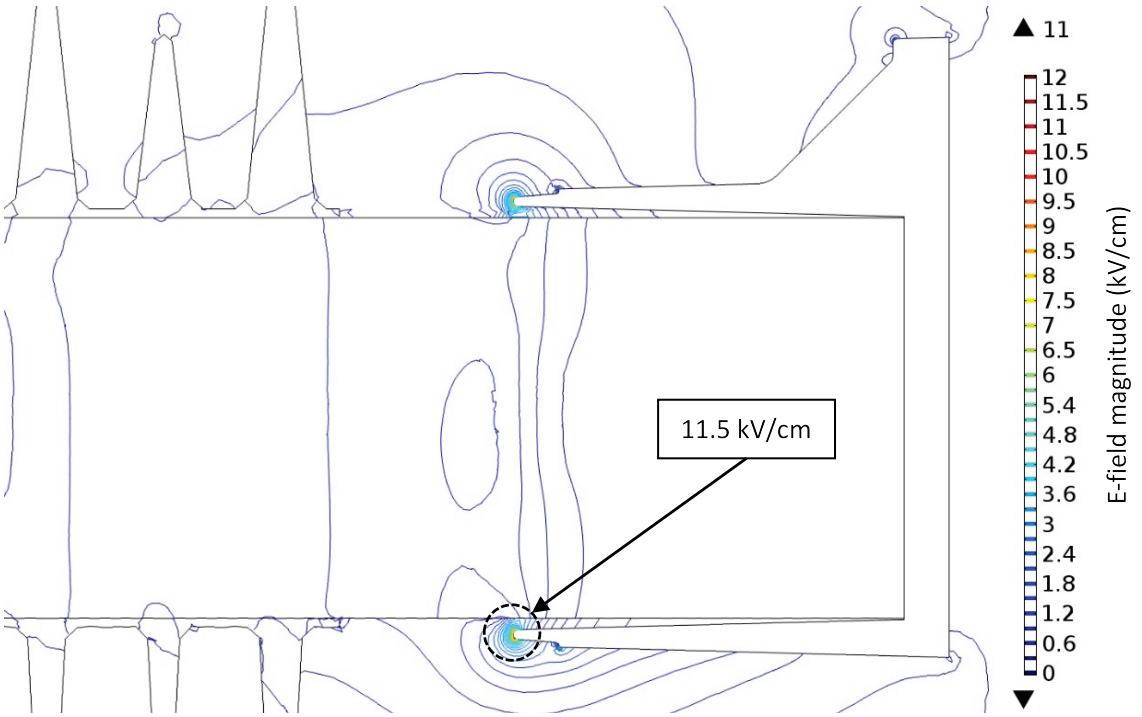

Figure 3.11 - LV-end reference model electric field contours

3.9.3.2 LV grading device design

To bring down the magnitude of the field, a grading device was designed using SolidWorks. The device is not strictly a ring since its shape follows the outline of the compression insulator (Figure 3.12). It is made out of tubular aluminium with diameter of 50 mm. This specific diameter of tube was chosen for several reasons. First, the electric field magnitude around a ring with such a tube diameter is a lot lower than the corona inception voltage at 400 kV. Additionally, it can be bend with a tight enough radius that it can follow the general shape of the compression insulator without needing special manufacturing methods. Finally, the commercially available grading rings used for the tension members of the cross-arm are made out of tube of similar diameter.

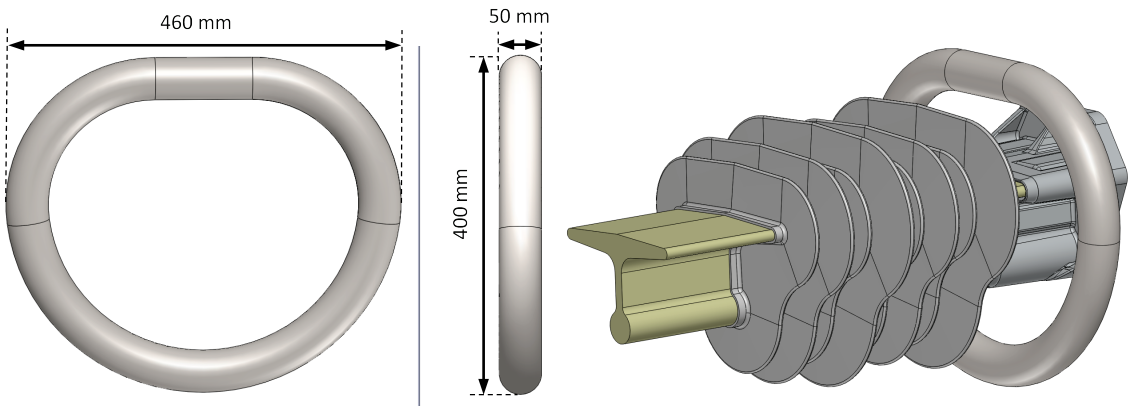

Figure 3.12 - LV grading device

The model of the LV grading device was imported into COMSOL and then integrated with the model of the compression member section of Figure 3.9. The computation domain and boundary conditions were set to be exactly the same as in the previous section. To find the optimal position for the grading device a parametric study was conducted by varying the horizontal distance of the vertical plane of the grading device from the edge of the end-connection closest to the sheds. The parametric sweep was run with parameter ***d*** ranging from 0 to 70 mm in steps of 10 mm. The initial and final positions of the grading device are shown in Figure 3.13. The electric field was computed for each position of the grading device. The maximum electric field magnitude values after applying the overlap factor were plotted against the value of parameter ***d*** and are also presented in Figure 3.13.

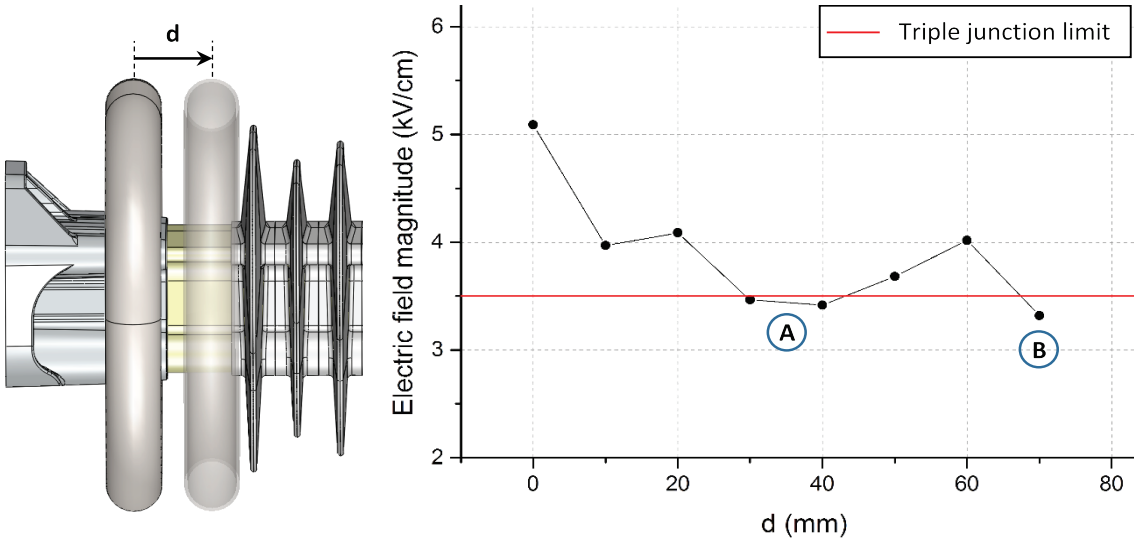

Figure 3.13 - LV grading device optimisation study results

The electric field magnitude is reduced to acceptable levels at the triple junction area for two positions of the grading device. ***Position A*** is when the centre of the device is directly on top of the triple junction. ***Position B*** is when the device is closest to the first shed of the insulator. Although slightly better, the second position was rejected because of the increased risk of discharges from the device to the shed which could erode the silicone rubber in the long term. It was decided therefore to place the device directly on top of the triple junction. The electric field distribution for this optimal position is presented in the form of a contour plot in Figure 3.14. The maximum electric field magnitude (after applying the overlap factor) is below 3.5 kV/cm which is the limit for the triple junction.

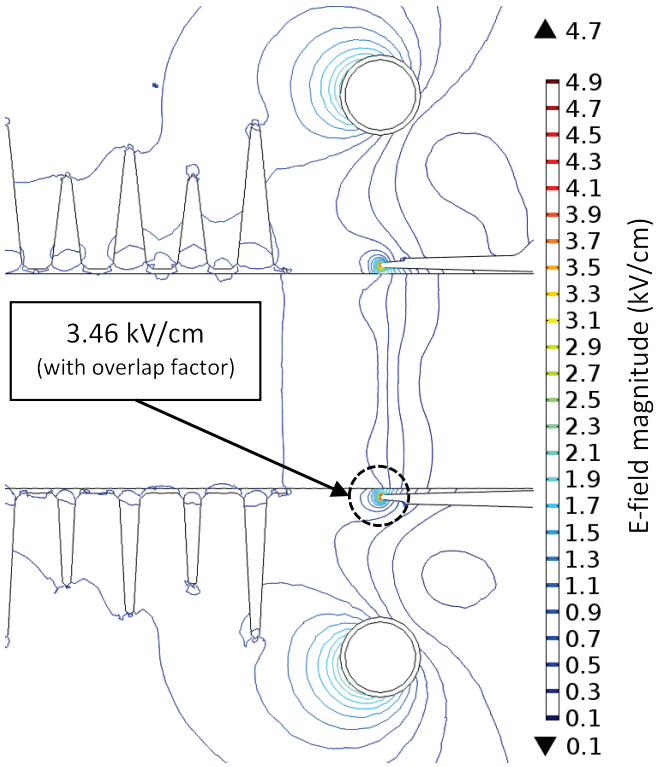

Figure 3.14 - Electric field contours for LV-end with grading device

3.9.4 HV-end Grading Device

On the high voltage side of the cross-arm assembly the four insulators meet at the nose cone which facilitates the attachment of the conductor. The proximity of the four insulators at this area of the assembly makes it impossible to install an individual grading ring for each member. It was decided that it would be more effective to develop a solution that could manage the electric field around all four members collectively.

3.9.4.1 Reference model

To identify where the areas of high electric field magnitude are located at the HV-end of the cross-arm, a model consisting of the nose cone, end-connections for the insulators and two short sections of the compression members was assembled in SolidWorks. The virtual parts of the model have exactly the same dimensions as the actual parts used for fabricating the cross-arm. Some of the features of these parts, such as bolt holes on the metal work, have been suppressed to reduce the complexity of the model and speed up the computation. Figure 3.15 shows the SolidWorks CAD model (top) and the meshed model (bottom) after it has been imported into COMSOL Multiphysics.

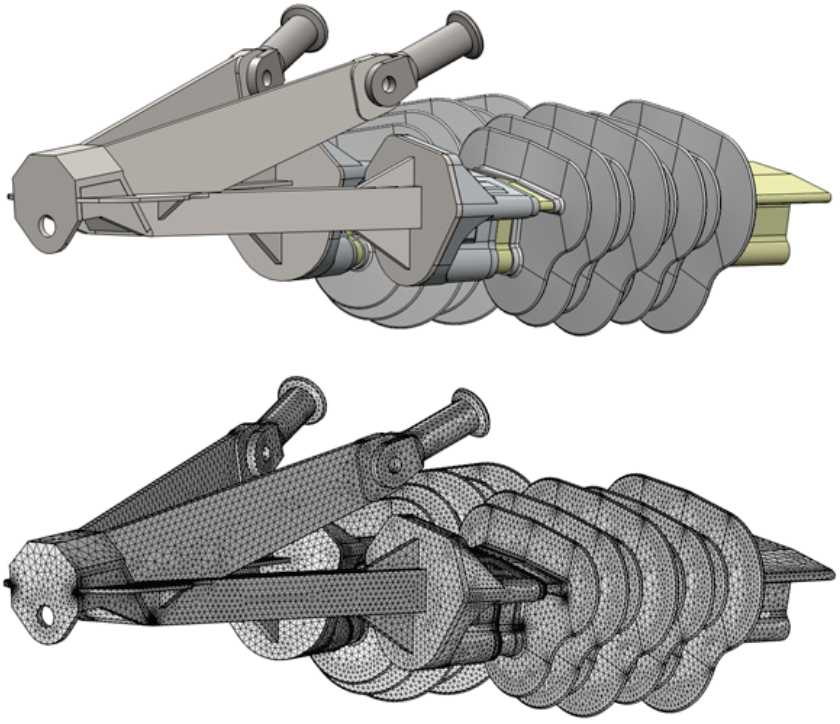

Figure 3.15 - HV-end reference model

The mesh parameters for the model are the following:

- Number of elements: 805 695 (tetrahedral)
- Minimum element size: 0.0012 m
- Maximum element size: 0.21 m

The computational domain for the simulation (Figure 3.16) was set to be a $6\text{m} \times 3\text{m} \times 3\text{m}$ box containing the model of Figure 3.15. Similarly to the LV-end simulation, the rightmost plane of the box substitutes the tower. The model of Figure 3.15 was placed within the box at the appropriate distance away from this plane to simulate the distance between the tower and the HV-end of the cross-arm. The materials and permittivities can be found in Table 3.1. The boundary conditions used for the computation are the following:

- Metallic surfaces: $V_{HV} = 231\ \text{kV}$ (phase-to-ground, rms)
- Other internal surfaces: continuity
- Tower (rightmost) plane: $V_G = 0\ \text{V}$
- Outer boundaries: zero charge

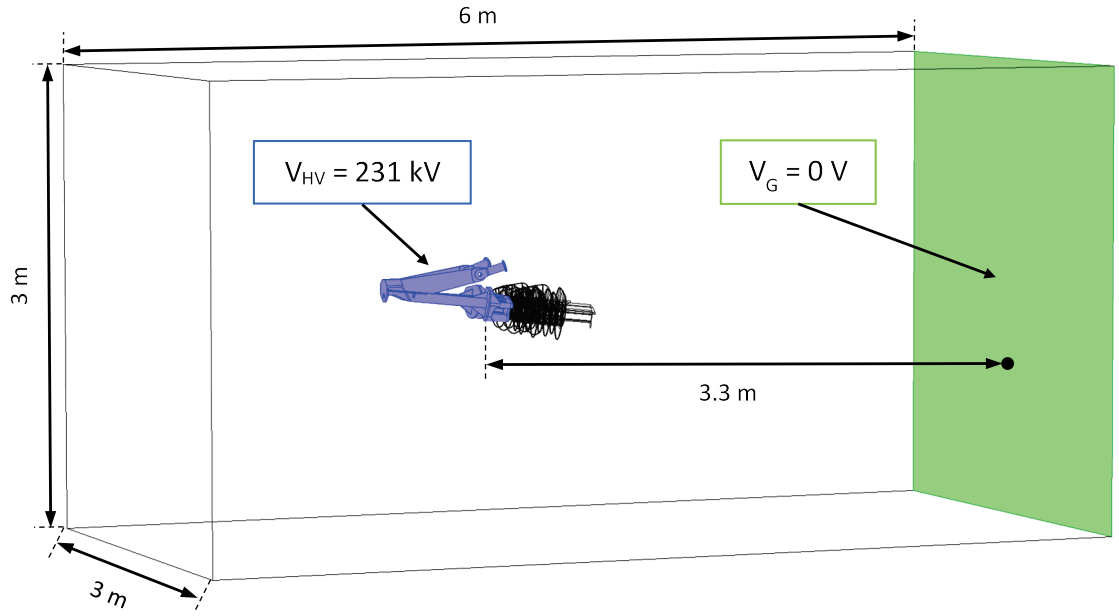

Figure 3.16 - HV-end computational domain

Figure 3.17 shows the results of the computation. The areas exhibiting high electric field magnitude lie at the tip of the nose cone (the conductor attachment point) and at the edge of the compression insulator end-fitting which is closest to the sheds. The latter observation coincides with what was observed for the LV-end of the compression member. In this case however, the magnitude of the electric field is approximately four times higher, reaching 31.5 kV/cm after the overlap factor has been applied, because the metal work is energised at operating voltage. Additionally, the field magnitude at the conductor attachment point reaches 22 kV/cm exceeding the 18 kV/cm limit for the metal work. The grading device would have to be designed in such a way as to minimise the electric field magnitude near the identified areas.

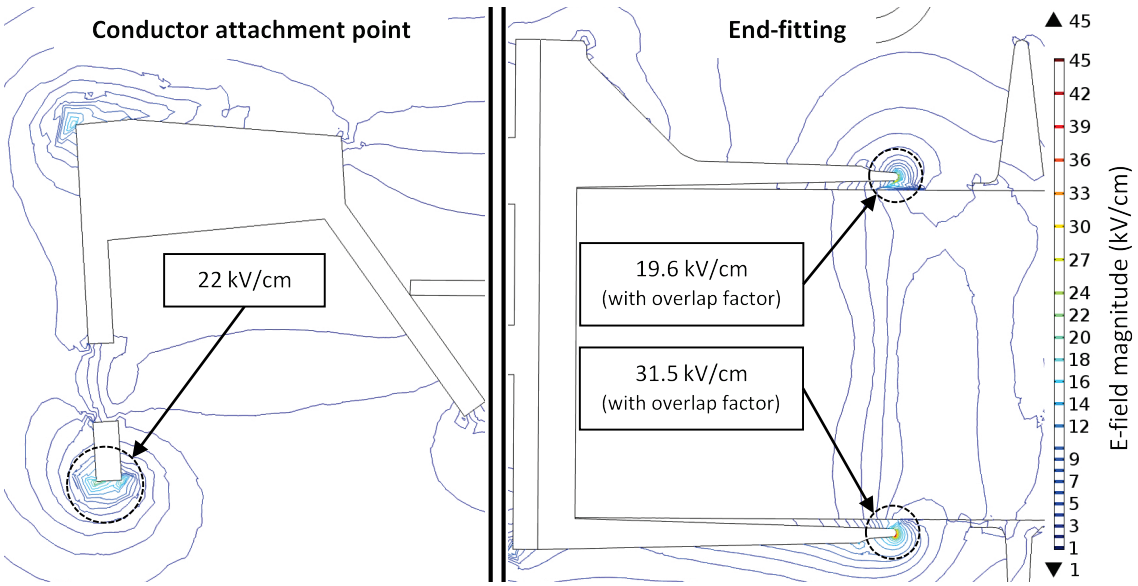

Figure 3.17 - HV-end reference model electric field contours

3.9.4.2 Design iterations

3.9.4.2.1 Design A – 'Cage'

The initial approach was to design a grading device that would tackle all the problematic areas of the HV-end of the cross-arm together. Since there was evidence of high electric field magnitude both at the front and at the back of the nose cone the first concept device was designed as a cage to enclose all the metal work of the HV-end. It was made out of 60 mm diameter tube since simulations showed that this size of tube was the minimum that did not result in electric fields with magnitudes above corona inception. The model of the device incorporated an additional component on its underside, the ladder hook, for the attachment of a ladder to facilitate access to the nose of the ICA from the tower for maintenance purposes. Design A is shown in Figure 3.18.

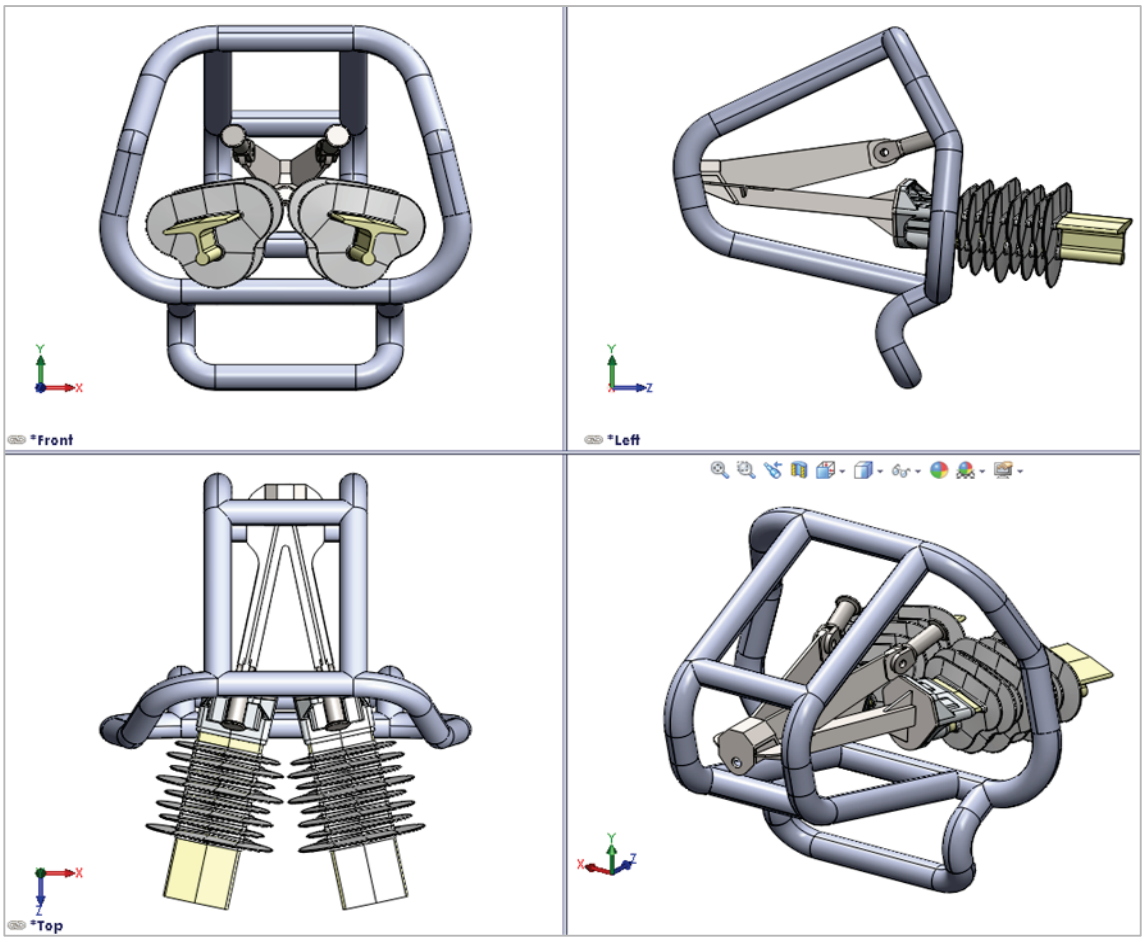

Figure 3.18 - HV grading device Design A

The model was imported into COMSOL and meshed. The computational domain, permittivities and boundary conditions were kept the same as in the previous study. The results can be seen in Figure 3.19 after the overlap factor has been applied where appropriate.

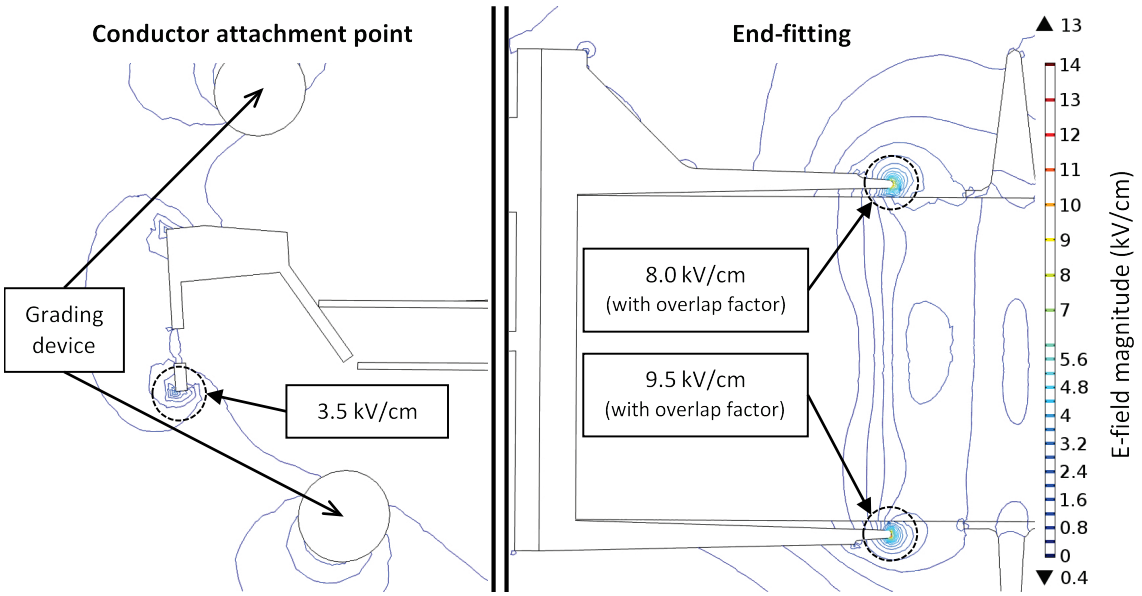

Figure 3.19 - Electric field contours for HV-end with Design A grading device

Design A reduced the electric field magnitude substantially at both the conductor attachment point and the triple junction of the compression insulator. However the reduction at the triple junction was not sufficient to bring the field below the 3.5 kV/cm limit primarily due to the distance between the grading device and the end-fitting. Also, it was made apparent that with this design the electric field distribution in the area between the compression and tension members (i.e. the topside of the end-fitting) could not be improved further even if the dimensions and position of the grading device were adjusted. Finally, the sheer size of *Design A* increased the overall visual impact of the assembly negating one of the main advantages of the composite cross-arm technology. For all the above reasons, *Design A* was rejected.

3.9.4.2.2 Design B – 'Muzzle'

The second iteration of the HV grading device design tried to improve upon the drawbacks identified for the first one. The main design idea of a 'grading cage' was maintained but the device was designed to be much more streamlined. The number of the 60 mm in diameter tubular sections that comprise the device was reduced and its general shape was adjusted to follow the geometry of the nose cone more closely. This reduced its size and brought it closer to the end-fittings. Furthermore, sections of tube were added in the area between the compression and tension members to tackle the electric field enhancement in that area. *Design B* is shown in Figure 3.20.

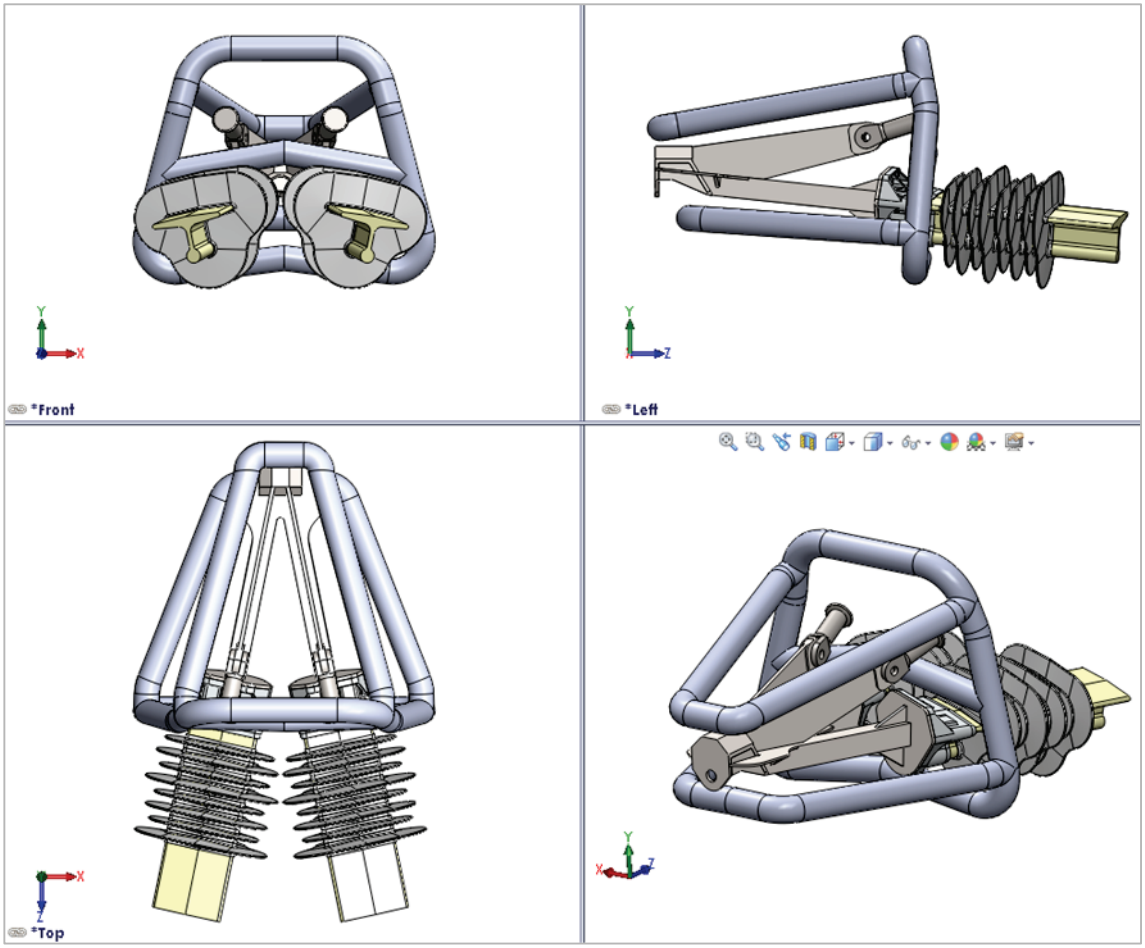

Figure 3.20 - HV grading device Design B

As before, the model was imported into COMSOL, meshed and the simulation run with the same computational domain, permittivities and boundary conditions. The results can be seen in Figure 3.21 after the overlap factor has been applied where appropriate.

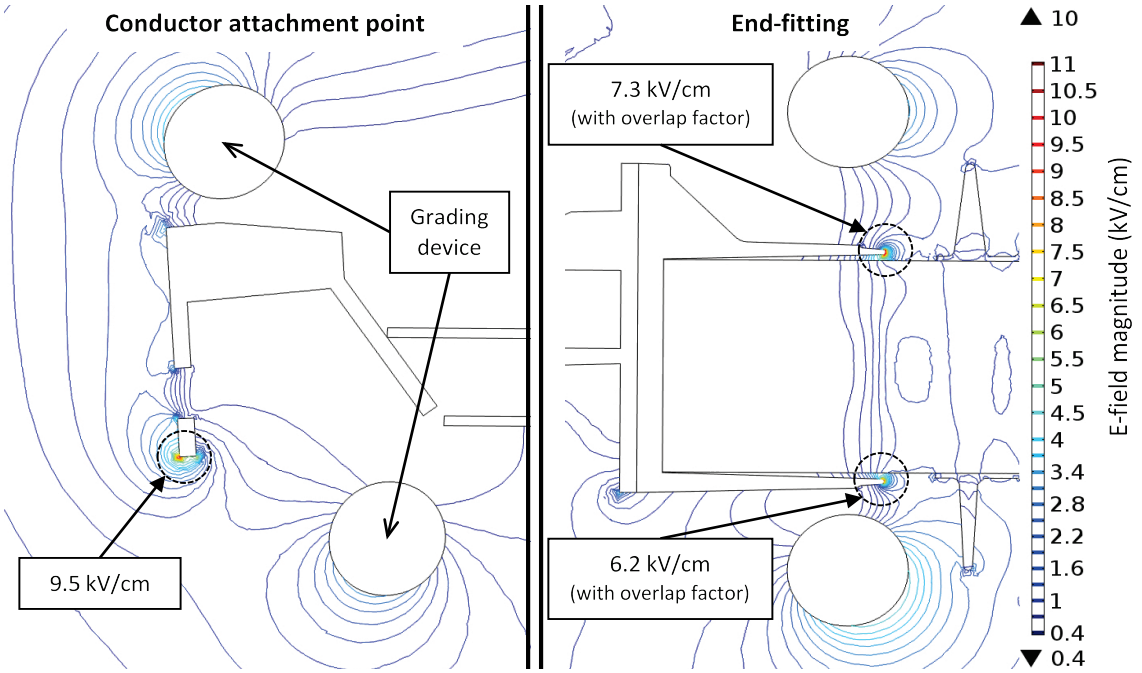

Figure 3.21 - Electric field contours for HV-end with Design B grading device

The study showed that the field at the conductor attachment point could be handled effectively since it was reduced to 9.5 kV/cm, almost half of the 18 kV/cm limit. On the triple junction of the end-fitting however and despite the fact that the grading device was much closer, the improvement compared to *Design A* was marginal. The tubular sections of the device could not come any closer to the end-fittings than what is depicted in Figure 3.21 because the device would not be able to physically fit between the four insulating members during installation. *Design B* had further disadvantages as well. The tight bending radii of the tubular sections with this diameter of tube would require special manufacturing techniques to achieve which would make the device difficult and expensive to produce. Moreover, parts of the grading device would be located very close to the sheds of the compression insulator increasing the risk of discharges from the device to the insulator. As a result, *Design B* was also rejected.

3.9.4.2.3 Design C – 'Butterfly'

From the *Designs A* and *B* it was made clear that the field at the tip of the nose cone was easier to control than the field around the end-fittings of the compression insulators. It was therefore decided to focus on designing a grading device to manage the electric field around the four insulating members. To avoid using bent tube which could create difficulties with manufacturing, a completely different grading device was designed. *Design C* was conceived to be a unibody piece of aluminium with holes of appropriate shape and size inside of which the end-connections of the four insulators would fit (Figure 3.22). *Design C* has smooth rounded surfaces facing the insulators while its other side, facing the conductor, is concave to make it lighter, cheaper and easier to manufacture.

Unlike the previous two designs, because of its shape the device can be cast, reducing the cost of making multiples of the device. The most expensive stage of manufacturing would be the construction of the mould which only happens once at the initial stages of the process. Furthermore, because *Design C* is independent of the electric field management solution used at the tip of the nose cone, it provides more flexibility regarding the adjustment of its position in order to optimise its performance.

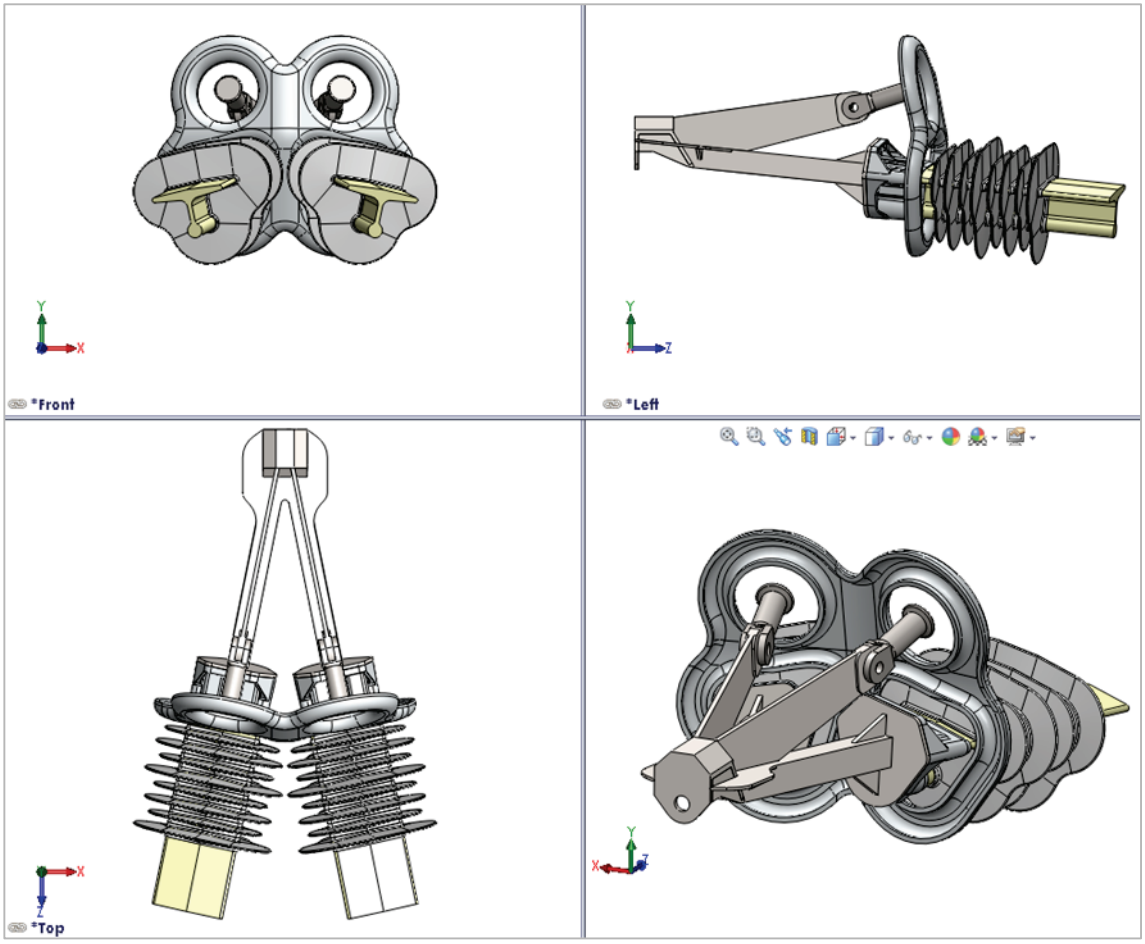

Figure 3.22 - HV grading device Design C

As before, Design C was integrated with the model of the HV-end of the ICA and imported into COMSOL. The electric field computation was carried out using the same parameters as for the other two designs. The results are presented in Figure 3.23.

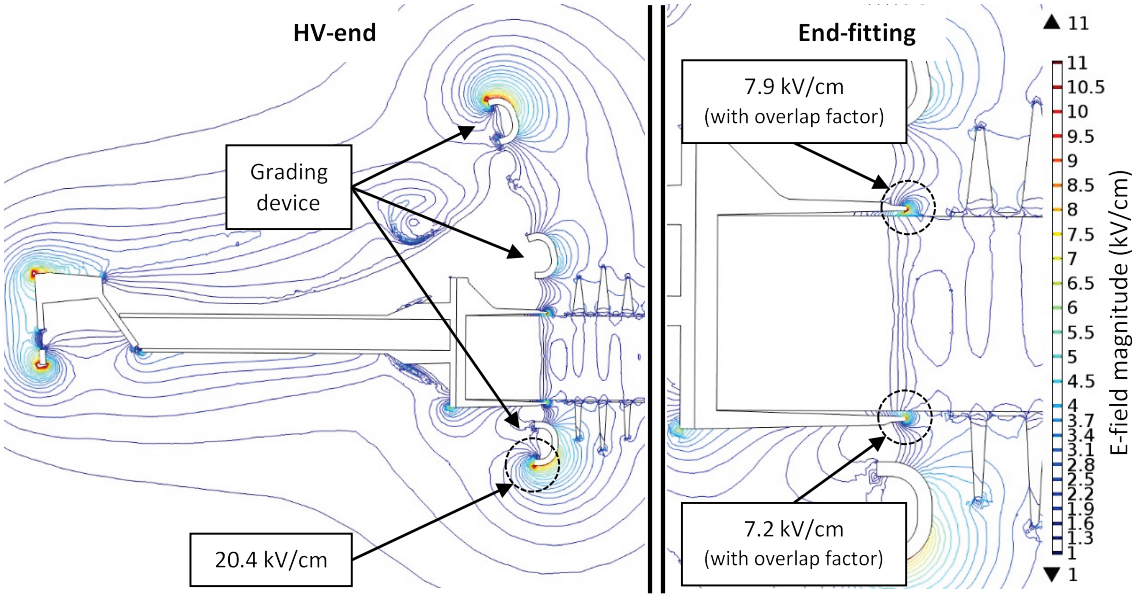

Figure 3.23 - Electric field contours for HV-end with Design C grading device

The maximum electric field magnitude at the triple junction of the compression insulator with *Design C* was found to be 7.9 kV/cm which is still above the 3.5 kV/cm limit. The issue again was the sharpness of the end-fitting edge facing the sheds. No matter how close the grading device was to the insulator it could not affect the field distribution significantly enough to reduce the electric field to acceptable levels. The results also indicate that the device itself when energised at 400 kV is likely to produce visible corona as the field magnitude on its outer rim consistently exceeded the 18 kV/cm limit set for metallic hardware.

3.9.4.2.4 'Butterfly' grading device for 132 kV ICA

Despite the inability of the '*Butterfly*' grading device to cope with the electric field at 400 kV, the minimalistic design and ease of manufacture make it a very attractive solution for use on lower voltage levels. To examine the performance of the device at 132 kV a model consisting of all the metallic hardware at the HV-end of the ICA and a full 132 kV class compression insulator was assembled in SolidWorks. The insulator has the same profile parameters as the 400 kV insulator detailed in *Chapter 2* except that it is shorter. The '*Butterfly*' grading device was added to the HV-end while a smaller diameter LV grading device was added to the LV-end of the compression insulator. The assembly was then imported into COMSOL and can be seen in Figure 3.24.

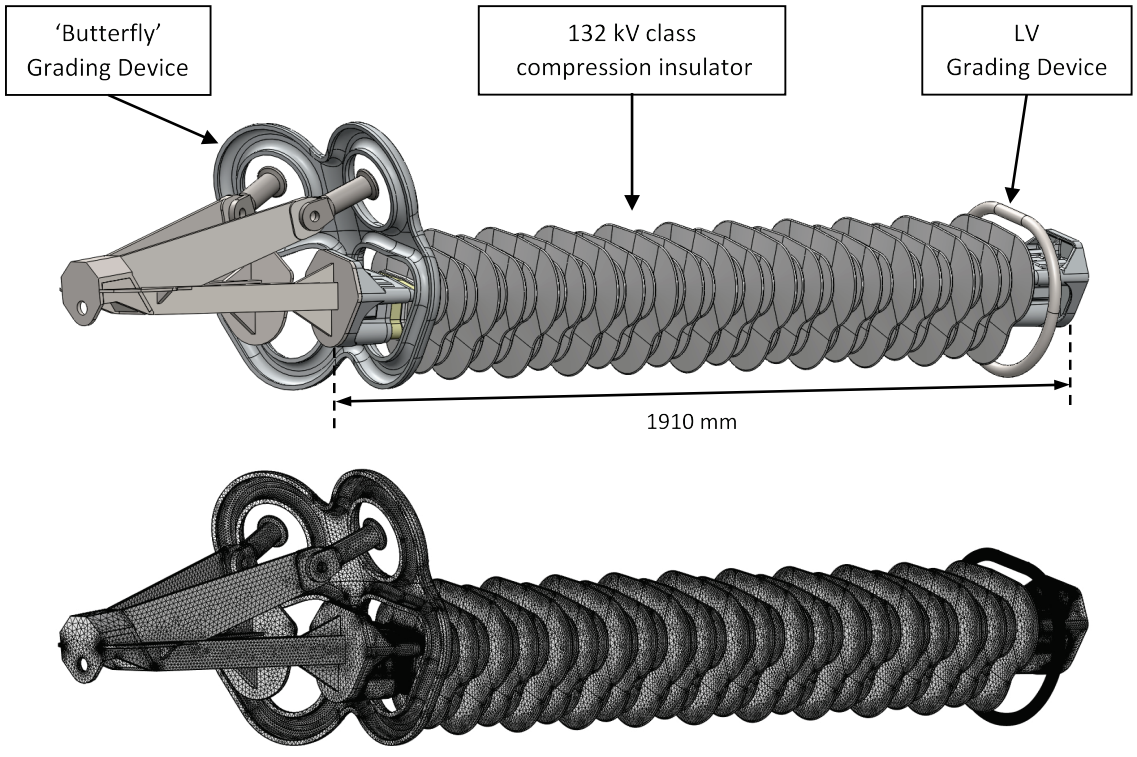

Figure 3.24 - 132 kV ICA model

The computational domain and permittivities were defined similarly to the previous studies. The boundary conditions in this case are the following:

- Nose cone, HV end-fittings, 'Butterfly': $V_{HV} = 76.2$ kV (phase-to-ground, rms)
- LV end-fitting, LV grading device: $V_G = 0$ V
- Other internal surfaces: continuity
- Outer boundaries: zero charge

Figure 3.25 shows a contour plot of the electric field taken on a plain running through the middle of the compression insulator. At this lower voltage level the electric field at the conductor attachment point is no longer an issue. Meanwhile the 'Butterfly' grading device manages to control effectively the electric field around the triple junction at the HV-end of the insulator reducing its magnitude below the 3.5 kV/cm threshold. Also because of the lower operating voltage the field magnitude on the device itself is within the acceptable values, well below 18 kV/cm. The highest electric field magnitude for the whole cross-arm is 12 kV/cm, which is still within the acceptable limits, and can be observed on the LV grading device.

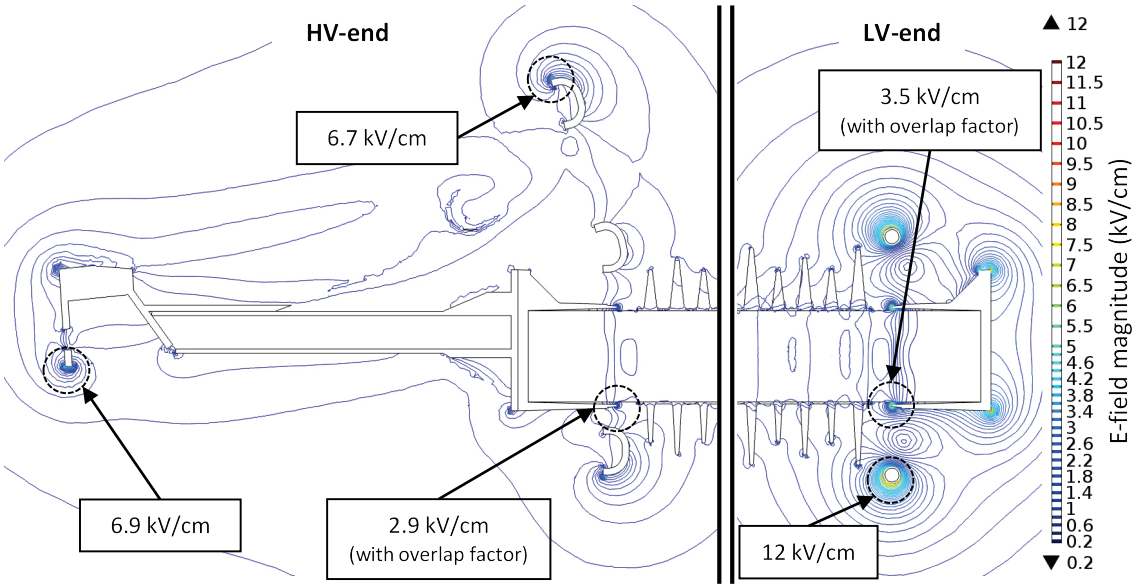

Figure 3.25 - 132 kV ICA with Design C grading device electric field contour plots

Figure 3.26 shows two plots of the electric field magnitude for the compression insulator. The red is plotted on a line 0.5 mm from the surface of the sheath of the insulator. The blue is plotted on line inside the FRP core. The field on the surface of the insulator does not exceed 1.9 kV/cm while the field in the core remains below 1.6 kV/cm. Both results are well within the acceptable limits defined in *Section 3.5.5* of this chapter.

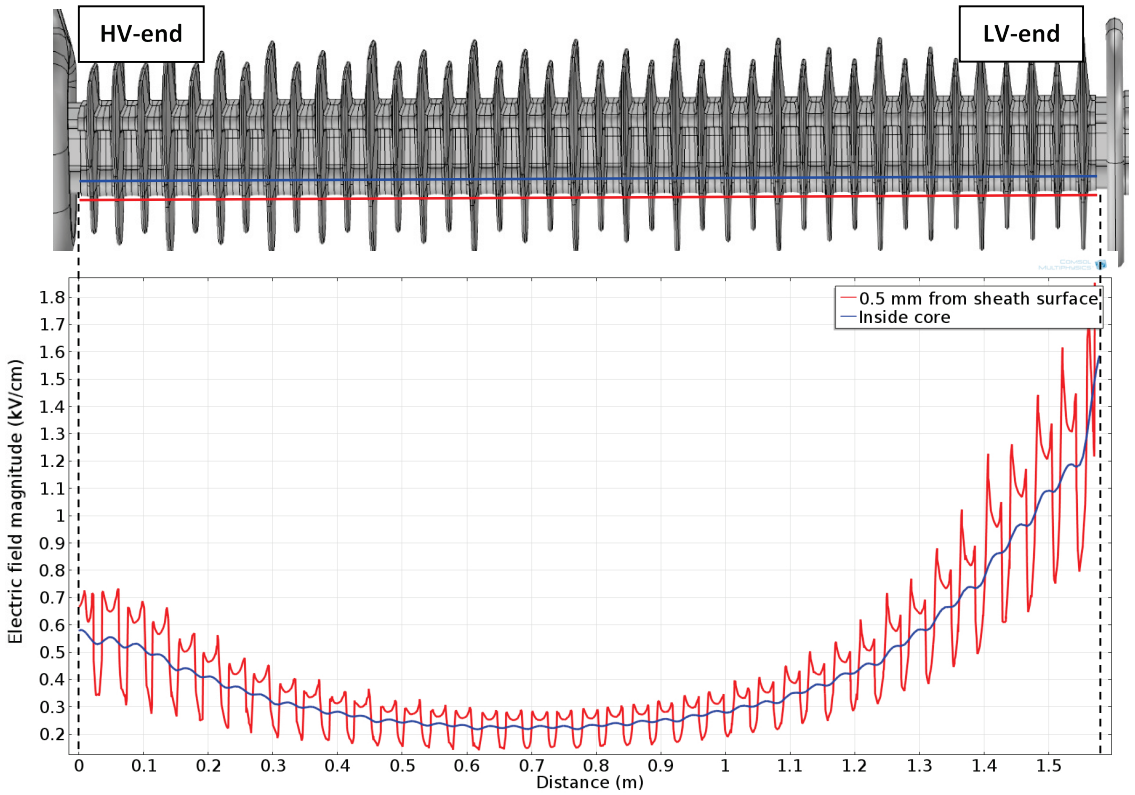

Figure 3.26 - Electric field on the surface and inside the core of the compression insulator at 132 kV

All the results above indicate that the '*Butterfly*' grading device can be used to successfully control the electric field at the 132 kV level. A prototype of the device was manufactured and installed on a 132 kV ICA. The cross-arm was subjected to and passed the corona extinction test (detailed in *Chapter 4*) in the HV laboratory. In August 2013 six 132 kV insulating cross-arms employing the '*Butterfly*' grading device were installed on a live line in Scotland (Figure 3.27). The innovative electric field grading solution of *Design C* has been patented [88].

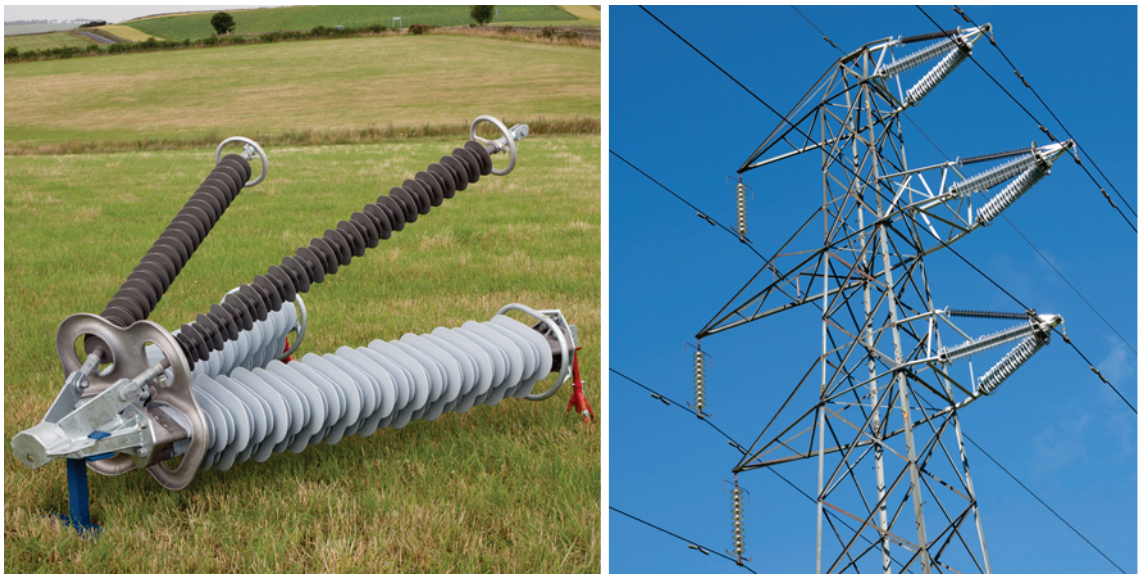

Figure 3.27 - 132 kV ICA with 'Butterlfy' grading device

3.9.4.2.5 End-fitting attachment

By performing FEA it has been deduced that none of Designs A to C could adequately control the electric field at 400 kV. Neither the size nor the position of the HV grading device affected the electric field magnitude to the appropriate extend. The main culprit was the geometry of the end-fitting of the compression insulator. Its sharp edge at the triple junction prevented the reduction of electric field magnitude below the 3.5 kV/cm limit. It was realised that to achieve the requirements, the end-fitting itself would have to be modified before an effective grading device could be designed. As mentioned in *Section 3.9.2* however, the edge of the end-fitting facing the sheds is an integral part of the insulator design and could not be changed without affecting the manufacturing process and associated tooling.

To work around the limitations, a separate attachment for the end-fitting was designed that could be fitted after the injection moulding process of the silicone rubber has been completed. The attachment is shaped similarly to the cross-section of the insulator core and consists of two metallic parts that clamp around the edge of the end-fitting. To save material the attachment only comes in contact on the top and bottom of the end-fitting and not on the sides. Its purpose is twofold: first to increase the radius of the edge and second to direct the electric field away from the triple junction. The end-fitting together with the attachment can be seen in Figure 3.28.

To determine the optimal radius (***R***) of the attachment as well as the optimum distance of the attachment from the edge of the end-fitting (***D***) the model, designed in SolidWorks, was imported into COMSOL. A parametric study was conducted varying the parameters ***R*** and ***D*** while computing the electric field. The target was to identify the optimum radius and position for which the maximum electric field magnitude did not exceed 18 kV/cm at the triple junction. This would ensure that even in the absence of a grading device the end-fitting would remain corona-free. The computational domain and boundary conditions were set to be identical as the ones of the reference model of *Section 3.9.1*. The results are summarised in Figure 3.29.

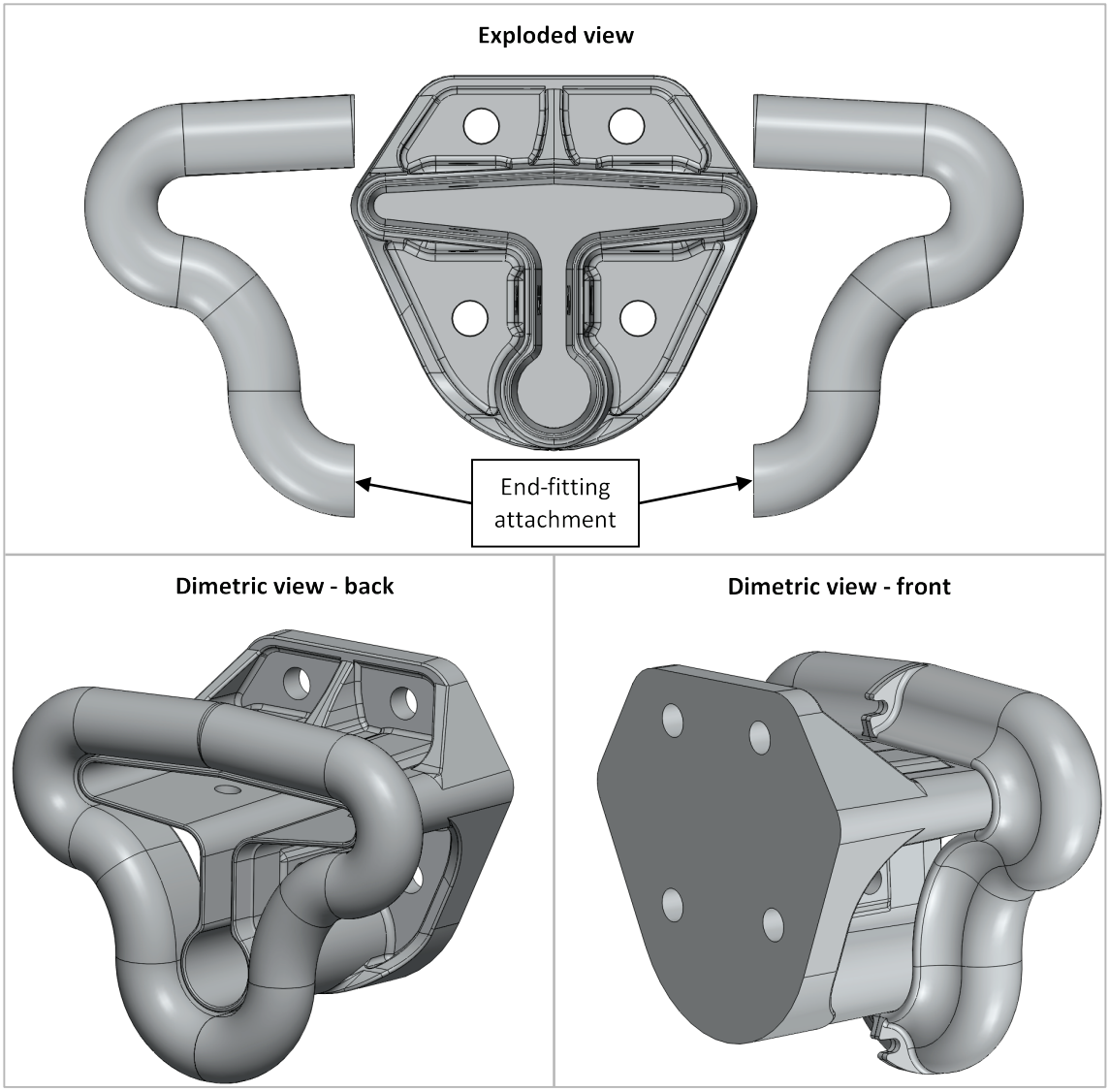

Figure 3.28 - End-fitting attachment

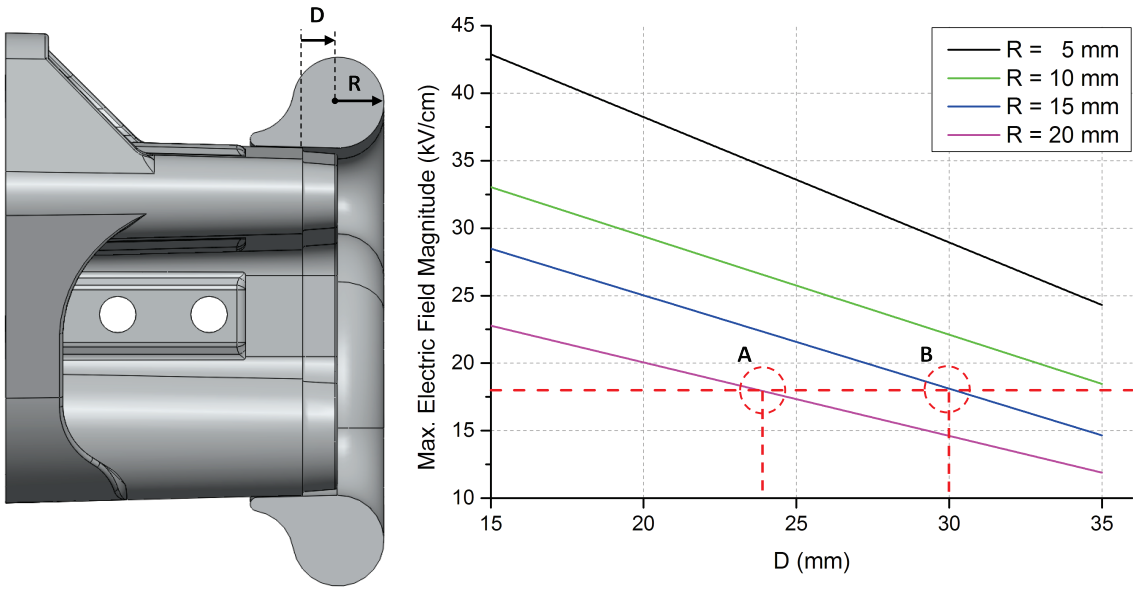

Figure 3.29 - End-fitting attachment optimisation study results

There are two combinations of radius and distance that meet the target. ***Combination A*** is a bigger attachment closer to the edge of the end-fitting while ***combination B*** is a smaller attachment but closer to the sheds. The former was selected (R = 20 mm, D = 25 mm) primarily because of its bigger distance from the first shed that reduces the risk of discharges from the attachment to the shed.

The electric field distribution for the optimal attachment compared to the reference model of *Section 3.9.1* is presented in the form of a contour plot in Figure 3.30. It is worth noting that the maximum electric field magnitude for the triple junction with the attachment installed on the end-fitting can no longer be observed on the underside of the fitting. Instead it can be seen on the middle of the spine of the end-connection, where the attachment is not physically touching the end-fitting. The electric field at this specific area is reduced from 52 kV/cm to 18 kV/cm, almost a three times improvement. The maximum electric field magnitude can now be observed on the attachment and it does not exceed 35 kV/cm. Additionally, the reduced density of the field lines near the end-fitting shows that the attachment helps direct the electric field away from the triple junction and the core of the insulator.

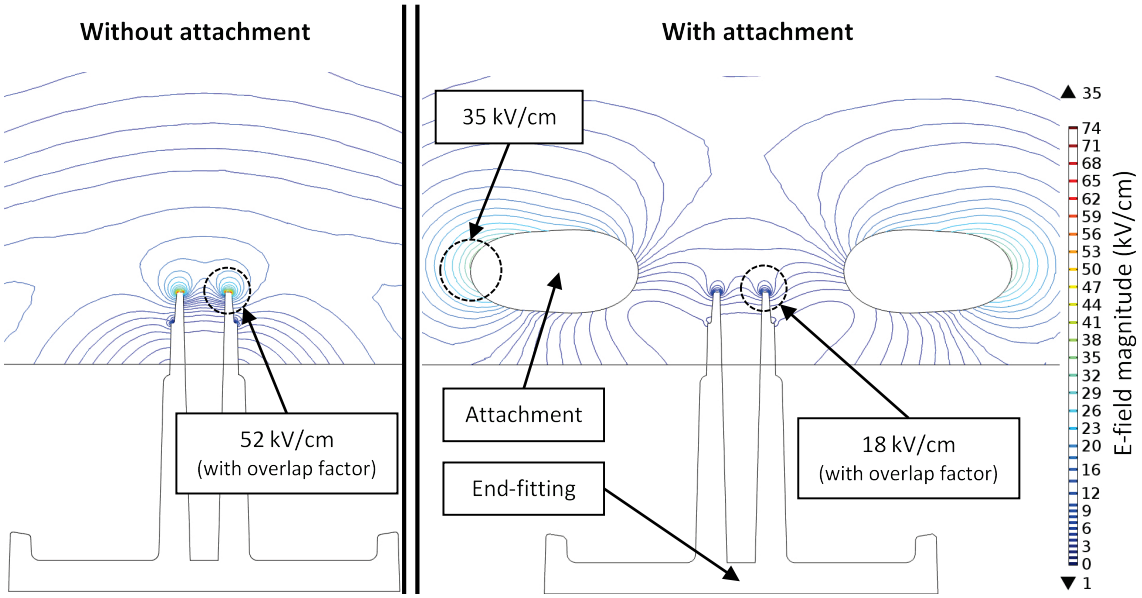

Figure 3.30 - Electric field contours for end-fitting with and without attachment

3.9.4.2.6 Design D – 'M-W'

Although the end-fitting attachment does an admirable job in reducing the electric field magnitude at the triple junction of the compression insulator it cannot bring it below the required threshold on its own. To complement the attachment and provide a grading solution for the entire HV-end of the cross-arm, ***Design D*** was conceived. It consists of three parts. At the tip of the nose cone, on top of the conductor attachment point, a semi-spherical device, the '*nose ball*', takes care of the electric field distribution at that area. At the back of the nose cone and located above the first sheds of the tension insulators an *'M'*-shaped device constructed out of 48 mm in diameter bend tube is responsible for managing the field around the tension insulator end-fittings. At the bottom of the assembly, directly below the first sheds of the compression insulators, a *'W'*-shaped device build out of the same diameter tube assists the end-fitting attachments to control the electric field around the compression insulator end-fittings. Design D can be seen integrated with the HV reference model in Figure 3.31.

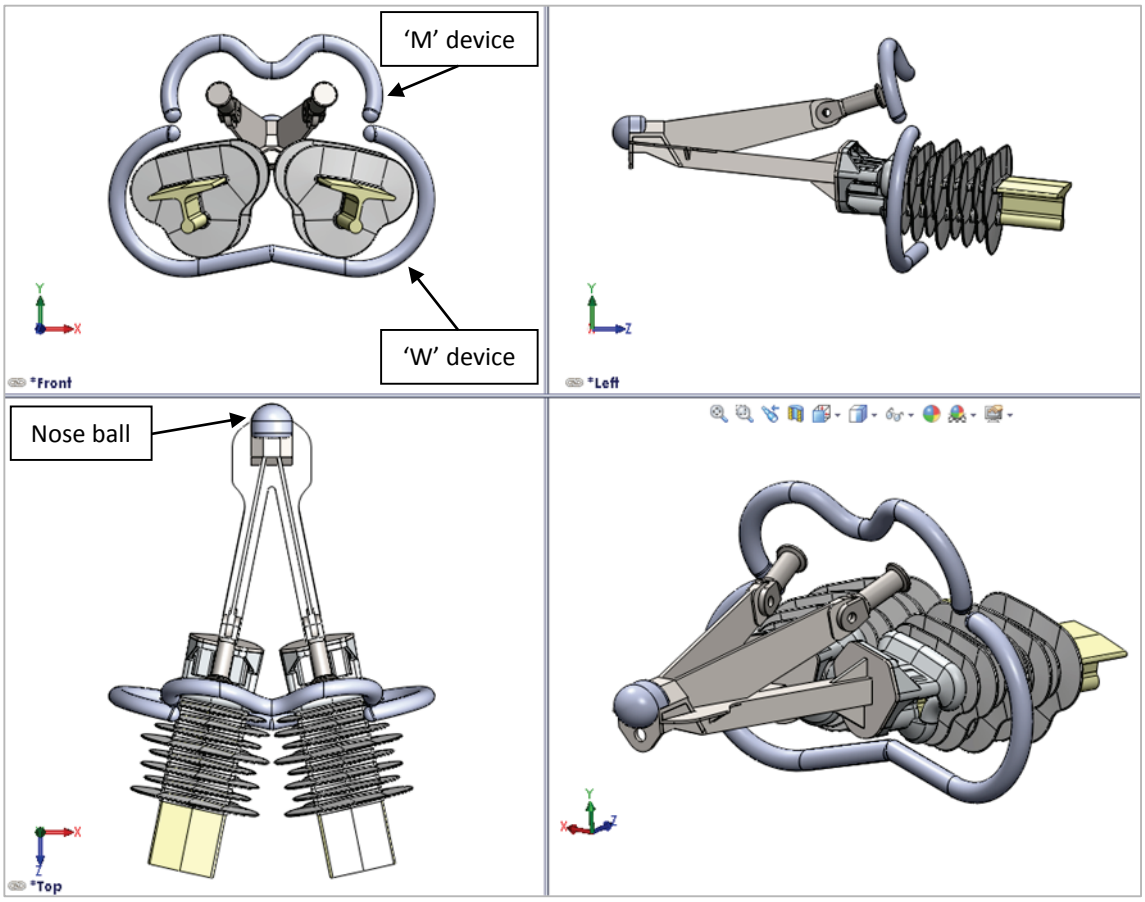

Figure 3.31 - HV grading device Design D

The model of Figure 3.31 has been imported into COMSOL and placed within the same computational domain as the previous designs. The boundary conditions have also been kept identical. Figure 3.32 shows the electric field contours viewed from the side of the ICA assembly plotted on a plane passing through the middle of the tension and compression end-fittings. Figure 3.33 shows the field contours viewed from the top of the cross-arm. The 'nose ball' reduces the electric field at the conductor attachment point below the 18 kV/cm limit. The 'M' device brings the electric field magnitude around the tension insulator end-fitting down to 3.3 kV/cm at its triple junction. The combination of the end-fitting attachment and 'W' device manages to control the field near the compression insulator triple junction effectively. The maximum value is registered on the middle of the spine of the end-fitting and reaches 3.3 kV/cm after the overlap factor has been accounted for. The electric field magnitude on the 'M-W' devices themselves does not exceed 16 kV/cm. This value can only be seen at the domed terminations of the tubes that comprise the devices.

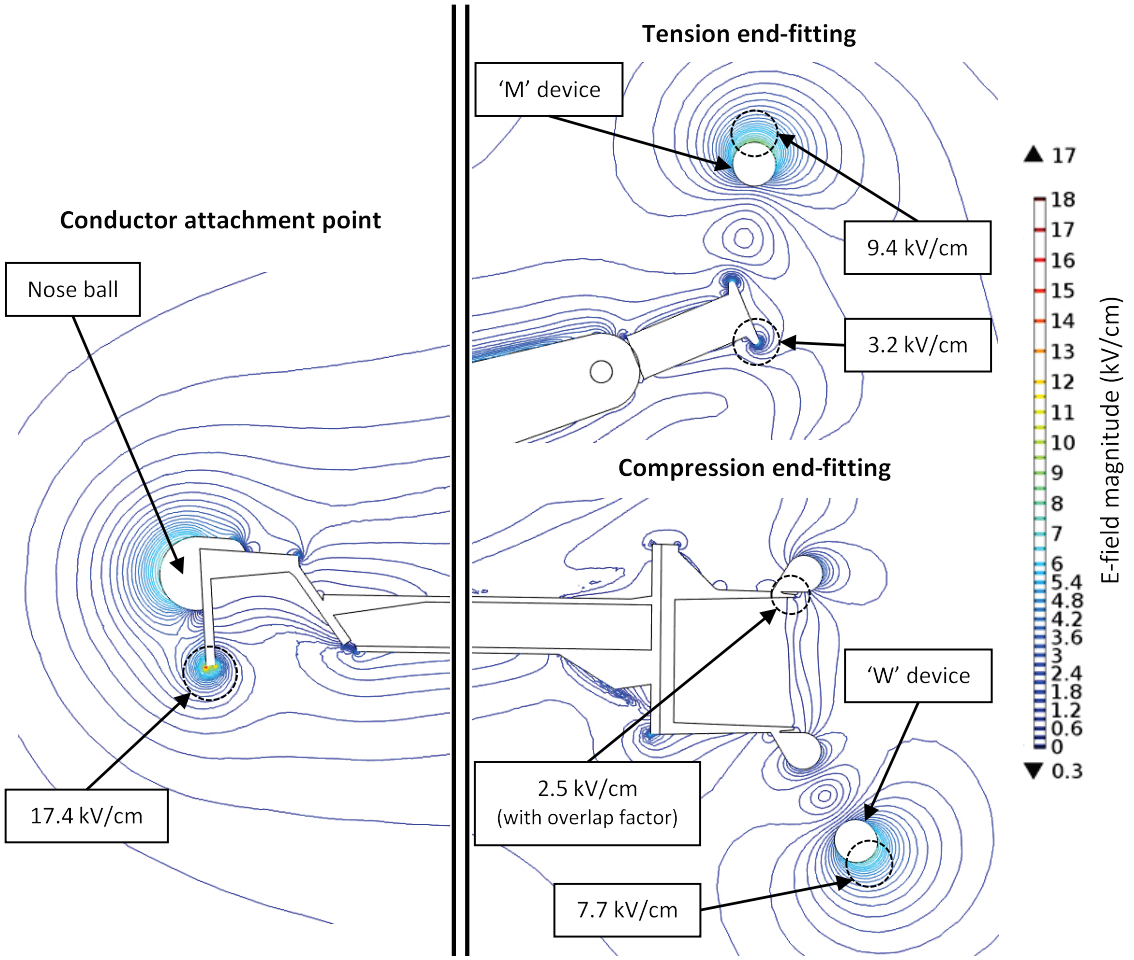

Figure 3.32 - Electric field contours for HV-end with Design D grading device (side view)

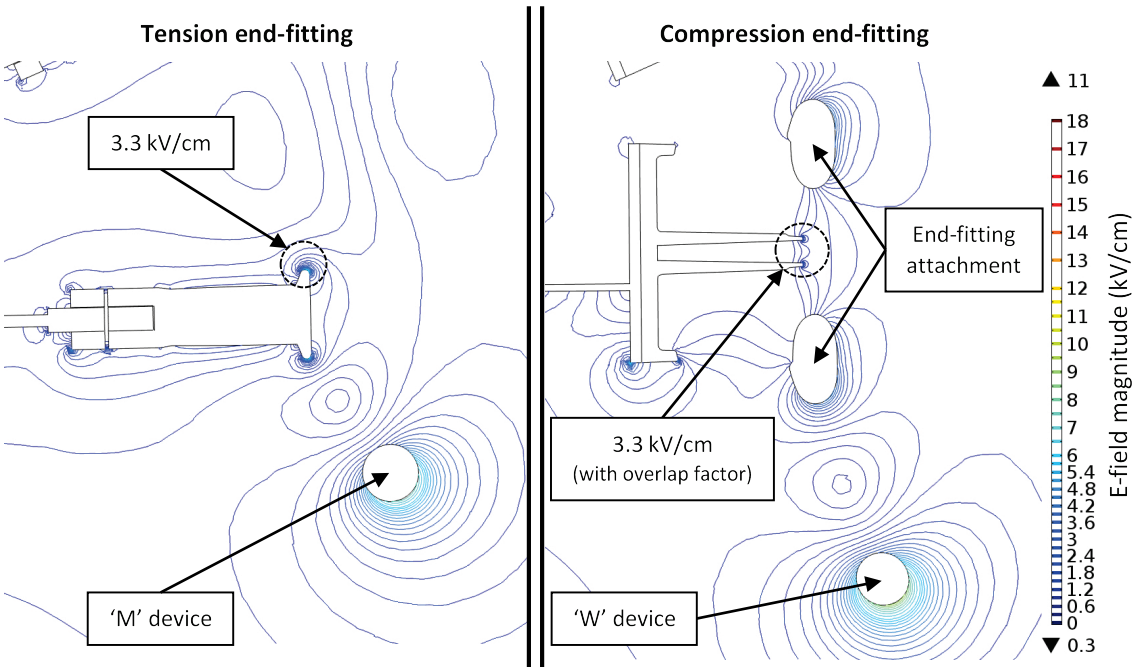

Figure 3.33 - Electric field contours for HV-end with Design D grading device (top view)

In addition to being able to meet all the electric field requirements, Design D offers others advantages when compared to the previous three designs. The bending radii of the tubular sections are not as small as in Designs A and B. As a result no special manufacturing methods have to be employed. Furthermore this grading device consists of two independent parts, top and bottom. Hence, it can be installed and replaced easier than the other designs. Also it is the design with the smallest overall volume which reduces its visual impact.

3.10 Discussion

The electric field can cause severe problems to polymeric insulators if its magnitude is not kept within the appropriate limits. The structural integrity of the core can be compromised by partial discharges that can develop inside cavities of the core material or at the interface between the sheath and the core. Enhanced surface discharge activity and corona can accelerate the ageing of the weathershed material reducing the service life of the insulator. In more extreme cases, the discharges can erode the sealing material between the end-fittings and the core allowing water ingress that can lead to catastrophic failure via the brittle fracture mechanism. Moreover, the corona phenomenon caused by high electric fields can contribute negatively to the perception of the public regarding overhead lines since it has been linked with noise pollution and radio interference. Managing the electric field on the ICA is arguably even more

important than for other OHL insulator applications because a line employing ICAs will have four times the insulators of a conventional line.

However, designing electric field stress management devices for the ICA presented unique challenges. The cross-sectional shape of the compression insulators and their end-fittings, the method of attachment of the end-fittings to the insulators and the proximity of the insulating members to each other at the nose end of the cross-arm meant that traditional solutions would not work effectively for the ICA. Using CAD (SolidWorks) and FEA (COMSOL) tools devices for both the LV and the HV ends of the cross-arm were designed. The LV device resembles the grading rings found on most OHL insulators with the difference that its shape follows the cross-sectional shape of the compression insulator. For the HV end, the third design iteration, the 'butterfly' grading device, was patented and used on six insulating cross-arms installed on a live network at 132 kV. The final design, the 'M-W' grading device, which is suitable for 400 kV applications based on the FEA results, was the outcome of the iterative design process and has the following properties:

a) **4-component solution:**
   - Nose ball
   - End-fitting attachment
   - 'M' device
   - 'W' device

b) **Effective e-field management:** it meets all the electric field criteria set by National Grid, IEEE and EPRI (*Section 3.5.5*). Specifically, according to the values produced by the FEA, the maximum electric field magnitude values for the 400 kV ICA are:
   - On the sheath and sheds : 1.9 kV/cm
   - At the triple junction : 3.3 kV/cm
   - Inside the core and weather-shed material : 1.6 kV/cm
   - On metallic hardware : 17.4 kV/cm

c) **Easy to install and service:** the four independent components can be installed before or after the ICA installation at no particular order with just one person required for their assembly. Furthermore, any of the four components can be replaced individually if damaged without requiring the removal of the conductor.

d) **Easy and cheap to manufacture:** The big components of the solution, the 'M' and 'W' devices, are manufactured using bend tube with relatively wide bending radii and welded plates that facilitate their attachment to the nose cone. As a result, no special manufacturing methods are required which reduces the complexity and cost of manufacture.

e) **Redundancy:** in the unlikely scenario that both the 'M' and 'W' devices fail, the end-fitting attachments can maintain the CIV below the critical 22 kV/cm on their own to prevent permanent damage from corona discharges to the structurally critical compression insulators.

f) **Minimal visual impact:** Every component serves a functional purpose with no additional parts required to interconnect them. This keeps the volume of the grading solution as low as possible with the visual appearance of the ICA remaining mostly unchanged, especially when viewed from a distance.

3.11 Conclusion

The use of FEA was proven to be particularly efficient for designing electric field stress control devices for the ICA, helping to overcome many of the challenges created by the unconventional shape of the compression insulator and the size of the assembly. By modelling the uniquely-shaped end-fitting of the compression insulator, the areas of high electric field enhancement were quickly identified and an original accessory, the end-fitting attachment, was created to control the field at the triple junction which can be added on after the insulator is manufactured. Substantial amount of time was saved by simulating the various designs for the HV-end grading device instead of manufacturing all the prototypes. The two final designs of the device are very different than what is currently used on traditional OHL insulators. The 'Butterfly' grading device, suitable for 132 kV ICAs, is a single component that can control the electric field on all four insulating members simultaneously. The 'M-W' device, suitable for 400 kV ICAs, is a complete four-component solution that works together with the end-fitting attachment to control the field not only on the insulating members but also on the nose cone and the conductor attachment point.

4. TYPE TESTING

4.1 Introduction

To ensure that any equipment placed on a power network will operate as intended over its lifetime, various tests are performed to examine all aspects of its design and performance. The testing procedure is normally agreed between the supplier and the customer while the tests in their majority are based on international standards in order to give confidence regarding the capabilities of the product. Since international standards for insulating cross-arms do not exist at the time of writing, a type testing regime has been drafted based on the standards used for composite OHL insulators, BS EN 61109 [19] and BS EN 62217 [89], and the Technical Specifications of National Grid, TS 3.4.17 [57] and TS 3.4.18 [80]. Some of the tests have been kept unchanged to evaluate the performance of the novel compression insulators. Others have been altered so that they can be performed on the cross-arm assembly rather than on individual insulators, since this arrangement is more representative of the service conditions.

Transmission line equipment is expected to be subjected to overvoltages during its service life. In the case of OHL insulators the design is mostly determined by the capability of the insulator to withstand them or not be damaged when they lead to flashover. For this reason this chapter begins with discussing the situations when overhead lines experience voltage stresses higher than the service voltage which can cause outages, disrupting the continuity of electrical supply. The main items of equipment used for high voltage testing are also reviewed in detail. Finally, the electrical tests performed on the 400 kV cross-arm assembly and the compression insulator are presented.

4.2 Lightning overvoltages

4.2.1 Lightning strike formation

Lightning strikes on transmission lines cause lightning overvoltages which in turn can cause lines to trip. A lightning strike is initiated when the field intensity at a point of a charged cloud exceeds the breakdown value of the air between the cloud and earth. A

streamer is formed in a series of steps originating from the cloud and heading towards earth which is known as a stepped leader. The leader often splits into branches and as it progresses it ionises the surrounding air giving a luminous effect. Just before the leader reaches earth, pre-discharges of the reverse polarity develop at prominent points such as trees, buildings and other structures. When the leader and the upward pre-discharges meet, a path is established between the cloud and earth that allows heavy current flow. This is known as the return strike and can be seen as a luminous flash heading towards the cloud. The return strike disappears before reaching the cloud however, the remaining charge in the cloud can give rise to successive strikes initiated by dart leaders that have lower velocity and current and use the same discharge channel as the original streamer. A complete lightning strike can last up to approximately one second and on average it consists of three to four discharges [16, 90]. The formation of the lightning strike can be seen in Figure 4.1.

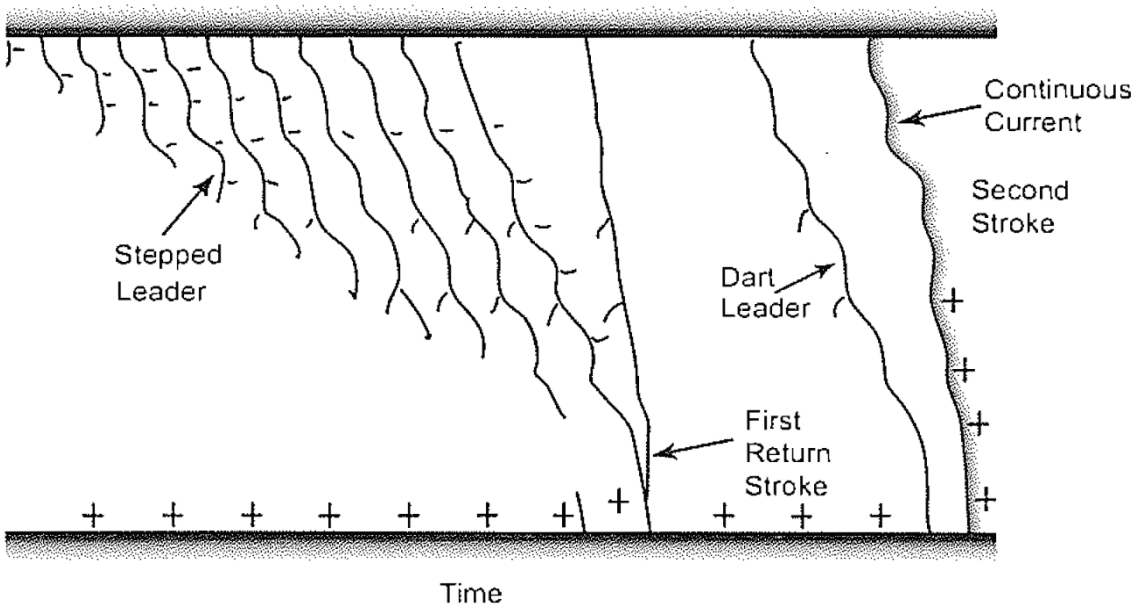

Figure 4.1 - Formation of lightning strike [70]

4.2.2 Categories of lightning overvoltages

Lightning overvoltages on transmission lines are classified in three categories depending on the point at which the strike connects to ground. ***Induced overvoltages*** are caused by lightning strikes hitting the ground near a line. They very rarely affect transmission lines, rated at 132 kV and above, since they seldom exceed 600 kV which does not exceed the withstand capability of the insulation [16].

When a lightning strike connects to a phase conductor an overvoltage due to ***shielding failure*** occurs, denoting the inability of the shield wire to intercept the lightning. In this case the potential of the conductor is raised much higher than the operating potential and if it is sufficiently high it may cause a flashover to the tower. The strike injects a current pulse into the phase conductor creating travelling waves originating from the strike point and propagating on either direction [70]. The peak value of the overvoltage is given by:

$$V_{OV} = I_{LI} \cdot \frac{1}{2} Z_{SC} \tag{4.1}$$

where I_{LI} is the current of the strike and Z_{SC} is the surge impedance of the conductor (typically 350 Ω – 600 Ω).

The majority of lightning strikes hit the shield wires or the tower itself, which are the highest points of a span, creating overvoltages due to ***back-flashovers***. Since a lightning strike can be considered as a high impedance current source, the strike connects the cloud in series with the ground. The current flowing through the tower raises its potential and if the potential is high enough a back-flashover can occur, a flashover from the tower to the phase conductor. Initially the lightning strike sees the impedance of the tower paralleled with the impedance of the shield wire on either side of the strike point making its surge impedance:

$$Z_{LI} = Z_{TR} \parallel \frac{1}{2} Z_{SW} \tag{4.2}$$

where Z_{TR} is the travelling wave surge impedance of the tower (100 Ω – 150 Ω) and Z_{SW} is the surge impedance of the shield wire (250 Ω – 350 Ω) . After approximately 3 μs the lightning strike current reaches the bottom of the tower and an overvoltage develops from earth that depends on the ground surge impedance, Z_{GD}. The surge impedance becomes:

$$Z_{LI} = Z_{GD} \parallel \frac{1}{2} Z_{SW} \tag{4.3}$$

The peak value of the overvoltage is given by:

$$V_{OV} = R_{GD} \cdot I_{LI} + L_{TR} \frac{dI_{LI}}{dt} \quad (4.4)$$

where R_{GD} is the ground resistance of the tower, L_{TR} is the inductance of the tower and I_{LI} is the current of the strike [70].

4.2.3 Lightning overvoltage performance of OHLs

The performance of overhead lines in relation to lightning strikes is usually specified as the number of flashovers per 100 km of line per year. Other times the performance is specified in terms of the storm outage rate (SOR) which is the number of unsuccessful reclosures per year and can be calculated by multiplying the number of lightning flashovers per year by the number of switching surge flashovers per switching operation. High voltage overhead lines of 345 kV and above exhibit low flashover rates typically below one flashover per 100 km per year [70].

4.2.4 Lightning impulse

For testing high voltage equipment to determine its withstand capability against lighting overvoltages the IEC 60060-1 [55] specifies the waveshape of the lightning impulse that is defined in terms of its front time, T_1, and its time to half-value, T_2. T_1 is defined as the time between the moments at which the impulse is 30 % and 90 % of its peak value, multiplied by 1.67. T_2 is defined as the time between the origin of the impulse and the moment the impulse has reached the half of its peak value. The standard lightning impulse has a front time of 1.2 µs and a time to half-value of 50 µs and is often referred to as a 1.2/50 impulse. The magnitude of the impulse depends on the operating voltage of the equipment. For OHL insulators this is defined in the NNAs and the values for the UK can be found in Table 2.1. The tolerances allowed for the variation of the test impulse parameters compared to the standard values are the following:

- Peak value : ± 3 %
- Front time : ± 30 %
- Time to half-value : ± 20 %

The waveshape of the full lightning impulse can be seen in Figure 4.2:

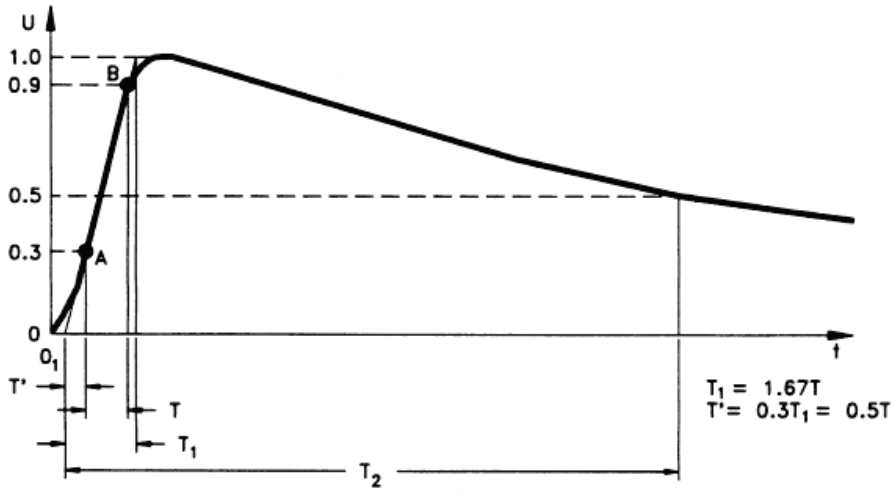

Figure 4.2 - Full lightning impulse [55]

4.3 Switching overvoltages

Power systems store energy in their electric and magnetic fields. The inductance stores magnetic energy while capacitance stores electrical energy. When switching operations take place energy is exchanged between a transmission line and the system resulting in switching overvoltages. The switching operations that mostly affect overhead lines are:

- Line energisation
- Line re-energisation with trapped charge on the line
- Load disconnection
- Transformer switching
- Reactor switching

4.3.1 Conditions affecting the magnitude of switching overvoltages

The magnitude of the overvoltage depends on the situation under which the stored energy in the system is released. Trapped charge on OHL conductors is caused by breaker operation at the energised end of the line. The breaker normally opens upon zero current detection which leaves the voltage at its peak, trapping charge on the line. The charge can be discharged trough the leakage path provided by the insulators but this can take several minutes as the resistance of the insulators is very high. It is possible therefore for the line to be re-energised before the trapped charge has been discharged. If the re-energisation happens with the supply and line sides of the breaker having opposite polarities, a travelling wave in the order of 2 p.u. can be injected into the line.

When the wave reaches the open-circuited end of the line it will be reflected and double in magnitude effectively creating an overvoltage in the order of 4 p.u. [70].

During line de-energisation switching overvoltages are less severe even if the circuit breakers do not open at current zero that results in a small transient. However, when a circuit breaker opens there is the possibility of a restrike occurring across the opening contacts because of the appearance of a transient recovery voltage. The magnitude of the current transient, I_{TR}, is a function of the voltage across the circuit breaker when the restrike occurs, V_{CB-R}, the natural impedance of the line, Z_{NL}, and the impedance of the source, Z_S [91]. It is given by:

$$I_{TR} = \frac{2V_{CB-R}}{Z_{LN}} \cdot \left[1 - \exp\left(\frac{-Z_{LN}}{Z_S} \right) \right] \tag{4.5}$$

The restrike can initiate a travelling wave which after reaching the other end of the line it can be reflected back provided that the circuit breaker at the other end of the line has already been opened. The overvoltage in this case can exceed 2.5 p.u. [91, 92]. Such overvoltages are likely to be limited by arresters so they normally would not be of primary concern to the line. However, they could result in breaker failure.

Table 4.1 *- Overvoltages due to switching operations [90]*

Type of operation		**Overvoltage (p.u.)**
Switching an open-ended line with:	infinite bus as source with trapped charge on the line	4.1
	infinite bus as source without trapped charge	2.6
De-energising an un-faulted line with:	a restrike in the circuit breaker	2.7
	a line to ground fault	1.3
Switching a:	500 kV line through an auto-transformer	2.0
	transformer terminated line	2.2
Switching a series capacitor compensated line with:	with 50 % compensation	2.2
	with shunt reactor compensation	2.6
High speed reclosing line after fault clearance		3.6

Faults on overhead lines, which are in their majority phase-to-ground, cause high current flow which leads to voltage collapse. Overvoltages can appear, on the un-faulted phases in particular, when a fault happens and a breaker opens to clear the fault and de-energise the line. The magnitude of these overvoltages can reach 1.3 p.u. unless single-phase switching is used and hence in does not pose significant risk for the line insulation [70]. Table 4.1 summarises the various conditions that can affect switching operations and the resulting overvoltages.

4.3.2 Switching overvoltage performance of OHLs

For overhead lines operating in the EHV range and above (i.e. above 345 kV), switching overvoltages are more of a concern than lightning overvoltages. Switching overvoltages are internal to the system, unlike lightning overvoltages, and therefore their magnitude depends on the system voltage. It has been shown that while the lightning impulse strength increases linearly with the distance between electrodes, the increase in switching impulse strength is less than proportional. Also, the withstand capability of air gaps to positive polarity switching impulses has been found to be less than their capability to withstand lightning overvoltages of the same magnitude. Furthermore, the duration of switching overvoltages is longer and as a result they can cause more damage [70, 90].

The performance of overhead lines in relation to switching overvoltages is given by the number of flashovers per 100 switching operations. Typically, lines are designed to withstand between 1 and 10 flashovers per 100 switching operations [70].

4.3.3 Switching impulse

The switching impulse waveshapes defined in [55] are used in laboratories for testing insulation systems. The standard switching impulse is defined by its time to peak, T_p, which is the time between the origin and the moment when the impulse reaches its peak, and its time to half-value, T_2, similarly to the lightning impulse. The standard lightning impulse has a time to peak of 250 μs and a time to half-value of 2500 μs and is often referred to as a 250/2500 impulse. The switching impulse has a longer front and a substantially longer duration than the lightning impulse. The impulse withstand requirements that depend on the operating voltage of the equipment can be found in

Table 2.1. The tolerances allowed for the variation of the test impulse parameters compared to the standard values are the following:

- Peak value : ± 3 %
- Time to peak : ± 20 %
- Time to half-value : ± 60 %

The waveshape of the full switching impulse can be seen in Figure 4.3:

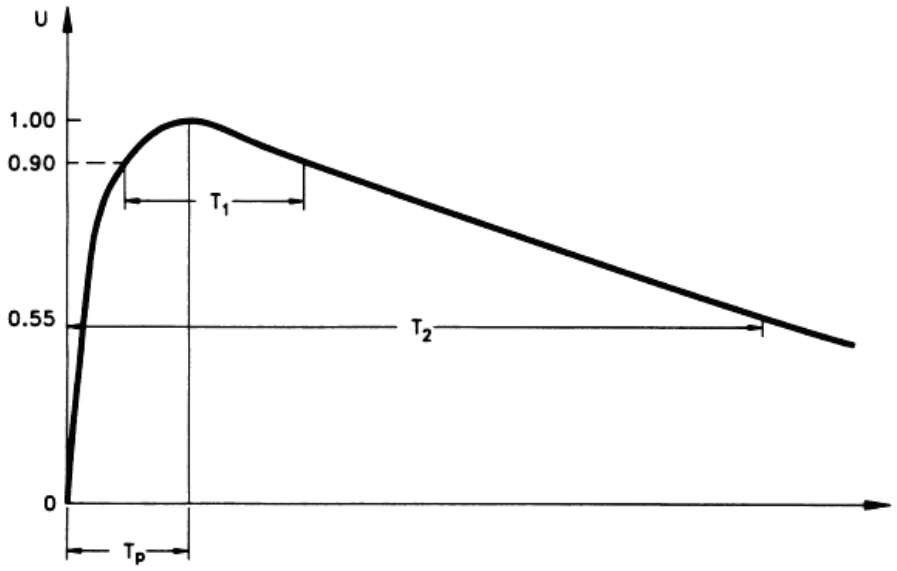

Figure 4.3 - Full switching impulse [55]

4.4 Power frequency overvoltages

Under normal service conditions, OHLs operate continuously at their operating voltage which is allowed a very small margin of deviation from its nominal value, typically no more than ± 10%. Temporary overvoltages, or power frequency overvoltages, occur during tap changing operations, because of the ferro-resonance phenomenon in large transformers and because of resonating overvoltages due to series capacitors with shunt reactors. Normally, they last between one or two cycles to a few seconds [90]. These overvoltages are usually not of significant concern to the line insulation since it is designed to withstand much higher voltage levels due to lightning or switching overvoltages. They can, however, become troublesome is they are combined with environmental stresses or if the insulation is damaged. Environmental factors affecting negatively the resistance of insulation to flashover include pollution accumulation, snow and ice accretion, guano (bird droppings) and rain. Causes of damage to the insulation

include ageing, gunshots and fires. Power frequency overvoltages are attributed to the Ferranti effect and the effects of faults [16, 70].

4.4.1 Ferranti effect

The Ferranti effect is the phenomenon where the steady state receiving end voltage of an uncompensated, open-ended or lightly loaded transmission line is greater than the sending end voltage. It occurs when the current associated with the load connected to a line is lesser than the capacitive charging current drawn by the distributed capacitance of the line itself. The capacitive current flowing through the line inductance creates a voltage drop which is in phase with the sending end voltage, raising the voltage at the receiving end. The Ferranti effect is not an issue for loaded lines because the load, which is inductive, consumes the reactive power generated by the capacitance. The voltage rise at the receiving end V_R of an uncompensated line (Figure 4.4) can be calculated using:

$$V_R = \frac{V_S}{l \cdot \cos\beta} \tag{4.6}$$

where:

V_S : sending end voltage

l : length of the line

β : phase constant of the line

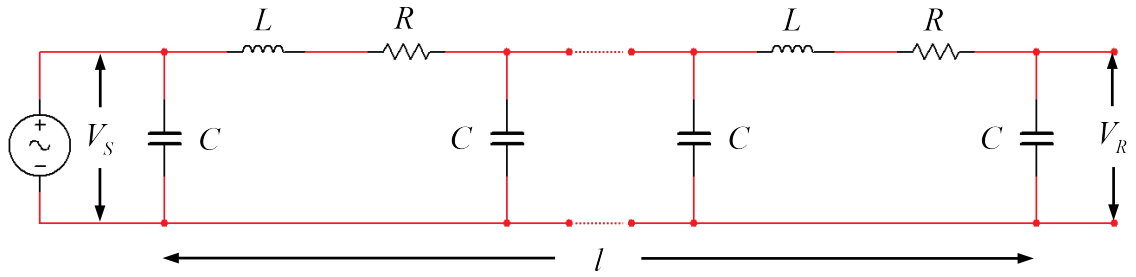

Figure 4.4 - Uncompensated long transmission line

The phase constant β depends on the impedance and admittance of the line and can be calculated using equation (4.7). For a 50 Hz system it is approximately 6° per 100 km of line.

$$\beta \approx \sqrt{\frac{(R + j\omega L) \cdot (G + j\omega C)}{LC}} \tag{4.7}$$

where:

ω : angular frequency

l : line length

R : resistance per unit length

C : capacitance per unit length

L : inductance per unit length

G : leakage conductance per unit length

If the distributed parameters of the line are not known, an approximate solution can be found by assuming that the capacitance is lumped in the middle of the line (Figure 4.5). The charging current I_C using this approximation is:

$$I_C = j\omega C V_S = \frac{V_S}{X_C} \tag{4.8}$$

The receiving end voltage becomes:

$$V_R = V_S\left(1 - \frac{X_L}{2X_C}\right) \tag{4.9}$$

where:

X_L : line inductive reactance

X_C : line capacitive reactance

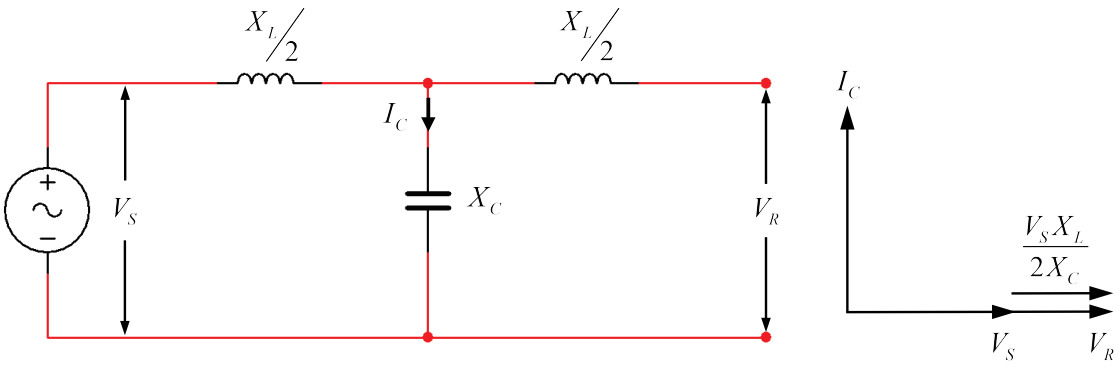

Figure 4.5 - Approximation of transmission line and phasor diagram for Ferranti effect calculation

Overvoltages due to the Ferranti effect are among the most common overvoltages for transmission lines operating at the EHV level and above. They are sinusoidal in nature and their magnitude increases as the line voltage and the length of the line increase and as the load at the receiving end becomes lighter. For 400 kV lines the overvoltages can

reach values up to 2.0 p.u. however, in most cases, shunt reactors are used to limit the overvoltages in the range of 1.2 to 1.5 p.u. [70, 90].

4.4.2 Effects of faults

As mentioned before, the most common faults on transmission lines are phase-to-ground especially for lines operating at the EHV level since the probability of three-phase faults decreases as the line voltage increases [93]. A fault does not only result in a switching overvoltage, as explained in the previous section, but also in a power frequency overvoltage. A large current is injected into the system from the fault point when a fault occurs, resulting in a voltage to be applied at the same point. Hence, traveling waves begin to propagate in both the faulted and unfaulted phases. The transients are damped normally within half a cycle but they are followed by longer, persistent overvoltages that continue to stress the insulation until the fault is cleared. These temporary overvoltages are generally sinusoidal unless the voltage is high enough to cause saturation in transformers. In such case, harmonics are injected into the system resulting in distortion. For single-phase-to ground faults the magnitude of such overvoltages is unlikely to exceed 1.6 p.u. and for effectively grounded systems the rise in system voltage remains even lower, usually below 1.4 p.u [70, 90].

4.5 Equipment

4.5.1 Impulse generator

The lightning and switching overvoltages, which have a fast increase and slow decay, can be described by the superposition of two exponential functions according to (4.10) [59]:

$$V_{imp}(t) = \frac{V_0}{k} \cdot \frac{1}{(a_2 - a_1)} \cdot [\exp(-a_1 t) - \exp(-a_2 t)] \tag{4.10}$$

where $k,\ a_1,\ a_2$ are constants that depend only on the circuit parameters (R, L, C).

To generate the appropriate waveshapes in order to test the withstand capability of HV equipment to lightning and switching transients, discharge circuits with dual energy storage can be utilised. The first source of stored energy for such a circuit would be the load which in most cases is capacitive (e.g. OHL insulator). The other source of energy

would have to be a capacitor in order to achieve the fast discharge time required to reproduce the transient waveshapes. A basic (single stage) impulse generator therefore would be comprised of primarily two capacitors and a combination of resistors. The test loop would also have some inductance which would usually be very small [90]. The equivalent circuit is shown in Figure 4.6.

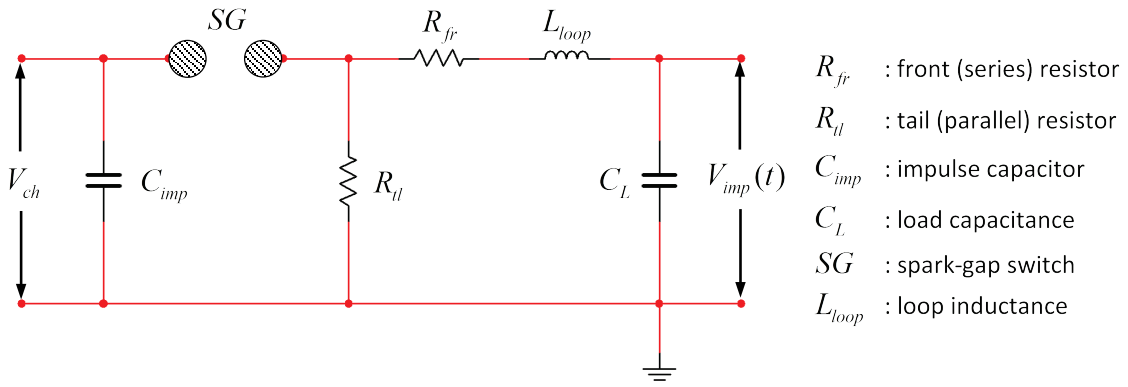

Figure 4.6 - Single stage impulse generator circuit

The capacitor C_{imp} which is slowly charged by a DC source, is discharged into the rest of the circuit when the breakdown voltage of the spark-gap SG is exceeded. The front R_{fr} and tail R_{tl} resistors together with the load capacitance C_L comprise the waveshaping part of the circuit. The front resistor is responsible for damping the circuit and controls the front time. The capacitors are discharged through the tail resistor and as a result it controls the wavetail. The load capacitance is normally composed of the capacitances of the test object, the additional load capacitor (if present) and the divider as well as any other stray capacitances in the test loop.

A single stage impulse generator stops being practical when the test voltages required exceed 200 kV. The size of the impulse capacitor becomes very large and both the capacitor and associated charging unit become expensive. Furthermore, the spheres comprising the spark gap would have to be very big as well in order to manage the electric field effectively and prevent unintended discharges. Therefore, for generating very high impulse voltages, multistage impulse generators are used which consist of a number of capacitors that are charged in parallel and then discharged in series. Impulse generators employing this arrangement are also known as Marx generators.

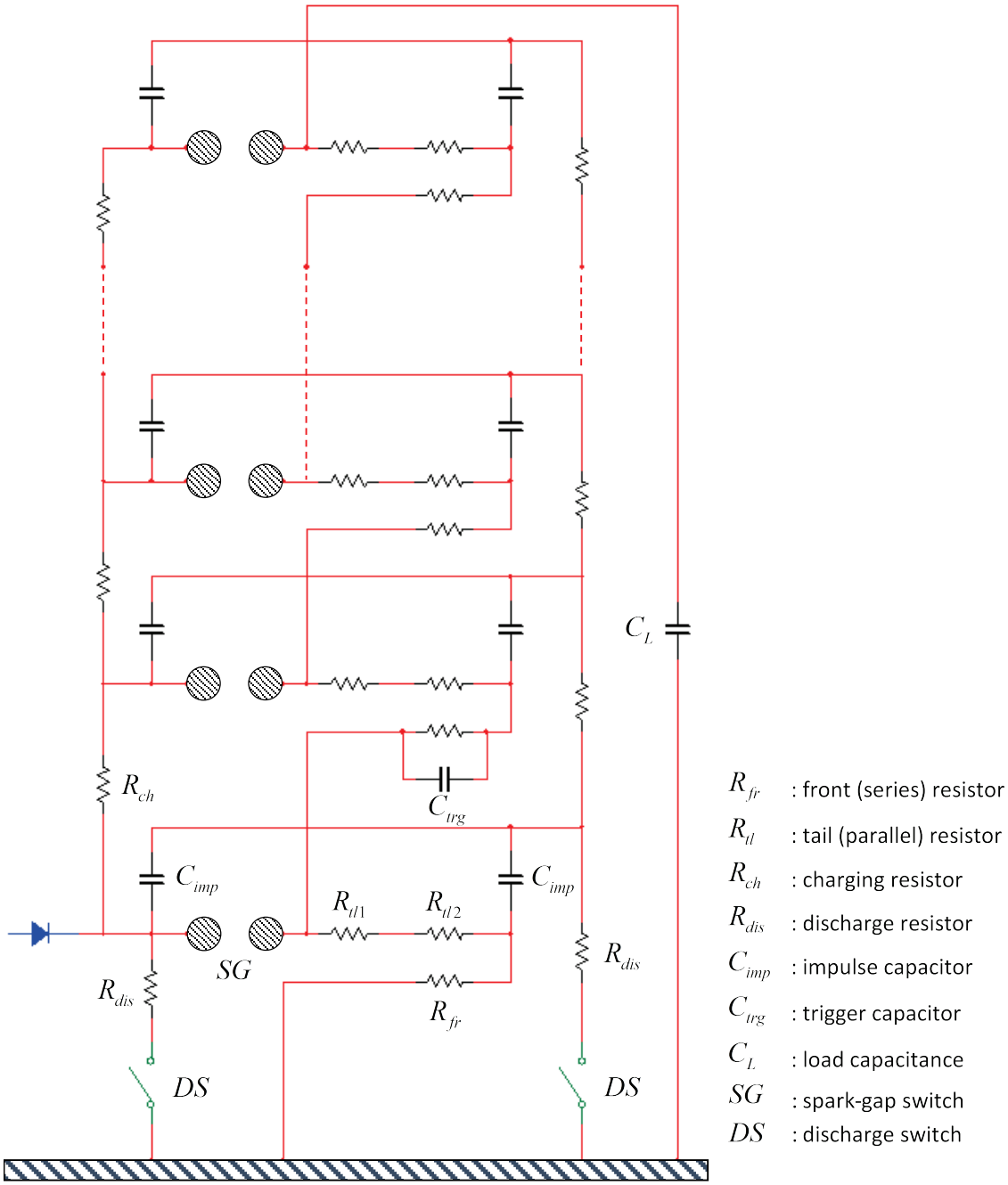

Figure 4.7 - Multistage impulse voltage generator

The HV laboratory of the University of Manchester has a ten stage impulse generator capable of producing voltages of up to 2 MV, 200 kV per stage, by using twenty 100 kV HV capacitors (Figure 4.7). The capacitors C_{imp} are charged through high value charging resistors R_{ch}, designed to limit the charging current. The spark-gap SG is set so that its breakdown voltage is bigger than the charging voltage. When the capacitors are fully charged the spark-gap of the first stage is externally triggered to break down followed by an almost simultaneous breakdown of the remaining gaps, discharging the generator. This happens because when the first gap breaks down the first two stages, i.e. their capacitors are effectively put in series, which overvoltages the next gap, which in turn

puts the next stage in series overvolting the next gap, until all gaps break down. The front and tail resistances are distributed between all stages by using appropriate resistors R_{fr} and R_{tl}. The polarity of the impulse voltage can be changed by changing the polarity of the DC charging unit.

4.5.2 AC test set

In an RLC circuit resonance occurs when the net inductive reactance is cancelled by the net capacitive reactance. Considering the equivalent circuit of a transformer and a purely capacitive load (Figure 4.8) resonance would be possible if:

$$\omega(L_1 + L_2) = \frac{1}{\omega C} \tag{4.11}$$

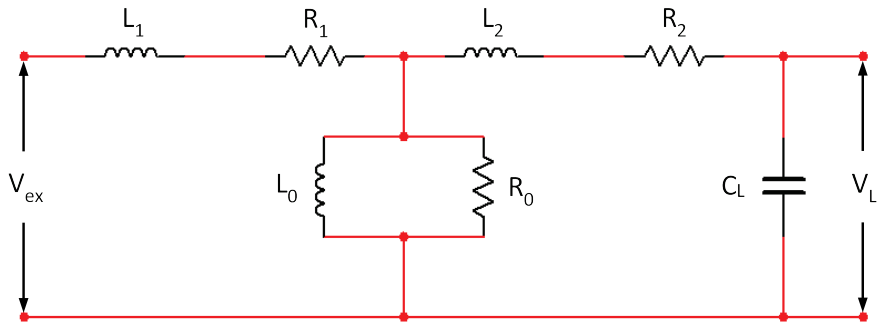

Figure 4.8 - Transformer equivalent circuit and capacitive load

Resonance can be exploited to supply a high voltage at the output of the circuit by providing only a fraction of that voltage at the input. The magnitude of the voltage at resonance across the load would be:

$$V_L = \frac{V_{ex}}{\omega C_L R_T} \tag{4.12}$$

where R_T is the total resistance of the circuit.

Equation (4.12) can be rewritten as:

$$V_L = QV_{ex} \tag{4.13}$$

where Q is the quality factor of the circuit that shows how many times bigger the voltage across the load would be compared to the input voltage. Q would typically range between 10 and 80 depending on the characteristics of the load.

A series resonant circuit is set to oscillate at the power frequency, i.e. 50 Hz, by having a reactor supplied by an excitation transformer. The impedance of the reactor can be varied to match the impedance of the load. After resonance has been reached the circuit is self-sustaining and does not require any additional reactive power. The apparent power becomes equal to the power dissipated by the resistive elements of the circuit. Except from the minimal power requirements, the series resonant circuit offers several other advantages when used for testing purposes:

- The output voltage has a pure sine waveshape since resonance is only possible at the fundamental and all other harmonics are attenuated
- In case of failure of the test object, the voltage collapse detunes the circuit bringing it out of resonance and preventing the development of high-power arcs that might damage the test object
- It is possible to connect multiple reactors in series to create cascade configurations for the generation of higher voltages

For generating high AC voltages above 400 kV for testing purposes the use of a single transformer/reactor becomes impractical and costly not only because of the weight of the unit which creates issues with transportation and erection but also because of the increased requirements for its insulation. As a result, the majority of AC test sets in large testing laboratories are cascaded transformers/reactors. Using a cascade arrangement the weight of the unit can be subdivided into a number of smaller units, usually between two and four, which can be transported and installed easier [59, 90].

The HV laboratory of the University of Manchester has a two stage cascade AC test set which operates on the series resonant principle (Figure 4.9). The first stage can produce 470 kV (V_1) while the second stage can produce 330 kV (V_2). The first reactor is fed by the LV supply through a moving coil voltage regulator that allows the variation of the input voltage. The second reactor is connected in series with the first to give a total output voltage of:

$$V_1 + V_2 = 800\ kV \tag{4.14}$$

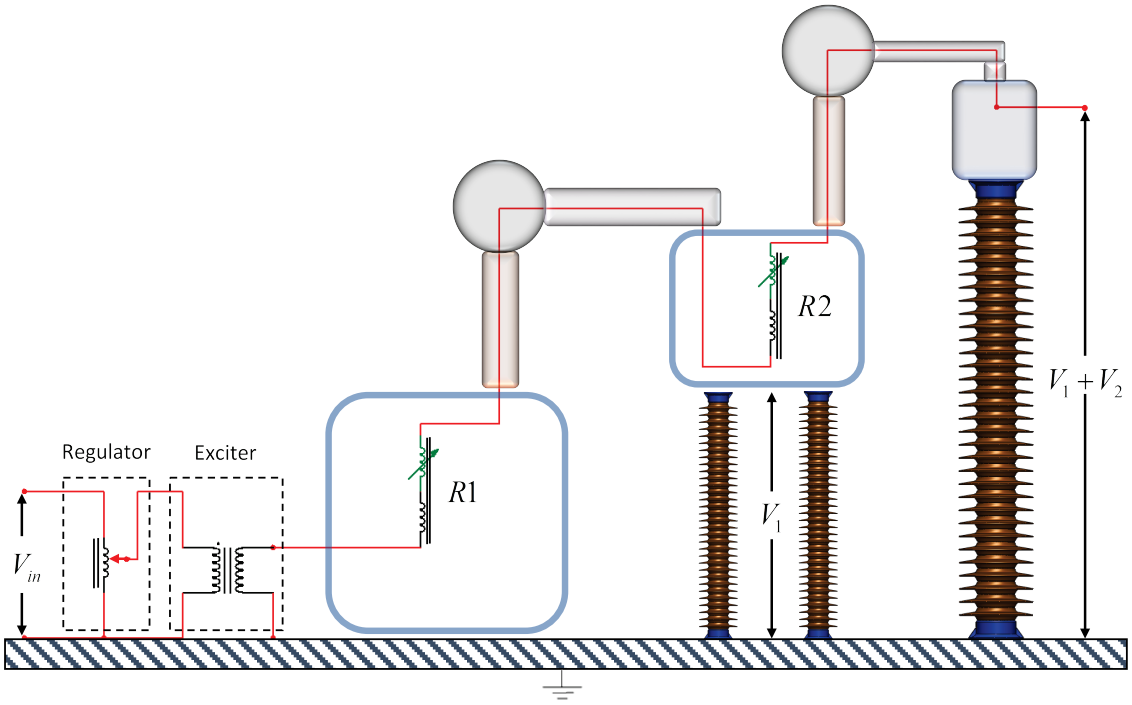

Figure 4.9 - Two-stage cascade resonant AC test set

4.5.3 Spray system

One of the biggest challenges with testing the insulating cross-arm was to perform the tests that involved wetting, specifically the wet power-frequency test and the wet switching impulse withstand voltage test [12]. The absence of international standards for insulating cross-arms and the size of the cross-arm assembly, which is much bigger than traditional insulators, mandated the development of a new spray system suitable for the task. The requirements for this system were determined to be the following:

- Simulate rainfall in the form of droplets (not mist)
- Match the precipitation conditions currently used for testing OHL insulators
- Spray all four cross-arm members uniformly along their entire length
- Allow for adequate clearance between the energised end of the assembly and the spray nozzles (minimum 2.6m) to avoid flashover to the spray system itself
- Be demountable; due to its size it would be impractical to be permanently installed in the laboratory
- Be able to be used with existing laboratory equipment and water supply

To comply with all the above, the spray system was built using the following components:

- Four 4 m long 1”-ID ABS water pipes, one for each insulator of the assembly (Figure 4.11)
- Sixteen spray nozzles (Figure 4.10 (a)), four per pipe, with the following specifications:
    - Pattern: 30^{o} solid cone (Figure 4.10 (b))
    - Flow rate: 2.7 L/min @ 3 bar
    - Droplet size: 400 μm (SMD)
- Two 3m x 1.5m rectangular FRP frames which support two water pipes each (Figure 4.11)
- One octagonal metallic frame with an inscribed circle diameter of 5 m from which the FRP frames are suspended. The octagonal frame can be suspended from the crane of the laboratory and then raised to the appropriate height.
- Approximately 30 m of 19 mm-ID water hose

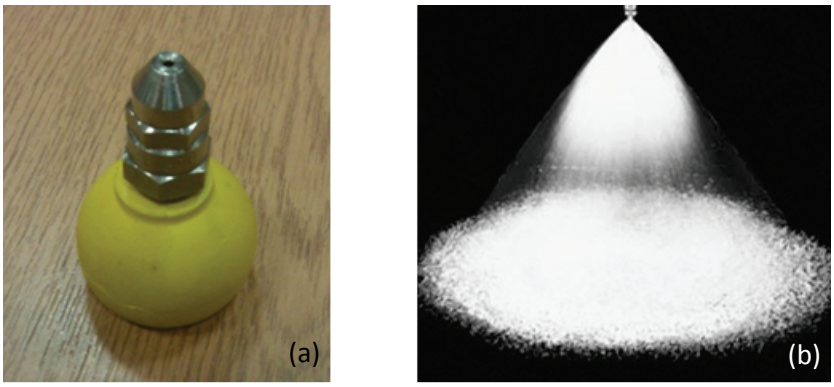

Figure 4.10 - Nozzle attached to ball joint (a) and solid cone spray pattern (b)

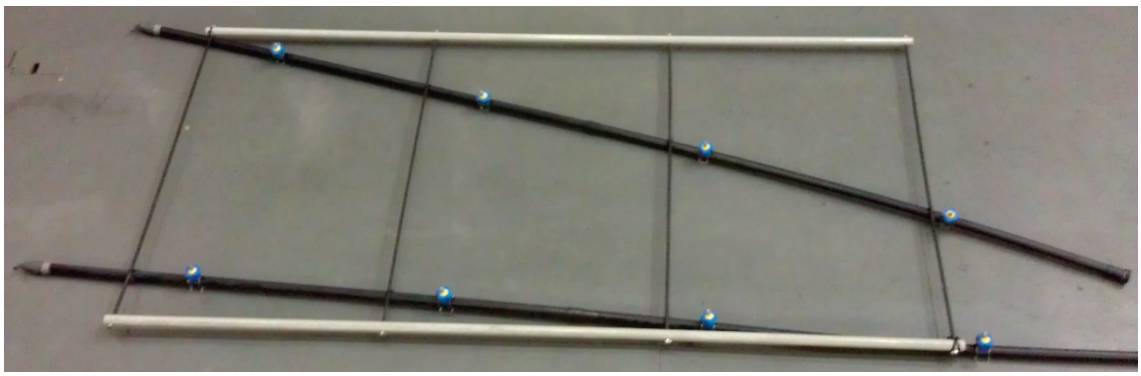

Figure 4.11 - GRP frame supporting two ABS water pipes

The droplet size of the nozzles was chosen specifically to simulate moderate rainfall. After the nozzles are installed on the water pipes, their position is adjusted to provide a small overlap of their spray pattern (Figure 4.12). This is to ensure the uniform wetting of the insulators since the water spray intensity deteriorates slightly when moving away

from the centre of the cone. The 30° spray angle and the flow rate were selected so that the water jet does not break up prematurely due to the fact that the nozzles are at least three meters away from the insulators to minimise the risk of flashover to the spray system.

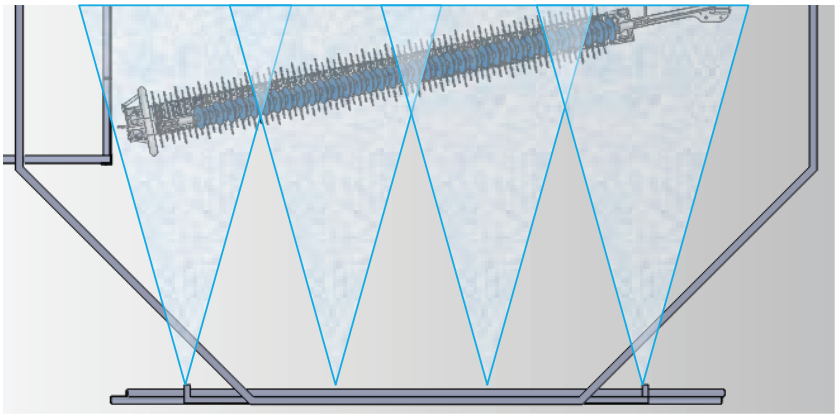

Figure 4.12 - Overlapping spray pattern

The precipitation rate of the spray system was measured using the collection vessel of Figure 4.13. The vessel has two square-shaped openings, one on the top and one to the side, to collect water in the vertical and horizontal directions respectively. Each opening converges to a small pipe that leads to a bottle used to measure the volume of water collected from each direction. The vessel was placed at three points along the length of each ICA insulator where water was collected and its volume measured. The average precipitation rate produced by the spray system is shown in Table 4.2.

***Table 4.2** - Spray system precipitation rate*

	Vertical component	**Horizontal component**
Collection area (mm^2)	25000	25000
H_2O volume (ml/min)	38	13
Precipitation rate (mm/min)	1.52	0.52

Figure 4.13 - Water collection vessel

When the spray system assembly was raised using the crane it was positioned in such a way that the nozzles would spray the insulating cross-arm members from above at an angle of approximately 30°. The crane was isolated from the metallic frame using a 400 kV tension insulator while the frame itself was not grounded to avoid flashovers to it. Figure 4.14 shows a rendering of the test setup including the tower, the cross-arm assembly and the spray system while Figure 4.15 shows the actual arrangement in the HV laboratory.

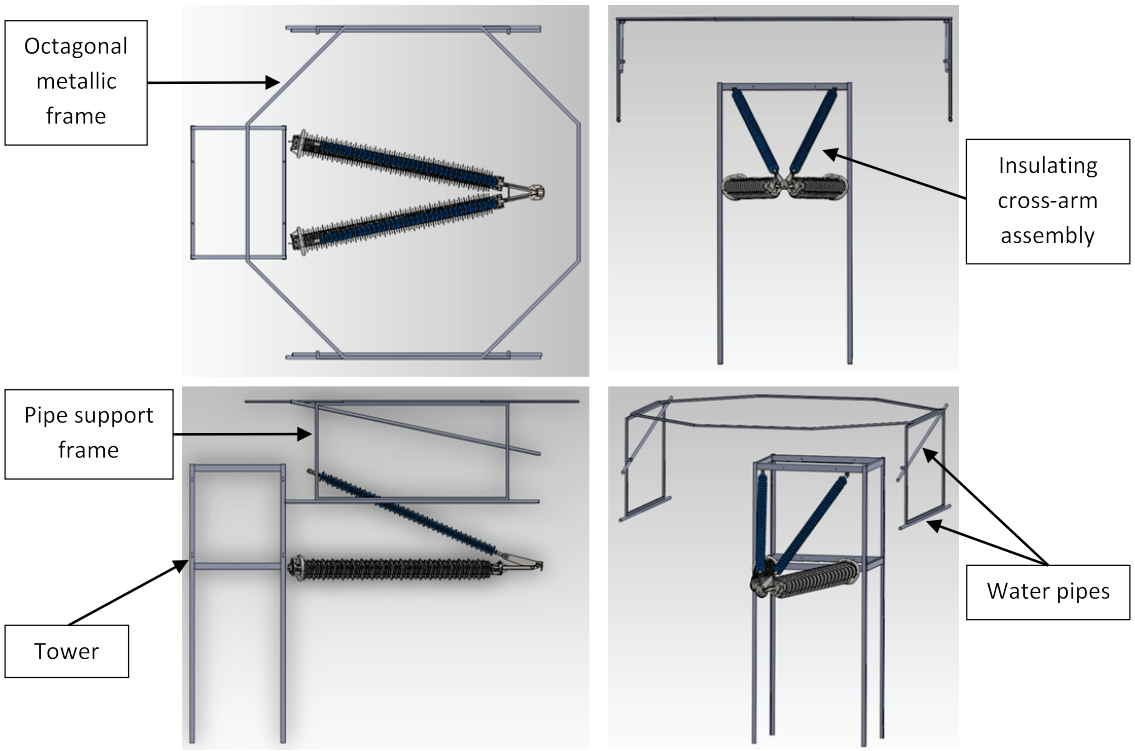

Figure 4.14 - Rendering of test setup including the spray system

Figure 4.15 - ICA and spray system in the HV laboratory

4.6 Testing of the cross-arm assembly at 400 kV

As mentioned in the introduction of this chapter, many of the tests normally performed on composite insulators have been adapted to be performed on the complete cross-arm assembly. Although the tests could have been performed on the individual insulating members, the change in the testing procedure was deemed necessary since most of the tests were originally devised with vertically installed insulators in mind. The change was made to match the in-service arrangement of the insulators and to also test the rest of the cross-arm hardware such as the nose cone and the electric field grading devices.

The following tests, detailed in the subsequent sections, were performed on the 400 kV ICA assembly:

- Wet power frequency voltage test
- Wet switching impulse withstand voltage test
- Dry lightning impulse withstand voltage test
- Corona extinction test

Figure 4.16 shows the arrangement of the equipment in the high voltage laboratory. Depending on the test performed either the AC test set or the impulse generator were connected to the ICA assembly.

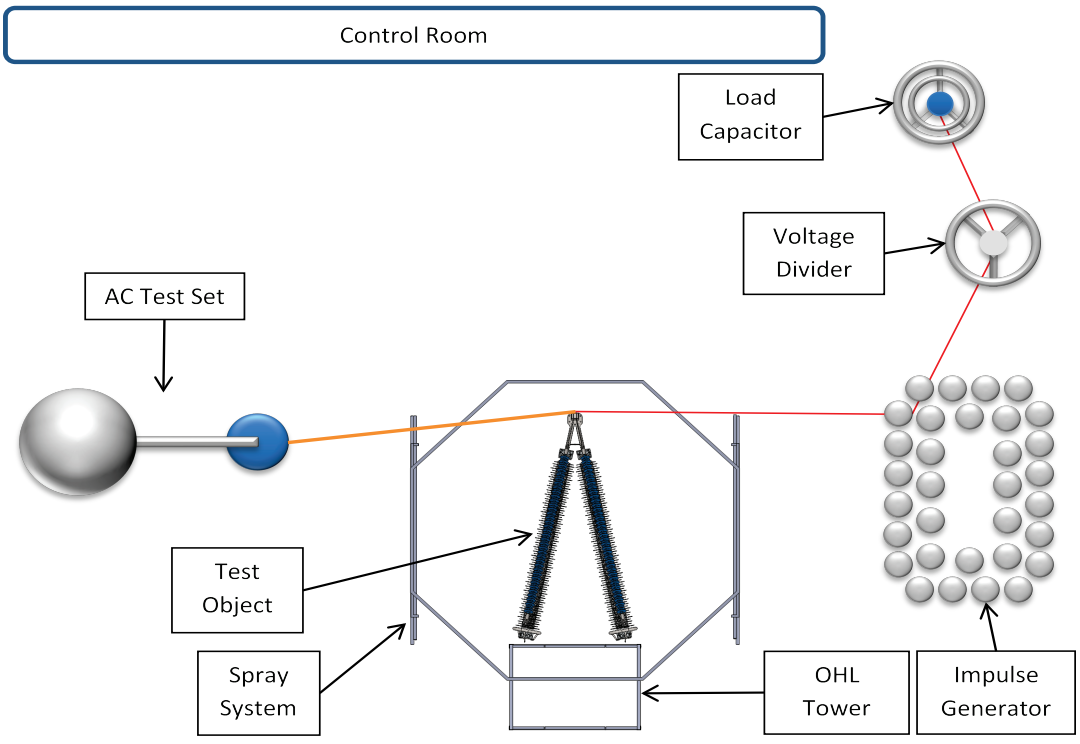

Figure 4.16 - High voltage laboratory floor plan

4.6.1 Wet power frequency voltage test

The power frequency voltage test is performed to assess the capability of the ICA to withstand temporary overvoltages at the supply frequency. To do that, a test voltage higher than the service voltage is applied to the assembly under wet conditions since the ICA is meant to be used outdoors. The phase-to-ground service voltage for the ICA is 231 kV_{rms}. The agreed test voltage was 340 kV_{rms} or 1.47 p.u. This value was chosen in order to be close to the theoretical maximum of 1.5 p.u. for power frequency overvoltages as explained in *Section 4.4*.

4.6.1.1 Procedure

The cross-arm assembly was connected to the AC resonance test set using smooth copper tube terminated with a corona sphere (Figure 4.17). The assembly was sprayed with water in the form of droplets using the spray system of Section 4.5.3 for 15 minutes before energisation. With the spray system running, the voltage was raised slowly but steadily (within 60 s) from 0 V to 255 kV_{rms} (or 75 % of the test voltage) to avoid any transients. From there it was raised rapidly (within 5 s) to the full value of the test voltage, 340 kV_{rms}, where it was maintained for 1 minute. The voltage was then dropped down to 0 V and the procedure was repeated three times.

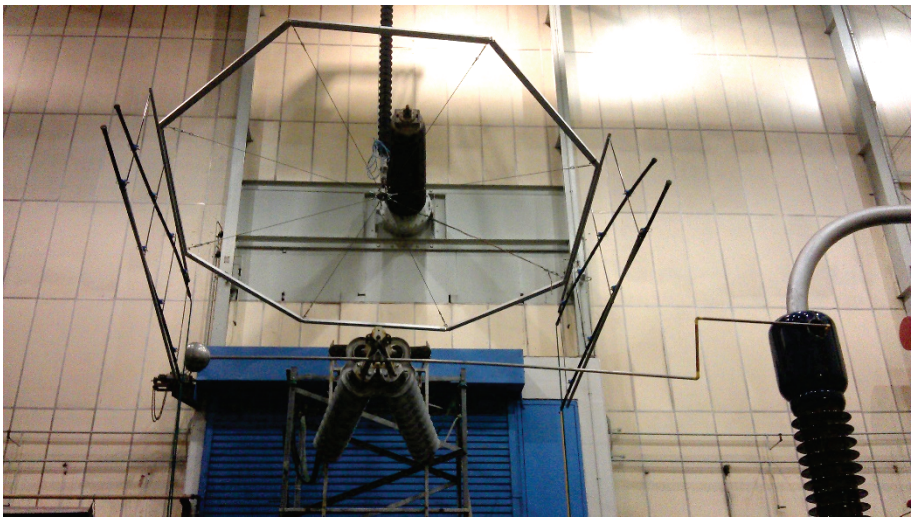

Figure 4.17 - ICA assembly connected to the AC test set

4.6.1.2 Acceptance criteria

If no flashover or puncture is observed on any part of the assembly, the test is considered successful.

4.6.1.3 Results

No flashovers or punctures have been observed.

4.6.2 Wet switching impulse withstand voltage test

The test assesses the capability of the cross-arm to withstand switching surges. It is normally performed with the 'approach' arcing horns installed but it was decided not to use them for the ICA in order to stress the insulators rather than the air gap between the arcing horns. The standards advise to use the worst impulse polarity for the test which in this case is the positive polarity. However, at the time of testing, the clearances between the ICA and its surroundings in the laboratory were not sufficient, resulting in flashover when a positive polarity impulse was applied. For this reason, negative polarity impulses were applied instead.

4.6.2.1 Procedure

The ICA conductor attachment point was connected to the impulse generator using thin insulated wire. The load capacitor was also connected in parallel with the test object. The impulse generator was configured as follows:

Table 4.3 *- Impulse generator configuration for switching impulse*

Efficiency (%)	84
Number of stages connected	10
Tail resistance (per stage)	6.4 kΩ
Front resistance (per stage)*	4.4 kΩ

*The front resistance used on stage one of the generator is different from that used on stage two to ten.

The assembly was sprayed with water in the form of droplets for 15 minutes before energisation. With the spray system running, fifteen 250/2500 (standard switching) impulses of negative polarity at 1050 kV were applied to the assembly. The impulses were recorded using the digital impulse analysing system (DIAS). Figure 4.18 shows one of the impulse waveforms.

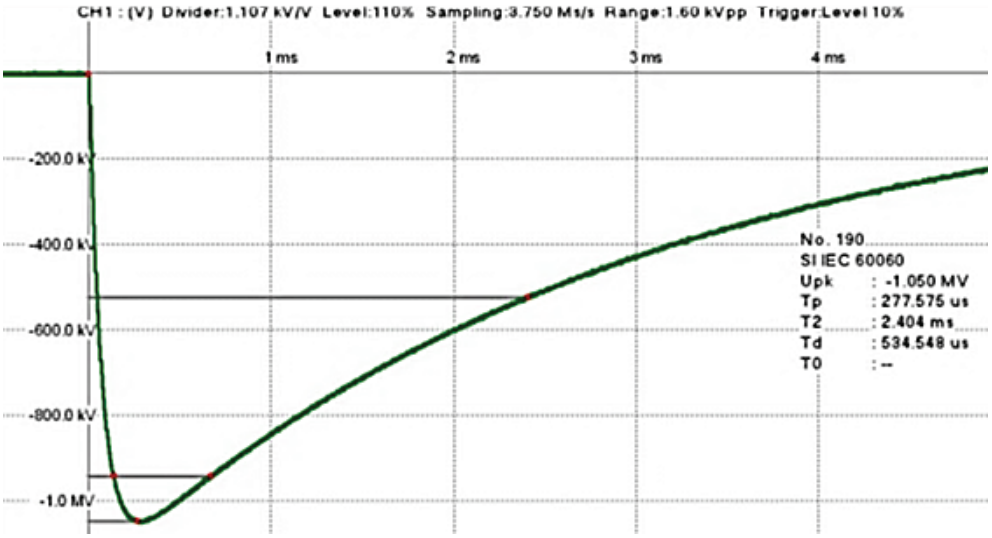

Figure 4.18 - Negative switching impulse waveform captured with the DIAS

4.6.2.2 Acceptance criteria

A maximum of two disruptive discharges (flashovers) are allowed in the self-restoring part of the assembly. The non-self-restoring part of the assembly, i.e. the solid insulation, shall not exhibit any signs of failure.

4.6.2.3 Results

Table 4.4 *- Switching impulse withstand voltage test results*

Impulse No.	Voltage (kV)	Time to peak T_p (µs)	Time to half-value T_2 (µs)	Flashover (yes/no)
1	1047	277	2411	No
2	1051	280	2406	No
3	1052	282	2495	No
4	1030	277	2398	No
5	1050	276	2401	No
6	1049	282	2411	No
7	not recorded			No
8	1049	275	2406	No
9	1048	279	2408	No
10	1050	279	2403	No
11	1048	281	2419	No
12	1050	278	2409	No
13	1050	278	2404	No
14	1050	279	2404	No
15	1051	280	2410	No

The maximum variations of the applied impulse parameters observed compared to the standard values were the following:

- Peak value : - 1.9 %, + 0.2 %
- Time to peak : + 12.8 %
- Time to half-value : - 4.1 %

All values were within the acceptable limits as detailed in *Section 4.3.3*.

4.6.3 Dry lightning impulse withstand voltage test

The test assesses the capability of the cross-arm to withstand lightning surges. As with the switching impulse withstand voltage test, the arcing horns were not used and the impulses applied were of the negative polarity because of the insufficient clearances between the test object and its surroundings.

4.6.3.1 Procedure

The ICA conductor attachment point was connected to the impulse generator using thin insulated wire. The load capacitor was also connected in parallel with the test object. The impulse generator was configured as follows:

Table 4.5 *- Impulse generator configuration for lightning impulse*

Efficiency (%)	93
Number of stages connected	10
Tail resistance (per stage)	92 Ω
Front resistance (per stage)	46 Ω

The impulse voltage level was first corrected to the standard reference atmosphere (Table 4.6) according to equation (4.15):

$$U = U_0 \cdot K_t \tag{4.15}$$

where:

U : applied voltage

U_0 : specified test voltage

K_t : atmospheric correction factor

The atmospheric correction factor K_t is the product of the air density correction factor k_1 and the humidity correction factor k_2.

Table 4.6 *- Lightning impulse withstand voltage test atmospheric conditions and correction factors*

	Standard reference
Pressure (kPa)	101.3
Temperature (°C)	20
Absolute Humidity (g/m³)	11

	Measured
Pressure (kPa)	100.79
Temperature (°C)	20.0
Relative Humidity (%)	58
Absolute Humidity (g/m³)	10.02

Correction factor	
k_1	0.995
k_2	1.000
K_t	**0.995**

Fifteen 1.5/50 (standard lightning) impulses of negative polarity at 1418 kV (corrected from 1425 kV) were applied to the assembly. Every impulse was recorded using the digital impulse analysing system (DIAS). Figure 4.19 shows one of the impulse waveforms.

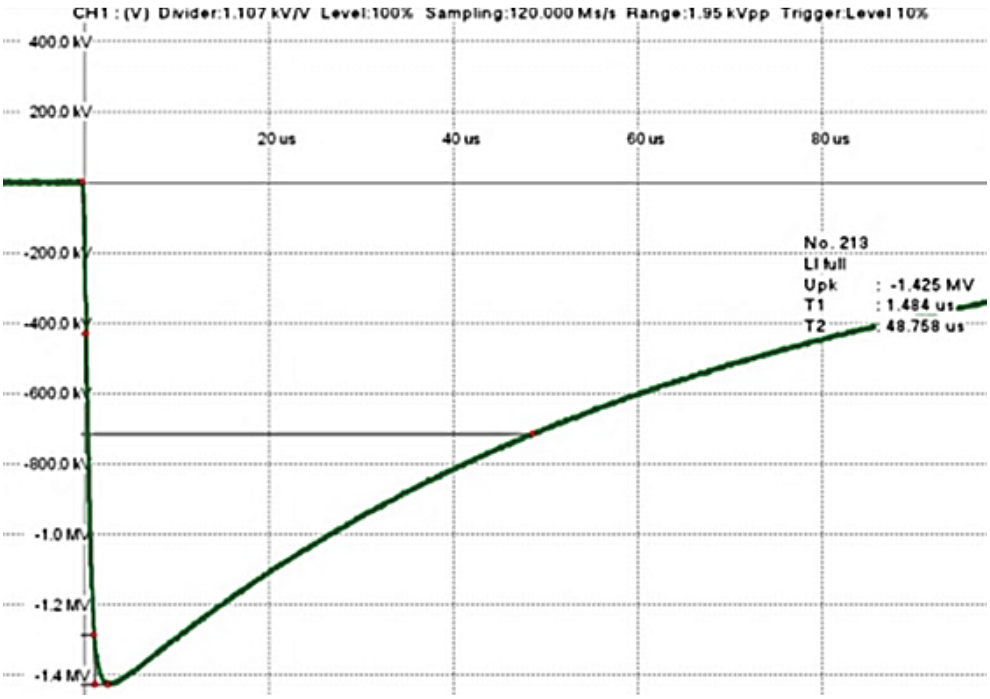

Figure 4.19 - Negative lightning impulse waveform captured with the DIAS

4.6.3.2 Acceptance criteria

A maximum of two disruptive discharges (flashovers) are allowed in the self-restoring part of the assembly. The non-self-restoring part of the assembly, i.e. the solid insulation, shall not exhibit any signs of failure in order for the test to be considered successful.

4.6.3.3 Results

Table 4.7 *- Lightning impulse withstand voltage test results*

Impulse No.	Voltage (kV)	Front time T_1 (µs)	Time to half-value T_2 (µs)	Flashover (yes/no)
1	1425	1.508	51.143	No
2	1421	1.498	48.814	No
3	1421	1.479	49.120	No
4	1420	1.470	48.999	No
5	1425	1.480	48.758	No
6	1421	1.472	49.081	No
7	1421	1.460	49.111	No
8	1421	1.459	49.040	No
9	1421	1.471	49.037	No
10	1423	1.484	40.008	No
11	1421	1.479	49.104	No
12	1421	1.479	49.157	No
13	1421	1.475	49.113	No
14	1421	1.469	40.017	No
15	1421	1.474	49.155	No

The maximum variations of the applied impulse parameters observed compared to the standard values were the following:

- Peak value : + 0.5 %
- Front time : - 2.7 %, + 0.5 %
- Time to half-value : - 20.0 %, + 2.3 %

All values were within the acceptable limits as detailed in *Section 4.2.4*.

4.6.4 Corona extinction test

The corona extinction test is used to establish the voltage at which corona discharges are no longer visible on an insulator and its fittings. For the ICA the test was adapted from the Technical Specifications of National Grid, specifically the TS 3.4.17 [57]. The maximum allowable corona extinction voltages for transmission line insulators, and consequently for the ICA, are shown in Table 4.8.

Table 4.8 *- Corona extinction test levels [57]*

Operating voltage (kV)	132	275	400
Corona extinction voltage (kV)	110	240	340

4.6.4.1 Procedure

The cross-arm assembly was connected to the High Voltage AC resonance test set using smooth copper tube terminated with a corona sphere. The room was darkened completely and the observer was allowed 15 minutes to get accustomed with the low light conditions. The applied voltage was increased until corona was observed. It was then reduced slowly until no more discharges were visible. The procedure was repeated three times. The measured values were corrected to the standard reference atmosphere using equation (4.15).

4.6.4.2 Acceptance criteria

The corona extinction voltage measured must exceed 340 kV_{rms}.

4.6.4.3 Results

4.6.4.3.1 'Butterfly' grading device

A prototype of the 'butterfly' grading device detailed in *Section 3.9.4.2.3* was manufactured and attached to the 400 kV ICA assembly. Table 4.9 shows the atmospheric conditions and correction factors while Table 4.10 shows the results of the test.

Table 4.9 *- Corona extinction test atmospheric conditions and correction factors – 'Butterfly' GD*

	Measured
Pressure (kPa)	101.93
Temperature (°C)	20.1
Relative Humidity (%)	56
Absolute Humidity (g/m³)	9.73

Correction factor	
k_1	1.001
k_2	0.997
K_t	**0.998**

Table 4.10 *- Corona extinction test results with 'butterfly' grading device*

	Corona extinction voltage (kV)	
	Observed	**Corrected**
1	165.0	165.3
2	178.0	178.4
3	177.0	177.4
Average	173.0	**173.7**

After the voltage exceeded 200 kV, corona discharges were visible at the conductor attachment point of the nose cone and on the outer rim of the HV 'butterfly' grading device. Figure 4.20 shows a photograph of the cross-arm assembly captured with the UV camera. Corona discharges can be seen in green and black, with black being more intense. These observations coincide with the results of the FEA analysis in *Section 3.9.4.2.3*.

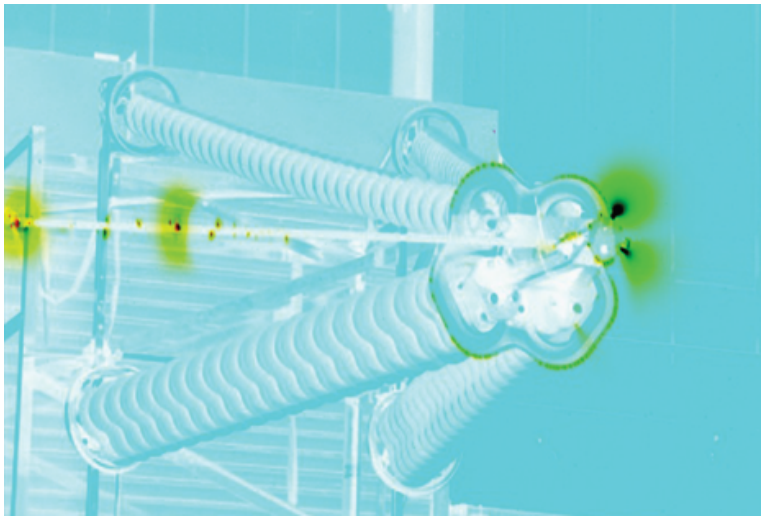

Figure 4.20 - Corona discharge from cross-arm assembly fitted with 'butterfly' grading device

The average corona extinction voltage was 173.7 kV which is almost two times less than the 340 kV limit required to pass the test for the 400 kV ICA. On the other hand, the corona extinction voltage is 58 % higher than the 110 kV requirement for the 132 kV ICA. Consequently, while the 'butterfly' grading device cannot be used at 400 kV, it is more than adequate to operate at 132 kV.

4.6.4.3.2 'M-W' grading device

A prototype of the 'M-W' grading device, described in *Section 3.9.4.2.6*, was also manufactured and installed on the nose cone of the ICA. To save time, the complete ICA assembly was not used in this occasion. Instead, the test was performed with the nose cone and grading device hanging from the crane of the HV laboratory, positioned at the appropriate distance away from the tower (Figure 4.21).

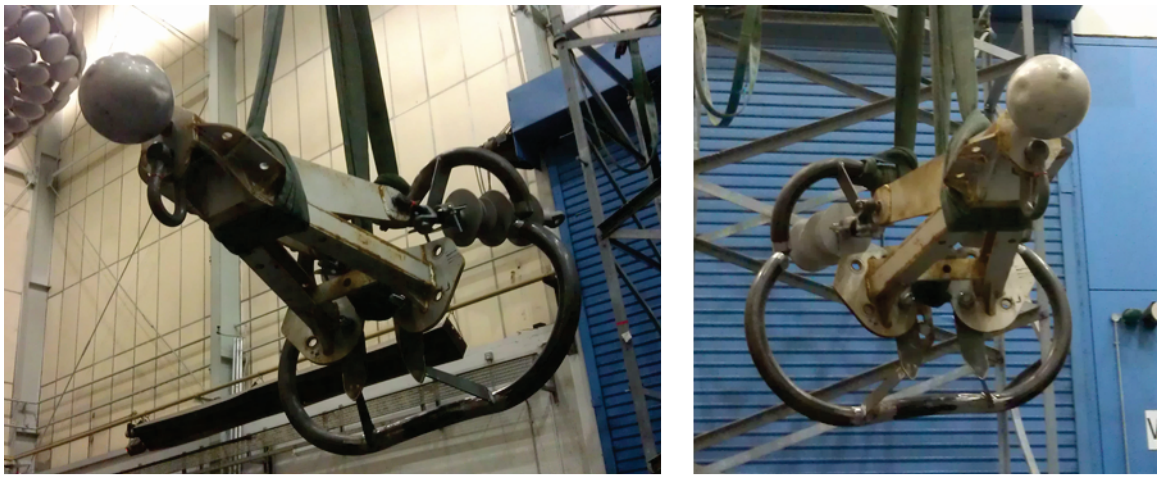

Figure 4.21 - ICA nose cone and prototype 'M-W' grading device

Table 4.11 shows the atmospheric conditions and correction factors while Table 4.12 shows the results of the test.

***Table 4.11** - Corona extinction test atmospheric conditions and correction factors – 'M-W' GD*

	Measured
Pressure (kPa)	99.99
Temperature (°C)	18.1
Relative Humidity (%)	42
Absolute Humidity (g/m^3)	6.60

Correction factor	
k_1	0.998
k_2	0.988
K_t	**0.987**

Table 4.12 *- Corona extinction test results with 'M-W' grading device*

	Corona extinction voltage (kV)	
	Observed	**Corrected**
1	245.0	248.2
2	242.0	245.2
3	249.0	252.3
Average	245.3	**248.6**

Raising the voltage above 250 kV resulted in corona discharges from the copper pipe supplying the voltage and the conductor shoe. Raising the voltage even higher to reach the required test level of 340 kV made it impossible to distinguish which parts of the test assembly were producing corona because of the high intensity of the discharges. The average corona extinction voltage was 248.6 kV. Although clearly better than the 'butterfly' grading device test, the results were inconclusive regarding whether or not the 'M-W' grading device can be used at 400 kV.

The problems with the test can be attributed to two factors: a) the small cross-section of the copper tube acting as the conductor and b) the use of a single conductor instead of a conductor bundle which is the norm for 400 kV lines. Future iterations of the test must address the aforementioned factors before testing can be completed successfully.

4.7 Testing of the compression insulator

Several of the tests described in the international standards that were not adapted to be performed on the ICA assembly were performed on the novel compression insulator. The testing procedures remained mostly unchanged except in the occasions where equipment was not available or scheduling the test was difficult.

4.7.1 Test on interfaces and connections of end-fittings

The test on interfaces and connections of end-fittings is regarded as one of the most onerous test that an insulator must pass in order to be qualified for service. As the name suggests, it aims to examine two factors: a) the interfaces, i.e. the bonding of the sheds to the sheath, and b) the quality of the attachment of the end-fittings to the insulator. The former should be a non-issue for the compression insulator of the ICA because the sheath and sheds are moulded together so there is no discernible interface between

them, unlike older insulator designs. Hence the focus of the test was on the end-fittings particularly due to their unique shape and method of attachment to the insulator. The test consists of the following combination of mechanical and electrical sub-tests that have to be performed in sequence:

a) Reference dry power frequency voltage test
b) Sudden load release test
c) Thermal-mechanical test
d) Water immersion test
e) Steep-front impulse voltage test
f) Dry power frequency voltage test

Table 4.13 *- Compression insulator specimen*

Description			**Diagram**
Insulator type		ASCM-##	
Drawing No. (*Appendix*)		ASCM-01	
Colour		Grey	
Dimensions			
Total length		660 mm	
Housing length		400 mm	
Core diameter (equivalent)		89.5 mm	
Shed width (max)	Large	384.8 mm	
	Medium	354.8 mm	
	Small	320.0 mm	
Components			
Core		Epoxy & glass fibre, acid resistant	
Sheds		Silicone rubber	
Fittings		Galvanized cast aluminium	

Figure 4.22 - ASCM insulator

For the ICA compression insulator the sudden load release test and the thermal-mechanical test were not performed. These sub-tests required simultaneous mechanical load application and temperature cycling ranging from -35 ^{o}C ± 5 ^{o}C to +50 ^{o}C ± 5 ^{o}C. There was no equipment available to conduct these tests. The remaining sub-tests were

performed using three identical short insulator specimens the specifications of which are shown in Table 4.13.

4.7.1.1 Reference dry power frequency voltage test

The reference dry power frequency voltage test is used to establish the reference flashover voltage of the three insulator specimens. The reference value is to be compared with the flashover voltage measured in the last sub-test of the test on interfaces and connections of end-fittings.

4.7.1.1.1 Procedure

The voltage applied on the insulator specimen was increased linearly from 0 V to flashover within one minute. The test was performed five times for each of the three specimens and the flashover voltage was recorded. For each specimen, the flashover voltage was calculated as the average of the five obtained values and then corrected to the standard reference atmospheric conditions (Table 4.14).

Table 4.14 *- Reference dry power frequency voltage test atmospheric conditions and correction factors*

	Measured
Pressure (kPa)	100.79
Temperature (°C)	20.5
Relative humidity (%)	58
Absolute humidity (g/m^3)	10.31

Correction factor	
k_1	0.998
k_2	0.998
K_t	**0.997**

4.7.1.1.2 Results

Table 4.15 *- Reference dry power frequency voltage test*

	Flashover voltage (kV)		
No.	**ASCM-01**	**ASCM-03**	**ASCM-04**
1	209.4	221.0	213.3
2	203.0	219.7	208.9
3	212.0	221.3	217.9
4	213.6	221.5	214.3
5	216.6	220.3	209.7
Average	210.9	220.8	212.8
Corrected average	**211.5**	**221.4**	**213.4**

4.7.1.2 Water immersion test

4.7.1.2.1 Procedure

The specimens were immersed in a warm bath containing an aqueous solution of $NaCl$ with a conductivity of 1750 µS/cm ± 80 µS/cm. According to IEC 62217 [89], the test period is 42 hours. The temperature was maintained at 99 °C, i.e. the solution was not allowed to boil, to avoid the use of a vessel with a condensation pipe that would be required to sustain the volume of the solution (Figure 4.23). Such a vessel was not available at the time and sourcing one that could accommodate the insulator specimens would induce delays in the type testing schedule which was bound by a deadline. The temperature was recorded at 1 minute intervals over the test period. The specimens were allowed to cool before the subsequent test begun. The maximum permissible period between the completion of this sub-test and the start of the next is 48 hours.

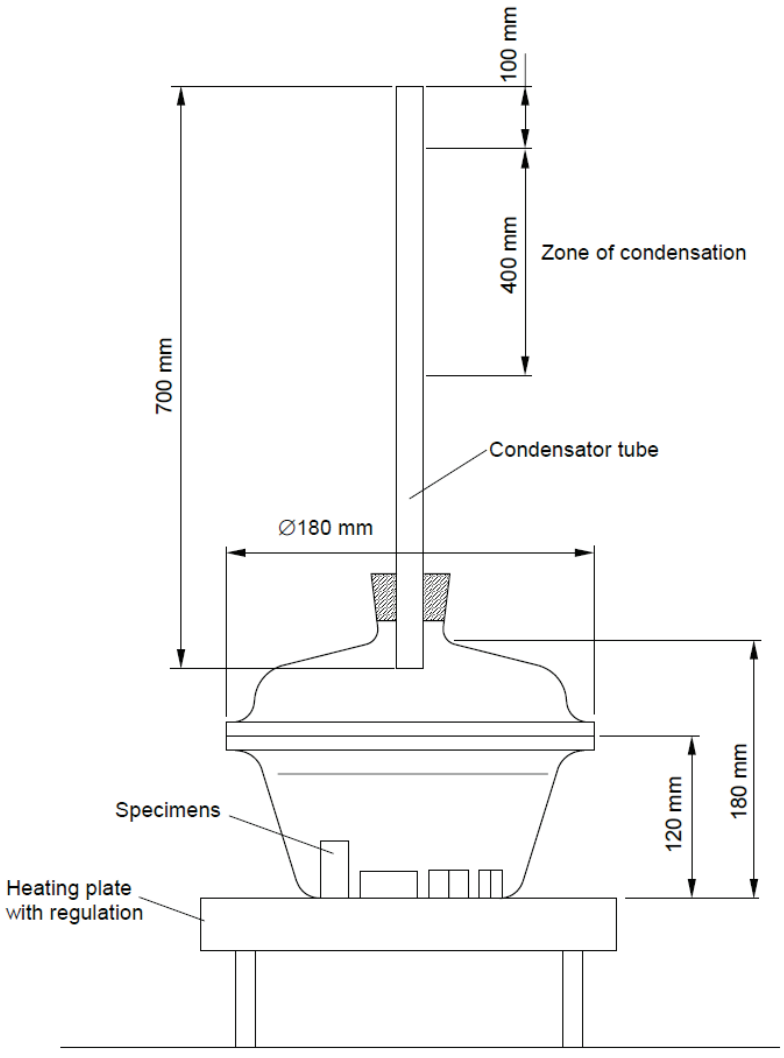

Figure 4.23 - Example of boiling vessel with condensation tube [89]

4.7.1.2.2 Results

Visual inspection of the specimens revealed no cracks. There was however a white, powdery residue deposited on the surface of the insulator specimen (Figure 4.24).

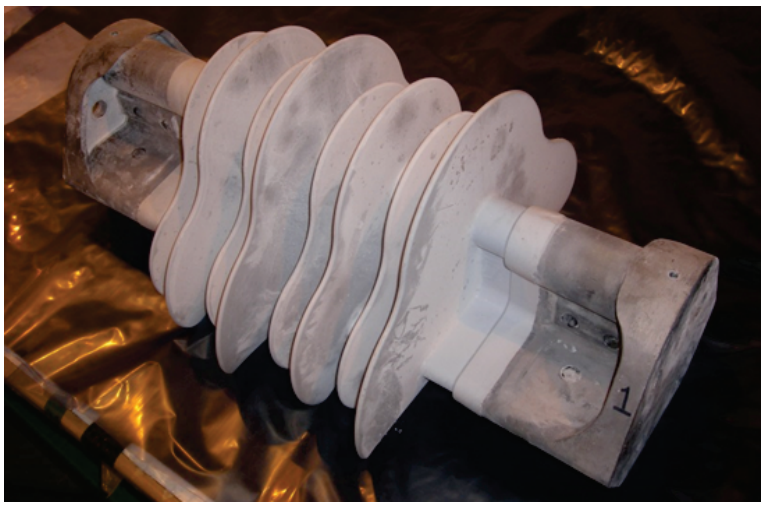

Figure 4.24 - White residue on insulator specimen after water immersion test

4.7.1.3 Steep-front impulse voltage test

4.7.1.3.1 Procedure

The insulator housing of each specimen was fitted with sharp-edged electrodes between the sheds in such a way that the distance between two adjacent electrodes was 500 mm or less. Each section formed by two neighbouring electrodes was stressed with 25 positive polarity impulses and 25 negative polarity impulses with voltage steepness of 1000 kV/µs, making sure that the gap between electrodes flashed over.

4.7.1.3.2 Acceptance criteria

The test is considered successful if only external flashover between electrodes occurs and no puncture is observed.

4.7.1.3.3 Results

Figure 4.25 shows one of the positive polarity steep-front impulse waveforms as recorded by the DIAS. For all three specimens no punctures were observed.

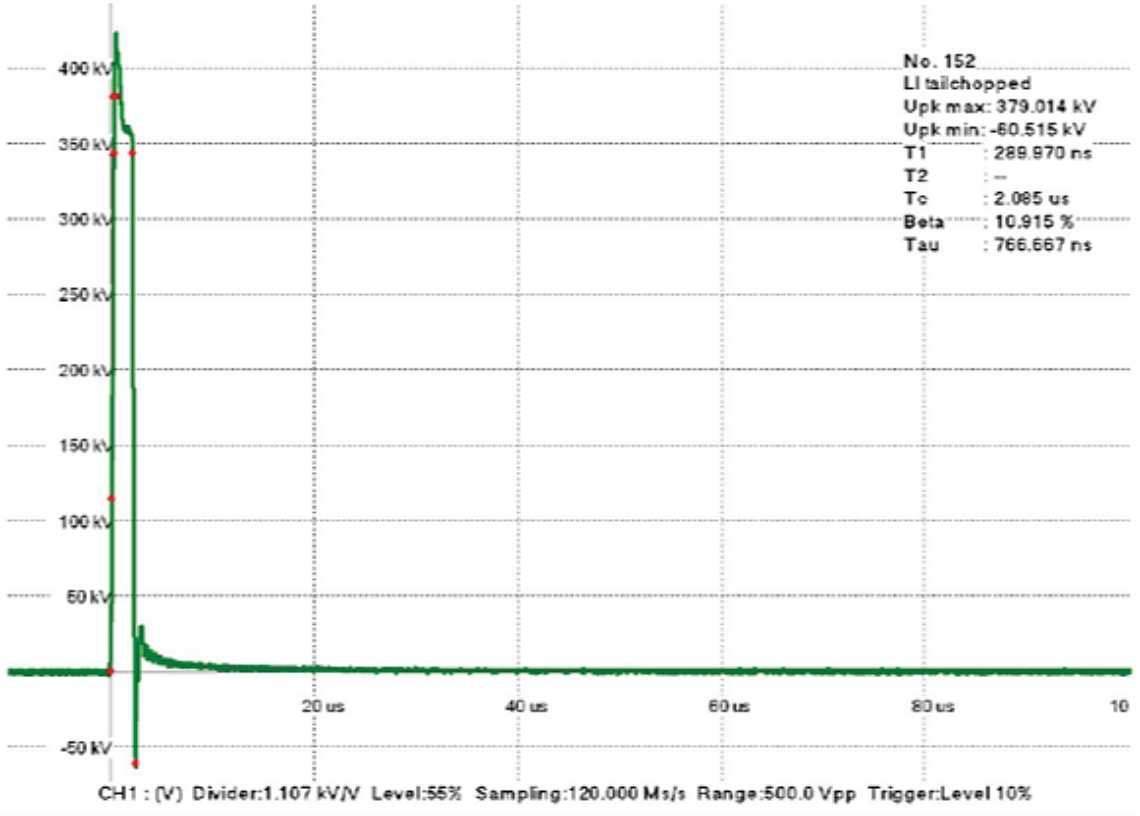

Figure 4.25 - Steep-front impulse waveform

4.7.1.4 Dry power frequency voltage test

4.7.1.4.1 Procedure

The flashover voltage for each specimen was re-evaluated using the same procedure as for the reference power frequency test. Afterwards all specimens were subjected to 80% of their originally determined flashover voltage for 30 minutes. Following the removal of the test voltage the temperature of each specimen's housing was measured. Measurements were performed at three places on each insulator in the space between sheds.

Table 4.16 *- Dry power frequency voltage test atmospheric conditions and correction factors*

	Measured
Pressure (kPa)	95.46
Temperature (°C)	15.1
Relative humidity (%)	38
Absolute humidity (g/m³)	4.90

Correction factor	
k_1	0.989
k_2	0.982
K_t	**0.971**

4.7.1.4.2 Acceptance criteria

The test is considered successful if the average flashover value for each specimen is not below 90% of the reference value. No flashover is allowed during the 30 minutes under the 80% reference flashover voltage. Additionally punctures shall not be observed and the average temperature rise on the insulator housing shall not rise above 20^{o}K from the reference temperature determined prior to testing.

4.7.1.4.3 Results

Table 4.17 *- Flashover voltage results*

	Flashover voltage (kV)		
No.	**ASCM-01**	**ASCM-03**	**ASCM-04**
1	194.7	203.5	193.5
2	195.0	204.5	191.7
3	196.0	201.2	189.6
4	195.5	205.1	189.6
5	195.0	204.0	190.4
Average	195.2	203.7	191.0
Corrected average	201.1	209.7	196.7

Table 4.18 *- Flashover voltage comparison*

	Average Flashover Voltage (kV)		
Specimen	**Before**	**After**	**Difference (%)**
ASCM-01	211.5	201.1	95.1
ASCM-03	221.4	209.7	94.7
ASCM-04	213.4	196.7	92.2

Table 4.19 *- Application of 80 % of reference flashover voltage*

	80 % of reference flashover voltage (kV)		
	ASCM-01	**ASCM-03**	**ASCM-04**
Average	169.2	177.1	170.7
Corrected average	164.3	172.0	165.7
Flashover (Yes/No)	**No**	**No**	**No**

Table 4.20 *- Temperature comparison*

	Average specimen temperature (°C)		
Specimen	**Before**	**After**	**Difference (°C)**
ASCM-01	13.2	13.9	+0.7
ASCM-03	14.3	14.1	-0.2
ASCM-04	13.8	13.4	-0.4

The average flashover voltage for all specimens remained above 90 % of the reference. The specimens also withstood successfully the 80 % of reference flashover voltage for 30 minutes and the temperature rise following the test was negligible.

4.7.2 Dye penetration test

As detailed in *Section 2.3.1*, the exposure of the rod to water contaminated with salt in the presence of electric field can lead to the formation of acids which attack the glass fibres, making them weaker. This phenomenon is progressive and depends upon the degree of exposure of the rod, the strength of the electric field, the mechanical load on the insulator and the environmental conditions. Exposure can result from erosion of the sheath due to discharge activity on the surface of the insulator, puncture of the sheath or from poor bonding between the sheath and the end fittings. It has been observed that under such conditions it is possible for a brittle fracture to occur in a matter of weeks.

Hence, the mechanical longevity of a composite insulator is dependent on the strength and quality of the core. A key factor determining the quality of the core material is porosity or in other words the percentage of voids present within the core. As it is very difficult, expensive and time consuming to look inside the material since it requires advanced imaging techniques, the dye penetration and water diffusion tests, specified in the IEC 61109 [19], are used to check the porosity of the core material.

The dye penetration test was performed on samples from two different batches of the pultruded core material of the compression member each from a different manufacturer in February 2012 and June 2013.

4.7.2.1 Procedure

A layer of steel balls of 2 mm diameter was placed in a glass container. Insulator core specimens with a length of 10 mm ± 5 mm cut using a diamond-coated circular saw blade were positioned with their fibres vertical on the balls. The container was filled with a dye consisting of 1% alcohol solution of fuchsin (a magenta dye with chemical formula $C_{19}H_{17}N_3 \cdot HCl$) up to approximately 2 mm above the level of the balls. A measurement was taken of the time required for the dye to rise through the core of the specimens by capillarity. A diagram of the test setup can be seen in Figure 4.26.

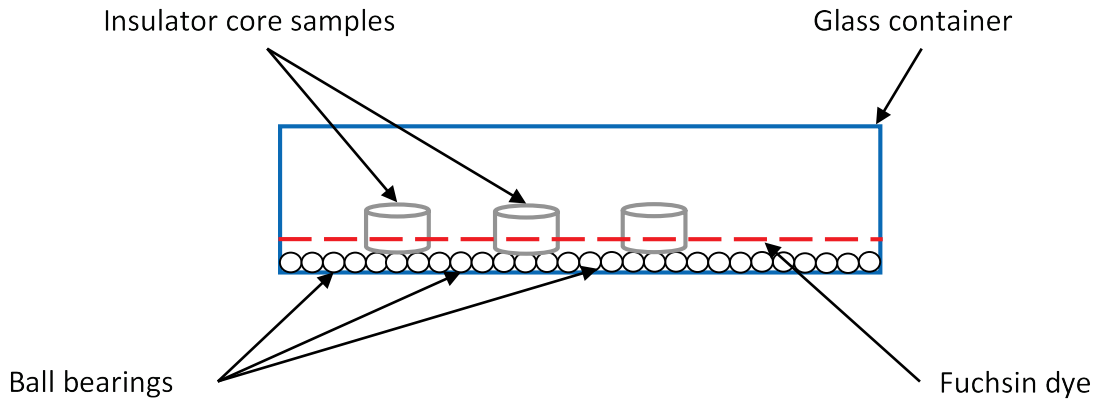

Figure 4.26 - Dye penetration test diagram

4.7.2.2 Acceptance criteria

The test is considered successful if the time required for the dye to rise through the core of the specimens by capillary action, as detected by the naked eye, is more than 15 minutes.

4.7.2.3 Results

Figure 4.27 shows a compression insulator core sample from the first batch placed in the fuchsin dye. From the first 10 seconds the dye had already risen through the core, indicated by the red spots on the top side of the sample. By testing multiple samples from the same batch it was made clear that the material did meet the specifications required to pass the test. Also it was observed that the dye did not rise uniformly or at the same locations for different samples indicating inconsistencies in the density of the material.

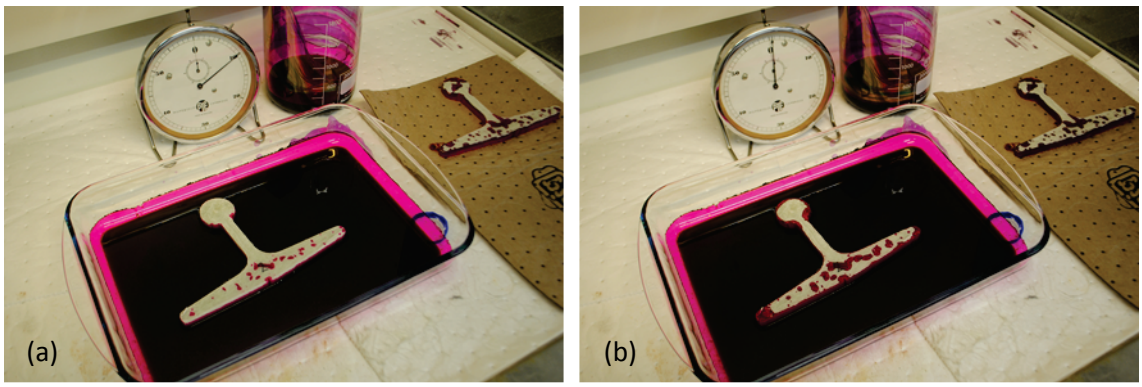

Figure 4.27 - First batch core sample at 10 seconds (a) and 120 seconds (b)

Figure 4.28 shows core samples from the second batch of core material. After 15 minutes there were no dye stains on the top side of the samples indicating that the dye did not rise through the bulk of the material. A cross-cut through the sample confirmed the result since it did not show full penetration of the dye inside the core material. Therefore, the FRP of the second batch was deemed of appropriate quality to be used for the manufacture of the compression insulators.

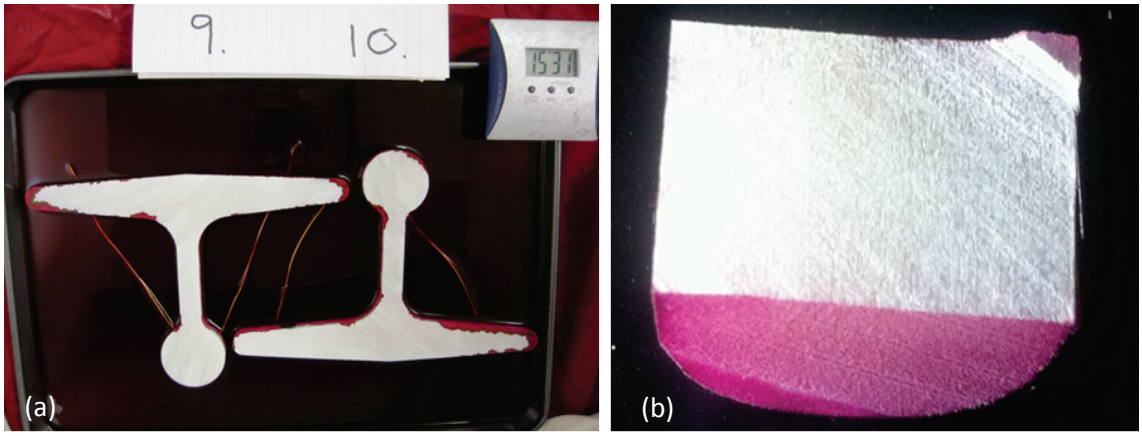

Figure 4.28 - Second batch core samples (a) and sample cross-cut (b) after 15 minutes

4.7.3 Water diffusion test

The water diffusion test is used in conjunction to the dye penetration test to assert the quality of the core material. Additionally, it is used to test the quality of the bonding between the silicone rubber sheath and the core of the insulator.

4.7.3.1 Procedure

Three samples with a length of 30 mm ± 5 mm were cut using a diamond-coated circular saw blade at a 90° angle from an insulator taken from the production line. After cleaning the specimens with isopropyl-alcohol and filter-paper they were boiled in a glass vessel containing deionised water with 0.1% by weight of $NaCl$ for 100 h ± 0.5 h. Then the

specimens were transferred to another glass vessel containing tap water at room temperature for a minimum of 15 minutes. Within 3 hours following the boiling and using the apparatus of Figure 4.30 the specimens, after being dried with filter paper, were subjected to a voltage test by raising the voltage at rate of approximately 1 kV/s. When the voltage reached 12 kV it was kept there for 1 minute before being decreased. The leakage current was measured throughout the test.

4.7.3.2 Testing apparatus

Figure 4.29 shows a diagram of the equipment used for performin the test. The electrode arrangement is energised by an HV AC transformer through a high value, current limiting resistor. The leakage current is measured in the form of voltage across a resistor connected between the LV electrode and ground. Figure 4.30 shows the test specimen and the equipment in the laboratory.

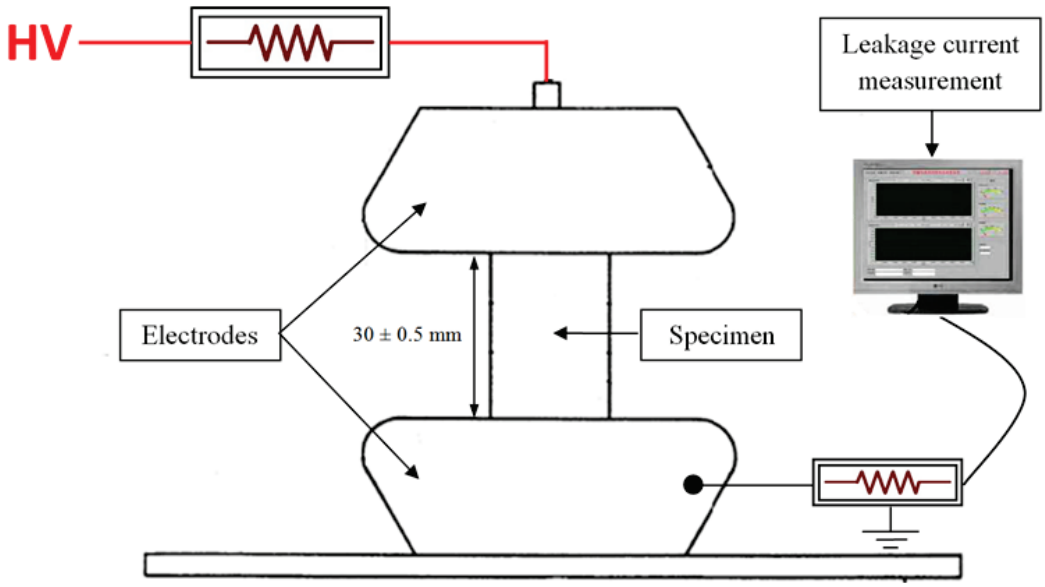

Figure 4.29 - Water diffusion test diagram

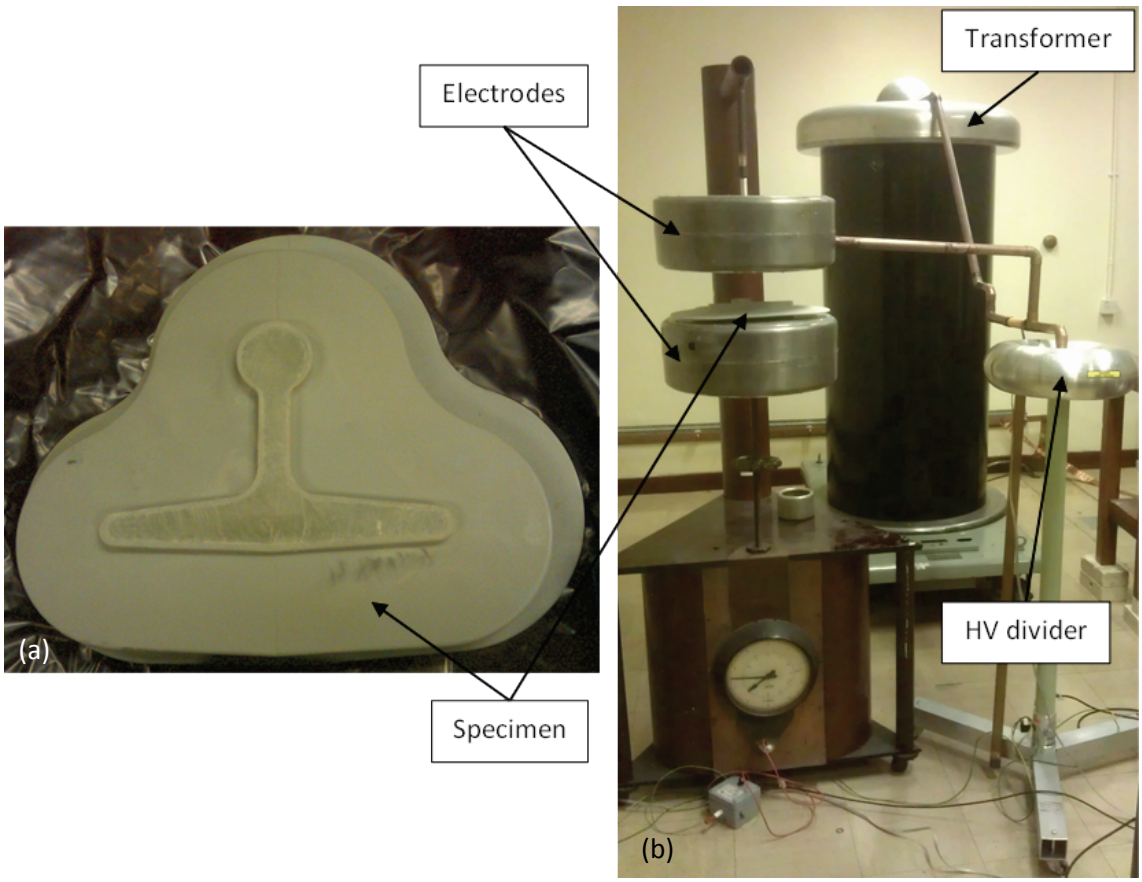

Figure 4.30 - Water diffusion test specimen (a) and testing apparatus (b)

4.7.3.3 Acceptance criteria

The test is considered successful if the following conditions are met:

- No puncture occurs
- No surface flashover is observed
- The current does not exceed 1 mA_{rms} for the whole duration of the test

4.7.3.4 Results

Table 4.21 *- Water diffusion test results*

Specimen	Leakage current (mA_{rms})	Flashover (Yes / No)
A	0.196	No
B	0.193	No
C	0.197	No

No flashovers or punctures were observed. The leakage current remained below 1 mA_{rms} for all the specimens.

4.8 Discussion

Type testing, also known as conformance testing, of power network equipment is an essential part of the product development cycle. Using technical criteria and test techniques established in international standards, performance and quality assurance tests are conducted to ensure that the product complies with the specified requirements and the regulatory framework that governs its operation.

In the absence of international standards for insulating cross-arms, several of the methods used for testing OHL composite insulators have been adapted for use on either the compression insulator or the complete cross-arm assembly. For this purpose, a bespoke spray system was developed, complementing the rest of the laboratory equipment, to facilitate the wetting of the cross-arm.

The 400 kV cross-arm assembly was subjected to and passed the wet power frequency voltage test, the wet impulse withstand voltage test and the dry lightning impulse withstand voltage test. This does not only provide assurances that the cross-arm will not be damaged by the overvoltages occurring in service but also shows that the profile of the novel compression insulators is up to the task. Furthermore, the ability of the insulators to remain watertight was demonstrated, an indication of the quality of both the design and the manufacturing process.

The successful completion of the test on interfaces and connections of end-fittings showed that the weathershed material has the appropriate properties to withstand arcing without puncturing. Also, no issues were observed with the attachment of the end-fitting to the rest of the insulator despite its unconventional shape and method of attachment. The dye penetration and water immersion tests showed that the core material and the bonding between the sheath and the core are also of appropriate quality to ensure the longevity of the insulator.

Out of the tests performed, only the corona extinction test was not completed successfully. Regarding the ‘butterfly’ grading device, testing confirmed the results of the FEA simulations, i.e. that the device is suitable for 132 kV but not for 400 kV. The test results with the ‘M-W’ grading device were unfortunately inconclusive since not all the appropriate components required for the test were available at the time.

Due to time limitations or equipment unavailability, it was not possible to conduct all the tests described in the Technical Specifications of National Grid. These are listed and described in brief below:

- **Assembled core load-time test:** Three compression insulator specimens to be subjected to tensile load equal to 60% of the average braking load, determined using another three specimens. The test is successful if no breakage or pullout of the core occurs within 96 hours of continuous load application.
- **Mechanical load-time test:** Maintain a tensile load equal to 70% of SML on three compression insulator specimens for 96 hours and then rapidly subject them to 100% of SML. The test is successful if no breakage or pullout of the core occurs and no fracture of the metal end-fittings is observed.
- **Tracking and erosion test:** 1000 hours salt fog test on two compression insulator specimens with applied voltage equivalent to specific creepage distance of 20 mm/kV. The test is considered successful if there is no tracking, the erosion depth is less than 3 mm and the core is not exposed, and no punctures are observed.
- **Hardness test:** The hardness of two housing material specimens, with thickness of 4 mm or greater, measured with a Shore A or D durometer (BS EN ISO 868 [94]) after boiling must be within ±20% of the original value.
- **Accelerated weathering test:** Subject three housing material specimens to 1000 hours of UV radiation in the presence of moisture, using either the xenon-arc method (BS EN ISO 4892-2 [95]) or the fluorescent UV method (BS EN ISO 4892-3 [96]), to simulate the effects resulting from the exposure of the material to daylight. At the end of the test, no indications of surface degradation must be visible. The mean roughness of the specimens, measured according to ISO 4287 [97], must be below 0.1 mm.
- **Flammability test:** Check the ignition and self-extinguishing properties of three housing material specimens with thickness of 3 mm using the procedure and apparatus described in the BS EN 60695-11-10 [98]. The specimens must belong to HB40 and V0 categories for horizontal and vertical burning respectively.

- **Radio interference test:** Measure RI characteristics at a frequency of 0.5 ± 0.05 MHz or 1.0 ± 0.1 MHz or at other agreed frequencies in the range of 0.5 MHz to 2 MHz at the test voltage using the test circuit described in CISPR/TR 18-2 [99]. For 400 kV insulators, the radio noise measured must not exceed 40 dB [57].
- **Audible noise test:** One compression insulator specimen to be placed in a wind tunnel; at the practical wind speed maximum of 20 m/s, no distinguishable audible tones should be generated by the specimen.

4.9 Conclusion

For type testing, priority was given to the electrical tests since they severely stress the cross-arm and the compression insulator, and could immediately reveal potential weaknesses in the design. However, both performed according to design expectations at almost all the conducted tests. The only exception was the corona extinction test which is believed to have been completed successfully if the required equipment had been available. The testing performed up to this point may not be complete but it shows that the insulating cross-arm concept works in principle and that the design is robust enough to withstand the most extreme of service conditions. The ICA is well on the way of achieving full type approval.

5. TRIAL INSTALLATIONS

5.1 Introduction

No matter how close the standards are followed when designing a piece of equipment or how accurate the simulations are or even how rigorous the testing is, nature can be very unpredictable and situations can arise in service that are very difficult to simulate or test for. In order to confirm that the design proposed in *Chapter 2* works in practice, to verify that the simulation results shown in *Chapter 3* reflect reality and to examine how the insulating cross-arm performs outside of laboratory conditions, two trials were set up, one aiming to examine the mechanical and the other the electrical performance.

The first part of the chapter describes the mechanical trial starting with an overview of the unenergised trial site. The instrumentation system installed on two of the four retrofitted with ICAs towers aimed to monitor mechanical performance through the use of embedded strain gauges in the compression insulators and a combination of load cell and vibration sensors at the cross-arm nose. A data capture and control platform was used to capture sensor outputs and store them until retrieval. Networked cameras with local storage capabilities were used to capture video recordings of the cross-arms to monitor ice/snow accretion and pollution accumulation. This part concludes with the results from the trial.

The second part is dedicated to the live trial, looking at the trial site and the protection and monitoring systems in place. The main task of the instrumentation was to observe the leakage current behaviour on the insulating members and correlate it with weather phenomena since leakage current is a good indication of how the electrical performance of an insulator changes over time and can be indicative of ageing. The analysis of results from the data obtained during the first year of the trial were used to also examine the effect of the prevailing weather as well as compare the performance of the compression insulators with the industry standard tension insulators and assess the effectiveness of the insulator profile designed in *Chapter 2*.

5.2 Mechanical trial

5.2.1 Purpose of the trial

In November 2010, four prototype cross-arms were installed, one on each of four PL16 towers, on a decommissioned 132 kV line in an exposed location of the Scottish Highlands. The cross-arms used for this trial preceded the design described in *Chapter 2*. The compression insulators were positioned with the spine of the T-shaped core facing up, like 'Profile A' in Table 2.6. Since this was a 132 kV line, the cross-arms had to be able to fit within the existing space envelope of the shorter and narrower PL16 towers. Furthermore, their length had to match the length of the steel lattice cross-arms they were replacing so the mechanical loads on the towers would not change significantly, something that could compromise the structural integrity of the towers. As a result, the profile of the compression insulators had similar parameters as the ones described in Table 2.13 but the insulators were shorter, with an arcing distance of 3000 mm and a creepage distance of 10213 mm. The primary purpose of the trial was to confirm the mechanical capabilities of the cross-arms using embedded strain gauges in the body of the compression insulators and a combination of vibration sensors and load cells at the nose of the cross-arms. The instrumentation in place was also responsible to monitor ice accretion and pollution accumulation in order to evaluate the effectiveness of the insulator profile of the cross-arm in coping with the environmental conditions. Instrumentation was installed on two of the four towers.

5.2.2 Trial site

The high altitude site of the trial is located in the Cairngorms national park in the Scottish Highlands (Figure 5.1). This location was specifically chosen due to the adverse weather it experiences especially during the winter months. At 637 meters above sea level, with temperatures reaching -20^{o}C and winds exceeding 100 mph (161 km/h) it represented one of the worst case scenarios that the cross-arms would face in service in the UK.

Regardless of the close proximity of the four towers to each other, it had been observed that the peculiarities of the local environment allowed for substantial difference between the two adjacent instrumented cross-arms. Points of interest included the effects of the prevailing wind as well as ice and snow accretion.

Figure 5.1 - High altitude trial site

5.2.3 Installation

The compression insulators of each ICA are substantially heavier than the tension members as a result of the increased mechanical requirements. Because of that, bespoke lifting handles were fabricated that attach to the end fittings which allowed for safe lifting and handling of the compression insulators by four persons. To safely transport the cross-arms to the installation site, a special rack – mounting frame was fabricated that enabled the packaging of both the compression and tension insulators of four complete cross-arms into a van. After the individual members were transported to site, the insulators that comprised the cross-arm were transported to the base of the tower where the ICA was assembled complete with the nose cone and field grading devices. Following the removal of the conductor, the metallic cross-arm was then removed from the tower and lowered to the ground (Figure 5.2 (a)). In this case the conductor was pinned directly to the tower body while the cross-arms were swapped. With the help of a specially designed lifting frame, the ICA was then raised into place. The two compression insulators were bolted first and the two tension insulators followed shortly after on the same mounting points as the previous metallic cross-arm (Figure 5.2 (b)).

Figure 5.2 - Removing the steel cross-arm (a) and raising the insulating cross-arm (b)

The installation was completed with the re-attachment of the conductor to the nose cone using the same accessories (clamps, hanger brackets) as the ones used previously on the glass insulator (Figure 5.3).

Figure 5.3 - Completed retrofit ICA installation

5.2.4 Instrumentation

Due to the unique non-cylindrical geometry of the composite core of the compression insulators there was no precedent of the profile's mechanical performance. Despite the cross-arm being designed to withstand loads 50% more than the specification (Table 5.1) and tested successfully in a controlled environment (Figure 5.4), service conditions are not always predictable. Therefore, it was deemed prudent to develop a system to monitor the forces and weather conditions that the cross-arms are subjected to during their first trial. Analysis of the data obtained would provide even better insight on the behaviour of the cross-arm and eventually give more confidence of its actual capabilities. A diagram of one of the instrumented towers can be found in *Appendix A*.

***Table 5.1** - ICA load cases*

Load case	Max. vertical (kN)	Max. transverse (kN)	Max Longitudinal (kN)
High ice	19.52	0.1	0.22
Wind and ice	9.74	15.03	0.15
Failure containment	2.1	0.02	17.6

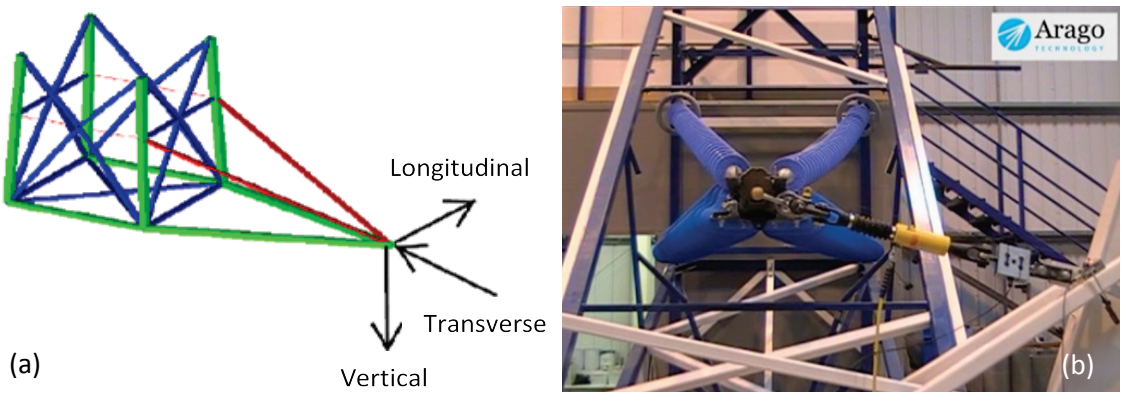

Figure 5.4 - ICA loading axes (a) and ICA failure containment testing (b)

5.2.4.1 Mechanical performance monitoring

5.2.4.1.1 Strain gauges

Strain gauges were embedded half way along the core of the horizontal members to measure the strain experienced by each member on three planes: vertical, horizontal and axial. This was possible because the conductors were not being energised.

A full Wheatstone bridge configuration was employed for the strain gauges measuring the strain on each plane (Figure 5.5 (a)). This arrangement, as well as the placement of the gauges (Figure 5.5 (b)), ensured that each bridge produced a signal related only to the stress applied in one plane. By bonding complementary pairs of strain gauges for each plane both the force and the direction of bending on each plain could be calculated since when one of the pairs is compressed the other is stretched. Additionally, the full bridge configuration has greater sensitivity than other strain gauge arrangements and it is also linear, i.e. the ouput voltage is directly proportional to the applied force, provided that the change in resistance as a result of the applied force is equal for all strain gauges [100].

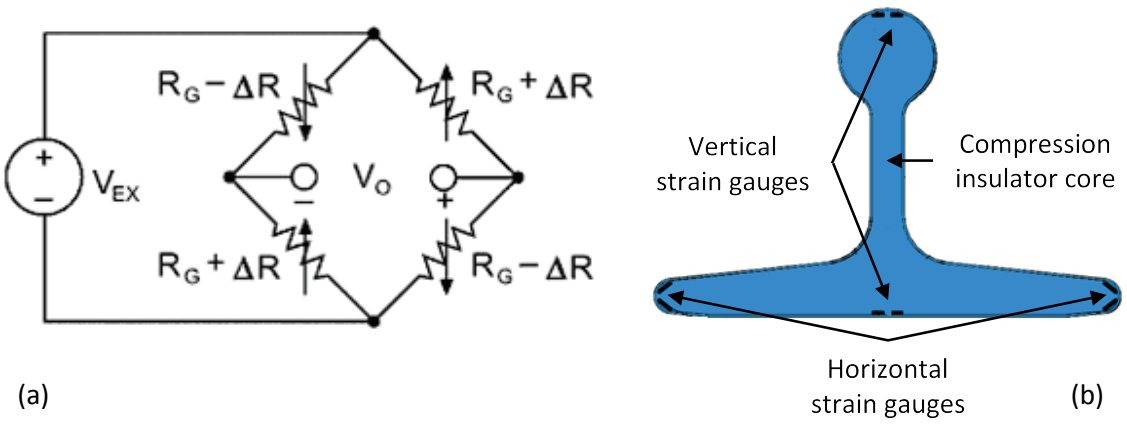

Figure 5.5 - Full Wheatstone bridge (a) and strain gauge placement on the compression insulator core (b)

The purpose of the strain gauges was to observe how the forces seen by each insulating member change with the varying wind loading and especially assess how the insulators bend, if at all. Also the gauges could help to identify whether or not the load was distributed evenly among the two compression insulators, which are the main structural supports, after installation. The strain gauges for each compression insulator were calibrated in the workshop of EPL Composite Solutions using the rig of Figure 5.6 by applying a load from 0 kg to 1500 kg in steps of 250 kg on each axis and measuring the deflection and the signal produced by the sensors.

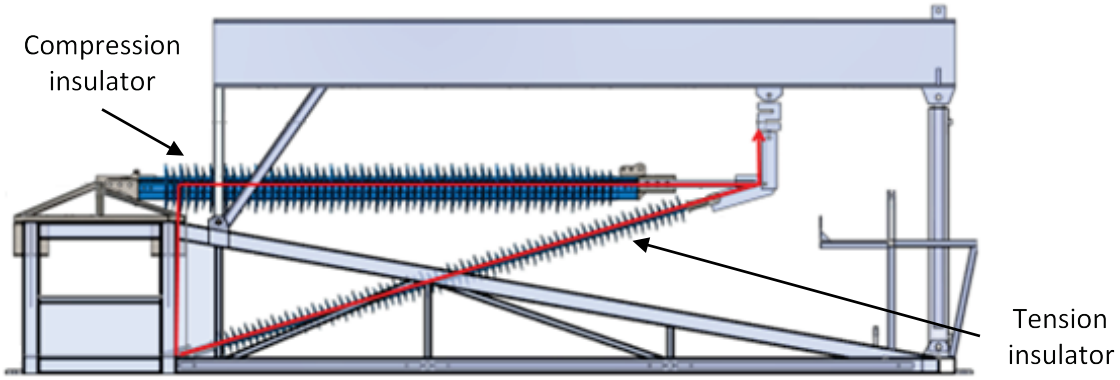

Figure 5.6 - Compression insulator mechanical test rig

5.2.4.1.2 Load cell

Ice accretion on the conductor during the winter months can significantly increase its weight and therefore the weight that the cross-arm needs to withstand. Furthermore conductor galloping due to high winds can put additional stress on the cross-arm. To monitor these effects, a five tonne load cell was installed between the nose attachment point and the conductor clamp (Figure 5.7). The load cell could provide useful information regarding the forces applied by the conductor to the cross-arm.

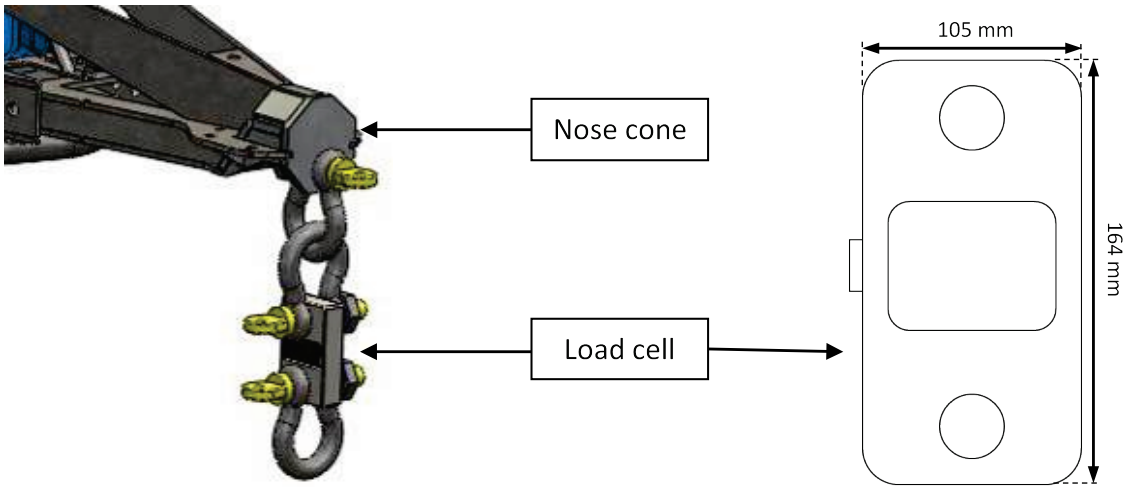

Figure 5.7 - In-line load cell at conductor attachment point

5.2.4.1.3 Vibration sensors

Two vibration sensors (Figure 5.8 (a)) per cross-arm were installed, one attached to the nose cone and the other to the hanger bracket adjacent to the conductor (Figure 5.8 (b)). The former aimed to log any vibrations experienced through the nose connection and monitor any up-lift experienced by the cross arm. The latter aimed to measure any relative movement of the conductor in respect to the cross arm.

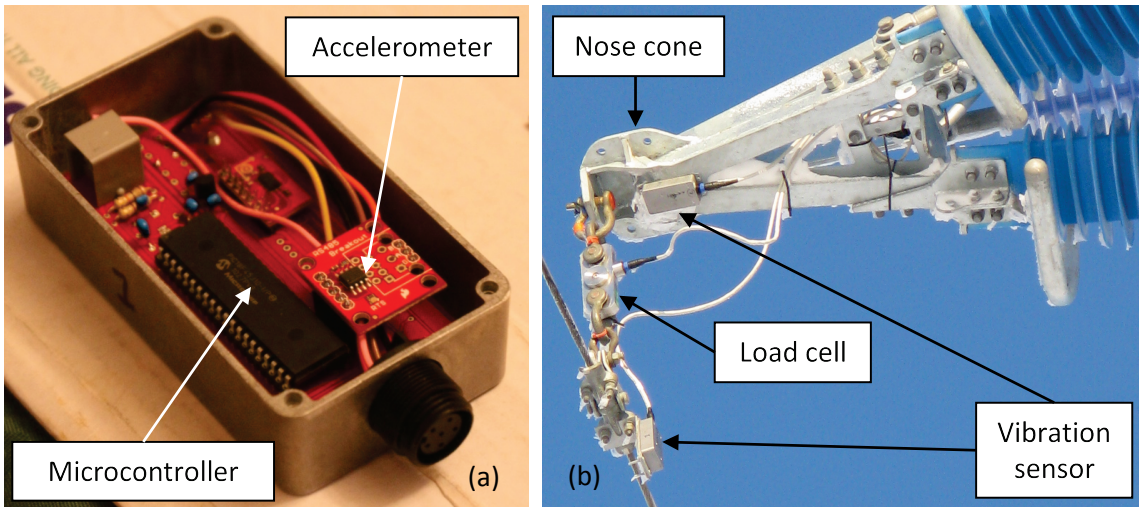

Figure 5.8 - Vibration sensor (a) and nose instrumentation placement (b)

The accelerometer-based sensors could measure acceleration on three axes in the range of ± 8g (where g represents 9.8 ms^{-2}) with a resolution of 16 bit. Readings were taken at a rate of 100 Hz while an 8 MHz microcontroller was used to control the sensor and transmit the data to the data acquisition system over a twisted-pair cable. That data could be used in conjunction with those obtained from the load cell to better estimate

the forces seen by the cross-arm under different weather conditions. Eventually, interpretation of the data would result in optimisation of the design.

The extensive sensitivity range for the accelerometers (± 8g) was chosen because at the beginning of the trial the magnitude of the forces resulting from conductor galloping on the cross-arms was unknown. Moreover, the sensitivity range was selected having in mind that a broken conductor test was scheduled to take place upon the conclusion of the trial.

5.2.4.1.4 Weather station

In order to get the most accurate weather data possible a weather station was installed on the top cross-arm of each instrumented tower. The weather station was able to record temperature, humidity, pressure, dew point, wind speed and direction. The data was to be used to match the mechanical loads on the cross-arm to specific weather phenomena.

5.2.4.2 Pollution and ice accretion monitoring

Although this trial did not test the electrical performance of the composite cross-arms, it was important to identify how the environmental conditions might hinder their capability in future applications and attempt to optimise the profile design beforehand. This was particularly important for the compression insulators since they had not been previously used in service.

For this purpose three cameras were installed on each of the instrumented towers. Two of them monitored the insulating cross-arm from different angles while the third monitored the glass insulator attached to the metallic cross-arm opposite the insulating one (Figure 5.9). Due to the limited storage capacity of the on-board memory cards and the limited bandwidth of the communication link to the nearby ski-centre, the cameras were set to record one minute of video every hour during daytime and they were powered off during the night to conserve energy. After examination of the videos from the first couple of months, the short duration of the videos was deemed sufficient by the Arago team to reveal ice/snow accretion and pollution accumulation patterns as well as provide adequate information regarding the water run-off behaviour on the surface of the insulators.

The installation site experiences heavy snowfall during the winter months. The cameras could provide useful information on how ice accreted on the surface of the cross-arm and how effective was the profile design in that respect. Moreover, the videos recorded would help identify which areas of the non-cylindrical compression insulators were more prone to accumulating pollution in the long term.

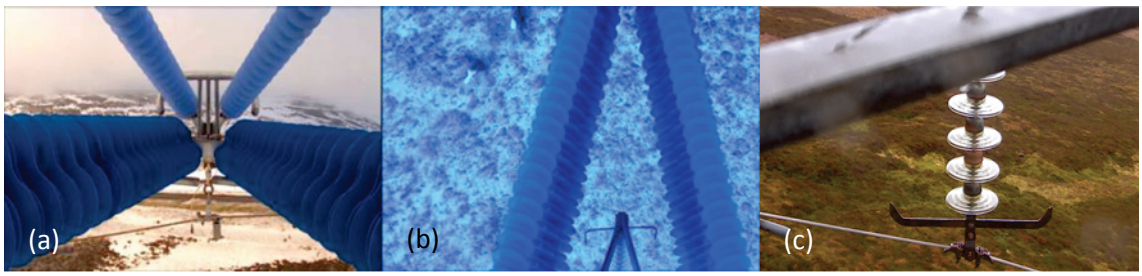

Figure 5.9 - Tower camera views - (a) ICA nose view, (b) ICA top view, (c) glass insulator view

5.2.4.3 Power sourcing and data acquisition

Despite the excellent scientific value of the site, the remoteness of the location posed a great challenge in respect to the monitoring system. Since the line was not live, the only viable option for powering the electronics was to generate the power locally using small scale wind turbines and storing it in batteries on the towers. The turbines were mounted on specially fabricated brackets on the towers. The power electronics and batteries were placed inside the main instrumentation enclosure which was installed on the tower on a specially made platform approximately 7 m from the base of the tower. A diagram of the energy harvesting system is shown in (Figure 5.10).

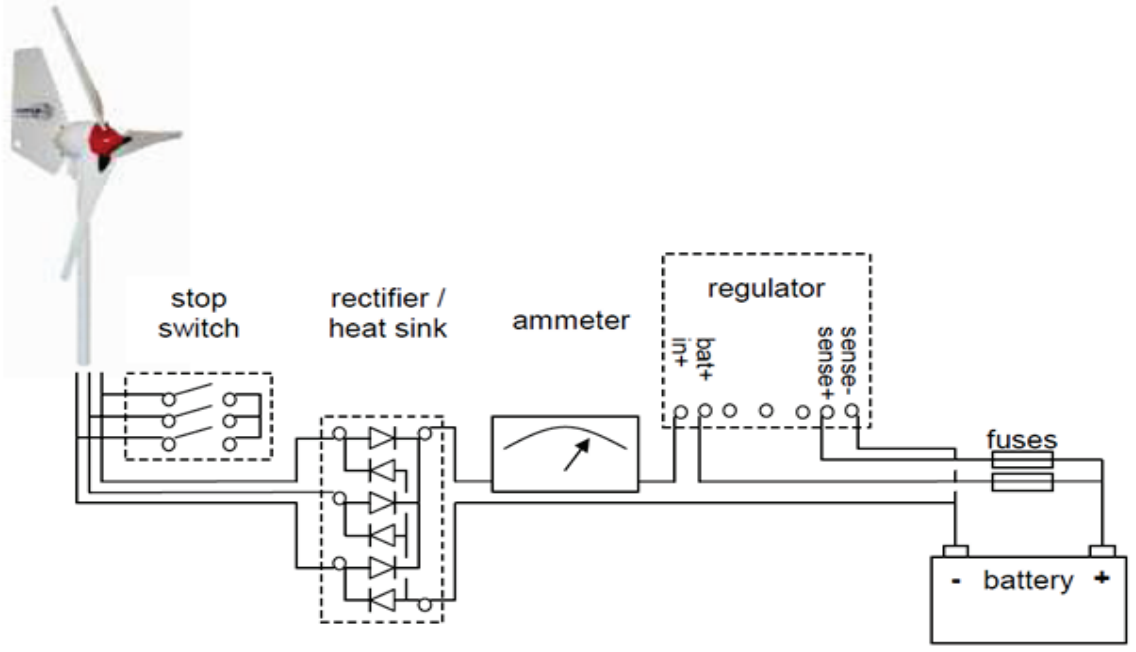

Figure 5.10 - Energy harvesting system for powering the instrumentation

While the cameras had the capability of storing their recordings on board, the rest of the equipment did not. An industrial data acquisition (DAQ) and control platform (National Instruments cRIO 9205) was used to capture sensor outputs and store the data. It also controlled the power cycling of the cameras through a relay module. Figure 5.11 shows the input/output functions of the DAQ device.

The DAQ device was placed in the main instrumentation enclosure. Because of that, the voltage signals from the strain gauges and load cells were converted to current signals and amplified in order to ensure their fidelity during transmission. The amplifiers were located inside an IP68 rated enclosure, from here onward referred to as the 'booster box', installed on the tower near the LV end of the cross-arm. Communication of the data logging system with the accelerometers and weather station was achieved via RS485 and RS422 serial links respectively, routed through the booster box, effective for transmitting data over the approximately 25 m long twisted pair cables from the booster box to the main instrumentation enclosure. Figure 5.12 shows the wiring between the sensors, booster box and main enclosure.

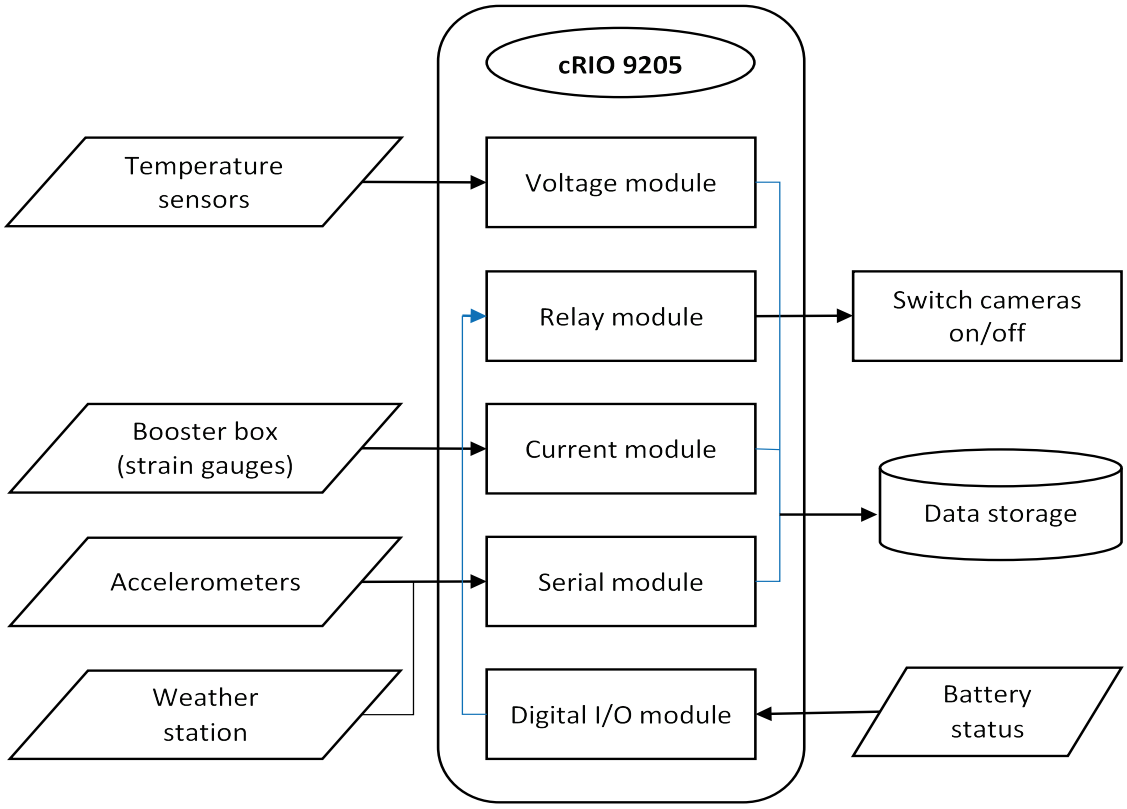

Figure 5.11 - Functions of the DAQ platform

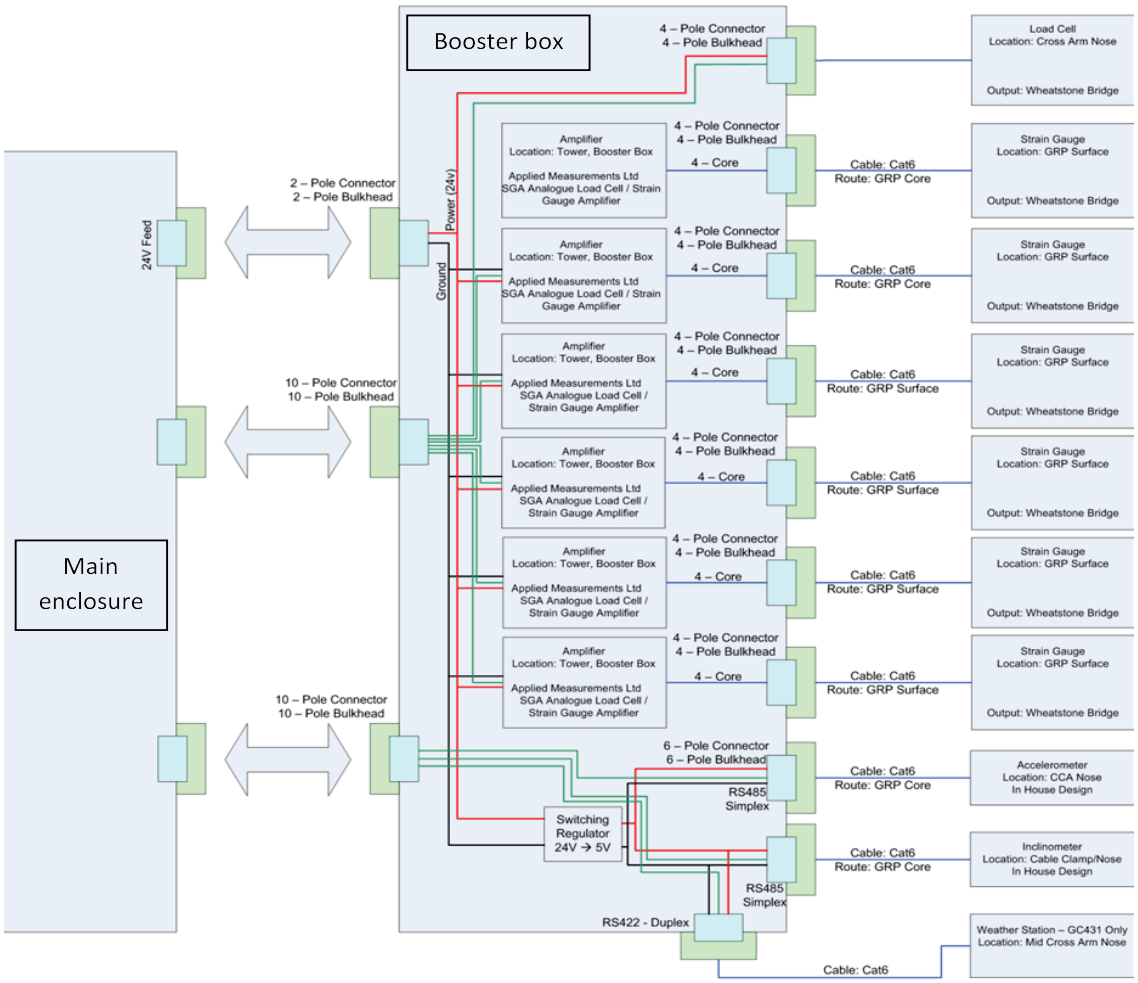

Figure 5.12 - Wiring between the sensors, booster box and main enclosure

The data acquisition system and the cameras were connected to wireless access points on each tower. With the help of high gain antennas, the data collected from each tower were relayed periodically to the nearby ski centre awaiting retrieval. The main enclosure was fitted with intake and extractor fans controlled by a thermostat to keep the electronics from overheating during the summer months. Figure 5.13 shows the power delivery system installed in the main instrumentation enclosure.

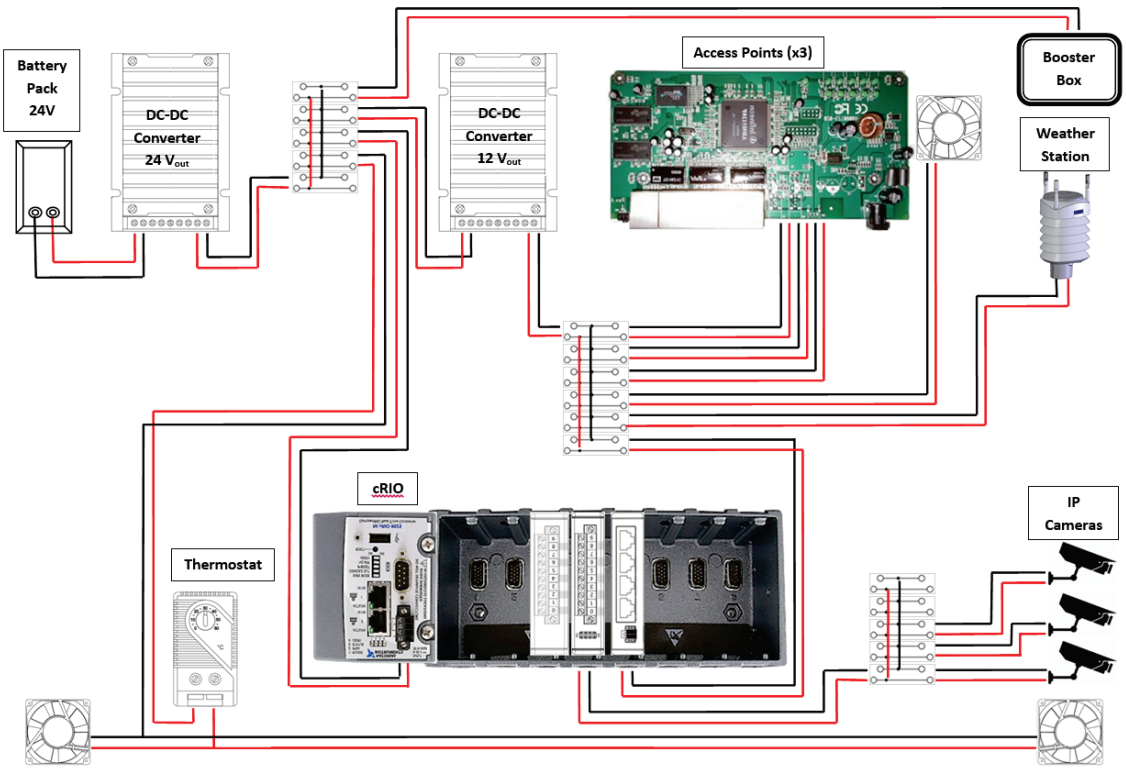

Figure 5.13 - Wiring of the instrumentation in the main enclosure

5.2.5 Results

Despite the best efforts of the Arago team, including the author, that have worked for the design, installation and commissioning of the trial, it was not possible to collect meaningful data from the strain gauges, load cells and vibration sensors for three reasons. Firstly, the conductor that was installed on the line was of smaller diameter than what was originally specified (a HORSE type conductor with outer diameter of 13.95 mm instead of a LYNX type conductor with outer diameter of 19.53 mm [56]). The smaller conductor coupled with the short line span (between 100 m and 200 m) resulted in substantially reduced forces applied at the nose of the cross-arm than what was originally calculated. Since the sensors were specifically build with the higher loads in mind, it was not possible to adjust their sensitivity and calibrate them to the reduced loads. Secondly, the energy harvesting system was plagued with frequent breakdowns of the wind turbines which, in most cases, happened during periods of high wind. As a result, a great amount of data was not recorded. Thirdly, some of the connectors used for connecting the sensors to the enclosures were destroyed due to the adverse weather conditions (Figure 5.14) which in turn compromised the cabling and the sensors themselves. The loss of even one of the strain gauges on an insulator meant that it was not possible to resolve the forces applied to that insulator.

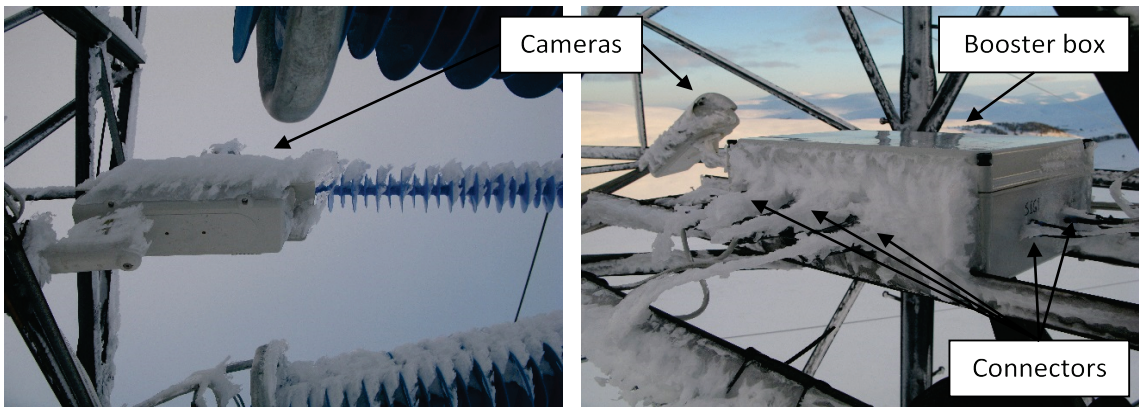

Figure 5.14 - Snow-covered cameras and booster box on one of the instrumented towers

Nevertheless, the trial did prove to be useful because of the weather data obtained and images recorded from the cameras. The highest wind speed observed was 67 m/s (or 151 mph) recorded on the 10th of March 2011. Furthermore the cross-arms experienced several periods of heavy snowfall, one of the most severe being between December of 2010 and February 2011. Despite the extreme weather conditions, the cross-arms did not show any signs of mechanical fatigue after two years at the site.

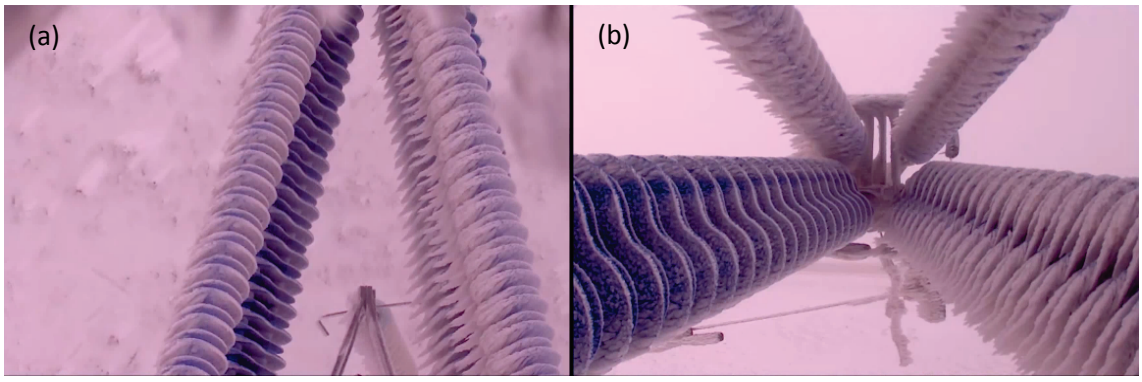

Figure 5.15 - Ice and snow accretion on ICA during December 2010 - top view (a) and nose view (b)

As Figure 5.15 shows, ice and snow were distributed uniformly along the length of the cross-arm. Initial concerns for greater concentrations near the nose cone, at the area where all four members meet, were unsubstantiated. While the ice accretion on the cross-arm was significant, the phenomenon was of a similar magnitude on both the compression and the more conventionally-shaped tension insulators of the ICA. Furthermore, the glass cap-and-pin tension insulators from nearby towers exhibited comparable levels of ice and snow accretion as shown in Figure 5.16. Images captured during the melting cycle and on-site inspections however, showed that the orientation of the compression insulators, with the spine of the profile facing up, allowed for snow to remain within the concave sections of the profile for longer periods than it did on the tension insulators.

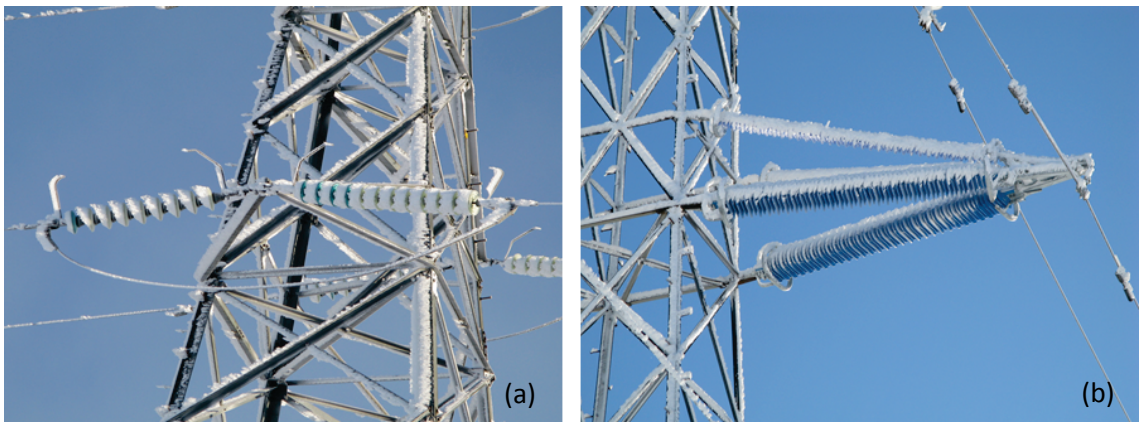

Figure 5.16 - Ice and snow accretion on glass tension insulators (a) and ICA (b) on adjacent towers

5.3 Live trial

5.3.1 Purpose of the live trial

Utilising a combination of innovative design, and proven materials and manufacturing methods, the main feature of the insulating cross-arm is its compressive elements. As mentioned in *Section 2.4*, their distinctive cross-sectional shape makes them lighter than cylindrical alternatives while providing high compressive strength as well as resistance to bending and buckling. While mechanically their performance has been proven both in laboratory tests and during a two year trial installation [101], the departure from traditional designs coupled with limited service experience requires verification of the electrical performance of the novel insulators and the reliability of the cross-arm in general.

To alleviate any concerns and prepare for deployment of the cross-arm on the network, a live test site was commissioned in north-east Scotland in May 2012. The main aims of the trial were:

- To observe the electrical behaviour of the cross-arm and how it changes in relation to the environmental conditions.
- To compare the performance of the novel compression insulators with that of the 'traditional' tension insulators.
- To identify aspects of the cross-arm that can be improved further (insulator profile, grading devices).

5.3.2 Trial site

A substation was identified on the east coast of Scotland able to accommodate a bespoke lattice tower on which two composite cross-arms were installed. The substation is situated 3.6 km from the coast. In the East, there is also a large industrial complex (Figure 5.17). The latitude of the location combined with its proximity to the sea provided the opportunity to examine electrical performance in an onerous environment with high conductivity pollution and wide temperature variations.

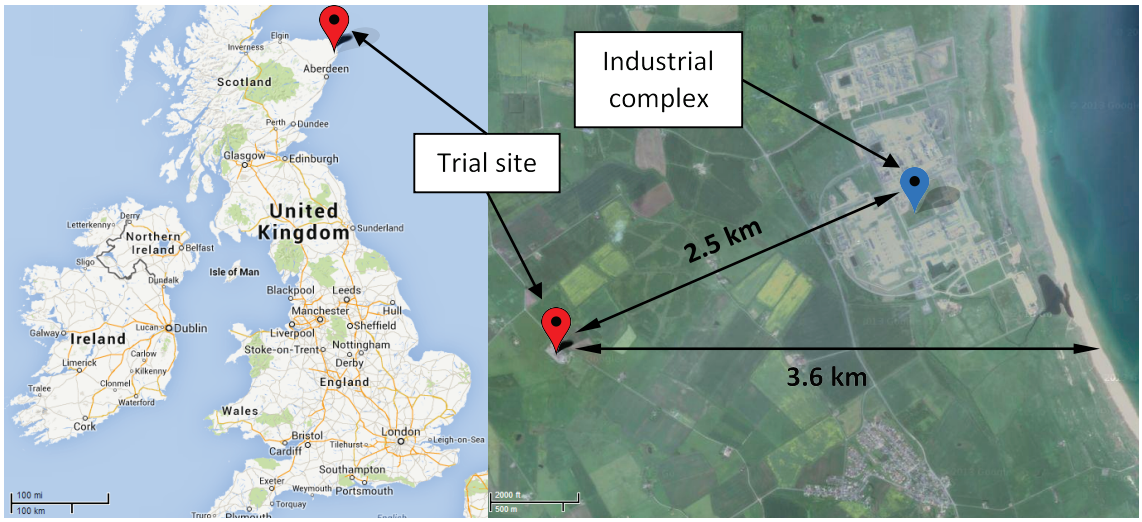

Figure 5.17 – Live trial site location

The two cross-arms were designed to be installed at an orientation of 90° from each other, with one cross-arm facing south while the other facing west, to investigate the effect of the direction of the prevailing weather. To electrically stress the cross-arms equivalent to a 400 kV phase-to-phase installation, they were energised at 231 kV phase-to-ground by a transformer that was powered from the 415 V three-phase supply of the substation. The transformer was rated at 50 kVA continuous operation or up to 100 kVA for 15 minutes per hour. The high voltage ends of the two cross-arms were connected by an 8 m span of 400 kV conductor which in turn was connected to the HV bushing of the transformer. Figure 5.18 shows how the different components of the trial were arranged at the site while Figure 5.19 shows the actual trial site.

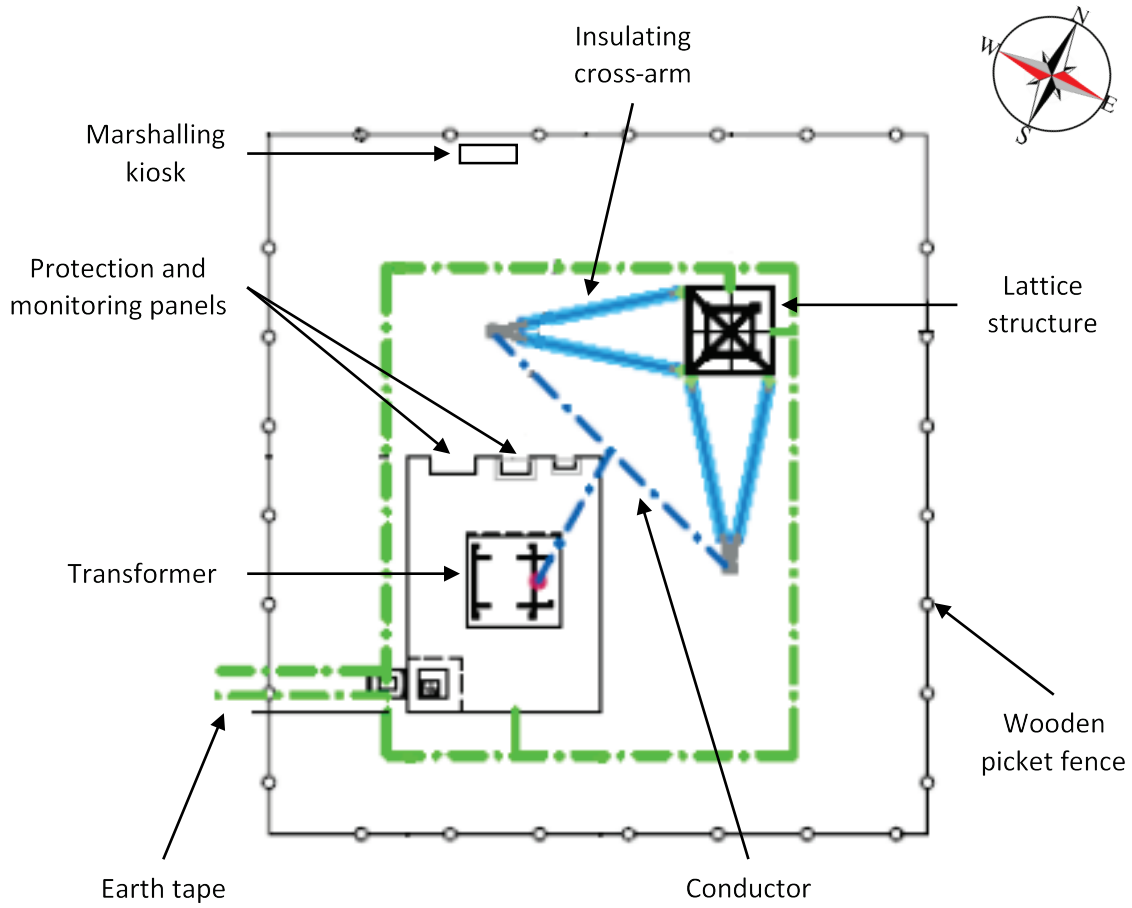

Figure 5.18 – Live trial site plan

Figure 5.19 – Live trial site overview

5.3.3 Protection system

The components of the live trial constituted a small scale power system and, despite its relative simplicity, it required electrical protection. A fast, reliable and sensitive protection system was designed specifically for the trial to keep the equipment within operating limits and prevent or at least minimise the damage from potential faults. A diagram of the protection system is shown in Figure 5.20.

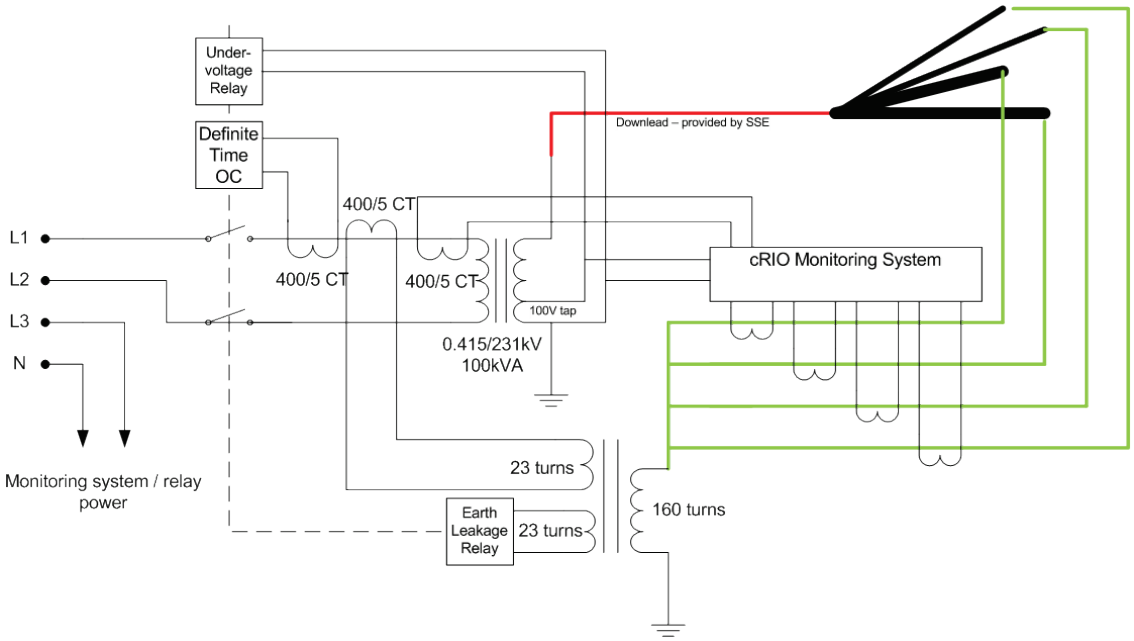

Figure 5.20 - Protection system diagram

5.3.3.1 Requirements

With the data provided by the substation administrator a fault analysis for different scenarios was performed that gave the following fault level values for a bolted fault:

- 415 V phase-to-phase: 3031 A
- 415 V phase-to-ground: 935 A
- 415 V phase-to-phase-to-ground: 3333 A
- 231 kV phase-to-ground: 1351 A

5.3.3.2 Overcurrent protection

To protect against winding faults in the transformer, a Definite Time Overcurrent relay was used on the low voltage (LV) input to the transformer. The steady state maximum load current was calculated to be 241 A (100 kVA at 415 V) but the relay was set using a slightly higher (+20%) value of 288 A to provide a margin for short time transients. The

5 A relay was fed through a 400/5 current transformer (CT) and was set at 72% (288/400) with a trip time setting of 0.25 s to prevent the higher inrush current tripping the system, an inhibit time of 1 s and a hysteresis of 5%.

5.3.3.3 Inrush protection

In order to protect the system from voltage dips as a result of high magnetising inrush currents, the transformer was energised through 0.5 Ω resistors, limiting the inrush current to 830 A. The resistors were rated at 40 kW for five seconds and they had to be taken out of the circuit before they overheated, therefore the following energisation sequence was employed:

1. Close command given to control panel.
2. The primary contactor energises the transformer through resistors and the first timer starts.
3. After two seconds, the bypass contactor closes and the second timer starts.
4. After two seconds, the primary contactor opens and disconnects the resistors.

To prevent current from flowing continuously through the resistors in case of a contactor or timer failure, a 5 A overcurrent relay fed by a 400/5 CT was used. The maximum continuous current through the resistors based on the thermal rating would be 92A and using 80% of that value the relay was set at 19% (74/400) with a trip time setting of 5 s, an inhibit time of 1 s and a hysteresis of 5%.

5.3.3.4 Undervoltage protection

A secondary undervoltage protection was installed to complement the overcurrent protection. The undervoltage relay was connected to a secondary 100 V tap of the transformer high voltage winding. To calculate the appropriate setting for the relay the following parameters were considered:

- Transformer impedance: 5%
- Transformer output voltage (secondary tap): 100 V
- Minimum statutory supply requirement: -6% or 0.94 p.u.
- Margin: 95 %

From the above, the trip level was calculated to be:

$$Trip\ level = 100\ V \times 0.94 \times 0.95 \times 0.95 \approx 85\ V \tag{5.1}$$

Therefore, the voltage seen by the relay would be:

$$Voltage\ at\ relay = \frac{85\ V \times 240\ V}{110\ V} \approx 185\ V \tag{5.2}$$

The relay was set at 62% (185/300) with a trip time of 1 s.

5.3.3.5 Differential protection

The final form of protection installed was a differential system which relied on a balanced current being seen at the low voltage winding of the transformer and at the low voltage end of the cross-arm members. Using a three winding transformer with the turns ratio set to account for the high voltage transformer turns ratio, any imbalance in the low and high voltage currents which would indicate a phase to earth fault would drive current through a third winding which supplied the overcurrent relay.

5.3.4 Monitoring system

An instrumentation system was developed (Figure 5.21) with primary purpose to monitor leakage current on the surface of the cross-arm members. Using weather detection equipment and cameras, it would be possible to associate the electrical behaviour of the cross-arms to specific weather phenomena.

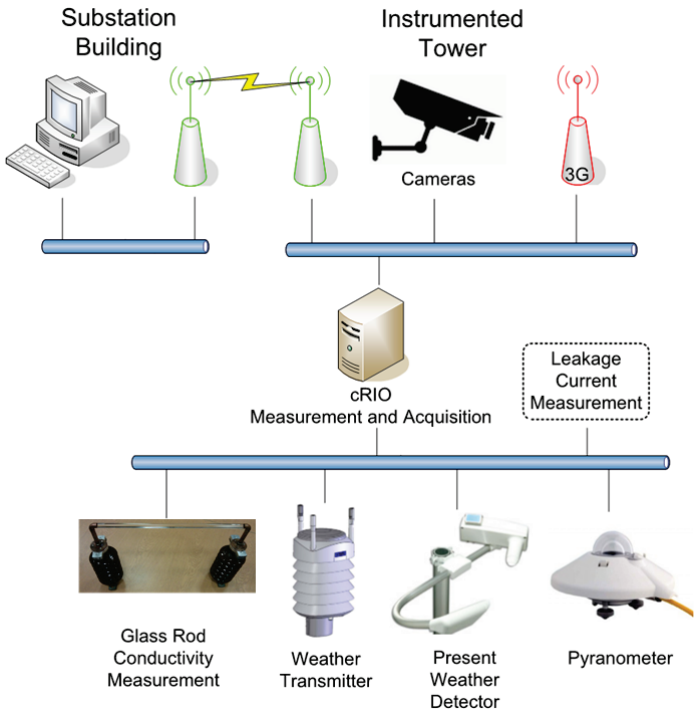

Figure 5.21 – Live trial monitoring system

5.3.4.1 Leakage current measurement

To measure the leakage current from the composite cross-arms, each of their members was installed on the tower using brackets which isolated them from earth. At the LV end of each member a shielded cable was attached that ran down the tower and into the monitoring enclosure. There, the individual cables were connected through 200 Ω resistors to a commercial data acquisition (DAQ) and control platform, responsible for recording the leakage current signals in the form of voltage. The software running on the DAQ platform was programmed to detect changes in the signals and above a certain threshold accelerate the acquisition rate to capture high leakage current events with better resolution.

Additionally, a separate system for measuring the conductivity of a glass rod was installed on the tower at the same height as the cross-arms. The system consisted of a 15 mm diameter glass rod, two copper pipes and two 11 kV porcelain insulators to isolate the system from earth. The rod was energised by a 50 V transformer through a 500 Ω resistor and its leakage current cable was terminated through a 50 Ω resistor to another channel of the DAQ platform. Its purpose was to provide reference values for the conductivity of the pollution present at the site which would help identify the pollution severity level using an identical system in the laboratory.

5.3.4.2 Weather monitoring

In order to be able to correlate the manifestation of leakage current and/or flashover events to specific environmental conditions, three weather monitoring instruments were installed at the top of the lattice tower.

Firstly, a small, lightweight weather transmitter could measure wind speed and direction, precipitation, atmospheric pressure, temperature and relative humidity. The precipitation and wind sensors were heated to prevent snow accumulation and maintain the accuracy of measurements. It was powered by a 12 V DC supply located in the monitoring enclosure and outputted serial data to the DAQ platform using the RS485 communications protocol.

Secondly, a ‘present weather’ detector (PWD) combined the measurements of precipitation water content, optical scatter and temperature to evaluate the prevailing visibility and weather type. Specifically, it characterised the weather as one of the

following types: no precipitation, precipitation, drizzle, rain, snow or sleet. The visibility estimation was provided in meters up to 2 km and was categorised into one of the following types: clear, mist, haze or smoke or dust. Similarly to the weather transmitter, the PWD was powered by a 12 V supply, but its heaters were powered by a more potent 24 V supply. Its data were transmitted using the RS485 communications protocol to the DAQ platform in 15 s intervals.

Thirdly, to measure solar irradiance, a pyranometer was installed. The intensity of solar radiation affects the speed at which moisture evaporates from the surface of insulators. Furthermore, UV radiation directly affects the ageing of composite materials and the sun impacts bio-film development. The pyranometer used a thermopile detector to output a voltage signal in the range of 0-20 mV and could measure a maximum irradiance of 2000 W/m^2.

5.3.4.3 Cameras

Four cameras were installed as part of the monitoring system. One of them was placed on the substation building over-looking the entire trial site and provided visual confirmation regarding the weather conditions in the immediate vicinity (Figure 5.22).

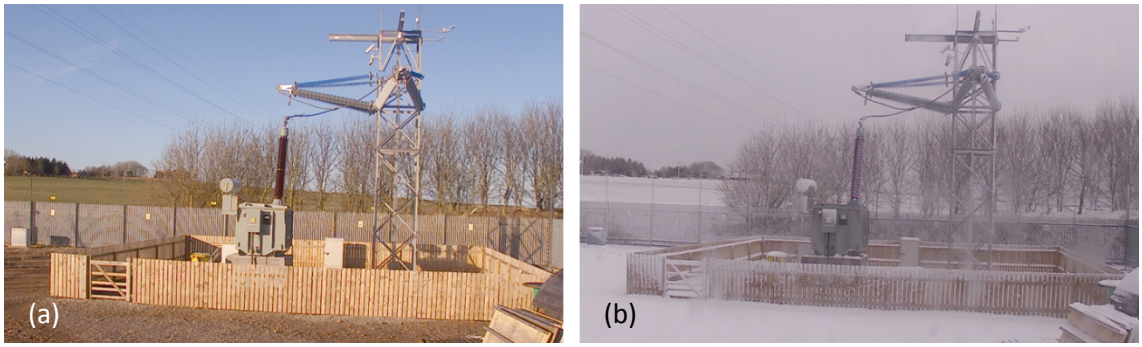

Figure 5.22 - Site camera view – (a) July 2012, (b) January 2013

The other three cameras were placed on the tower. Two of them monitored the cross-arms from above to capture snow and ice accretion patterns while the third was focused on one of the compression members to record water behaviour, pollution accumulation and possible changes in hydrophobicity (Figure 5.23). The three tower cameras were powered by the 12V supply in the monitoring enclosure while the site camera was powered directly from the mains supply of the substation.

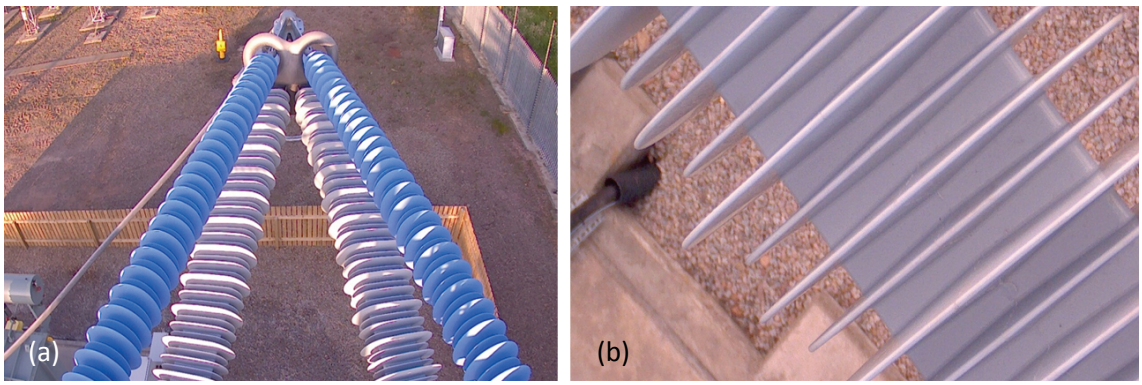

Figure 5.23 - ICA camera view (a) and compression insulator camera view (b)

5.3.4.4 Data acquisition

A commercial DAQ and control platform (National Instruments cRIO 9075) was responsible for collecting the data from the various instruments. Leakage current readings were taken for the first five seconds of every minute to reduce the amount of data recorded. During these five seconds the sampling rate was 1 kHz. Additionally, the DAQ platform collected data related to the transformer powering the trial, such as supply and output voltage. All the recordings were timestamped using the time from an internet time server so they could be analysed later.

All the leakage current and weather data were initially stored locally inside the monitoring enclosure on a flash drive. The camera recordings were stored on SD cards installed inside the camera units themselves. The DAQ platform and the cameras were all connected to a wireless router within the monitoring enclosure via Ethernet cables. A PC located in the substation was programmed to run an FTP script each day to pull all the data wirelessly and store them on a network attached storage (NAS) with mirrored drives for redundancy.

A separate router in the monitoring enclosure was connected to the 3G network via a USB dongle. The antenna lead of the dongle was extended to the top of the tower, using low loss coaxial cable, where a 3G antenna was installed to improve reception. Using the 3G link, data were transmitted periodically to a remote computer where, after processing, they were uploaded and displayed graphically as live weather and leakage current information on a website that updated every five minutes.

5.3.5 Results

In the following sections short periods of leakage current activity during the first year of the trial (June 2012 – May 2013) in the form of graphs are used to demonstrate how the leakage current on the cross-arm insulators changes with the weather. The monthly leakage current graphs can be found *Appendix E*. The leakage current waveforms from the individual insulating cross-arm members are labelled based on the direction the cross-arm is facing, the type of insulator and the proximity to the conductor as follows:

SC : **S**outh **C**ompression

ST : **S**outh **T**ension

STc : **S**outh **T**ension near **c**onductor

SCc : **S**outh **C**ompression near **c**onductor

WC : **W**est **C**ompression

WT : **W**est **T**ension

WTc : **W**est **T**ension near **c**onductor

WCc : **W**est **C**ompression near **c**onductor

5.3.5.1 Effect of insulator type and capacitive coupling

The component of leakage current that is of interest for examining the behaviour of the insulting cross-arms at the trial site is the resistive component that flows on the surface of the insulators. Changes in surface leakage current indicate changes to the surface condition of the insulator and, as explained earlier, can be indicative of ageing or even used to predict flashovers. Inevitably however, there is another component of leakage current present, the capacitive component. This second component is a result of capacitive coupling between the conductor, the insulating cross-arm members and earth. Hence, the leakage current measured by the instrumentation at the trial site is the sum of both the resistive and the capacitive components of leakage current.

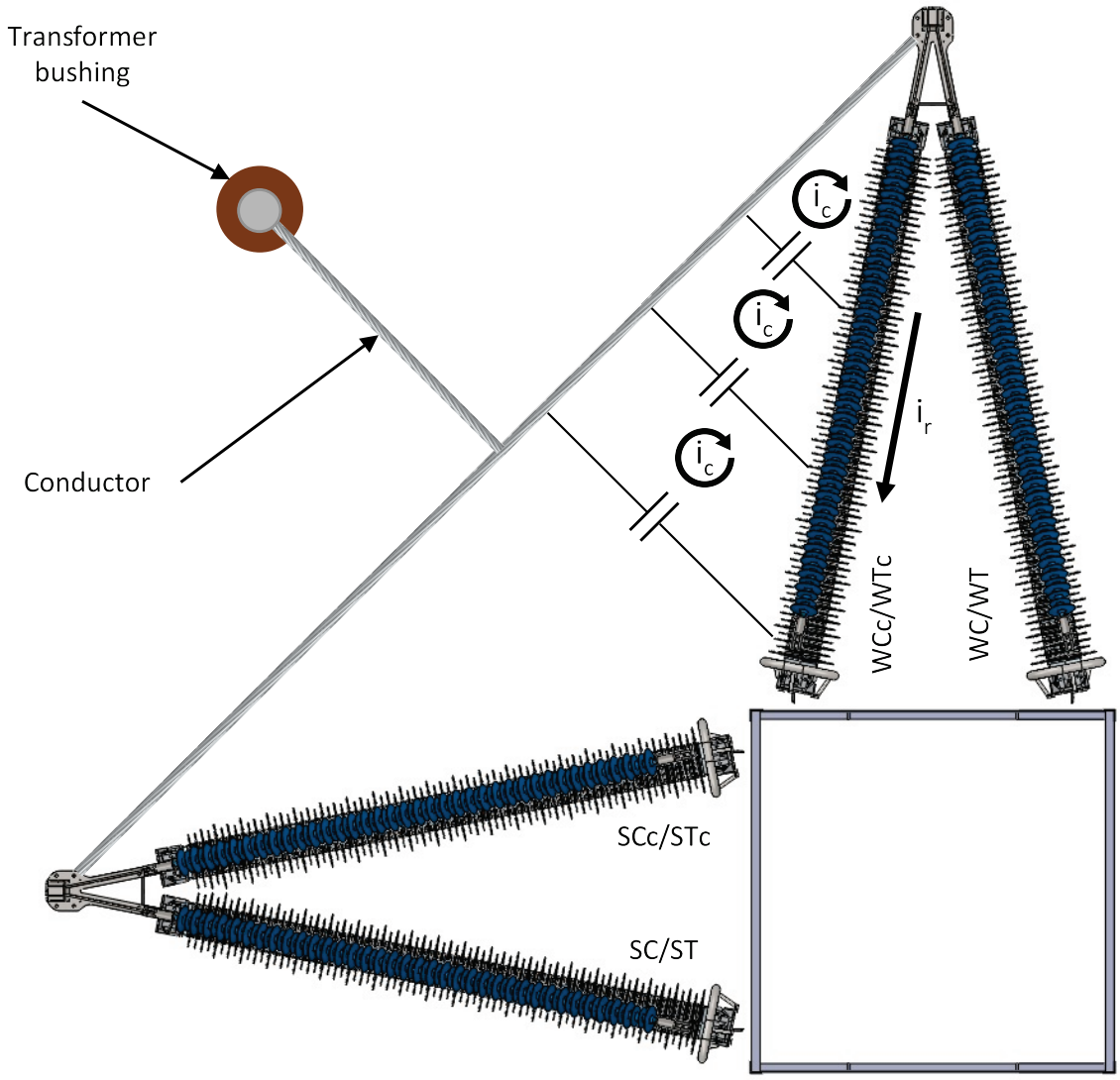

Figure 5.24 - Capacitive coupling effect at the live trial site

Owing to different geometric position of the insulators relative to the conductor and each other (Figure 5.24) the steady state leakage current values of the insulators differ due to the capacitive coupling effect. Another reason for the different leakage current values is the difference in surface area between the compression and tension insulators which causes higher steady state leakage current on the compression insulators.

Figure 5.25 shows the steady state leakage current of all the insulators a few days after the trial site was turned on. As shown, the insulators that are closer to the transformer bushing and the conductor (STc, SCc, WTc, WCc) exhibit higher steady state leakage current than their counterparts located further away (ST, SC, WT, WC). Also, the compression insulators (SC, SCc, WC, WCc) exhibit higher steady state leakage current than the tension insulators directly above them (ST, STc, WT, WTc).

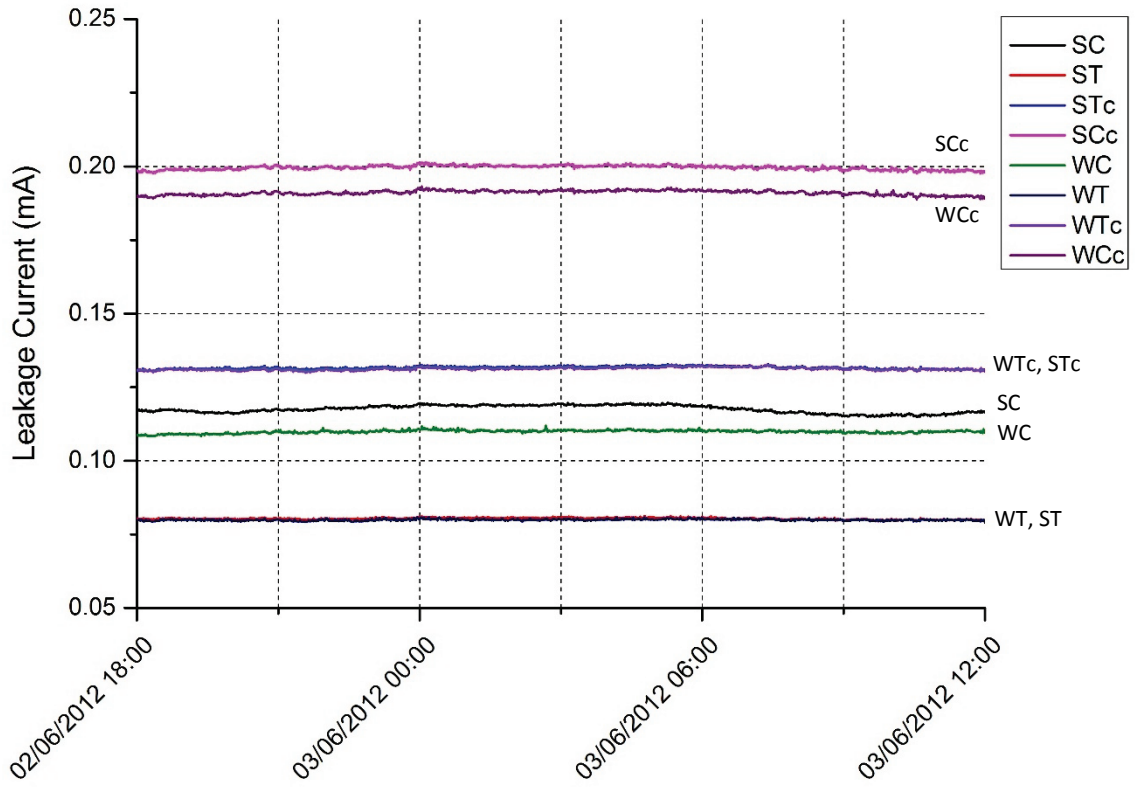

Figure 5.25 – Typical steady state leakage current activity

5.3.5.2 Effect of humidity

Figure 5.26 shows the leakage current activity on the two cross-arms in the period between 18:00 on the 5th of June and midnight on the 10th of June 2012. The days preceding this period were dry, with humidity ranging between 45% and 80%, and easterly wind persisting for the entire period. At approximately 03:00 on the 5th, the relative humidity (RH) level exceeds 93% which causes the leakage current on all insulators to rise above their base value. The increase is higher on the tension insulators. At 12:00 on the 6th, a spell of light rainfall (5 mm/h) reduces the leakage current magnitude temporarily, especially on the tension insulators. With RH remaining at the previous level, leakage current rises again until 18:00 on the 9th when RH drops below 93% and the leakage current activity subsides.

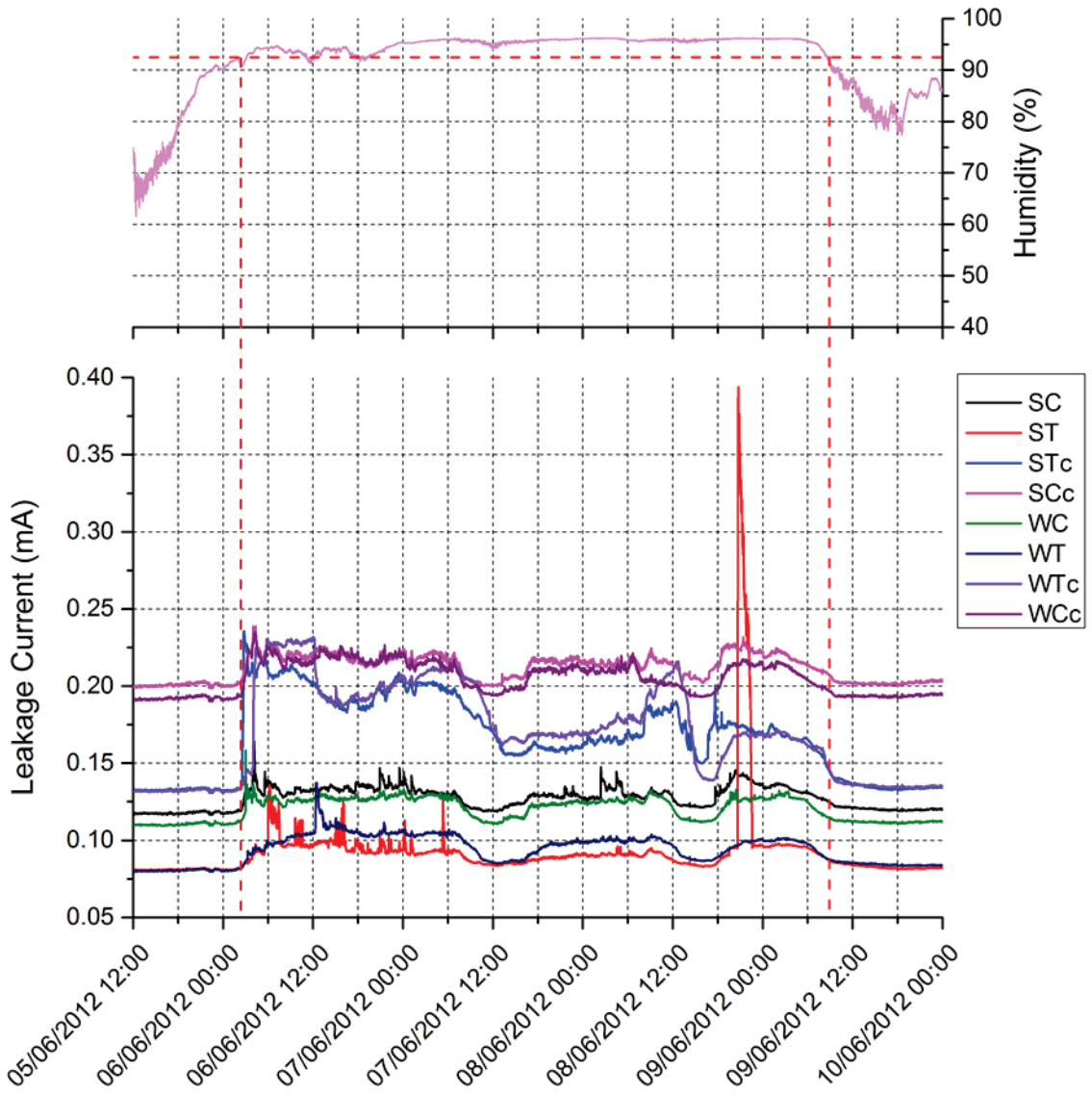

Figure 5.26 – Effect of relative humidity on Leakage current – 5th to 10th of June 2012

Similarly, in the period between the 6th and 8th of July 2012 shown in Figure 5.27, a rise in the RH level above 94% makes the leakage current on all insulating members to rise above the steady state value. The increased leakage current activity persists until the RH level drops below 94%.

From the two periods examined above as well as others not shown here, it can be deduced that there is a relative humidity threshold between 93% and 94% that triggers leakage current activity on all insulators. The effect is more pronounced in the summer months when dry periods of easterly wind from the sea build up conductive pollution on the insulators. The average percentage increase attributed to the rise of humidity above the aforementioned threshold is in the range of 15% for the compression insulators and 20% for the tension insulators.

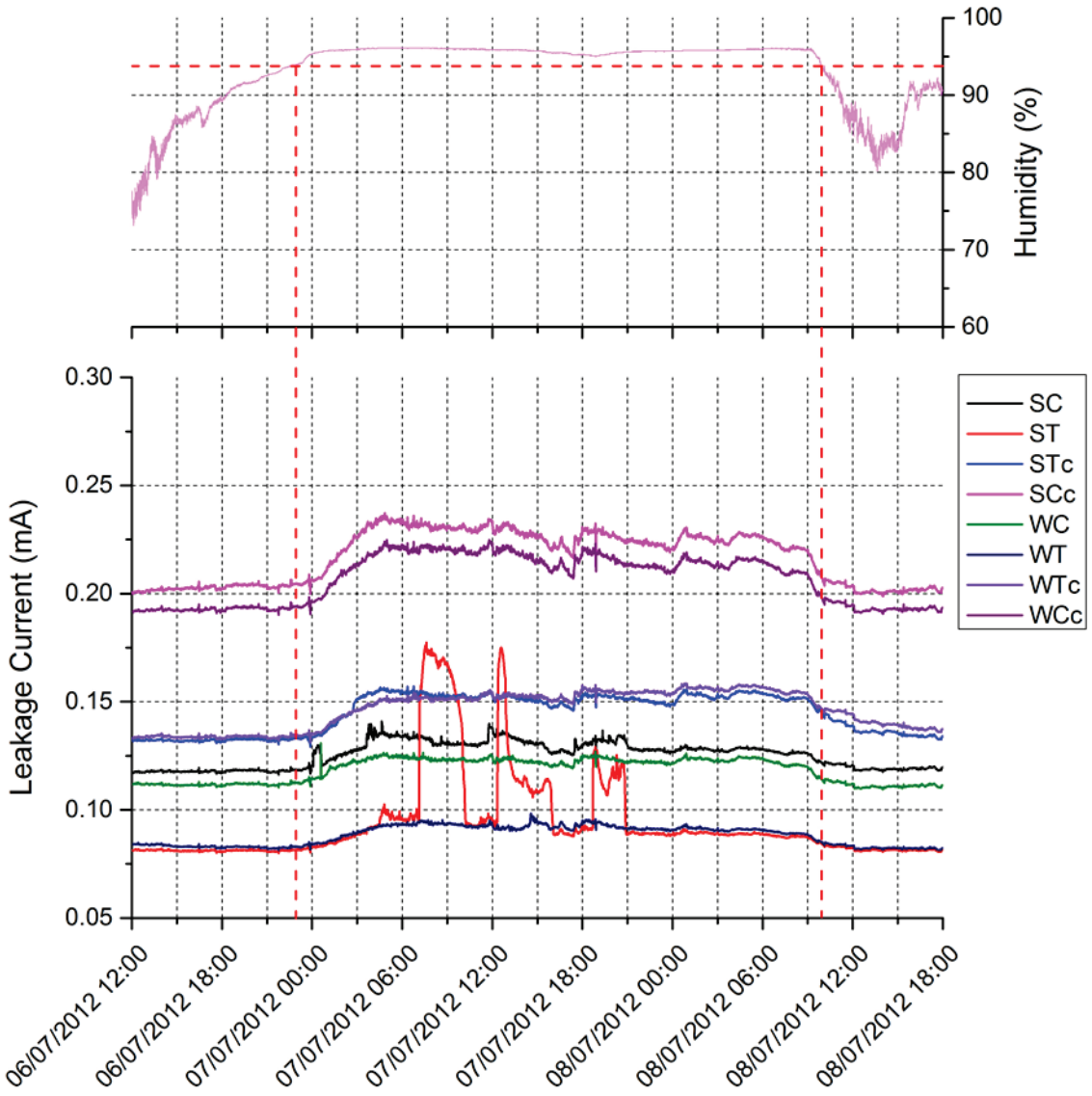

Figure 5.27 - Effect of relative humidity on Leakage current – 6th to 8th of July 2012

5.3.5.3 Effect of fog

Visibility is used to define fog, mist or haze. Fog is a visibility of less than 1 km, mist is a visibility between 1 km and 2 km while haze is a visibility between 2 and 5 km. Figure 5.28 shows a four day period in August 2012 during which very low, near zero visibility was registered by the present weather detector. On three separate occasions, dense fog, indicated by the drop in visibility, descents in the evening and lasts through the night hours, dissipating the following morning. The tiny water droplets in the air sit on the insulators forming larger water droplets that dissolve the ionic particles present in the pollution layer. As a result, fog is accompanied by rise in leakage current activity on all insulators.

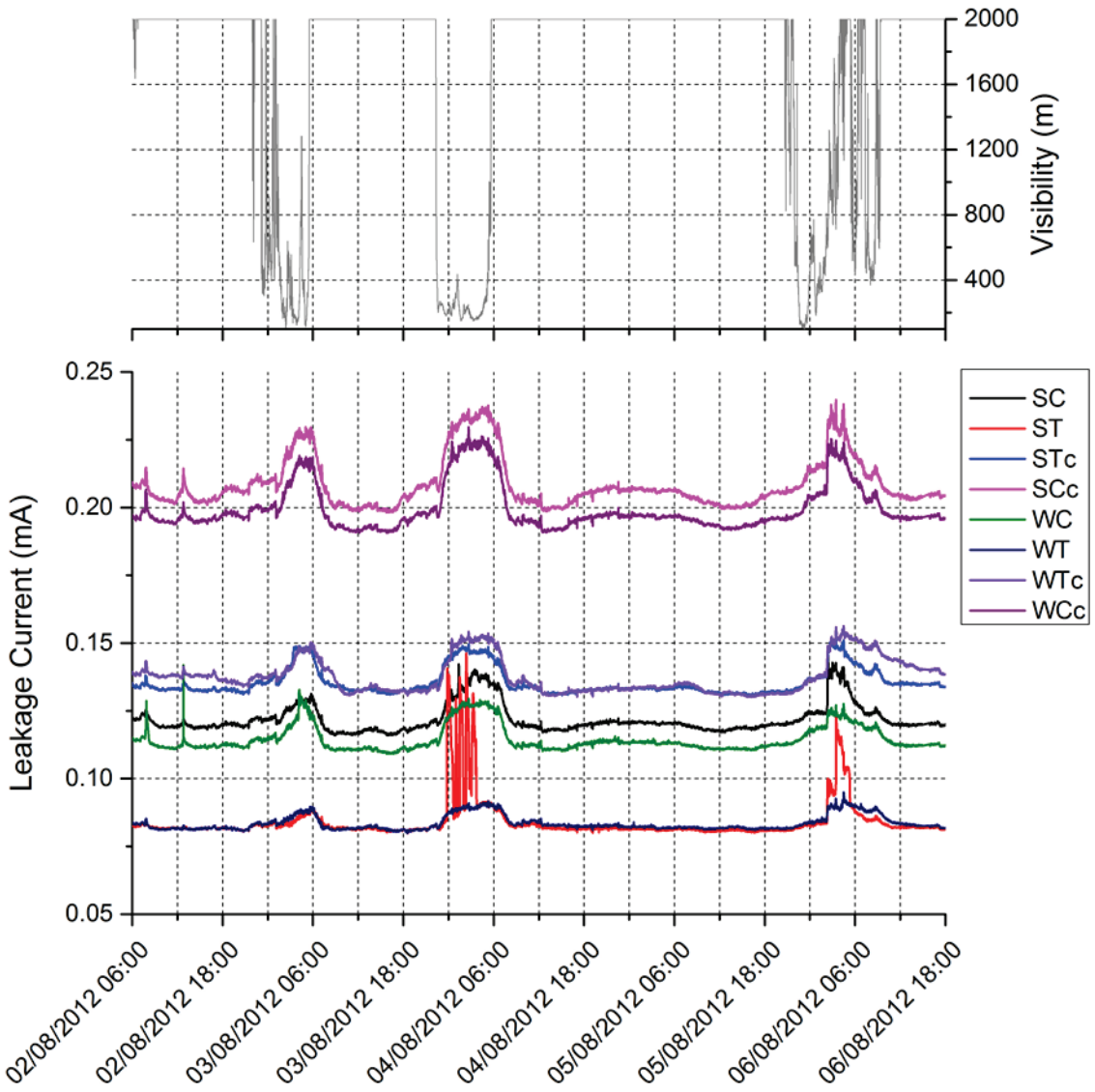

Figure 5.28 – Effect of fog on Leakage current– 2nd to 6th of June 2012

In Figure 5.29 another period with heavy fog is presented during May 2013. By then the insulators were installed at the trial site for almost a year. Like before, two occasions with heavy fog during the night result in increased leakage current activity, subsiding by the following morning when the fog dissipates.

An interesting observation from Figure 5.29 is that the leakage current rise due to fog on the SC (black trace) and ST (red trace) insulators is substantially higher than for the rest of the insulators. The difference in behaviour can be attributed to the fact that these two insulators are the most exposed to the prevailing weather. Because they are facing south, their longitudinal axis is frequently perpendicular to the easterly wind from the sea. Consequently, they are more likely to accumulate pollution faster than the west-facing insulators or the SCc and STc insulators which are somewhat sheltered from the wind by the SC and ST insulators.

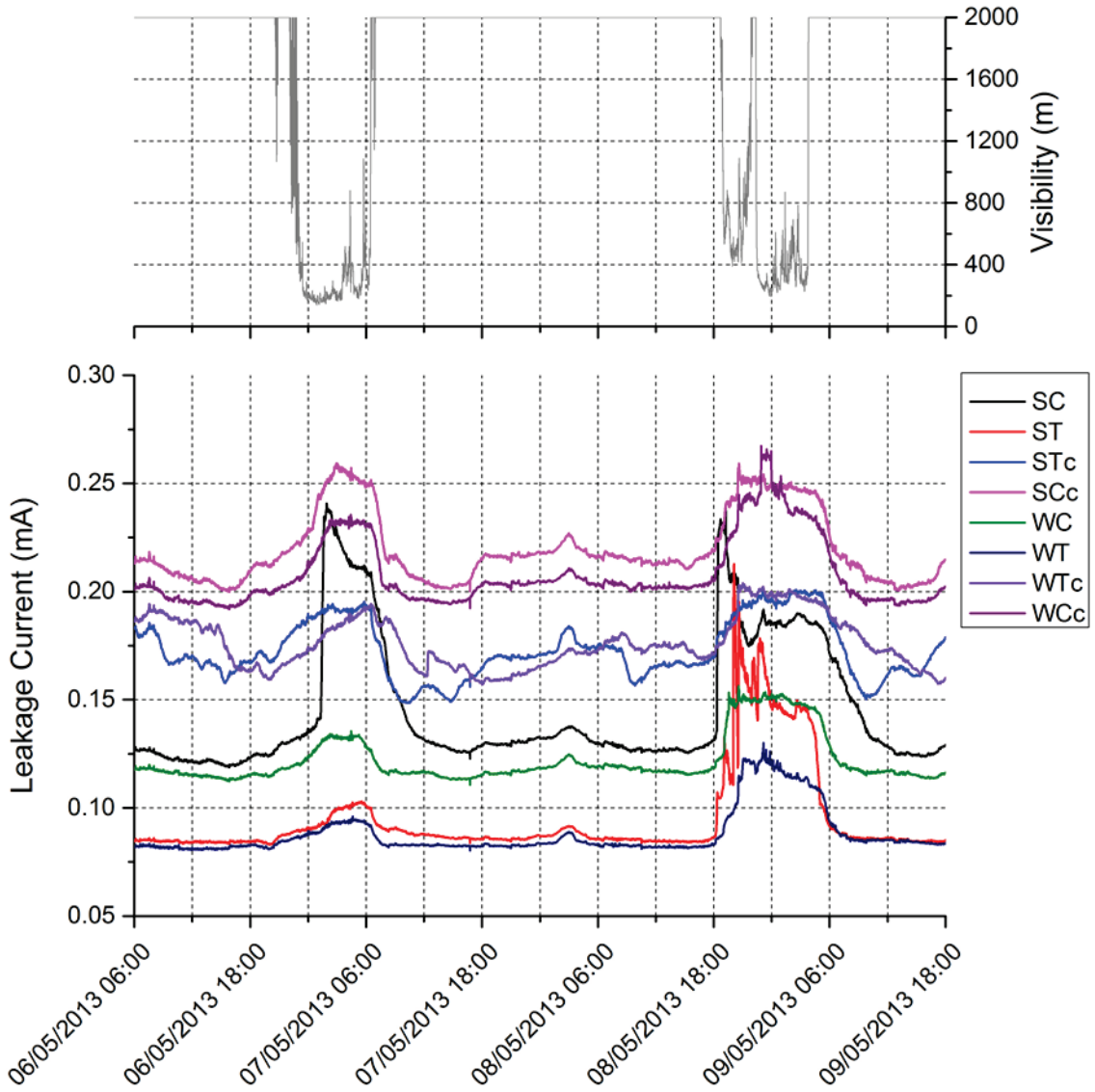

Figure 5.29 - Effect of fog on Leakage current – 6th to 9th of May 2013

As mentioned earlier, the cameras on the site can be used to verify the weather instrumentation readings. Figure 5.30 (a) shows the foggy weather conditions at the site at 07:00 on the 7th of May. At the same time, water droplets are clearly visible on the compression insulator of Figure 5.30 (b), marked in red circles.

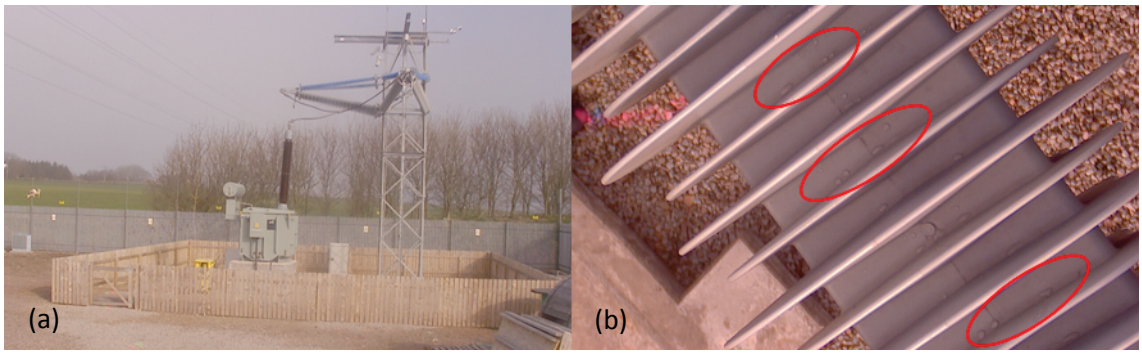

Figure 5.30 - Site camera view (a) and insulator view showing water droplets on the compression insulator (b) at 07:00 on 7th May 2013

The effect of fog at the site is similar to that of humidity described in *Section 5.3.5.2*. In average values the leakage current rises approximately 15% for the compression insulators and 20% for the tension insulators when the visibility drops below 400 m. However, the effect is not observable throughout the year but mainly between May and August. In order for the effect to manifest, it requires the fog to descent after dry periods with no rainfall that allow for pollution to be accumulated on the insulators. During the autumn and winter months, precipitation tends to wash the insulators more frequently reducing the build-up of pollution and minimising the effect of fog.

5.3.5.4 Effect of rain

Figure 5.31 shows the period between 12:00 on the 11th of October 2012 and 06:00 on the 13th of October 2012. The wind the few days before was gradually turning from south on the 9th to east on the 13th, with wind speeds reaching up to 60 mph. There was no rainfall at the site from the 8th until the evening of the 11th. A spell of moderate precipitation beginning at 22:00 on the 12th with average rate not exceeding 20 mm/h, initially raises the leakage currents on all insulators. The increase in leakage current is substantially higher on the SC insulator with 0.28 mA, an increase of 133 %, and the ST insulators with 0.4 mA, an increase of 567 %. These high values however do not last more than a few minutes as the rain dissolves and washes off most of the conductive pollution that has accumulated on the insulators.

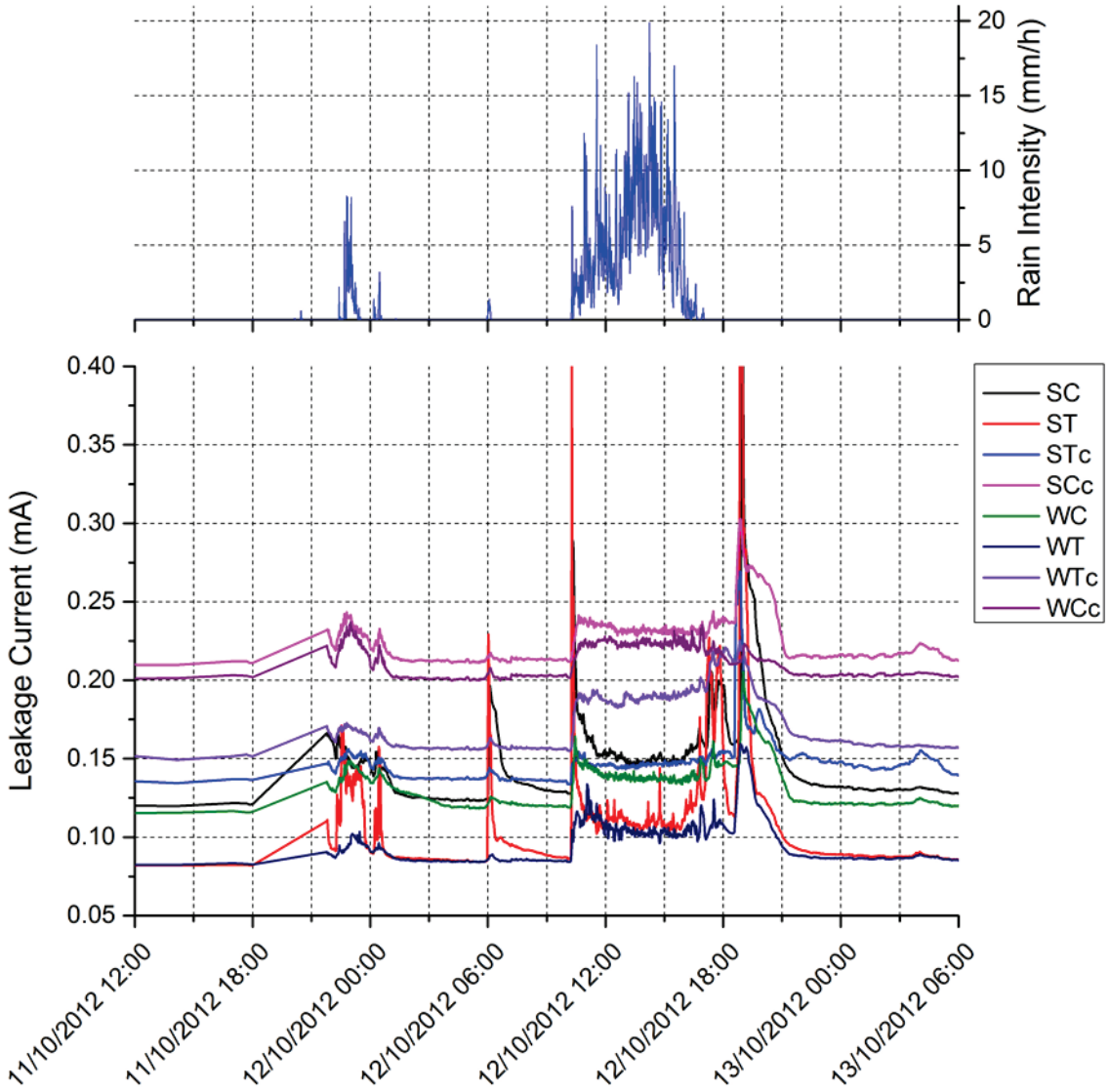

Figure 5.31 – Effect of rain intensity on Leakage current – 11th to 13th of October 2012

Figure 5.32 shows a longer four-day period between 25th and the 29th of November 2012. During this period rainfall is more frequent with several spells of moderate precipitation occurring on a daily basis. The wind initially blows from the east but quickly changes direction to become northerly on the 26th. The combination of the wind not blowing from the coast and the frequent rainfall that washes the pollution from the surface of the insulators prevents the large variations in leakage current activity shown in Figure 5.31.

The effect of precipitation on the insulating cross-arms is twofold. On one hand, it results in high increase in leakage current especially on the south facing insulators that have a bigger surface area exposed to the prevailing wind. This becomes more pronounced if the rainfall is preceded by dry a period that allows pollution to accumulate on the insulators. On the other hand, rainfall has a beneficial effect on the insulators since it

tends to clean them, reducing the build-up of pollution. However, when rainfall becomes heavy, i.e. the precipitation rate exceeds 60 mm/h, the volume of water alone is sufficient to increase the leakage current on all insulators.

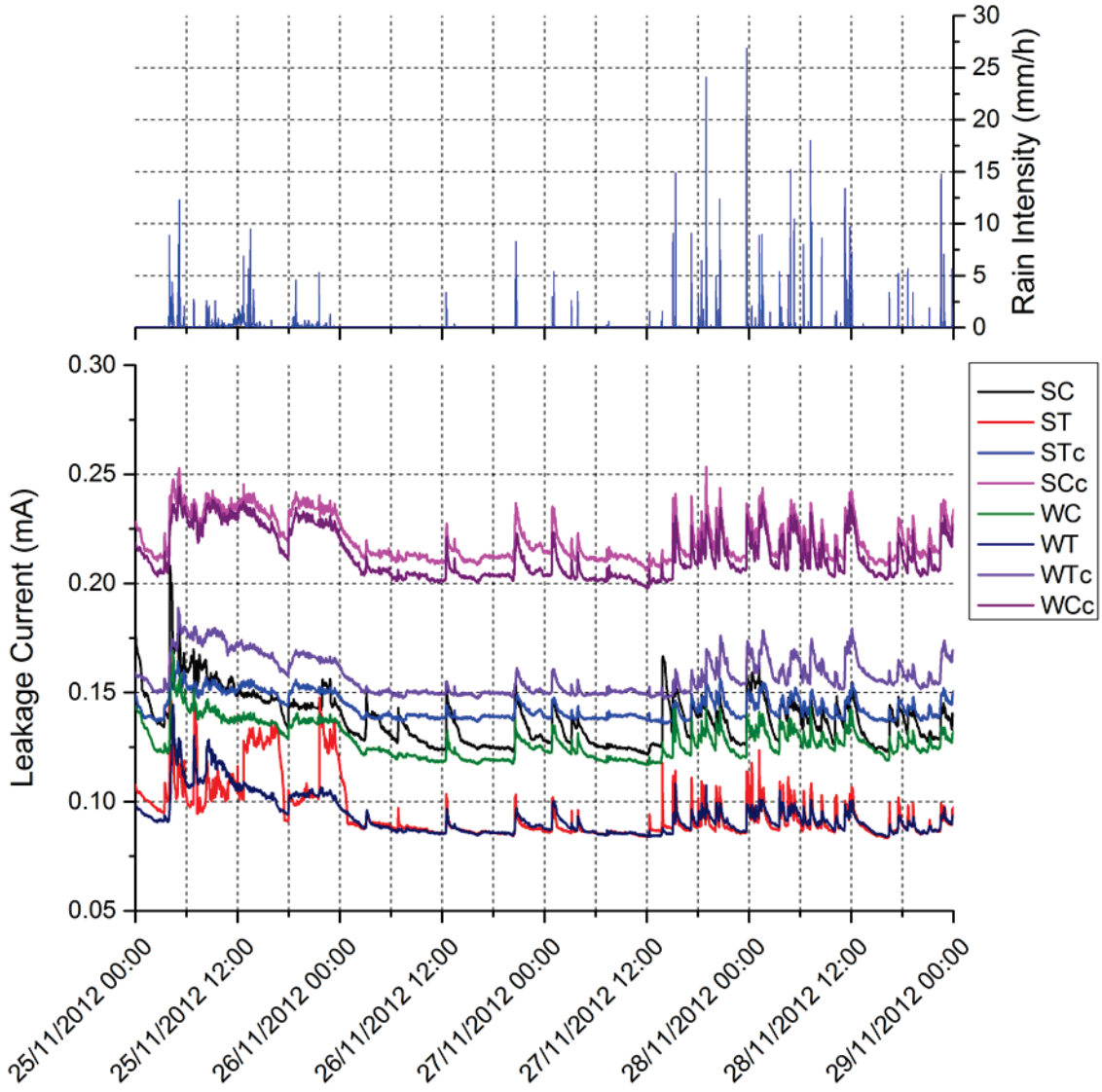

Figure 5.32 - Effect of rain intensity on Leakage current – 25th to 29th of November 2012

5.3.5.5 Effect of wind

From the previous sections it was made obvious that easterly wind blowing from the coast accelerated the deposition of conductive pollution on the cross-arms. This together with humidity, fog or rain resulted in increased leakage current activity. However, it is not only the direction of the wind that affects the leakage currents on the insulators but also its speed. Especially in the winter months it is common for wind speeds to exceed 60 mph at the trial site.

An example is shown in Figure 5.33 where from the 24th until the 26th of September 2012 the wind had a north-easterly direction and reached speeds of up to 88 mph. The strong wind is accompanied by rainfall which begins at approximately 20:00 on the 24th and lasts until 12:00 on the 25th. The rise of leakage current on all insulators follows the rise in wind speed. The maximum wind speed was observed at 08:00 on the 25th while at the same time the leakage current on the ST insulator that was mostly affected by the weather reached its peak at 0.77 mA, an increase of more than ten times the steady state value.

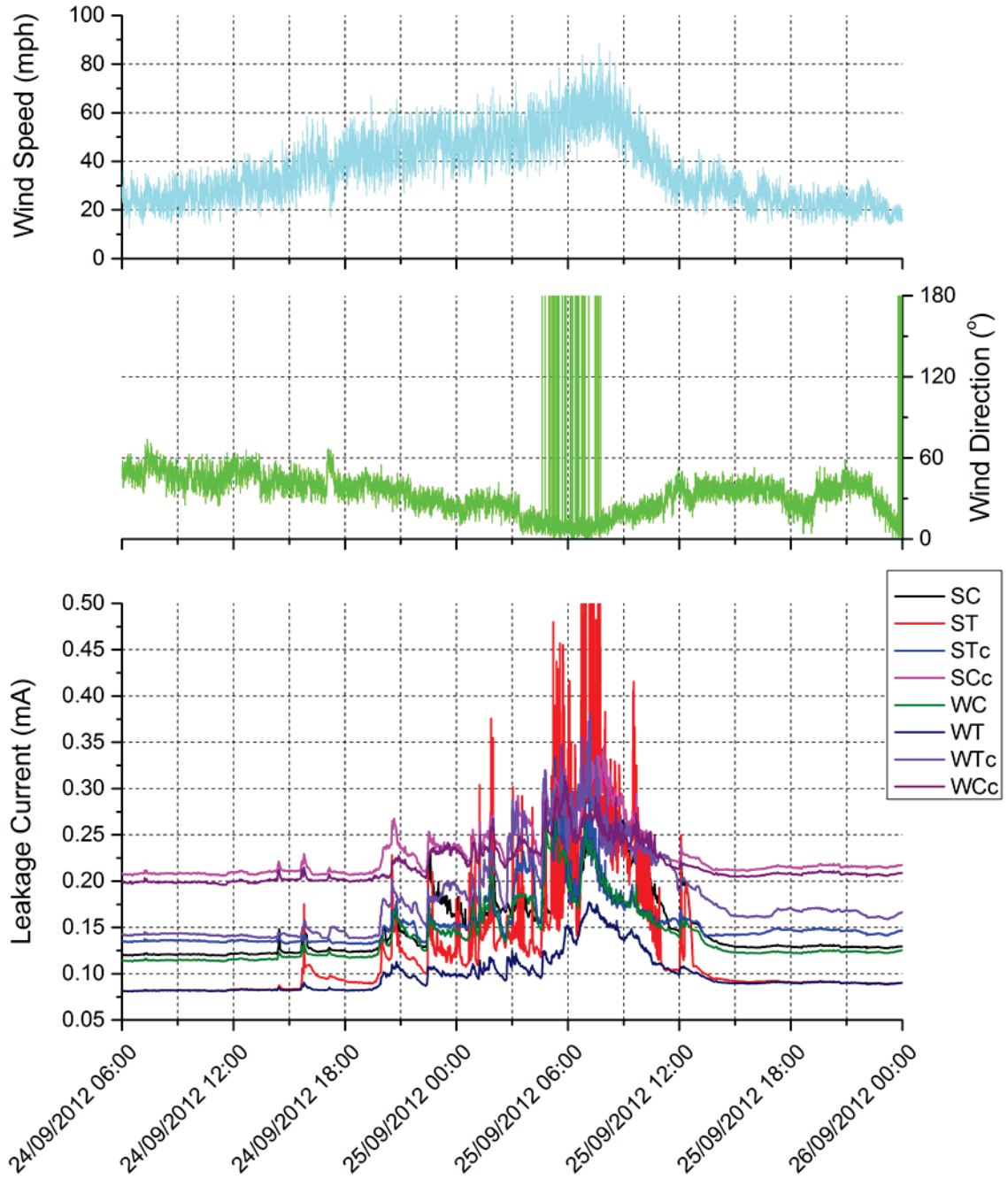

Figure 5.33 – Effect of wind speed and direction on Leakage current – 24th to 26th of September 2012

In Figure 5.34 the wind direction from the midnight of the 14th of December until 15:00 on the 15th of December 2012 changes by the full 360°. Starting as southerly, it quickly turns easterly with the wind speed also picking up, reaching 80 mph at 22:00 on the 14th. When the wind is at its maximum speed the leakage currents also reach their maximum with the SC and ST insulators showing the highest values. This period of strong wind also goes along with rainfall but the increase in leakage current is not as high as in Figure 5.33 due to the gradually changing wind direction which does not allow pollution to accumulate at the same rate since the wind is not constantly blowing from the east.

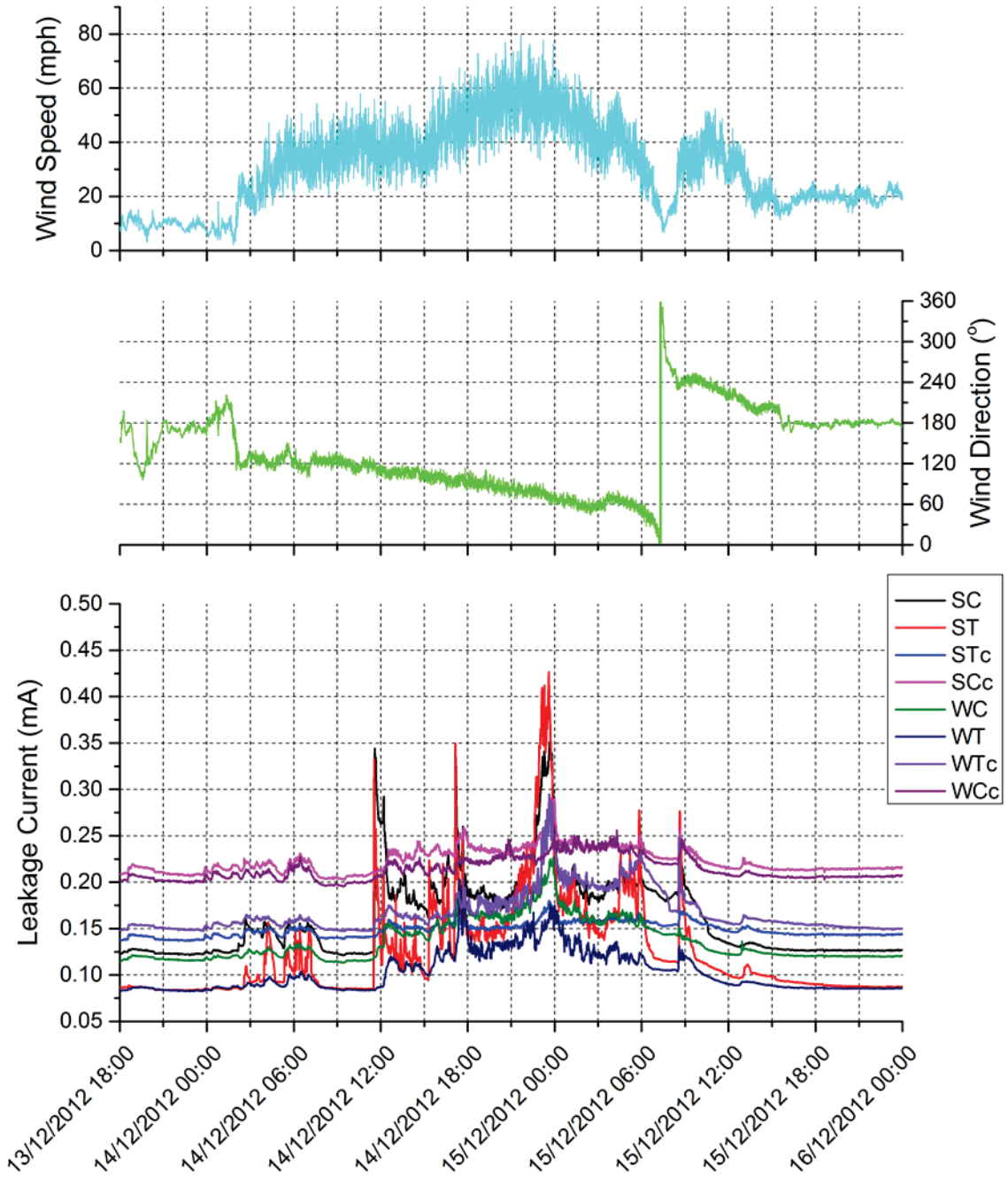

Figure 5.34 - Effect of wind speed and direction on Leakage current – 13th to 16th of December 2012

In general throughout the first year of the live trial the highest leakage currents have been observed during periods of very strong winds exceeding 80 mph combined with rainfall. The highest leakage current was recorded on the SC insulator during such a period in March 2013 which peaked at just over 1.4 mA.

5.3.5.6 Year one review

To examine the performance of the insulating cross-arms during their first year on a live installation, the leakage current recordings for each of the first twelve months of the trial were averaged and plotted (Figure 5.35). The average leakage current values for most of the insulators show a rise during the winter and spring months but by May 2013 they return down to their original level at the beginning of the trial. This behaviour is an indication that no significant ageing has taken place.

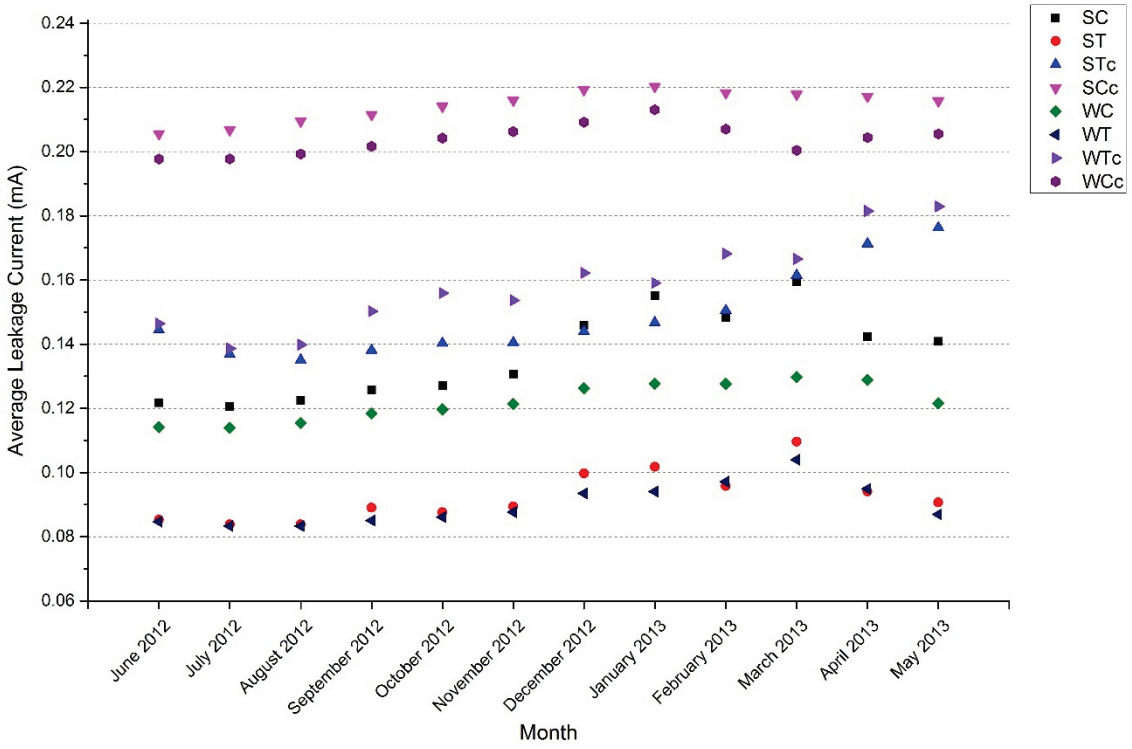

Figure 5.35 - Monthly average leakage currents for live trial year one

Exception to the behaviour described above were the STc and WTc insulators. As Figure 5.35 shows, from November 2012 onwards their average leakage current was increasing month over month. From the data collected it was not possible to find a correlation between a specific weather phenomenon and the difference in leakage current activity of these two insulators. During the regular inspections at the trial site however, a couple of observations were made that could explain the discrepancy. Firstly, corona discharges were observed from the first few sheds of these tension insulators during rainy nights.

Secondly there was charring on the first shed of the insulators, an indication of intense corona activity. It is believed that the 'butterfly' grading device was the culprit. The combination of proximity to the conductor and the non-optimised for 400 kV geometry of the grading device resulted in higher than appropriate electric field at the vicinity which in turn led to corona discharges (Figure 5.35 (a)) that slowly damaged the surface of the insulators (Figure 5.35 (b)). The magnitude of leakage current recorded is not sufficient to warrant any concern regarding the reliability of the insulators at this stage but the upward trend is an indication of accelerated ageing for the STc and WTc insulators.

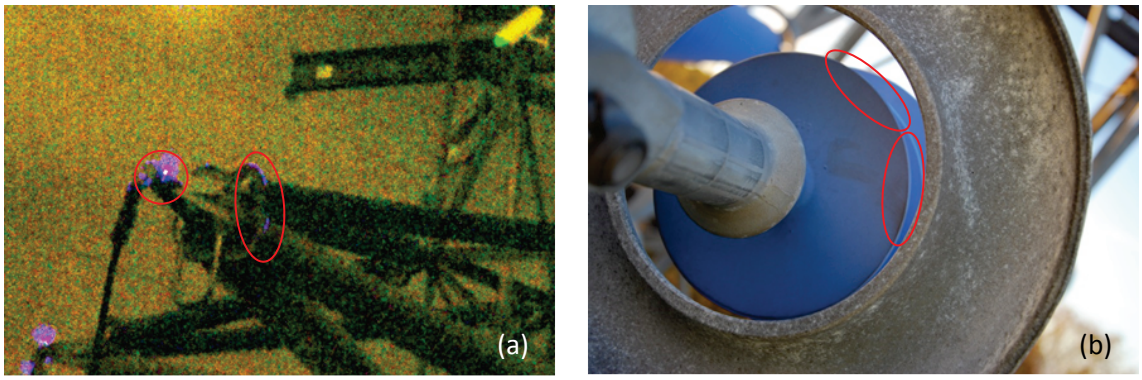

Figure 5.36 - Corona discharges from ICA (a) and charring on insulator shed (b)

Despite the fact that the readings from the various instruments at the trial site were timestamped, not all of the sensors recorded data at the same intervals. For example, leakage current readings were taken at a rate of 1 kHz whereas the fog sensor was taking a reading once every 15 seconds. To statistically analyse the entire first year of the trial, from June 2012 to May 2013, the available data had to be reduced in order to obtain the recordings from all instruments corresponding to the same intervals and also to limit the amount of data in order to speed up the processing. To achieve this, the readings from the various instruments were averaged over 2.5 hour intervals, amounting to a total of 3522 data points for each sensor.

To compare the leakage current of each insulator to that of every other insulator and also to key weather parameters, the Spearman correlation coefficients were calculated using a two tailed test with significance of 5 %. Spearman's correlation coefficient or Spearman's rho (ρ) measures the strength of association between ranked variables or in other words it tests whether there is significant evidence to suggest that a monotonic relation exists between the variables. It was deemed more appropriate than the most

common Pearson correlation because it is more suitable for data that are not normally distributed and is better at detecting non-linear relationships. Spearman's correlation coefficient is defined as:

$$\rho = 1 - 6 \cdot \sum \frac{d^2}{N \cdot \left(N^2 - 1\right)} \tag{5.3}$$

where:

d : the difference in statistical rank of corresponding variables

N : the sample size

In addition to the correlation coefficients between the leakage currents, the correlation coefficients between the leakage currents and temperature (T), relative humidity (RH), rain intensity (RI) and dew point (DP) were also computed (Table 5.2). The dew point was calculated using the Magnus approximation of equation (5.4):

$$DP = \frac{257.14 \cdot \left[\ln\left(\frac{RH}{100}\right) + \frac{18.678 \cdot T}{257.14 + T} \right]}{18.678 - \left[\ln\left(\frac{RH}{100}\right) + \frac{18.678 \cdot T}{257.14 + T} \right]} \tag{5.4}$$

Table 5.2 *- Spearman correlation coefficients for live trial year one*

	SC	**ST**	**STc**	**SCc**	**WC**	**WT**	**WTc**	**WCc**	**T**	**RH**	**RI**	**DP**
SC	1.00	0.92	0.78	0.82	0.93	0.89	0.76	0.85	-0.45	0.10	0.09	-0.37
ST	0.92	1.00	0.77	0.78	0.90	0.90	0.76	0.82	-0.42	0.12	0.11	-0.33
STc	0.78	0.77	1.00	0.63	0.78	0.73	0.88	0.64	-0.36	0.03	0.05	-0.33
SCc	0.82	0.78	0.63	1.00	0.87	0.78	0.60	0.95	-0.31	0.33	0.07	-0.15
WC	0.93	0.90	0.78	0.87	1.00	0.92	0.76	0.90	-0.41	0.17	0.08	-0.31
WT	0.89	0.90	0.73	0.78	0.92	1.00	0.73	0.82	-0.42	0.16	0.08	-0.32
WTc	0.76	0.76	0.88	0.60	0.76	0.73	1.00	0.63	-0.40	0.02	0.05	-0.36
WCc	0.85	0.82	0.64	0.95	0.90	0.82	0.63	1.00	-0.35	0.30	0.11	-0.20

The cells in blue in Table 5.2 show the existence of a very strong, positive monotonic correlation between the leakage current on the insulators of the south facing cross-arm

and their counterparts on the west facing cross-arm. In other words, when the current on the south facing cross-arm increases so does the current on the west facing cross-arm albeit not necessarily by the same amount. The lack of significant variation in the leakage current behaviour of the two cross-arms indicates that their performance should be similar if their orientation in relation to the prevailing weather was the same.

The red cells show the correlation coefficients between the pairs of compression insulators on either cross-arm, i.e. SC and SCc, WC and WCc. The correlation between the SC and SCc insulators is weaker than the correlation between the WC and WCc insulators. The difference can be attributed to the orientation of the insulators and direction of the prevailing weather which as mentioned earlier is from the east. The south facing insulators have their longitudinal axis perpendicular to the direction of the prevailing weather, exposing more of their surface. Because of their orientation, the SC insulator is partially shielding the SCc insulator, potentially reducing its pollution accumulation rate. The situation is not the same for the WC and WCc insulators since one does not shield the other, something that makes their behaviour more similar.

The correlation coefficients in the green cells are between the compression insulators and the tension insulators directly above them. Interestingly, there is a very strong monotonic correlation for the insulators pairs that are located the furthest away from the conductor, indicating that the novel compression insulators exhibit similar leakage current behaviour to the industry standard tension insulators. The same is not true for the insulator pairs that are close to the conductor with a moderate correlation between the compression and the tension insulators. This corroborates the evidence found by analysing Figure 5.35 which show that the STc and WTc insulators behave differently than the rest of the insulators, most likely due to corona discharges from the HV grading device.

Looking at the correlation between the various weather phenomena and the leakage currents on the individual insulators, it can be seen that the monotonic correlation, positive or negative, is moderate at best. This is not to say that the weather phenomena and leakage current are not correlated since the correlation coefficients in almost all cases are higher than the significance level. What the numbers suggest is that the leakage current behaviour on the insulators is not majorly affected by any individual weather phenomenon but it is the result of the combination of more than one factors.

5.4 Discussion

The insulating cross-arm has to perform the functions of both the steel cross-arm and the insulator string. As a result the mechanical requirements for the ICA are much more demanding than for traditional OHL insulators. The mechanical trial commissioned in late 2010 in a service-like environment did not manage to produce useful data regarding the mechanical performance of the ICA due to the instrumentation malfunctioning because of the hostile environment. What the trial did manage to provide was useful information regarding snow and ice accretion. Despite their radically different geometry, the compression members of the ICA exhibited similar behaviour to the tension members and the older glass insulators that were still installed on the line. Also the arrangement of the insulating members in the cross-arm assembly did not appear to worsen the accretion of ice and snow. The above observations provided confidence that the ICA could be used even in the most adverse of weather conditions. The only negative aspect of the ICA design identified during the trial was that the orientation of the compression insulators with the spine of the profile facing up hindered their self-cleaning properties. This shortcoming was taken into account when designing the updated profile for the insulators as described in *Chapter 2*.

The effects of pollution accumulated on composite insulators are relatively minimal under dry conditions. However, in the presence of moisture the ionic salts usually present in the pollution layer tend to dissolve, forming a conducting band. The pollution layer heats and dries non – uniformly due to the non – uniform pollution distribution. This causes increase of the voltage stress dropped across the newly formed dry band of high resistance and consequently spark discharges can be initiated when the breakdown stress of the surrounding medium is exceeded. Then, the dry band can be more easily bridged by arc discharge often resulting in the burning of the insulator surface followed by the development of a conductive track ultimately causing complete flashover under the right conditions [102, 103].

As discussed in *Section 2.3.8*, increased leakage current flow on the surface of insulators is an intrinsic part of the contamination flashover process. As such, leakage current has been used to study the performance of insulators and identify changes in their surface properties indicative of ageing. To examine how the insulating cross-arms perform in an

outdoor environment more representative of the service conditions, a trial site was commissioned to look into how the weather affects the leakage current on the insulating members and how the insulators perform compared to one another. Summarising the findings from the first year of the trial, the following observations were made:

a) The insulators closest to the conductor show higher base leakage current than their counterparts further away due to capacitive coupling between the conductor, the cross-arm members and the tower. The effect which is a result of the geometric placement of the components at the trial site is not an indication of the performance of the insulators but it was not possible to be excluded from the analysis.
b) A relative humidity threshold exists around 93% - 94% which if exceeded, raises the average leakage current values of all insulators regardless of other weather conditions. The increase is in the order of 15% for the tension insulators and 20% for the compression insulators.
c) Fog has a very similar effect to humidity. A drop in visibility below 400 m triggers leakage current activity on all insulators of the same order of magnitude as humidity. The effect is mainly observed during months with low cumulative precipitation that allow pollution to build up on the surface of the insulators.
d) All insulators show self-cleaning properties. Their leakage current reduces even after minor periods of precipitation despite the fact that the leakage current on some of the tension insulators increases briefly when a prolonged dry period is followed by rainfall.
e) The orientation of the cross-arm can affect its performance. The leakage current on the insulators of the south facing cross-arm is consistently higher than that of their west facing counterparts because the predominant wind (from the east) is perpendicular to their longitudinal axis. A bigger area exposed to the prevailing weather accelerates pollution accumulation.
f) The compression insulators exhibit slightly higher base leakage current than the tension members directly above them. This can be attributed to their larger circumference and their bigger surface area.
g) The base leakage current for all insulators after a year has remained at the same low levels as at the beginning of the trial, indicating that no significant ageing has

taken place. Also, this shows that the novel compression insulators are ageing in a similar manner as the industry standard tension insulators.

h) In terms of monthly average leakage current, the STc and WTc insulators have shown to behave differently than the other insulators, exhibiting an increasing trend. Onsite inspections have revealed that discharges originating from the HV-end electric field grading device, also known as 'butterfly', have begun damaging the first shed of the aforementioned insulators. This observation corroborates the results of both the FEA analysis and the testing which point out that the 'butterfly' grading device is not suitable for operation at 400 kV.

5.5 Conclusion

The first trial installation of insulating cross-arms mainly aimed to test their mechanical performance. Although this was not achieved, through the process, handling, transportation and installation procedures were established and tried successfully. Additionally, the photographic evidence of snow and ice accretion collected have helped to design a more efficient compression insulator profile.

The two cross-arms installed at the live trial site have seen minimal interruptions of supply during the first year of the trial. More importantly, even with a subpar HV grading solution installed, no flashovers have been observed, a testament to the robustness of the design and the manufacturing process. All in all, the first results from the live trial show that the insulating cross-arm performs according to design expectations.

6. CONCLUSION

The study was set out to advance the development of a new insulating cross-arm from the early prototype stage to a fully functional product capable for operation on the UK's 400 kV transmission network. The ICA can be used to either directly replace the steel cross-arms and insulators on existing lattice towers to enable the upgrading of existing infrastructure or for building new towers with smaller footprint. Except from the benefits that the ICA offers compared to other solutions, the use of the technology can help to reduce the environmental, social and economic impact of overhead lines which is vital for the expansion of the network required to satisfy the increasing demand for electricity and the connection of new sources of generation.

The study sought to answer the following four questions:

1. Is it be possible to design a profile for an insulator with an unconventionally shaped, non-circular cross-section that can be used as the main structural element of the ICA?

2. What grading devices are required to effectively manage the electric field on and around the ICA?

3. Do the novel insulator and the ICA assembly pass the tests that certify their ability to handle the service conditions?

4. How does the ICA perform in an outdoor environment energised at 400 kV and what are the effects of the weather?

6.1 Findings

Using a combination of past knowledge from existing literature, experimental work and recommendations from international standards, a novel insulator was developed based on a unique, non-cylindrical, T-shaped core which has 85% smaller cross-sectional area than a cylindrical core while exhibiting similar mechanical characteristics. After examining six profile variations, it was determined that the lateral orientation which would give the best performance in wet and icy conditions, less likelihood of biological growth and reduced weight and cost would be with the flat face of the core facing

upwards and tilted by 6°. The results obtained from performing flashover tests on a conventional 145 kV composite insulator indicated that the elevation angle that would give the optimum wet performance lay between 0° and 10°. Therefore, the elevation angle for the compression insulator was set to 6°. The dimensions of the insulator were calculated based on the assumption that the ICA would be used to uprate an OHL with L3 towers from 275 kV to 400 kV. The optimal insulator profile that met all specifications and did not deviate from the standard recommendations was determined to be an alternating profile with three different shed sizes, an arcing distance of 3083 mm and a creepage distance of 12470 mm.

With the help of CAD and FEA, electric field grading devices were designed for both the LV and HV ends of the ICA. It was discovered that the end-fitting of the compression insulator played a detrimental role on how the electric field was distributed around the triple junction of the insulator, making the control of the field at that area a priority. For the LV end, a simple grading device was designed for the compression insulator, resembling a ring which follows the general shape of the cross-section of the insulator, which can be installed on each insulator individually. For the HV end, an iterative process yielded two designs. First, the 'butterfly' grading device was a unibody piece of cast aluminium for all four ICA members. FEA simulations and tests in the laboratory showed that it could effectively control the electric field at voltages of up to 132 kV. The design was patented and the device was used on six cross-arms installed on a live line in Scotland in August 2013. Second, the 'M-W' grading device was a solution made out of four components for managing the field at voltages of up to 400 kV. In addition to meeting all the electric field criteria according to the results of the FEA, the design exhibited a degree of redundancy while the device was designed to be easy to install and service, easy and cheap to manufacture and have minimal visual impact.

The compression insulator and the cross-arm assembly were subjected to a multitude of tests adapted from international standards and the Technical Specifications of National Grid. The performed tests aimed to test the electrical characteristics of the cross-arm and the quality of the materials and manufacturing process of the compression insulator since these two areas were identified to present the most risk. All of the tests were completed successfully except from the corona extinction test for which the appropriate equipment was not available at the time.

To examine how the cross-arm performs in a service-like environment, two trials were commissioned, an unenergised mechanical trial and a 400 kV live trial. Although the mechanical trial did not manage to provide any information regarding the mechanical performance of the ICA, the snow and ice accretion patterns recorded were able to be used for optimising the profile of the compression insulator. The monitoring equipment installed at the live trial recorded the leakage currents on two cross-arms and the weather conditions at the site. The results after a year of continuous monitoring showed that there were humidity and visibility thresholds, above 93% for the former and below 400 m for the latter, which increased the average leakage current by 15% on the tension insulators and by 20% on the compression insulators. It was found that the orientation of the cross-arm in relation to the prevailing weather affected its performance. When its longitudinal axis was perpendicular to the weather the leakage current was higher because more of its surface was exposed. The performance of the novel compression insulators was found to be as good as that of the industry standard tension insulators, reaffirming the potency of the design. Finally, on-site observations showed that the 'butterfly' grading device could not effectively manage the electric field on the cross-arm at 400 kV, confirming the results of the FEA simulations and testing.

6.2 Implications

The use of international standards and technical specifications for design purposes was extensive throughout this study. However, none of them specifically mentions insulating cross-arms since they are aimed at conventional OHL insulators. Evidence from this thesis point to the fact that insulating cross-arms have more degrees of complexity not only because they consist of more than one insulators but also because their function dictates different requirements, mechanical and electrical.

The same argument is true for standards that relate to testing. Most of the testing procedures have been specified with tension insulators in mind. Many of them are not suitable for assemblies of multiple insulators or for insulators that are subjected to compressive or cantilever forces. Furthermore, some of the tests such as the dye penetration test, the tracking and erosion test and others, which are often considered essential for the certification of an insulator, provide very little information regarding the performance of an insulator. In some cases these procedures also fail to take into

account new materials and manufacturing processes, requiring tests that may no longer be relevant. Therefore, some of the existing standards need to be revisited and new ones need to be introduced to cover the new usage scenarios of composite insulators such as insulating cross-arms.

The study has used FEA simulations to identify areas of high electric field on the ICA and design electric field grading devices. Although the limits that have been established for the electric field magnitude are based on solid theoretical principles and well documented research, the details of performing the FEA studies are vague at best and are not included in international standards. The majority of FEA studies presented in existing literature take advantage of the inherent rotational symmetry present in conventional OHL insulators to reduce the complexity of the computation. As a result most of the studies are two dimensional. By not taking into account all three dimensions, there is great risk of leaving out a big portion of data, producing results that might not reflect reality. Additionally, not all problems are symmetric. The compression insulator of the ICA for example is not cylindrical and therefore the electric field around its end-fitting is not uniform. A set of clear guidelines is required so that FEA studies can produce meaningful results that can be used to compare the performance of different solutions with consistency.

6.3 Limitations and future research

Certain limitations have been encountered as a consequence of the methodologies used in the study that need to be considered. Regarding the compression insulator, only one of the ICA usage scenarios was taken into account for designing its profile. Although all the parameters are within the acceptable limits, the fact remains that the insulator is optimised for just the case of uprating an OHL from 275 kV to 400 kV. This is not necessarily negative since this scenario is probably one of the most difficult to implement, especially given the use of L3 towers which are relatively compact. However, for other applications of the ICA technology, such as lower voltages and new builds, different profiles might prove to be more efficient in terms of performance and cost.

As mentioned earlier in this chapter, 3-D FEA was used to design the grading devices for the ICA due to the non-symmetrical nature of the compression insulator and the ICA assembly. One of the disadvantages of the this approach was the greatly increased

number of finite elements required for the representation of the models which was only made worse due to the scale and complexity of the ICA components. Although every attempt has been made to not compromise the fidelity of the models, limitations of the computing hardware prevented increasing the element count further to achieve even more accurate results. Furthermore, due to the aforementioned hardware limitations, it was not possible to include more than one cross-arms or other associated components, such as the tower or the conductors, in the simulations.

For testing, time was the biggest limitation. The scale of the ICA assembly and the alterations that needed to be made to the testing procedures to accommodate it in addition to the lengthy manufacturing times of prototype components did not allow for the completion of all the scheduled tests. Moreover, some of the subtests of the test on interfaces and connections of end-fittings had to be bypassed due to unavailability of testing equipment at the time of testing. For the same reason, the corona extinction test with the 'M-W' grading device was not completed successfully. Consequently, the results of these tests cannot be characterised as conclusive.

The geometric placement of the different components at the live trial site created some unnecessary complications to the analysis of the results. The effect of capacitive coupling, which was different on each of the insulators and could not be quantified, could not be isolated from the resistive leakage current that was of interest. It would have been more straightforward to be able to compare the behaviour of the insulators if the capacitive leakage current could be removed from the equation. Another limitation of the trial was the limited storage available for data. A consequence of this was the fact that leakage current was recorded only during the first five seconds of every minute. Also due to storage limitations, it was not possible to continuously record video with the cameras; still photos were taken instead at regular intervals. Due to the data collection methodology employed, it is possible that some aspects of the behaviour of the ICA have remained unexamined.

6.4 Future research

Drawing from additional case studies showcasing more ICA usage scenarios, a range of compression insulators based on the non-cylindrical core can be designed in the future, each optimised for a specific application. In addition to the different upgrade

possibilities of existing towers, the compression insulator could be used on its own or with just one other tension insulator for monopole structures and other tower designs that do not require a three dimensional cross-arm. Another area that could be explored is the use of ICAs for DC transmission which is quickly gaining popularity.

By expanding the scale of the FEA simulations, it will not only be possible to increase the accuracy of the results and optimise the grading devices even further, it will also be possible to get a better insight on how the field affects the surroundings of the ICA. For example, it is of interest to examine by how much the field emitted from one cross-arm affects the field on a cross-arm of another phase. Also it is important to quantify by how much the EMF is reduced at ground level because of a line employing ICAs compared to a traditional line. Furthermore, extended FEA studies can be used to design other associated hardware, such as conductor shoes and arcing horns, and optimise them for low EMF emission.

In addition to completing the remaining tests, in the future tests not included in the international standards can be added to the test regime for the ICA. A salt fog test of the entire ICA assembly can potentially reveal if the arrangement of the insulators has an impact on their longevity. The round robin pollution test, which is specifically designed for composite insulators, can be used to examine the effects of pollution to the performance of the cross-arm. Also, ice testing of the compression insulator and the assembly as a whole can be used to optimise the ICA for environments experiencing heavy snowfall and icing.

To make the analysis of the data easier, the placement of the conductor at the trial site can be changed to reduce the capacitive coupling discrepancies that are present with the current arrangement. Moreover, expansion of the storage capabilities will ensure that no valuable data is left unrecorded. The addition of equipment that can measure soluble deposit density (SDD) at the site will help to quantify the effect of surface pollution on the insulators. It will also be very beneficial if a steel cross-arm and conventional tension insulator were installed and fitted with the same monitoring equipment to provide a direct comparison between the performance of the ICA and that of the conventional solution.

To summarise, the work presented in this study aimed to bring the insulating cross-arm concept as close as possible to a finished product. The main structural member of the ICA, a novel compression insulator with non-circular cross-section, meets all the standard specifications and can perform at the same level as industry standard products. FEA simulations showcased the effectiveness of the grading solution at controlling the electric field around the cross-arm and laboratory testing has shown that the ICA has the potential to achieve full type approval. Furthermore, the live trial has established the capability of the ICA to perform according to design expectations in an outdoor environment while subjected to harsh weather conditions. Overall, the study has shown that the insulting cross-arm is a viable option for upgrading existing infrastructure and building compact lines in theory and in practice. It paves the way for certification of the ICA for operation and large scale deployment on live networks of up to 400 kV.

REFERENCES

[1] Department of Energy and Climate Change (DECC), "The UK Low Carbon Transition Plan: national strategy for climate and energy", DECC, London, 2009.

[2] M. Cotton and P. Devine-Wright, "Discourses of energy infrastructure development: a Q-method study of electricity transmission line siting in the UK," *Environment and Planning A,* vol. 43, pp. 942-960, 2011.

[3] W. P. Erickson, G. D. Johnson, and D. P. J. Young, "A summary and comparison of bird mortality from anthropogenic causes with an emphasis on collisions," presented at the Third International Partners in Flight Conference, Asilomar, California, 2005.

[4] C. Lomas, R. L. Jackson, and G. A. Speed, "Integrating overhead lines into an environmentally sensitive world," *CIGRÉ Session 1996,* vol. 22-206, 1996.

[5] G. Draper, T. Vincent, M. E. Kroll, and J. Swanson, "Childhood cancer in relation to distance from high voltage power lines in England and Wales: a case-control study," *British Medical Journal,* vol. 330, pp. 1290-1293, 2005.

[6] S. Jay, "Pylons in the back yard: local planning and perceived risks to health," *Environment and Planning C: Government and Policy,* vol. 25, pp. 423-438, 2007.

[7] T. Priestley and G. W. Evans, "Resident Perceptions of a Nearby Electric Transmission Line," *Journal of Environmental Psychology,* vol. 16, pp. 65-74, 1996.

[8] S. Sims and P. Dent, "High-voltage Overhead Power Lines and Property Values: A Residential Study in the UK," *Urban Studies,* vol. 42, pp. 665-694, April 1, 2005 2005.

[9] I. Albizu, A. J. Mazon, and I. Zamora, "Methods for increasing the rating of overhead lines," *Power Tech, 2005 IEEE Russia*, 2005, pp. 1-6.

[10] T. Kavanagh and O. Armstrong, "An evaluation of High Temperature Low Sag conductors for uprating the 220kV transmission network in Ireland," *Universities Power Engineering Conference (UPEC), 2010 45th International*, 2010, pp. 1-5.

[11] D. F. Shankle, "Incremental Voltage Uprating of Transmission Lines," *Power Apparatus and Systems, IEEE Transactions on,* vol. PAS-90, pp. 1791-1795, 1971.

[12] I. Kimoto, K. Kito, and K. Ueno, "Insulator Crossarms for 345-KV EHV Transmission Line," *Power Apparatus and Systems, IEEE Transactions on,* vol. PAS-90, pp. 756-767, 1971.

[13] K. Kopsidas, S. M. Rowland, M. N. R. Baharom, and I. Cotton, "Power transfer capacity improvements of existing overhead line systems," *Electrical Insulation (ISEI), Conference Record of the 2010 IEEE International Symposium on*, 2010, pp. 1-5.

[14] G. I. Gilchrest, "Application of Theory and Practise to the Design of Transmission Line Insulators," *American Institute of Electrical Engineers, Transactions of the,* vol. XXXVII, pp. 805-832, 1918.

[15] E. A. Cherney, "50 years in the development of polymer suspension-type insulators," *Electrical Insulation Magazine, IEEE,* vol. 29, pp. 18-26, 2013.

[16] F. N. Kiessling, P.; Nolasco, J.F.; Kaintzyk, U. , *Overhead Power Lines: Planning, Design, Construction*. Berlin: Springer-Verlag, 2003.

[17] The British Standards Institution, "National Normative Aspects (NNA) for the United Kingdom and Northern Ireland," *BS EN 50341-3-9*, ed, 2006.

[18] D. Dumora, D. Feldmann, and M. Gaudry, "Mechanical behavior of flexurally stressed composite insulators," *Power Delivery, IEEE Transactions on,* vol. 5, pp. 1066-1073, 1990.

[19] The British Standards Institution, "Insulators for overhead lines - Composite suspension and tension insulators for a.c. systems with a nominal voltage greater than 1 000 V - Definitions, test methds and acceptance criteria," *BS EN 61109*, ed, 2008.

[20] S. Wright and D. Dumora, "Design criteria for composite insulators," *Non-Ceramic Insulators for Overhead Lines, IEE Colloquium on*, 1992, pp. 4/1-4/4.

[21] J. Montesinos, R. S. Gorur, B. Mobasher, and D. Kingsbury, "Mechanism of brittle fracture in nonceramic insulators," *Dielectrics and Electrical Insulation, IEEE Transactions on,* vol. 9, pp. 236-243, 2002.

[22] J. T. Burnham, T. Baker, A. Bernstorf, C. de Tourreil, J. M. George, R. Gorur, R. Hartings, B. Hill, A. Jagtiani, T. McQuarrie, D. Mitchell, D. Ruff, H. Schneider, D. Shaffner, j. yu, and J. Varner, "IEEE Task Force Report: brittle fracture in nonceramic insulators," *Power Delivery, IEEE Transactions on,* vol. 17, pp. 848-856, 2002.

[23] M. Kumosa, L. Kumosa, and D. Armentrout, "Failure analyses of nonceramic insulators. Part 1: Brittle fracture characteristics," *Electrical Insulation Magazine, IEEE,* vol. 21, pp. 14-27, 2005.

[24] M. Kumosa, L. Kumosa, and D. Armentrout, "Failure analyses of nonceramic insulators: part II - the brittle fracture model and failure prevention," *Electrical Insulation Magazine, IEEE,* vol. 21, pp. 28-41, 2005.

[25] J. F. Hall, "History and bibliography of polymeric insulators for outdoor applications," *Power Delivery, IEEE Transactions on,* vol. 8, pp. 376-385, 1993.

[26] L. H. Meyer, E. A. Cherney, and S. H. Jayaram, "The role of inorganic fillers in silicone rubber for outdoor insulation alumina tri-hydrate or silica," *Electrical Insulation Magazine, IEEE,* vol. 20, pp. 13-21, 2004.

[27] I. Gutman, R. Hartings, R. Matsuoka, and K. Kondo, "Experience with IEC 1109 1000 h salt fog ageing test for composite insulators," *Electrical Insulation Magazine, IEEE,* vol. 13, pp. 36-39, 1997.

[28] A. Tzimas, C. Zachariades, and S. M. Rowland, "Electric field analysis of 132kV EPDM insulator and correlation with ageing features," *Electrical Insulation Conference (EIC), 2013*, Ottawa, 2013.

[29] International Electrotechnical Commission, "Selection and dimensioning of high-voltage insulators intnded for use in polluted conditions - Part 3: Polymer insulators for a.c. systems," *IEC/TS 60815-3*, ed, 2008.

[30] S. Kumagai, B. Marungsri, H. Shinokubo, R. Matsuoka, and N. Yoshimura, "Comparison of leakage current and aging of silicone rubbers and porcelain in both field and salt-fog tests," *Dielectrics and Electrical Insulation, IEEE Transactions on,* vol. 13, pp. 1286-1302, 2006.

[31] K. Iida and R. Hackam, "Low molecular weight of fluid in an alloy of EPDM/SIR [insulator applications]," *Electrical Insulation and Dielectric Phenomena, 2004. CEIDP '04. 2004 Annual Report Conference on*, 2004, pp. 607-610.

[32] International Electrotechnical Commission, "Selection and dimensioning of high-voltage insulators intnded for use in polluted conditions - Part 1: Definitions, information and general principles," *IEC/TS 60815-1*, ed, 2008.

[33] R. Matsuoka, S. Ito, K. Sakanishi, and K. Naito, "Flashover on contaminated insulators with different diameters," *Electrical Insulation, IEEE Transactions on,* vol. 26, pp. 1140-1146, 1991.

[34] A. J. Phillips, J. Kuffel, A. Baker, J. Burnham, A. Carreira, E. Cherney, W. Chisholm, M. Farzaneh, R. Gemignani, A. Gillespie, T. Grisham, R. Hill, T. Saha, B. Vancia, and J. Yu, "Electric Fields on AC Composite Transmission Line Insulators," *Power Delivery, IEEE Transactions on,* vol. 23, pp. 823-830, 2008.

[35] K. Sokolija and M. Kapetanovic, "About some important items of composite insulators design," *High Voltage Engineering, 1999. Eleventh International Symposium on (Conf. Publ. No. 467)*, 1999, pp. 284-287 vol.4.

[36] Hydro-Québec Transmission Committee and Hydro-Québec Distribution Committee, *Committee of Experts Appointed by Hydro-Québec's Board of Directors Report on January 1998 Ice Storm*: Hydro-Québec, 1998.

[37] M. Farzaneh, "Ice accretions on high–voltage conductors and insulators and related phenomena," *Phil. Trans. Roy. Soc.,* vol. 358, pp. 2971-3005, 2000.

[38] M. Farzaneh and O. T. Melo, "Properties and effect of freezing rain and winter fog on outline insulators," *Cold Regions Science and Technology,* vol. 19, pp. 33-46, 1990.

[39] M. Farzaneh, J. Zhang, and S. S. Aboutorabi, "Effects of insulator profile on the critical condition of AC arc propagation on ice-covered insulators," *Electrical Insulation and Dielectric Phenomena, 2002 Annual Report Conference on*, 2002, pp. 383-387.

[40] M. C. Farzaneh, W.A., *Insulators for Icing and Polluted Environments*. Hoboken, New Jersey: John Wiley & Sons, 2009.

[41] T. Udo, "Switching Surge Sparkover Characteristics of Air Gaps and Insulator Strings Under Practical Conditions," *Power Apparatus and Systems, IEEE Transactions on,* vol. PAS-85, pp. 859-864, 1966.

[42] Y. Watanabe, "Flashover Tests of Insulators Covered with Ice or Snow," *Power Apparatus and Systems, IEEE Transactions on,* vol. PAS-97, pp. 1788-1794, 1978.

[43] H. Qin, S. Lichun, J. Xingliang, S. Caixin, Z. Zhijin, and H. Jianlin, "Effects of shed configuration on AC flashover performance of ice-covered composite long-rod insulators," *Dielectrics and Electrical Insulation, IEEE Transactions on,* vol. 19, pp. 200-208, 2012.

[44] H. Jianlin, S. Caixin, J. Xingliang, and S. Lichun, "Flashover Performance of Pre-contaminated and Ice-covered Composite Insulators to be Used in 1000 kV UHV AC Transmission Lines," *Dielectrics and Electrical Insulation, IEEE Transactions on,* vol. 14, pp. 1347-1356, 2007.

[45] C. L. Phan and M. Hara, "Leakage Current and Flashover Performance of Iced Insulators," *Power Apparatus and Systems, IEEE Transactions on,* vol. PAS-98, pp. 849-859, 1979.

[46] E. A. Cherney, "Flashover Performance of Artificially Contaminated and ICED Long-Rod Transmission Line Insulators," *Power Apparatus and Systems, IEEE Transactions on,* vol. PAS-99, pp. 46-52, 1980.

[47] G. G. Karady, M. Shah, and R. L. Brown, "Flashover mechanism of silicone rubber insulators used for outdoor insulation-I," *Power Delivery, IEEE Transactions on,* vol. 10, pp. 1965-1971, 1995.

[48] G. G. Karady, "Flashover mechanism of non-ceramic insulators," *Dielectrics and Electrical Insulation, IEEE Transactions on,* vol. 6, pp. 718-723, 1999.

[49] S. Wang, X. Liang, and L. Huang, "Experimental study on the pollution flashover mechanism of polymer insulators," *Power Engineering Society Winter Meeting, 2000. IEEE*, 2000, pp. 2830-2833 vol.4.

[50] B. F. Hampton, "Flashover mechanism of polluted insulation," *Electrical Engineers, Proceedings of the Institution of,* vol. 111, pp. 985-990, 1964.

[51] S. Rowland, J. Robertson, Y. Xiong, and R. Day, "Electrical and material characterization of field-aged 400 kV silicone rubber composite insulators," *Dielectrics and Electrical Insulation, IEEE Transactions on,* vol. 17, pp. 375-383, 2010.

[52] M. Shah, G. G. Karady, and R. L. Brown, "Flashover mechanism of silicone rubber insulators used for outdoor insulation-II," *Power Delivery, IEEE Transactions on,* vol. 10, pp. 1972-1978, 1995.

[53] I. Cotton, M. N. R. Baharom, S. M. Rowland, D. Chambers, N. Weatherby, and M. Thorne, "Support Towers, Insulating Cross-arms and Insulating Members for High Voltage Power Networks," International Patent WO 2011/021006 A2, 2011.

[54] R. C. Hibbeler, *Statics and Mechanics of Materials*, 2nd ed. Singapore: Prentice Hall Inc., 2004.

[55] The British Standards Institution, "High-voltage test techniques - Part 1: General definitions and test requirements," *BS EN 60060-1*, ed, 2010.

[56] National Grid, "Technical Guidance Note - Electrical Parameters and Impedance Characteristics of Plant, Lines and Cables," *TGN(E) 166*, ed, 2002.

[57] National Grid, "Technical Specification - Insulator Sets for Overhead Lines," *TS 3.4.17*, ed, 2006.

[58] The University of Manchester, "Mouldings used in cross-arms of electricity pylons," United Kingdom Patent 002028720-0001, 2012.

[59] E. Kuffel, W. S. Zaengl, and J. Kuffel, *High Voltage Engineering Fundamentals*, 2nd ed.: Butterworth-Heinemann, 2000.

[60] J. S. Chang, P. A. Lawless, and T. Yamamoto, "Corona discharge processes," *Plasma Science, IEEE Transactions on,* vol. 19, pp. 1152-1166, 1991.

[61] H. Raether, *Electron avalanches and breakdown in gases*. Washington: Butterworths, 1964.

[62] L. B. Loeb, *Electrical coronas: their basic physical mechanisms*. Berkeley, LA: University of California Press, 1965.

[63] N. G. Trinh, "Partial discharge XIX: Discharge in Air - Part I: Physical Mechanisms," *Electrical Insulation Magazine, IEEE,* vol. 11, pp. 23-29, 1995.

[64] G. W. Trichel, "The Mechanism of the Negative Point to Plane Corona Near Onset," *Physical Review,* vol. 54, pp. 1078-1084, 12/15/ 1938.

[65] L. B. Loeb, "The Mechanism of the Trichel Pulses of Short Time Duration in Air," *Physical Review,* vol. 86, pp. 256-257, 04/15/ 1952.

[66] L. L. Grigsby, Ed., *The Electric Power Engineering Handbook: Electric Power Generation, Transmission and Distribution*. CRC Press, 2012, p.^pp. Pages.

[67] N. G. Trinh and J. B. Jordan, "Modes of Corona Discharges in Air," *Power Apparatus and Systems, IEEE Transactions on,* vol. PAS-87, pp. 1207-1215, 1968.

[68] N. G. Trinh and J. B. Jordan, "Trichel Streamers and Their Transition into the Pulseless Glow Discharge," *Journal of Applied Physics,* vol. 41, 1970.

[69] F. W. Peek, *Dielectric Phenomena in High Voltage Engineering*, 3rd ed. New York: McGraw-Hill Book Company, 1929.

[70] EPRI, *AC Transmission Line Reference Book - 200 kV and Above*, 3rd ed. Palo Alto: Electrical Power Research Institude, 2005.

[71] N. G. Trinh, "Partial Discharge XX: Partial Discharges in Air - Part II: Selection of Line Conductors," *Electrical Insulation Magazine, IEEE,* vol. 11, pp. 5-11, 1995.

[72] G. E. Adams, "The Calculation of the Radio Interference Level of Transmission Lines Caused by Corona Discharges [includes discussion]," *Power apparatus and systems, part iii. transactions of the american institute of electrical engineers,* vol. 75, 1956.

[73] G. W. Juette, "Evaluation of Television Interference from High-Voltage Transmission Lines," *Power Apparatus and Systems, IEEE Transactions on,* vol. PAS-91, pp. 865-873, 1972.

[74] A. J. Phillips, D. J. Childs, and H. M. Schneider, "Aging of nonceramic insulators due to corona from water drops," *Power Delivery, IEEE Transactions on,* vol. 14, pp. 1081-1089, 1999.

[75] Z. Yong, K. Haji, M. Otsubo, and C. Honda, "Surface Degradation of Silicone Rubber Exposed to Corona Discharge," *Plasma Science, IEEE Transactions on,* vol. 34, pp. 1094-1098, 2006.

[76] A. J. Phillips, D. J. Childs, and H. M. Schneider, "Water drop corona effects on full-scale 500 kV non-ceramic insulators," *Power Delivery, IEEE Transactions on,* vol. 14, pp. 258-265, 1999.

[77] E. A. Cherney, "Partial discharge. V. PD in polymer-type line insulators," *Electrical Insulation Magazine, IEEE,* vol. 7, pp. 28-32, 1991.

[78] K. Sokolija, M. Kapetanovic, R. Hartings, and M. Hajro, "Considerations on the Design of Composite Suspension Insulators Based on Experience from Natural Ageing Testing and Electric Field Calculations," *CIGRÉ Session 2000,* vol. 33-204, 2000.

[79] V. M. Moreno and R. S. Gorur, "Impact of corona on the long-term performance of nonceramic insulators," *Dielectrics and Electrical Insulation, IEEE Transactions on,* vol. 10, pp. 80-95, 2003.

[80] National Grid, "Technical Specification - Composite Insulators for Overhead Lines," *TS 3.4.18*, ed, 2008.

[81] R. Hartings, "Electric fields along a post insulator: AC-measurements and calculations," *Power Delivery, IEEE Transactions on,* vol. 9, pp. 912-918, 1994.

[82] G. H. Vaillancourt, S. Carignan, and C. Jean, "Experience with the detection of faulty composite insulators on high-voltage power lines by the electric field measurement method," *Power Delivery, IEEE Transactions on,* vol. 13, pp. 661-666, 1998.

[83] P. M. Kurowski, *Finite Element Analysis for Design Engineers*. Warrendale, USA: Society of Automotive Engineers, Inc., 2004.

[84] O. C. Zienkiewicz, R. L. Taylor, and J. Z. Zhu, *Finite Element Method - Its Basis and Fundamentals*, 6th ed. Barcelona, Spain: Elsevier, 2005.

[85] COMSOL Inc. (2014). *COMSOL Multiphysics Software Product Suite*. Available: http://www.uk.comsol.com/products

[86] D. Stefanini, J. M. Seifert, M. Clemens, and D. Weida, "Three dimensional FEM electrical field calculations for EHV composite insulator strings," *Power Modulator and High Voltage Conference (IPMHVC), 2010 IEEE International*, 2010, pp. 238-242.

[87] COMSOL Inc., "COMSOL Multiphysics User's Guide," *version 4.3*, ed, 2012.

[88] S. M. Rowland, I. Cotton, C. Zachariades, V. Peesapati, and D. Chambers, "A Grading Device," United Kingdom Patent GB1208885.2, 2012.

[89] The British Standards Institution, "Polymeric insulators for indoor and outdoor use with a nominal voltage > 1 000 V - General definitions, test methods and acceptance criteria," *BS EN 62217*, ed, 2006.

[90] N. S. Naidu and V. Kamaraju, *High Voltage Engineering*, 2nd ed. USA: McGraw-Hill, 1995.

[91] C. H. Flurscheim, Ed., *Power Circuit Breaker Theory and Design* (IET Power and Energy Series 1. United Kingdom: The Institution of Engineering and Technology, 2008, p.^pp. Pages.

[92] W. Bretuj and K. Wieczorek, "Influence of composite insulator operating position on the development of aging process under AC high voltage and water precipitation," *High Voltage Engineering and Application (ICHVE), 2010 International Conference on*, 2010, pp. 540-543.

[93] E. W. Kimbark and A. C. Legate, "Fault Surge Versus Switching Surge A Study of Transient Overvoltages Caused by Line-to-Ground Faults," *Power Apparatus and Systems, IEEE Transactions on,* vol. PAS-87, pp. 1762-1769, 1968.

[94] The British Standards Institution, "Plastics and ebonite - Determination of indentation hardness by means of a durometer (Shore hardness)," *BS EN ISO 868:2003*, ed, 2003.

[95] The British Standards Institution, "Plastics - Methods of exposure to laboratory light sources - Part 2: Xenon-arc lamps," *BS EN ISO 4892-2:2006+A1:2009*, ed, 2009.

[96] The British Standards Institution, "Plastics - Methods of exposure to laboratory light sources - Part 3: Fluorescent UV lamps," *BS EN ISO 4892-3:2006*, ed, 2006.

[97] The British Standards Institution, "Geometrical product specification (GPS) - Surface texture: Profile method - Terms, definitions and surface texture parameters," *BS EN ISO 4287:1998+A1:2009*, ed, 2009.

[98] The British Standards Institution, "Fire hazard testing - Part 11-10: Test flames - 50 W horizontal and vertical flame test methods," *BS EN 60695-11-10:1999+A1:2003*, ed, 2003.

[99] The British Standards Institution, "Radio interference characteristics of overhead power lines and high-voltage equipment - Part 2: Methods of measurement and procedure for determining limits," *PD CISPR/TR 18-2:2010*, ed, 2010.

[100] T. R. Kuphaldt. (2012). *All About Circuits: Volume I - DC*. Available: http://www.allaboutcircuits.com/

[101] C. Zachariades, S. M. Rowland, I. Cotton, P. R. Green, C. A. Veerappan, and D. Chambers, "A Trial Installation of High Voltage Composite Cross-arms," *XVII International Symposium on High Voltage Engineering*, Hannover, Germany, 2011.

[102] A. A. J. Al-Baghdadi, "Flashover mechanisms of polluted insulation," PhD, Electrical Engineering and Electronics, UMIST, Manchester, 1970.

[103] A. Blythe and D. Bloor, *Electrical properties of polymers*, 2nd ed. Cambridge: Cambridge University Press, 2005.

Appendix A

List of publications

1. Rowland, S.M. Maclaren, R. Cotton, I. Chambers, D. Peesapati, V. Zachariades, C. "Development of insulating cross-arms for compact HV lattice structures," *2014 CIGRÉ Session*, Paris, 2014.

2. Zachariades, C. Rowland, S.M. Cotton, I. "Real-time Monitoring of Leakage Current on Insulating Cross-arms in Relation to Local Weather Conditions," *IEEE Electrical Insulation Conference (EIC)*, Ottawa, 2013.

3. Zachariades, C. Peesapati, V. Cotton, I. Green, P.R. Chambers, D. Rowland, S.M. "Design and Testing of a 400 kV Insulating Cross-arm," *12th International Electrical Insulation Conference (INSUCON)*, Birmingham, 2013.

4. Peesapati, V. Zachariades, C. Li, Q. Rowland, S.M. Cotton, I. Chambers, D. Allison F., "Electric Field Computation for a 400 kV Composite Cross-Arm," *IEEE Conference on Electrical Insulation and Dielectric Phenomena (CEIDP)*, Montreal, Canada, 2012.

5. Zachariades, C. Cotton, I. Rowland, S.M. Peesapati, V. Green, P.R. Chambers, D. Queen, M., "A Coastal Trial Facility for High Voltage Composite Cross-arms," *IEEE International Symposium on Electrical Insulation (ISEI)*, San Juan, Puerto Rico, 2012.

6. Peesapati, V. Zachariades, C. Cotton, I. Rowland, S.M. Green, P.R. Chambers, D. Allison F., "3D Electric Field Computation of a Composite Cross-Arm," *2012 IEEE International Symposium on Electrical Insulation (ISEI)*, San Juan, Puerto Rico, 2012.

7. Zachariades, C. Rowland, S. M. Cotton, I. Green, P. R. Veerappan, C. A. Chambers, D., "A Trial Installation of High Voltage Composite Cross-Arms," *XVII International Symposium on High Voltage Engineering (ISH)*, Hannover, Germany, 2011.

Appendix B

Mechanical trial instrumentation

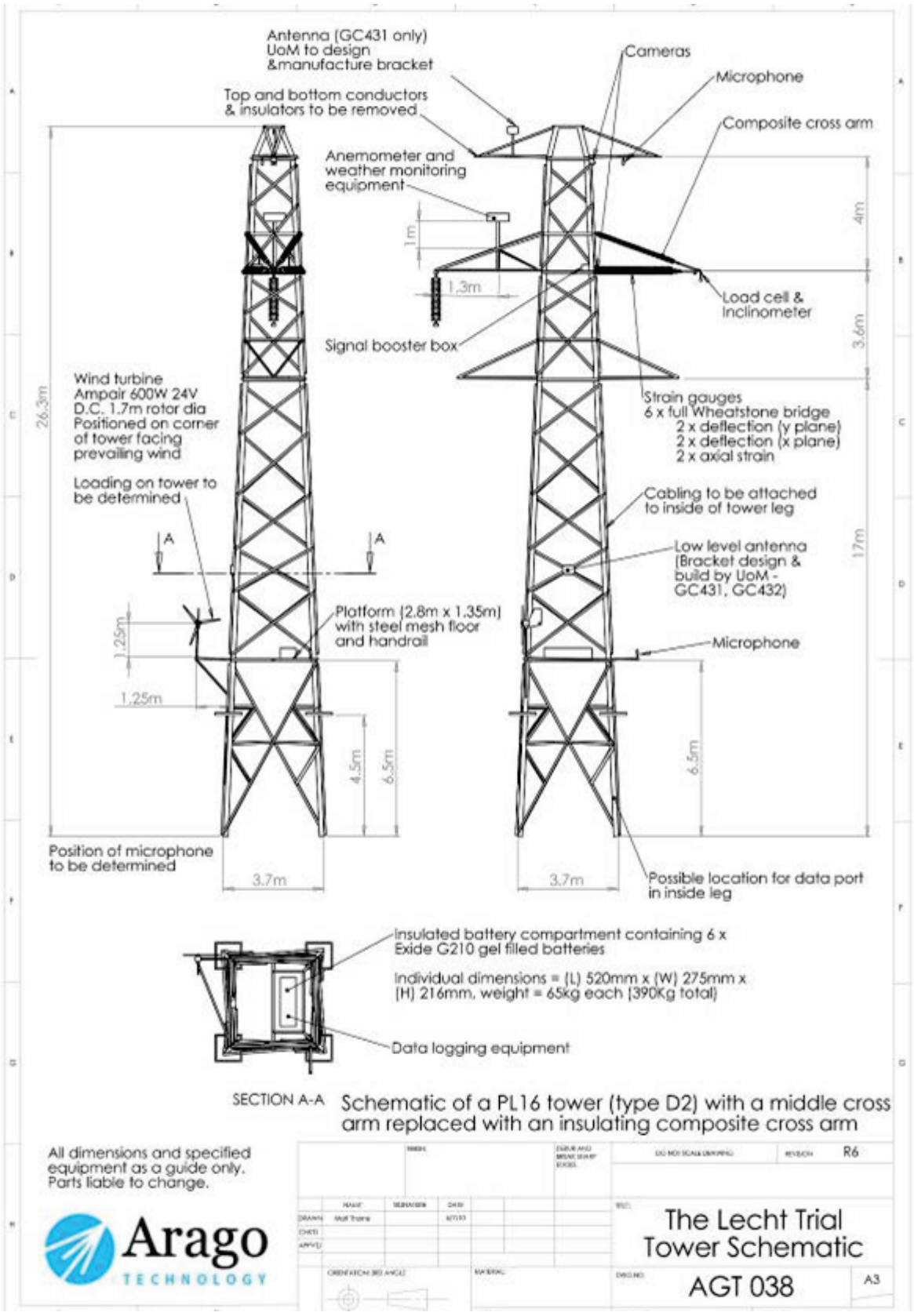

Figure B. 1 – Mechanical trial instrumentation arrangement on PL16 tower

Appendix C

Live trial instrumentation

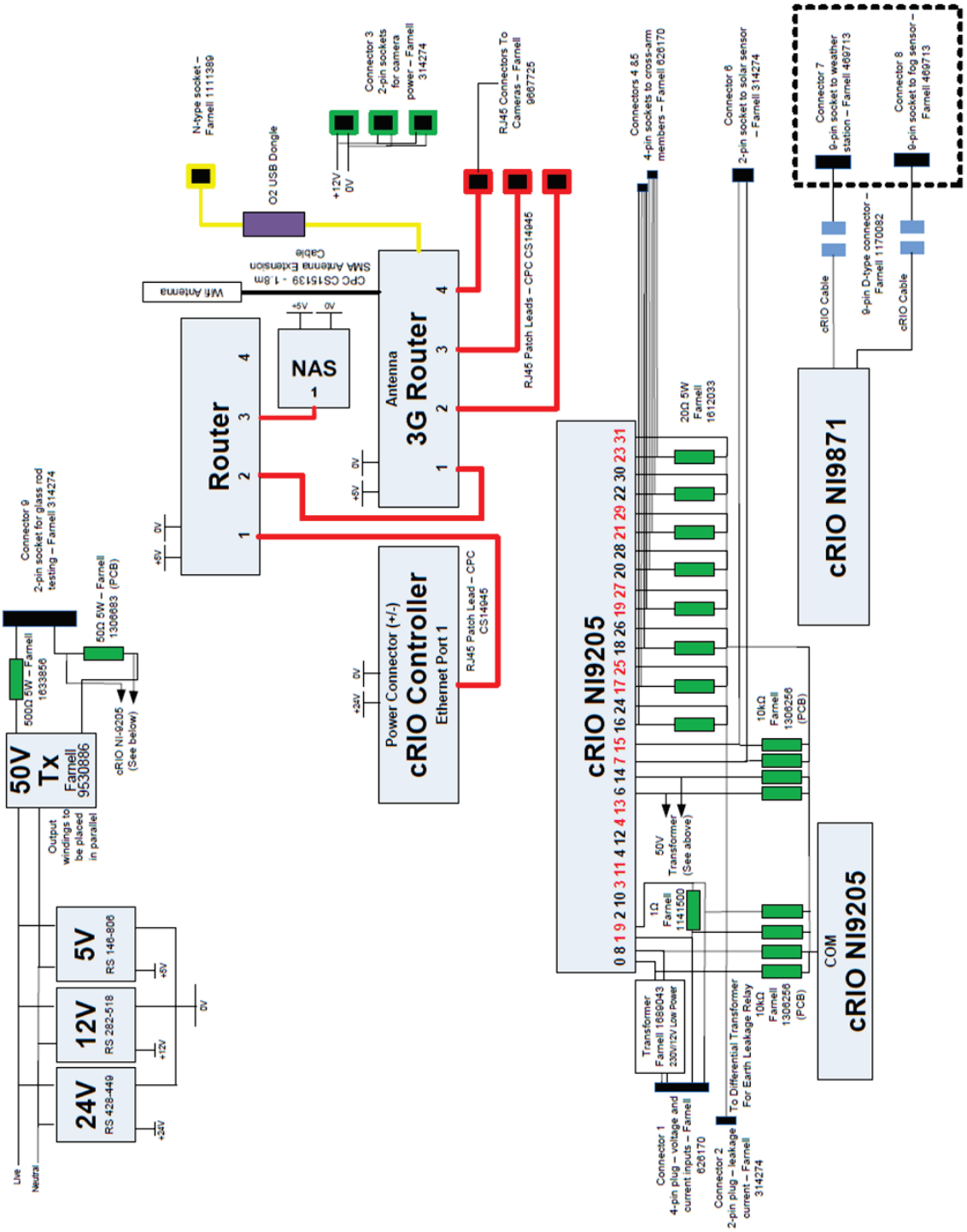

Figure C. 1 - Monitoring system wiring diagram

Appendix D

Specimen for compression insulator testing

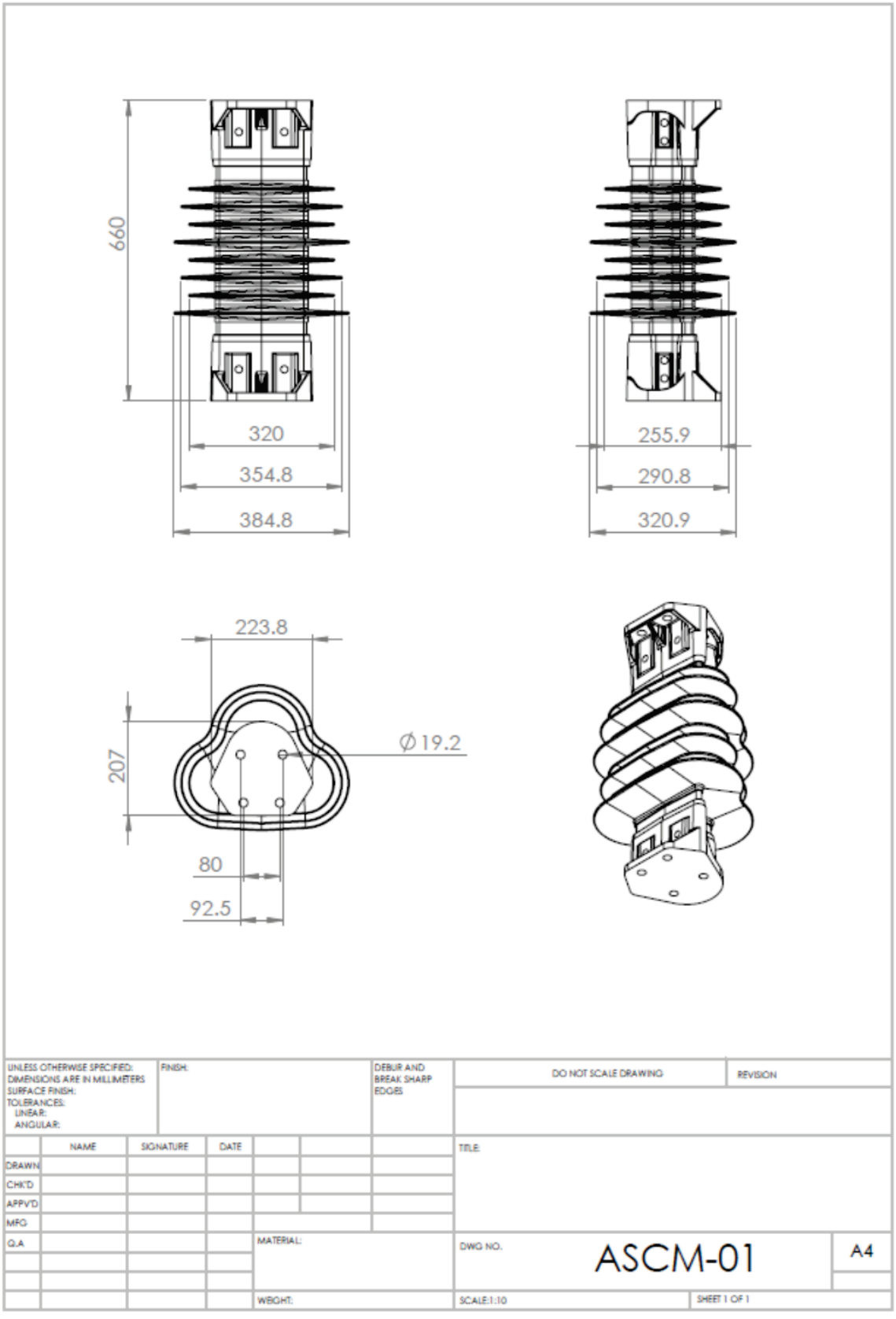

Figure D. 1 – Diagram of specimen for compression insulator testing

Appendix E

Live trial monthly leakage current plots

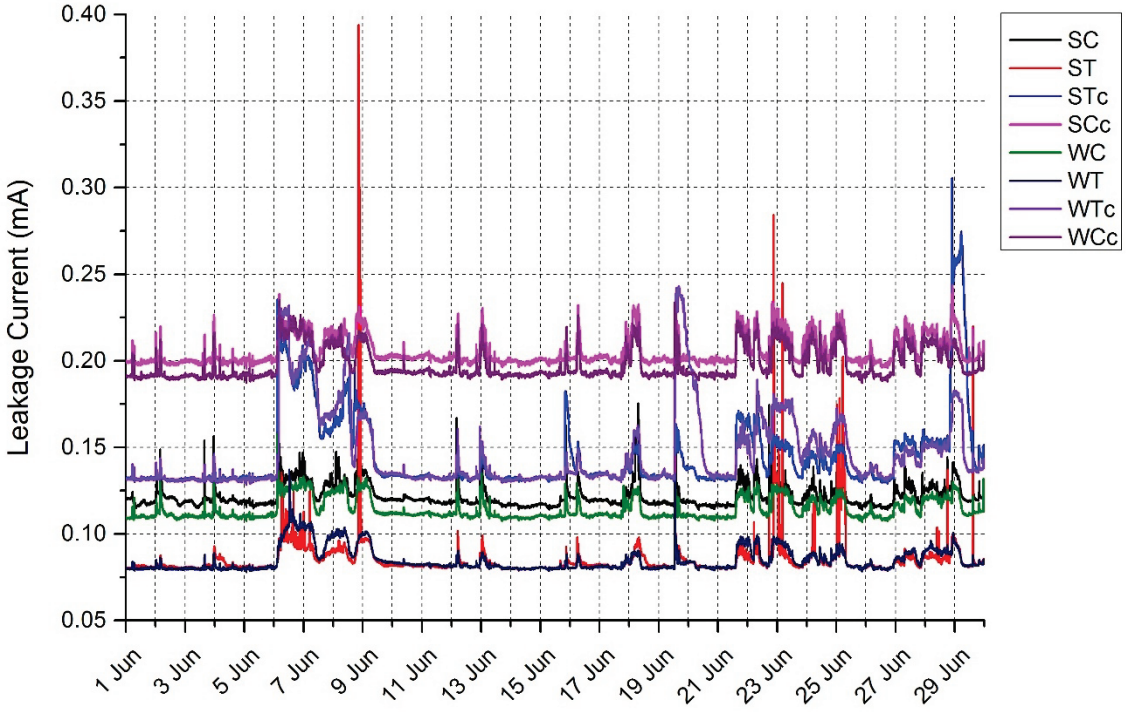

Figure E. 1 – Leakage currents for June 2012

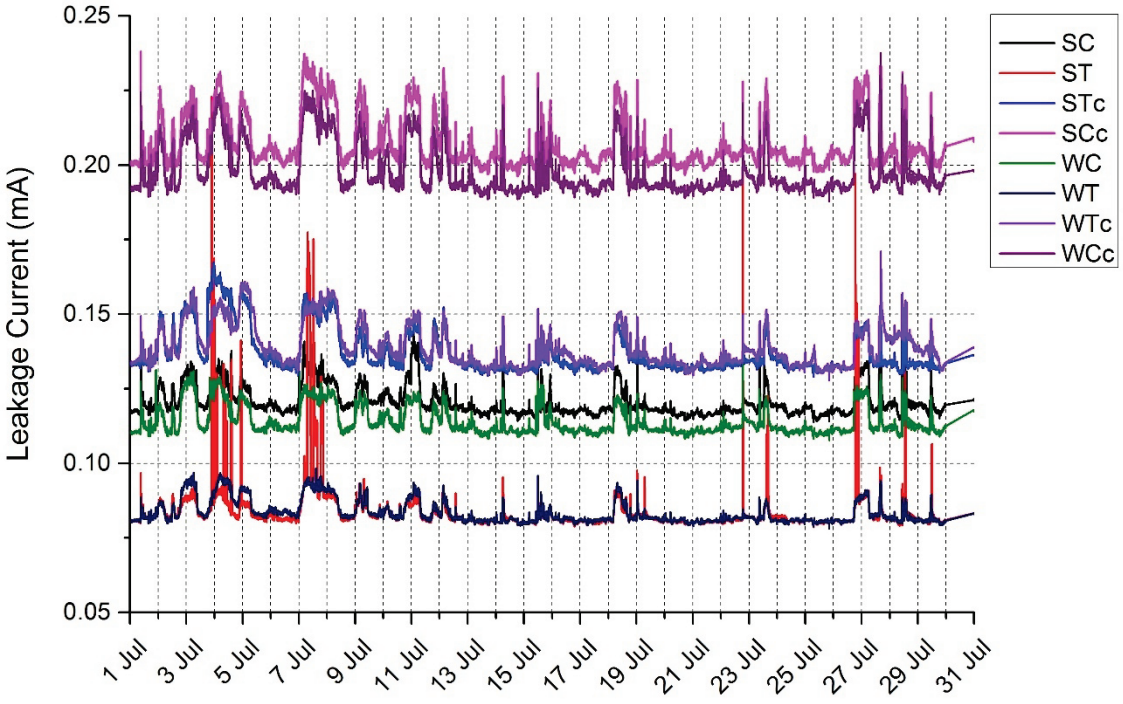

Figure E. 2 – Leakage currents for July 2012

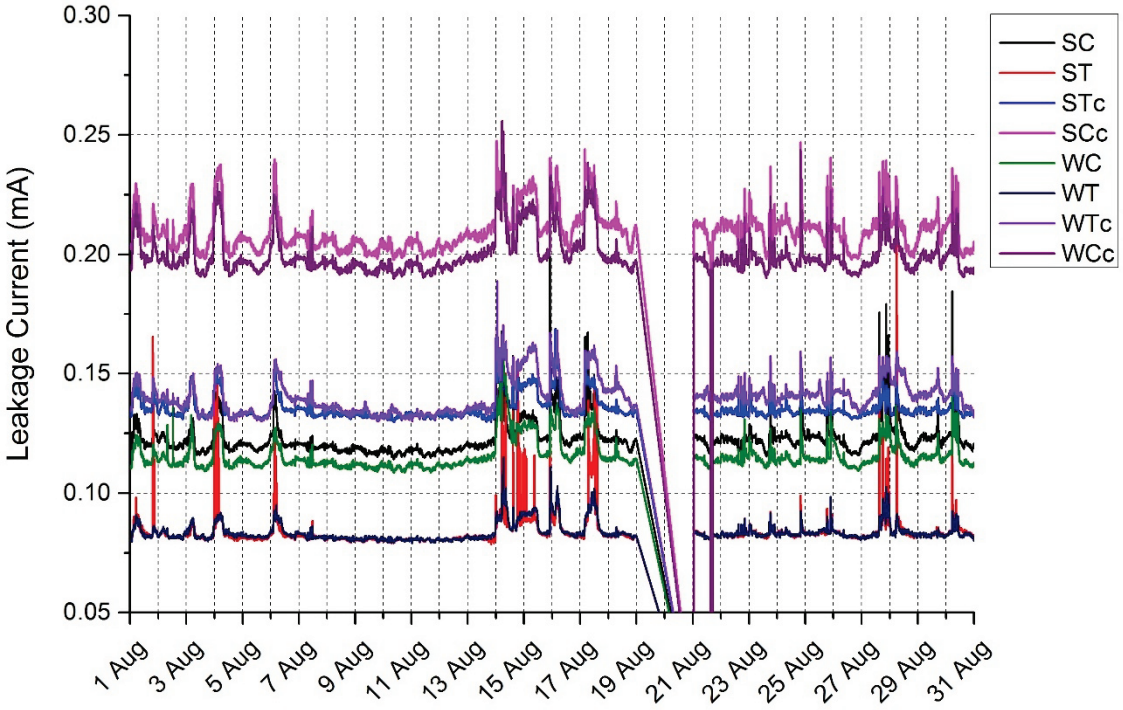

Figure E. 3 – Leakage currents for August 2012

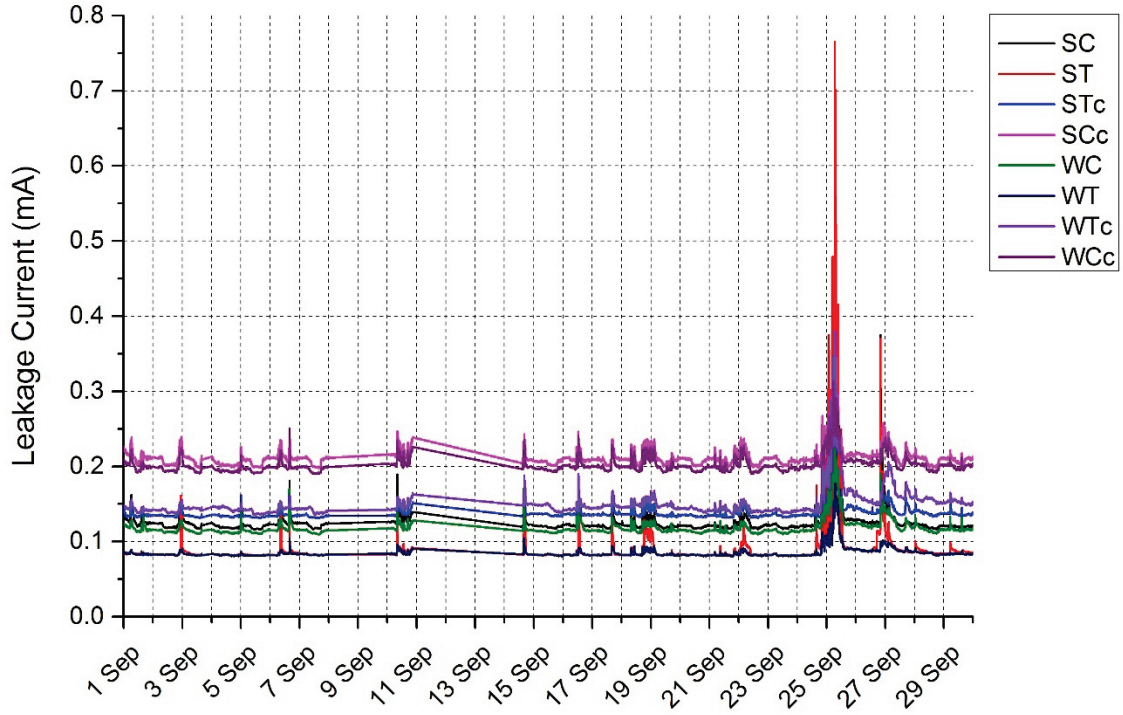

Figure E. 4 – Leakage currents for September 2012

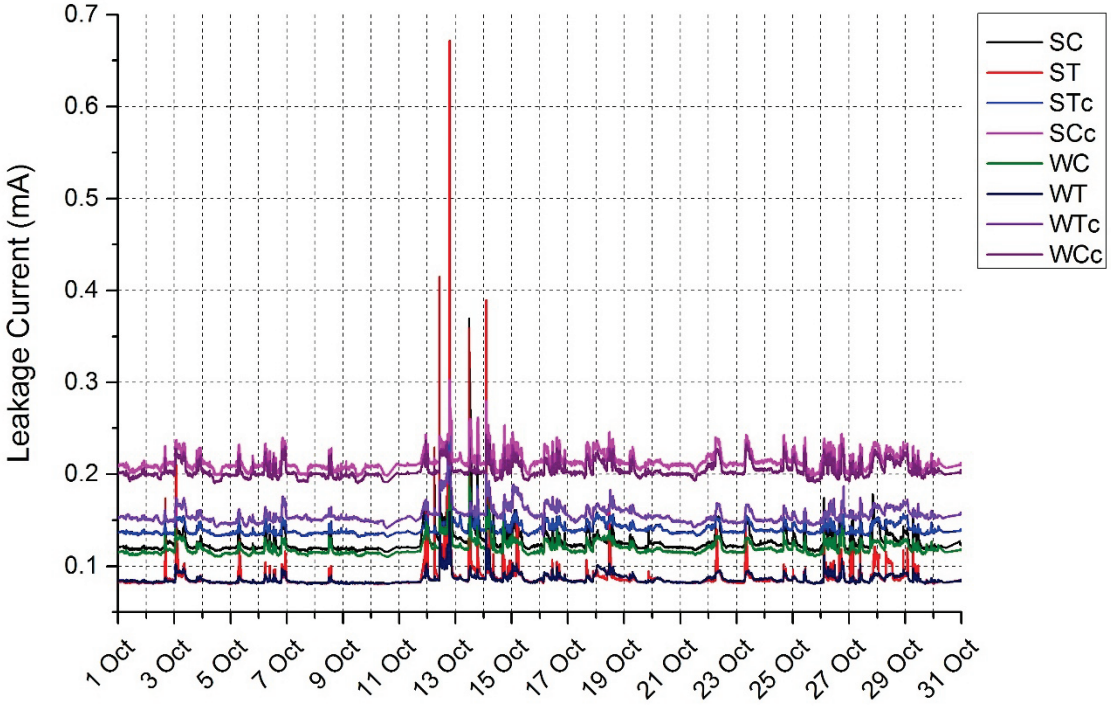

Figure E. 5 – Leakage currents for October 2012

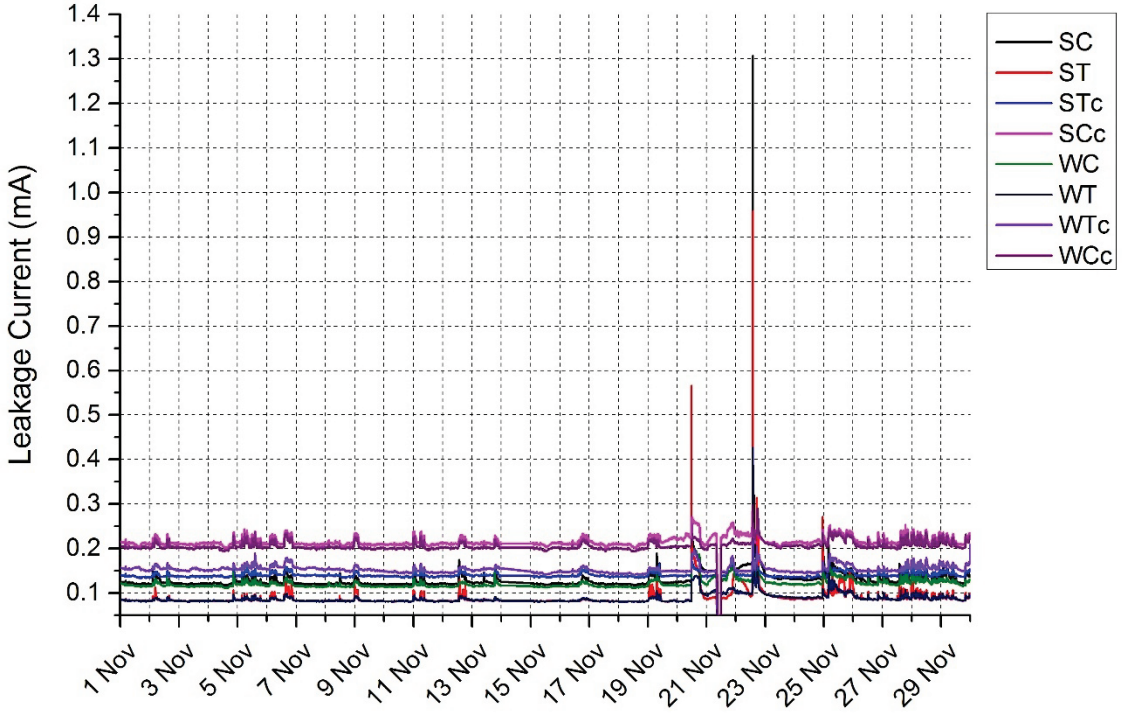

Figure E. 6 – Leakage currents for November 2012

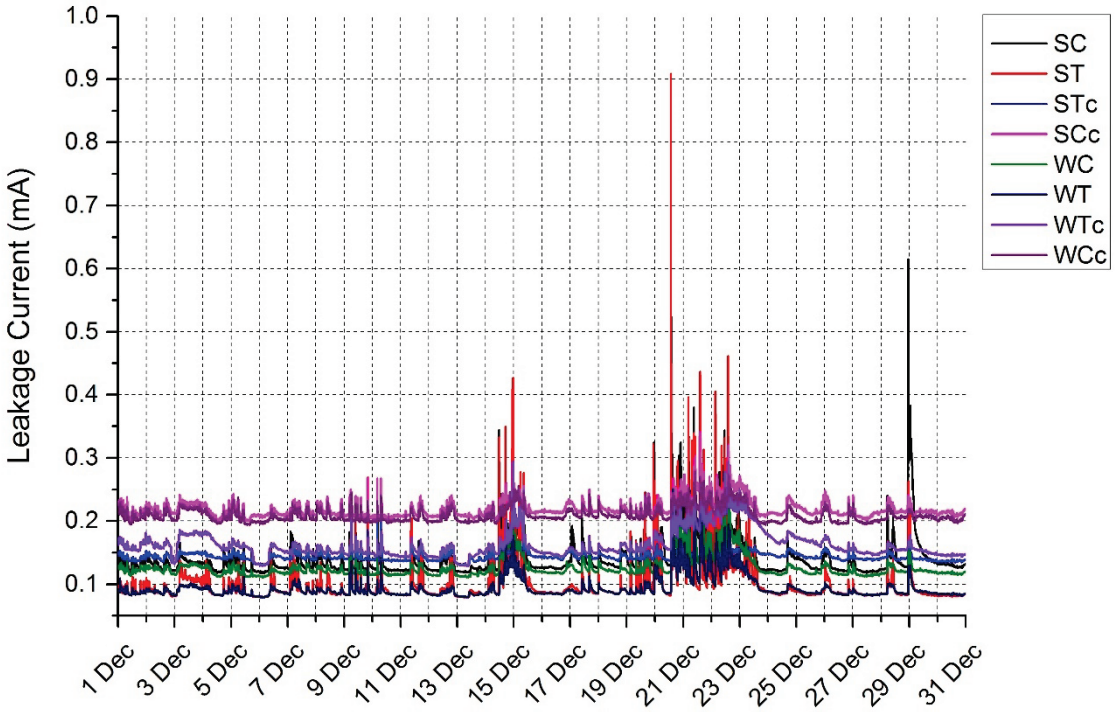

Figure E. 7 – Leakage currents for December 2012

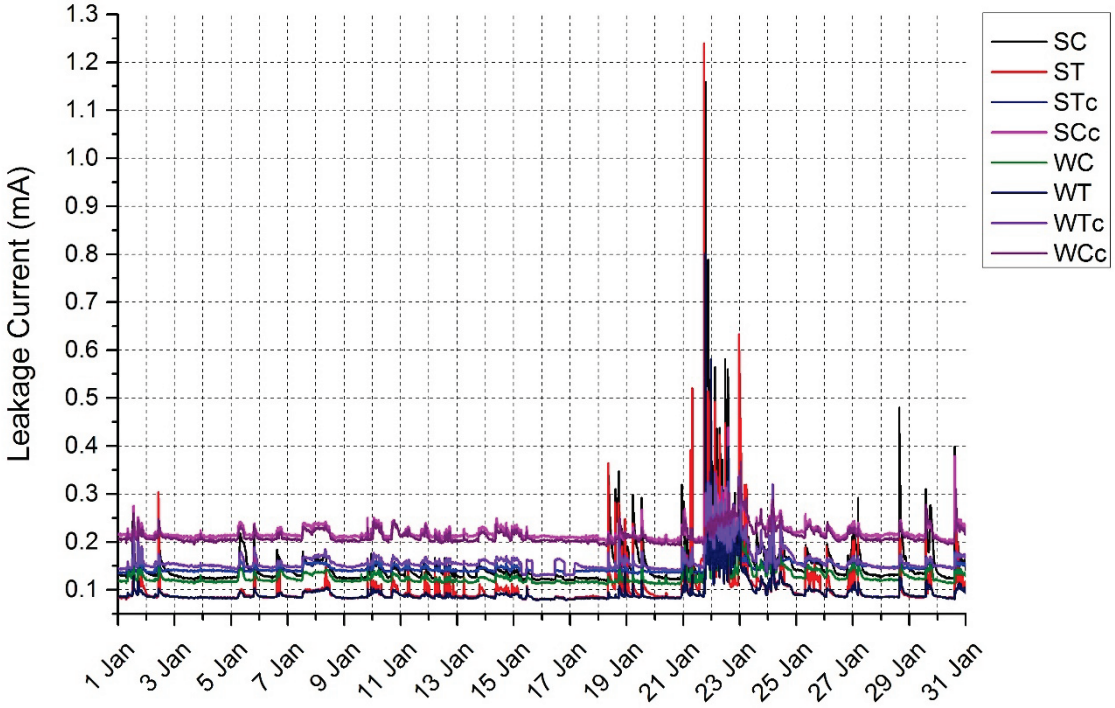

Figure E. 8 – Leakage currents for January 2013

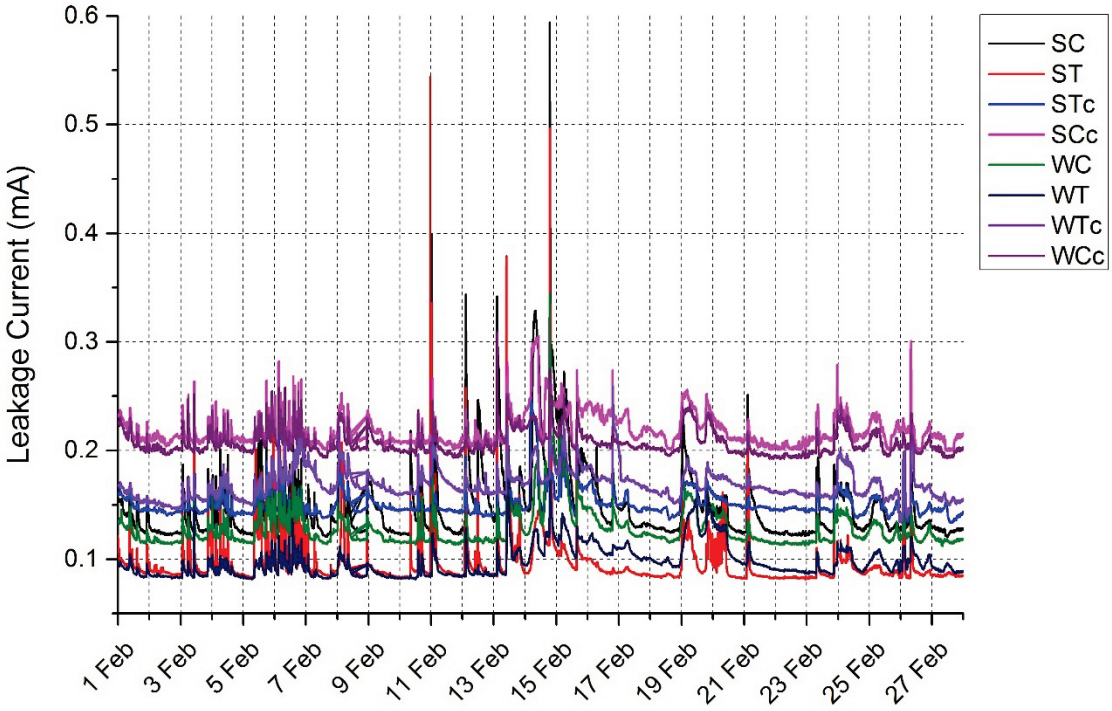

Figure E. 9 – Leakage currents for February 2013

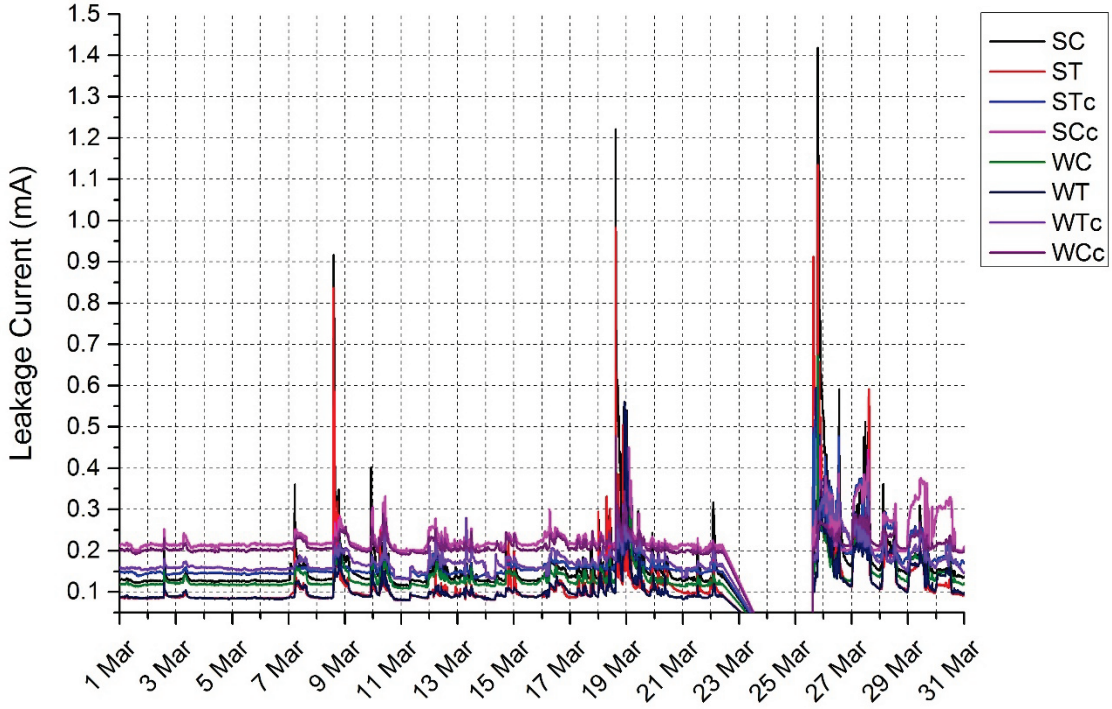

Figure E. 10 – Leakage currents for March 2013

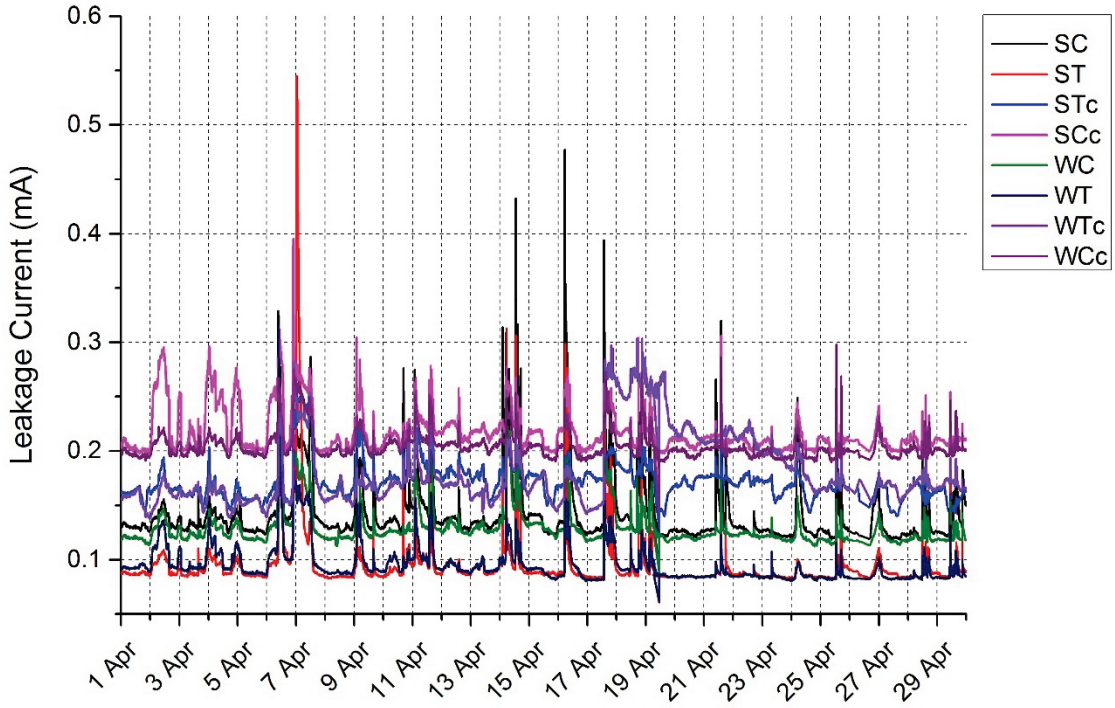

Figure E. 11 – Leakage currents for April 2013

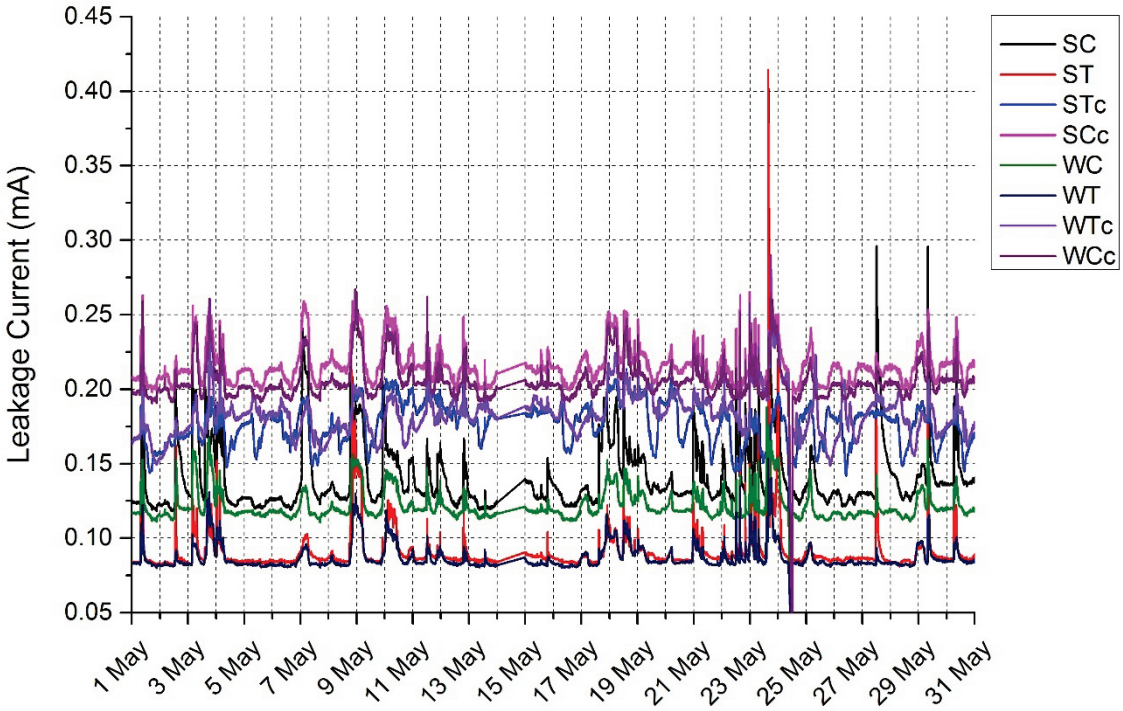

Figure E. 12 – Leakage currents for May 2013